High power, high intensity few-cycle pulses in the mid-IR for strong-field experiments

DISSERTATION

submitted in fulfilment of the
requirements for the degree of
Doctor of Philosophy
by

Matthias Baudisch

ICFO - The Institute of Photonic Sciences
UPC - Universitat Politècnica de Catalunya

Thesis Advisor: Prof. Dr. Jens Biegert

Barcelona, 2017

Abstract

High energy, few-cycle, mid-IR radiation sources featuring high pulse repetition rates are of tremendous interest for a variety of strong-field physics and attoscience applications. Such systems could be used in combination with the high harmonic generation process as novel, tabletop, high flux X-ray radiation sources providing photon energies up to the keV level. Additionally, strong-field ionization experiments of atom and molecules could help unravel the underlying physics of photo-chemical reactions and molecular transformations.

Nevertheless, implementing such sources remains challenging due to the absence of suitable mid-IR laser gain materials. One approach to overcome current limitations is optical parametric chirped pulse amplification (OPCPA). While this method is already commonly used in the visible and near-IR spectral range, just few demonstrations emitting mid-IR, high energy, few-cycle pulses meeting the stringent requirements set by strong-field physics experiments have been demonstrated. In this thesis is present our effort to push the performance of current high power, mid-IR OPCPA systems to overcome existing limitations and to match and even exceed the performance of similar visible and near-IR radiation sources.

We report on the design and implementation of a high efficiency, frequency up-conversion extension of the one-of-a-kind, high power, few-cycle, mid-IR OPCPA system located in the AUO group at the Institute of Photonic Sciences in Barcelona. The unique multi-color source provides optically synchronized, high energy, femtosecond outputs at wavelength ranging from the deep-UV up to the mid-IR regime and a high pulse repetition rate beyond 100 kHz. The short output pulse durations in combination with the all-optical synchronization scheme makes the source a unique tool to drive highly nonlinear and strong-field pump-probe experiments in the tunnel or multi-photon ionization regime.

In the second part, is reported the fundamental redesign and rebuild of the original high power, mid-IR source yielding the first implementation of a GW-level peak-power, mid-IR OPCPA system featuring simultaneously pulse repetition rates beyond 100 kHz. The upscaling of the pulse energy

by a factor of 6 while maintaining the pulse repetition rate yields a mid-IR output average power of 19 W. In order to enable such high mid-IR average power, we performed an in-depth study of common, nonlinear mid-IR crystals in respect to their thermal, via residual absorption induced parametric amplification limitations.

In the third part, is presented one of the first realizations of few-cycle, mid-IR pulse self-compression via filamentary propagation in the anomalous dispersion regime in a bulk medium. The spectro-temporal behavior of the self-compressed pulses is studied as a function of the driving mid-IR pulse parameters resulting in temporal pulse shortening down to sub-3 optical cycles. We prove the suitability of this technique as compact and stable post-compression method featuring CEP-stable, few-cycle pulse generation in the mid-IR spectral range.

Resumen

Las fuentes de radiación que producen pulsos ultra-rápidos de alta energía con longitudes de ondas en el infrarrojo medio, son de inmensa importancia por sus múltiples aplicaciones en la física de altos campos y attosegundos. Estos sistemas pueden ser utilizados para la generación de rayos X de alto flujo mediante el proceso de altos armónicos, alcanzando energías de fotón del orden de miles de electrónvoltios. Por otro lado, los experimentos de ionización de altos campos de átomos y moléculas podrían ser de gran ayuda para investigar las procesos físicos de reacciones foto-químicas y transformaciones moleculares.

Sin embargo, el desarrollo de estas fuentes presenta grandes dificultades a cause de la falta de materiales láser que emitan ondas en el infrarrojo medio. Una solución para superar estos obstáculos son los sistemas con una arquitectura de optical parametric chirped pulse amplificación (OPCPA). Mientras este método es muy común en sistemas que emiten radiación visible o en el infrarrojo cercano, muy pocos sistemas se han demostrado que generen radiación ultra-corta en el infrarrojo medio. En esta tesis presentamos una nueva fuente de radiación de infrarrojo medio, que sobrepasa las limitaciones actuales y proporciona unos parámetros de radiación similares a fuentes parecidas que emiten en el visible e infrarrojo cercano.

En el primer parte de la tesis presentamos el diseño y la implementación de una extensión del sistema previo situado en el grupo de investigación AUO del Institute of Photonic Sciences (ICFO) en Barcelona. Esta extensión del sistema permite la generación de múltiples colores de radiación desde el ultravioleta hasta el infrarrojo medio. Todos los pulsos generados son de una duración temporal ultra-corta, de alta energía y sincronizados pasivamente entre ellos, con una frecuencia de repetición de pulsos de 100 kHz. La corta duración de los pulsos en combinación con el sistema de sincronización temporal son las propiedades claves para facilitar experimentos únicos de pump-probe en el régimen de ionización altamente no-lineal y de altos campos.

En la segunda parte de la tesis presentamos un rediseño y reconstrucción fundamental del sistema original con el propósito de sobrepasar los límites

existentes e implementar el primer sistema OPCPA capaz de producir pulsos ópticos en el infrarrojo medio con potencias pico del orden de los GW y frecuencias de repeticiones de 160 kHz. El nuevo sistema es capaz de incrementar la energía de los pulsos por 6, resultando en una potencia media de 19 W. Para permitir este incremento importante, diversos cambios fueron implementados en la fuente de radiación y llevamos a cabo un estudio meticuloso de múltiples cristales de amplificación para investigar su compatibilidad con los altos gradientes de temperatura asociados a estos procesos no-lineales de alta potencia.

En la tercera parte de la tesis presentamos una de las primeras demostraciones de auto-compresión temporal de pulsos ultra-cortos en el infrarrojo medio. Este proceso esta implementado haciendo uso de la propagación filamentaria en la región espectral de dispersión anormal en medios sólidos. Investigamos la evolución de la auto-compresión del pulso electromagnético en función de los parámetros iniciales. Demostramos la utilidad de este método como técnica compacta y estable de auto-compresión temporal, obteniendo pulsos ultra-cortos con una duración temporal de unos pocos ciclos ópticos.

Acknowledgements

First I would like to thank my supervisor Jens Biegert for giving me the opportunity to perform the doctoral study in his research group. His support and advice guided me throughout the years and I learned a lot from his persistent effort to push our experiments and results to higher levels.

Further I want to thank Michaël Hemmer who familiarized and excited me about the world of nonlinear optics, OPCPAs and lasers. His deep knowledge about the underlying physics and his hard working discipline had a lasting impression on me.

I am also very thankful to all my colleagues who worked with me over the years on OPCPA development: Daniel Sánchez, Ugaitz Elu, Alexandre Thai and Hugo Pires. Thank you for all the nerdy office discussions and the fun work together on such unique systems.

Special thanks goes to the ”REMI guys” Benjamin Wolter, Michael Pullen and Michele Sclafani, for the insightful conversations about the curious world of strong-field ionization and the endless nights spend together in the lab. I would not want to miss them.

I also want to thank all the other members of the AUO group for the good time spend together and for making our lab such a great work place. Thanks to Stephan Teichmann, Francisco Silva, Seth Cousin, Alexander Grün, Judith Durá, Dane Austin, Barbara Buades, Nicola Di Palo, Idoia Martí, Noslen Suárez, Aurelien Sanchez, Iker León and Biplob Nandy.

Special thanks goes to my parents Susanne and Ronald and to my sister Elisabeth for all their support, help and advice whenever it was needed.

Y finalmente muchísimas gracias a mi esposa Karen Noelia por su amor y apoyo infinito durante todos estos años.

Contents

List of Figures

List of Tables

Chapter 1

Introduction

Since the first demonstration of the light amplification by stimulated emission of radiation (laser) in 1960 [1], laser devices have become an indispensable tool for a variety of scientific and industrial applications. The ability to create coherent, spectrally broadband electromagnetic radiation, allows the generation of high intensity, ultrashort light pulses, with sufficient electric field strength to drive and investigate a multitude of nonlinear light-matter interaction processes.

A drawback of laser amplification is the restriction of the output pulse center frequencies by the laser gain material specific emission spectra. Therefore, laser sources are often used in combination with optical parametric frequency mixing stages based on second order nonlinearities in order to substantially expand the accessible output pulse frequency range. Nowadays coherent radiation sources emitting in the visible to near-IR spectral range can produce a variety of output characteristics. In contrast, the development of coherent, mid-IR (3-8 μm wavelength) radiation sources remains challenging, especially when high energy, few-cycle pulses at high repetition rates far beyond 1 kHz are required. The most common approach for the generation of high energy, few-cycle, mid-IR radiation are cascaded frequency down-conversion schemes driven by titanium doped sapphire (Ti:sapphire) based amplified laser systems. However, these sources are typically restricted to pulse repetition rates in the 1 kHz regime, especially when microjoule pulse energy levels in the mid-IR are desired. The relatively low repetition rates make these systems suboptimal for investigations of processes with small light-matter interaction cross-sections.

This thesis aims to address the existing source limitations by redesigning and developing a novel, mid-IR radiation source which emits high energy, few-cycle pulses at high repetition rates of 160 kHz. Hereby we use optical parametric chirped pulse amplification (OPCPA) as the amplification method [2, 3]. The OPCPA technique relies on optical parametric amplification (OPA) of the temporally stretched seed pulses by high energy,

transform-limited, narrow-band pump pulses in the near-IR. After amplification the amplified seed is recompressed close to the transform-limited pulse duration. The advantages of the OPCPA method compared to common laser amplification are manifold. The temporal stretching of the seed pulses during the OPA process reduces the involved pulse peak power and therefore allows the amplification to much higher pulse energies until the damage threshold of the gain material is reached. Furthermore the spectral gain bandwidth is only dictated by the phase-matching conditions (see section 2.1.3) and can therefore easily be tuned by a change of orientation or temperature of the nonlinear amplification crystal. Additionally, the quasi-instantaneous nature of the OPA process ensures that almost no energy is absorbed in the gain material. As a result, average power limitations and the related requirements for heat management are transferred from the nonlinear amplification crystal to the used pump laser system.

In addition the OPCPA concept also exhibits requirements on the interacting pulses. For instance, a temporal synchronization with a low timing jitter between the seed and pump pulses and a good beam pointing stability is needed in order to ensure good spatio-temporal overlap between the interacting waves. Additionally the seed and pump pulses require a specific direction of linear polarization in order to contribute to the parametric amplification process. Also the duration of the temporally stretched, spectrally broadband seed pulses has to be roughly matched to the transform-limited, narrow-band pump pulses in order to achieve reasonable conversion efficiencies.

Nowadays the OPCPA technique is a commonly used optical amplification method for the generation of high energy, few-cycle pulses in the visible and near-IR frequency range, enabling output pulse energies up to the ten to hundred joule level [4, 5], peak powers in the petawatt range [5], pulse durations down to sub-2 optical cycles [6] and output average powers around 20 watts [6, 7]. In contrast, only very few OPCPA systems allowing few-cycle, high energy pulse generation in the mid-IR spectral region have been demonstrated so far (see section 1.3).

1.1 Motivation for high peak-power, mid-IR radiation sources

Coherent radiation sources emitting in the mid-IR spectral region (3-8 µm wavelength) are of high interest for multiple spectroscopic applications, since numerous rotational and vibrational molecular resonances occur in this spectral range [8, 9]. Possible application are for example environmental trace gas detection [8] and medical diagnostics [9]. Most of these applications are based on linear absorption and can therefore be driven by sources operating in the continuous wave or nanosecond regime.

In contrast, high peak-power radiation sources emitting ultrafast pulses in the mid-IR spectral region enable various nonlinear optical spectroscopy methods such as vibrational sum frequency generation spectroscopy [10], two-dimensional infrared (2D IR) spectroscopy [11] and three-dimensional infrared (3D IR) spectroscopy [12]. Also the feasibility of nonlinear, 2D IR microscopy was recently demonstrated [13]. These techniques are of high scientific interest, since they can provide important information regarding the chemical structure and chemical dynamics of molecules in the condensed phase [11, 12, 14]. Nowadays most of these investigation methods are driven by Ti:sapphire based, amplified laser systems with pulse repetition rates around 1 kHz. Mid-IR OPCPA sources providing similar pulse energies but much higher repetition rates would enable a substantial reduction of the required measurement time and would increase the possible, spectroscopic signal-to-noise ratio. Bradley *et al.* could recently demonstrate the first implementation of 2D IR spectroscopy driven by a high repetition rate, mid-IR OPCPA system [15].

Another application of high peak-power, mid-IR radiation sources is as a driver for strong-field physics or attoscience experiments. In case a focused, high peak-power laser pulse reaches an electric field strength on a gas target of the magnitude close to the Coulomb binding energy E_{bind}, one valence electron can be ejected from the ionized parent molecule. This strong-field ionization process can be achieved either by multi-photon ionization, where N photons are absorbed by the molecule (with $N \cdot E_{photon} > E_{bind}$) or by tunnel-ionization, where the Coulomb potential is sufficiently tilted to allow tunneling of the valence electron outside the Coulomb barrier. An estimation of which ionization process is predominant, is given by the Keldysh parameter γ [16]:

$$\gamma = \sqrt{\frac{E_{bind}}{2 \cdot U_P}} \propto \frac{1}{\lambda\sqrt{I}}, \tag{1.1}$$

where U_P is the so-called ponderomotive energy and I the pulse peak intensity. For $\gamma > 1$ multi-photon ionization takes place, while for $\gamma \ll 1$ tunnel-ionization occurs. In contrast to near-IR driving lasers at 800 nm wavelength, strong-field ionization driven by long, mid-IR wavelengths allows unequivocal ionization in the deep tunneling regime while maintaining a low ionization fraction of the target gas. This unique characteristic has enabled various strong-field ionization experiments which resulted in the discovery of new features in the low kinetic-energy spectrum of the ejected electrons. Examples are the so-called low-energy structures [17], the very low-energy structures [18], and the zero-energy structures [19,20], which discoveries yielded a better physical understanding of the strong-field photo-ionization process.

Long driving wavelength are furthermore important for strong-field ionization processes which are governed by electron recollision dynamics. These processes can be described by a three-step-model [21, 22], where: (i) the electron liberated during ionization is accelerated in the driving laser field, (ii) the electron is redirected toward the parent ion due to the sign change of the oscillating optical electric field, and (iii) the returning electron can be recombined with or scattered from the parent ion. Hereby scales the ponderomotive energy U_P, which the electron gains during its trajectory quadratic with the driving wavelength ($U_P \propto \lambda^2$ [22]). In the case of high harmonic generation (HHG), where the returning electron is recombined with the parent ion, a higher ponderomotive energy leads to the generation of high energy X-ray radiation and potentially shorter attosecond pulses [23]. Popmintchev *et al.* could for example demonstrate the generation of X-ray radiation with photon energies beyond the keV level using a mid-IR driving laser at 3.9 µm center wavelength [24].

Similarly, long driving wavelength are also of high importance when the returning electrons elastically scatter off the parent ion. It has been shown that the rescattered, high kinetic energy electrons contain structural information of the molecule they were deflected from. This fact is used in the so-called laser-induced electron diffraction (LIED) method, where the full kinematic information of the rescattered electrons is detected and used as in situ probe for molecular structure information. This technique has recently been successfully used to image the structure of diatomic [25] molecules. Furthermore, LIED in combination with the mid-IR OPCPA system presented in this thesis recently enabled imaging of the structure of polyatomic molecules [26] and even the structural change of bond-breaking dynamics of acetylene [27]. Further information on the strong-field experiments realized with our OPCPA source is given in appendix A.

1.2 Desired source characteristics to drive strong-field processes

The output pulses of a coherent, pulsed radiation source have to be able to reach electric field strength on the order of the molecule binding energy to drive strong-field ionization. In the case of gaseous media typically peak intensities in the 10^{13} to 10^{14} GW/cm^2 range are demanded for strong-field experiments. As a consequence, an ideal, mid-IR radiation source requires high pulse energies of at least µJ level, short pulse durations below 100 fs and a good beam focusing ability in order to reach the required peak intensities. For example, a mid-IR pulse with 10 µJ energy, 50 fs duration focused to a waist of 15 µm would reach peak intensities of multiple 10^{13} GW/cm^2. Some applications such as HHG require satisfying stringent phase-matching conditions between the responses of an ensemble of atoms, in order to be driven efficiently [28]. In this case it can be beneficial to use longer focusing geometries, requiring driving lasers with higher pulse energies.

A drawback of strong-field ionization driven by mid-IR radiation compared to near-IR is the dramatically reduced interaction cross section of recollision processes, such as HHG or LIED [29–31]. For instance, in the case of HHG the calculated single atom harmonic yield scales for longer driving wavelength λ roughly with $\lambda^{-(5 \text{ to } 6)}$ [29, 30] or even with around λ^{-8} [31]. As a consequence, the next generation of strong-field physics experiments demand mid-IR systems capable of providing intensities sufficiently high to drive strong-field processes, but with pulse repetition rates far beyond the common 1 kHz of amplified Ti:sapphire laser systems. A detailed analysis of the advantages of our mid-IR OPCPA system operating at 160 kHz with respect to for example data acquisition time and signal-to-noise ratios of strong-field experiments is discussed by Wolter *et al.* [32].

In the case when the driving pulse duration gets in the few optical cycle range, the pulse-to-pulse stability and control of the carrier-to-envelope phase (CEP) gets highly attractive for strong-field experiments. Note that one optical cycle at 3 µm center wavelength corresponds to 10 fs duration. In the few-cycle regime the CEP value influences strongly the shape and height of the maximal electric field amplitude and has therefore a huge influence for many strong-field processes. For example CEP-stable, sub-2 cycle pulses allow the generation of isolated attosecond pulses via HHG, where a controlled shift of the CEP value leads to a changing HHG cut-off frequency [33, 34]. Furthermore the CEP value of few-cycle, CEP-stable

pulses influences the direction of direct electron emission from strong-field photo-ionized atoms and molecules, which can be used as direct CEP-phase measurement tool using the so-called Stereo-ATI spectrometer [35]. Further information about generation schemes of CEP-stable pulses can are discussed in section 2.1.4.

The ideal mid-IR radiation source for strong-field experiments should exhibit a high peak-power, CEP-stable, mid-IR output in synchronization with further femtosecond outputs at multiple other wavelengths to allow a multitude of time resolved strong-field photo-ionization studies. The high photon energy of UV pulses could be used for instance to trigger dynamic photo-chemical reactions such as photo-isomerization [36] or photo-dissociation [37]. After the initialization of such process, the mid-IR pulses could be employed in a pump-probe setup to image the dynamic structural change via the LIED or via the Fourier analysis-based 1-dimensional LIED method (FT-LIED) [38]. Additionally, a femtosecond, near-IR pulse could be used to prepare the orientation state of the investigated molecule beforehand via molecular alignment to enable a better control of the strong-field photo-ionization process [39].

All these multi-color pump-probe schemes require pulse durations in the sub-100 fs range in order to allow sufficient temporal pump-probe resolution for most of the photo-chemical processes. Furthermore the output pulses should be all-optically synchronized to ensure a negligible time jitter. Further applications would be enabled by a superposition of various, CEP-stable pulses at different frequencies such as for instance the controlled synthesis of few-cycle, optical waveforms [40]. Furthermore superimposed, CEP-stable pulses can be used for the precise control of the recollision electron trajectories, tailoring for instance the LIED or HHG process [41].

The mid-IR OPCPA system presented in this thesis addresses all of the above mentioned requirements, specifically the generation of mid-IR pulses featuring (i) high peak power, (ii) few-cycle duration, (iii) CEP-stability and (iv) high pulse repetition rates. Furthermore all-optically synchronized, high energy, femtosecond output pulses from the UV to near-IR range are provided.

1.3 State-of-the-art of few-cycle, high energy, mid-IR radiation sources

Despite the growing interest of the strong-field physics community for high energy, mid-IR radiation sources providing coherent light with femtosecond pulse durations, the development of these sources remains challenging and only a handful of systems have been reported worldwide that fulfill the requirements set by strong-field physics experiments. In figure 1.1 is given an overview, to the best of my knowledge, of all the reported broadband mid-IR sources supporting sub-10 optical cycle pulse durations and sufficient pulse energies to drive strong-field ionization processes. The detailed information about the mentioned systems is provided in table C.1 in the appendix C. The mid-IR systems can be roughly divided in Ti:sapphire laser driven OPA/DFG schemes, mid-IR OPCPA architectures emitting radiation between 3 µm and 5 µm wavelengths and novel OPA/OPCPA approaches exploiting pump lasers at 2 µm wavelength and emitting wavelengths above 5 µm wavelengths (blue).

The traditional approach for high energy, mid-IR pulse generation is cascaded parametric frequency down-conversion via OPA and DFG processes driven by amplified Ti:Sapphire laser systems [42–44] or by DFG mixing between the outputs of two temporally synchronized, amplified near-IR lasers [45] (red dots in figure 1.1). The typically low conversion efficiencies of these approaches limit the pulse repetition rate to the kHz regime, in the case when µJ-level pulse energies are required. Schultz *et al.* could for example demonstrate the generation of 160 µJ energy pulses at 3.6 µm wavelength and 1 kHz repetition rate [45]. In contrast, by moving to higher repetition rates of 250 kHz, Reed *et al.* could only generate 60 nJ pulse energies at 4 µm wavelength, which would be insufficient to drive strong-field ionization experiments [46].

Another way to generate few-cycle, high energy radiation in the mid-IR spectral range, is based on OPCPA architectures. This approach, which was strongly developed for the mid-IR spectral range in the last decade, combines the chirped pulse amplification (CPA) scheme with amplification via the OPA process. As result, the systems can be pumped by high power, picosecond-duration pump lasers and high energy conversion efficiencies from the pump laser to the mid-IR output pulses of over ten percent can be reached. The few, currently reported, mid-IR OPCPA systems (red dots in figure 1.1) can be divided according to their repetition rates. On one side there are two, low repetition rate systems at around 10 to 20 Hz, reaching

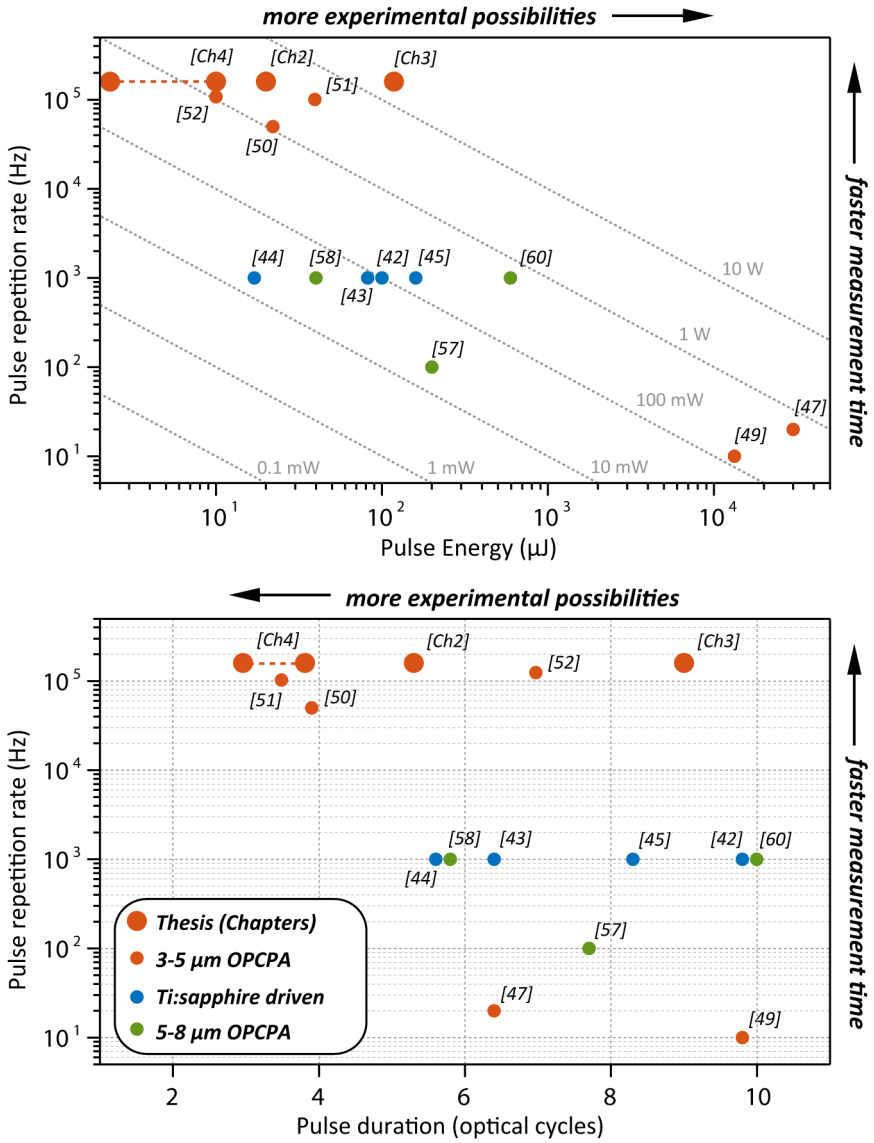

Figure 1.1: Overview of currently existing few-cycle, high energy mid-IR radiation sources suitable for strong-field experiments. Considered are only systems, which support sub-10 optical cycle pulse durations, above 10 µJ pulse energies and center wavelengths beyond 3 µm. Shown are the system parameters of pulse repetition rate, pulse energy, average power (top graph) and pulse duration (bottom graph). Each system is identified by the reference (numbers in square brackets). Detailed information about all systems is given in table C.1 in the appendix C.

pulse energies in the mJ range. Mitrofanov *et al.* demonstrated 30 mJ, 80 fs pulses at 20 Hz [47,48] and Zhao *et al.* presented 13 mJ, 130 fs pulse at 10 Hz repetition rate [49]. On the other side, much higher repetition rates in the 50 kHz to beyond 100 kHz regime are achieved by four sources which support pulse energies in the tens to hundred µJ-range. Mayer *et al.* reported the generation of 22 µJ energy, 44 fs duration pulses at a 50 kHz repetition rate [50], Thiré *et al.* reported the generation of 40 µJ energy, 38 fs duration pulses at a 100 kHz repetition rate [51] and Rigaud *et al.* demonstrated 10 µJ energy, 72 fs duration pulses at 125 kHz repetition rates [52]. In contrast, the high power OPCPA system, reported in this thesis operates at higher pulse repetition rate of 160 kHz, providing pulse energies of 20 µJ (see chapter 2). Figure 1.1 also includes the two main OPCPA system improvements, highlighted in the course of this thesis, which are the further pulse shortening down to 3 optical cycle duration via filamentation in solid media (see chapter 4) and the energy up-scaling to 118 µJ pulse energies (see chapter 3) while maintaining the 160 kHz repetition rate. The latter energy up-scaling yields an output average power of 19 W, which is around 5 times higher than the closest competing systems shown in figure 1.1.

The high pulse repetition rate of our OPCPA system is favorable if not crucial for the experimental investigation of physical processes with low interaction cross-sections. To put the system pulse repetition rate into context for strong-field ionization experiments, note that to achieve similar statistical quality of a 12 h measurement driven at 160 kHz, one would need 1.5 days of data acquisition at 50 kHz and close to 3 months with a 1 kHz repetition rate system. At 10 Hz pulse repetition rate, the same measurement would require multiple years, making the mentioned low repetition rate, mJ energy-level OPCPA systems unsuited for the investigation of low cross-section processes.

Aside from high repetition rates, also high output pulse energies and short output pulses durations are desired in order to enable the investigation of a wider range of highly nonlinear physical processes. The demanded up-scaling of the output pulse energy while providing high pulse repetition rates is challenging due to the higher average powers (product of pulse energy and repetition rate) in the system, which yield an increased heat load on all the optical elements. High beam average power can be an issue for OPA based systems, despite the fact that OPA processes are commonly claimed to be average power independent due to the parametric nature of the energy transfer. Rothhardt *et al.* have for example shown, that residual absorption in BBO crystals can strongly influence the parametric amplification process [53]. In particular in the course of this thesis, the

beam average power influence on the OPA performance of common, mid-IR amplification, nonlinear crystals had to be investigated (see section 3.2 and publication in [54]) in order to enable the high power OPCPA upgrade to the 19 W level, presented in chapter 3.

For completeness, it should be mentioned, that apart from the four highlighted mid-IR OPCPA systems, also two other research groups are more recently developing mid-IR OPCPA systems [55,56]. These very recent developments are not included in figure 1.1, since up to now only preliminary results were presented and neither of these systems could demonstrate yet the pulse compression of their stretched, mid-IR output pulses, making a comparison with the established mid-IR OPCPA systems complicated.

Note that all the above mentioned mid-IR OPCPA systems apply 1 µm wavelength, picosecond-duration pump lasers to drive the OPA process. The applied nonlinear amplification crystals are oxide-based nonlinear crystals, such as potassium titanyl arsenate (KTA) in [47, 48] or periodically poled lithium niobate (PPLN) in [49–52], restricting the accessible mid-IR output wavelength to below 5 µm wavelength due to the limited optical transmission window of these materials. A very novel class of mid-IR OPCPA systems, which was just reported in 2016, focuses on the generation of even longer mid-IR wavelength of above 5 µm (blue dots in figure 1.1). Sanchez *et al.* could demonstrate 180 fs, 200 µJ pulses at 100 Hz repetition rate [57], Malevich *et al.* showed 40 µJ energy, 100 fs pulses at 1 kHz repetition rate [58, 59] and Grafenstein *et al.* reported 240 µJ energy, 166 fs pulses at 1 kHz repetition rate [60]. These output parameters at mid-IR wavelength around 5 µm were enabled by recent advances in holmium-doped fluoride and garnet based, picosecond pump lasers which emit at 2 µm wavelength [61–63] in combination with non-oxide nonlinear crystals such as CSP and ZGP (for non-oxide crystal review see [64]). This long wavelength OPCPA development branch is extremely young and it can be assumed, that multiple years are required, until their performance reaches the more established oxide crystal based OPCPA systems with output wavelength in the 3 to 5 µm range.

1.4 Thesis outline

This thesis focuses on the development and further improvement of a unique high power, mid-IR OPCPA system operating at a high repetition rate of 160 kHz. Hereby we address the different limitations, which previous high energy, few-cycle, mid-IR systems showed. The demonstrated OPCPA

system is specifically designed for applications in the field of strong-field physics and attoscience.

In chapter 2 we introduce the basic concepts, which govern the nonlinear process of parametric amplification and influence the general performance of OPCPA systems. Afterwards, the existing high power, mid-IR OPCPA system is described, whose design and construction process were already started years before my PhD work and ended in the second year of my PhD studies. The second half of chapter 2 highlights the design and experimental realization of a multi-color, high power extension of the mid-IR OPCPA emitting simultaneously high energy, femtosecond pulses in the ultraviolet, visible, near-IR and mid-IR spectral ranges. The spectral variety of the output pulses is outstanding for ultrashort, high power OPCPA systems and enables a multitude of high energy, pump-probe experiments at high repetition rates.

Chapter 3 is dedicated to the power upscaling of the mid-IR OPCPA system to GW-level peak-powers while the high pulse repetition rate of 160 kHz is preserved. This improvement is achieved by multiple changes in the OPCPA design, resulting in high energy conversion efficiencies from the pump pulses to the mid-IR output pulses. In the first part of the chapter, we discuss the theoretical constrains which govern the energy conversion efficiency of OPA processes. Afterwards we study various nonlinear crystals regarding the occurrence of thermally-induced processes which limit the OPA upscaling due to residual absorption of the interacting, high average-power beams in the amplification crystal. In the second part of the chapter we describe the design and output performance of the high peak-power OPCPA system.

In chapter 4 we demonstrate one of the first realizations of a novel approach for the mid-IR, few-cycle pulse generation. Hereby, the output pulses of the mid-IR OPCPA system are post-compressed down to sub-3 optical cycles via self-compression during filament propagation in the anomalous dispersion regime of a bulk material. In the chapter, we first introduce the previously existing pulse compression techniques and describe the theoretical background of the demonstrated, mid-IR compression scheme. Afterwards, the experimental implementation of the few-cycle, mid-IR self-compression method is presented and the spectro-temporal output pulse dynamics are investigated in dependence of multiple input parameters.

Finally in chapter 5 the presented thesis is summarized, and a conclusion and future outlook is given. A brief overview of the multiple strong-field ex-

periments which were enabled by the demonstrated mid-IR OPCPA system is afterwards discussed in the attachment A.

Chapter 2

High power, UV to mid-IR OPCPA

The direct generation of coherent, high energy, mid-IR radiation is challenging due to the absence of suitable laser gain materials in the mid-IR spectral region. One alternative approach is optical parametric amplification (OPA) of mid-IR seed pulses via the optical parametric chirped pulse amplification (OPCPA) technique.
In this chapter the building blocks and characteristics of a unique, high power, mid-IR OPCPA system are presented. The system combines few-cycle, CEP-stable, high energy pulses with high repetition rates of 160 kHz, which are far above the typical 1 kHz of common amplified Ti:sapphire systems. The state-of-the-art radiation source is built at the Attosecond and Ultrafast Optics (AUO) research group at the Institute of Photonic Sciences (ICFO) in Barcelona, Spain and undergoes constantly further developments in order to upscale the output parameters. The system performance before the start of my PhD is documented in [65–68]. The further developments during my PhD time which where realized by myself together with my colleagues Michaël Hemmer and Alexandre Thai are published in [69] and [70]. One of the main source improvements during my PhD is the design and construction of a high efficiency, frequency up-conversion chain (published in [71]), which allows the simultaneous generation of multiple outputs spanning from the ultraviolet to the mid-IR spectral range. All output pulses obtain femtosecond durations and peak-powers in the MW regime, enabling time-resolved, pump-probe experiments in the strong-field ionization regime.

In the following, the theoretical basics of the OPA process and general design considerations of OPCPA systems will be elaborated in section 2.1. Afterwards, in section 2.2 the building blocks of the high power, mid-IR OPCPA will be described. This system is the basis for the development of a high power, femtosecond, multi-color module. The motivation, design

constrains and output characteristics of this multi-color extension of the mid-IR OPCPA system are presented in section 2.3. And finally, possibilities for the further scaling of the multi-color system output parameters are discussed in section 2.4.

2.1 Background of OPA process and OPCPA design

In the following section we will introduce the basic theoretical concepts of nonlinear optics and second order nonlinearities in particular with the focus on optical parametric amplification (OPA). It will be focused on the main physical relationships, which are fundamental for the understanding of the working principles of broadband OPCPA systems and which were used for the design of the high power, multi-color OPCPA systems presented in section 2.2, 2.3 and chapter 3. The interested reader can find more detailed descriptions on the underlying physics in textbooks such as [72,73] or reviews such as [74, 75].

2.1.1 Nonlinear light-matter interaction

During the propagation of light through a medium, the light-matter interaction can be described in the classical electromagnetic picture by an induced macroscopic polarization $\vec{P}$ in the material. The polarisation is dependent on the strength of the applied electric field $\vec{E}$ and can be expressed as a Taylor expansion in $\vec{E}$ under the assumption of an instantaneous response to [73]:

$$\vec{P} = \epsilon_0 \cdot \left(\chi^{(1)}\vec{E} + \chi^{(2)}\vec{E}^2 + \chi^{(3)}\vec{E}^3 + ...\right), \tag{2.1}$$

where ϵ_0 is the permittivity of free space and $\chi^{(n)}$ is the electric susceptibility, which describes the polarization response of the material. The first term of the equation represents the linear propagation of light through the material and describes for example the influence of dispersion on the propagation of ultrashort pulses through a transparent medium. Due to the frequency dependency of the linear electric susceptibility $\chi^{(1)}(\omega)$, which is related to the linear refractive index $n_0(\omega)$ by $n_0(\omega) = 1 + \frac{1}{2}Re[\chi^{(1)}(\omega)]$, the phase velocity $v_{Ph} = \frac{c_0}{n_0(\omega)}$ and the wave vector $k = \frac{\omega \cdot n_0(\omega)}{c_0}$ are frequency dependent. The influence of this linear dispersion on ultrashort pulse propagation is described in detail in section 4.2.1 and is exploited in the scope of this thesis for the design of the temporal stretcher and compressor devices of the OPCPA system (see section 2.1.5).

At high electric field strength such as for example in the case when using ultrashort, high energy laser pulses, the higher order terms in equation 2.1 are no longer negligible and can lead to the generation of new frequencies. Apart from the possible generation of perturbative harmonics of the fundamental electric field, also different seeded light waves can nonlinearly interact in the material and emit waves at new frequencies. The most important second-order nonlinear processes in the scope of this thesis are optical parametric amplification, second-harmonic generation (SHG), difference frequency generation (DFG) and sum-frequency generation (SFG). All these three-wave-interaction processes have to fulfill the photon energy conservation and the momentum conservation:

$$\hbar\omega_p = \hbar\omega_s + \hbar\omega_i, \tag{2.2}$$

$$\hbar\vec{k}_p = \hbar\vec{k}_s + \hbar\vec{k}_i, \tag{2.3}$$

where the different waves are called idler (i), signal (s) and pump (p) wave, implying that $\omega_i < \omega_s < \omega_p$. The energy diagrams of the SHG, OPA, DFG and SFG processes are pictured in figure 2.1.

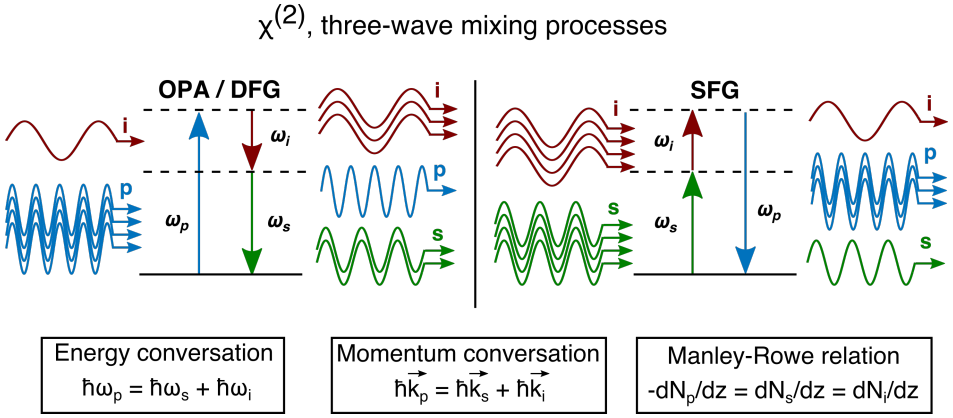

Figure 2.1: Photon energy scheme for various second-order, nonlinear, three-wave mixing processes based on excitation of virtual energy levels (black, dotted lines) in the material. In optical parametric amplification (OPA) and difference frequency generation (DFG) a seeded idler wave is amplified via the annihilation of a pump photon (p). Simultaneously a signal photon (s) at $\omega_s = \omega_p - \omega_i$ is generated. In sum-frequency generation (SFG) one seeded idler (i) and signal photon are annihilated and a pump photon at $\omega_p = \omega_s + \omega_i$ is generated. The nonlinear, three-wave mixing processes have to fulfill energy conservation, momentum conservation and the Manley-Rowe relation.

On the other side, the third-order $\chi^{(3)}$ nonlinearities are especially important in centrosymmetric materials, since in this case the $\chi^{(2)}$ influence vanishes to zero. Important third-order nonlinear effects are for example beam self-focusing and self-phase modulation, which are crucial for filamentation propagation and temporal self-compression, highlighted in chapter 4.

2.1.2 Coupled wave equation of OPA process

Optical parametric amplification (OPA) is a second-order nonlinear, three-wave mixing process, where a seeded wave (in our OPAs at ω_i, with $\omega_i < \omega_s < \omega_p$) is amplified by the reduction of a strong pump wave at w_p. At the same time, a third wave at $\omega_s = \omega_p - \omega_i$ is generated (see scheme in figure 2.1). The nonlinear interaction between the three waves in an OPA process, which propagate collinearly along the z-axis, can be described by a system of coupled wave equations which are projected along the z-axis (see derivation in [76]):

$$\frac{\mathrm{d}A_i}{\mathrm{d}z} = -i\frac{\omega_i d_{eff}}{n(\omega_i)c_0}A_s^* A_p e^{-i\Delta kz}, \tag{2.4}$$

$$\frac{\mathrm{d}A_s}{\mathrm{d}z} = -i\frac{\omega_s d_{eff}}{n(\omega_s)c_0}A_i^* A_p e^{-i\Delta kz}, \tag{2.5}$$

$$\frac{\mathrm{d}A_p}{\mathrm{d}z} = -i\frac{\omega_p d_{eff}}{n(\omega_p)c_0}A_i A_s e^{i\Delta kz}. \tag{2.6}$$

These equations consider the interacting waves as linearly polarized, plane waves under the assumption of the slowly varying envelop approximation $|\frac{\mathrm{d}^2 A_n}{\mathrm{d}z^2}| \ll k_n|\frac{\mathrm{d}A_n}{\mathrm{d}z}|$. The parameter $\Delta k = k_p - k_i - k_s$ expresses the wave-vector mismatch or phase-mismatch of the OPA process. d_{eff} is the effective nonlinear optical coefficient, which is calculated from the second-order susceptibility $\chi^{(2)}$ in dependence of the propagation directions and polarizations of the three coupled waves. Note that the intensity of each wave can be calculated from the electric field by:

$$I(z) = 2\epsilon_0 c_0 n_0(\omega)|A(z)|^2. \tag{2.7}$$

The evolution of the coupled waves along propagation has to be calculated numerically. In the special case of a neglectable pump depletion ($A_p \simeq$ const.) and assuming no initial signal $A_s(0) = 0$, an analytical solution for the evolution of the idler and signal intensities can be found:

$$I_i(z) = I_i(0)\left[1 + \frac{\Gamma^2}{g^2}\sinh^2(g \cdot z)\right], \tag{2.8}$$

$$I_s(z) = I_i(0)\frac{\omega_s}{\omega_i}\frac{\Gamma^2}{g^2}\sinh^2(g \cdot z), \tag{2.9}$$

where the parameter Γ and the gain parameter g are defined as:

$$\Gamma = \sqrt{\frac{2\omega_i\omega_s d_{eff}^2}{n_i n_s n_p \epsilon_0 c_0^3} \cdot I_p}, \tag{2.10}$$

$$g = \sqrt{\Gamma^2 - \left(\frac{\Delta k}{2}\right)^2}. \tag{2.11}$$

By analyzing equation 2.11 it can be seen, that the gain parameter g is strongly dependent on the phase-mismatch Δk and the parameter Γ, which is a function of the pump intensity I_p and the effective nonlinear coefficient d_{eff}. The parametric gain of the seeded idler wave can be expressed as:

$$G = \frac{I_i(z)}{I_i(0)} = 1 + \frac{\Gamma^2}{g^2}\sinh^2(g \cdot z). \tag{2.12}$$

In case of perfect phase-matching $\Delta k = 0$, the expression for the parametric gain G of the seeded idler wave simplifies to $G = 1 + \sinh^2(\Gamma z)$ and under the additional assumption that $\Gamma z \gg 1$, G can be expressed by:

$$G \approx \frac{1}{4} \cdot \exp\left(2\Gamma z\right) \propto \exp\left(2d_{eff}\sqrt{I_p} \cdot z\right). \tag{2.13}$$

From equation 2.13 it can be seen, that the amplification of the idler wave in an OPA scales roughly exponentially with the effective nonlinear optical coefficient d_{eff}, the crystal length z and the square root of the pump wave intensity. These dependencies have various important implications on the design of an OPA stage:

- It is desirable to choose a nonlinear medium, which features a high effective nonlinear coefficient d_{eff}. In the opposite case, an OPA stage using for example a nonlinear crystal with half the d_{eff} compared to a reference OPA stage, requires twice the crystal length (possibly reducing the amplification bandwidth, see section 2.1.3) or four time the pump intensity (potentially reaching the material damage threshold) in order to obtain a similar amplification gain.
- The exponential scaling of the parametric gain with the square root of the pump intensity implies a strong requirement on the shot-to-shot output energy stability of the pump laser. This condition is relaxed in the case of amplification in the strong pump depletion or pump

reconversion regime. Additionally, this exponential scaling implies, that pulsed laser systems, supporting high energy, ultrashort pulses in the femtosecond to nanosecond regime, are perfectly suited as high gain OPA pump sources, since the pulse peak intensity I of a laser pulse scales linear with the pulse energy E and inverse with the pulse duration τ ($I \propto E/\tau$).

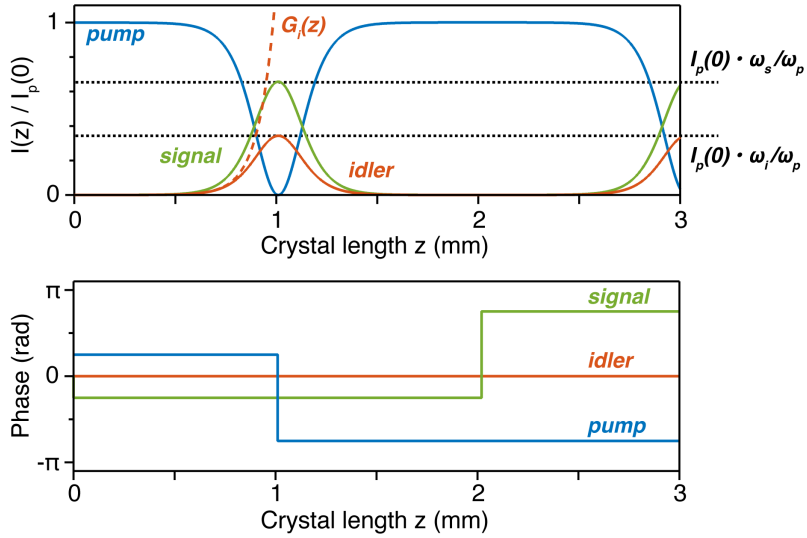

Figure 2.2: Simulated evolution of the intensities (top, normalized to initial pump intensities $I_p(0)$) and phases (bottom) for idler, signal and pump wave in an OPA process with perfect phase-matching and monochromatic waves. The simulation is performed by the split-step method of the coupled wave equation. The evolution of the seeded idler wave can be divided in exponential growth (z < 0.8 mm), linear growth with strong pump depletion (0.8 mm < z <1 mm) and energy reconversion regime (1 mm < z < 2 mm). Also shown are the parametric idler gain $G_i(z)$ in the case of no pump depletion (orange, dotted) and the maximal possible signal and idler intensities (black, dotted) according to the Manley-Rowe relations. The initial simulation parameters are chosen similar to the OPCPA presented in section 2.2: λ_p = 1064 nm, λ_i = 3100 nm, d_{eff} = 14.8 pm/V, $I_p(0)$ = 10^{14} W/m^2, $I(0)_s$ = 0, $I_i(0)$ = 2·10^9 W/m^2.

Phase relation in OPA process

The phases of the three coupled waves play a crucial role for the evolution and energy flow during a second-order nonlinear process. In the case of

an OPA process, an OPA phase can be defined as $\varphi_{OPA} = \varphi_p - \varphi_s - \varphi_i$. Assuming perfect phase-matching, the energy flow from the pump wave to the signal and idler waves is maximal at $\varphi_{OPA} = +\pi/2$. In contrast, in the case of $\varphi_{OPA} = -\pi/2$, the energy is transferred from the signal and idler waves to the pump wave, resulting in an effective SFG process. This dependency of the energy flow direction of the OPA phase is shown experimentally for example in case of a degenerate OPA ($\omega_p = 2\omega_i = 2\omega_s$) in [77].

In an OPA process, where the initial signal wave is set to zero, the phase evolution can be derived from the coupled wave equation to [78]:

$$\varphi_i(z) = \varphi_i(0) - \frac{\Delta k z}{2} + \frac{\Delta k \gamma_i^2}{2} \int \frac{\mathrm{d}z}{f + \gamma_i^2}, \tag{2.14}$$

$$\varphi_s(z) = \varphi_p(0) - \varphi_i(0) - \frac{\Delta k z}{2} - \frac{\pi}{2}, \tag{2.15}$$

$$\varphi_p(z) = \varphi_p(0) - \frac{\Delta k}{2} \int \frac{f\, dz}{1 - f}, \tag{2.16}$$

with the parameters of the fractional pump depletion $f = 1 - I_p(z)/I_p(0)$ and the input intensity ratio of the idler and pump waves $\gamma_i^2 = [\omega_p I_i(0)]/[\omega_i I_p(0)]$. Figure 2.2 shows the intensity and phase evolution of the three waves, obtained by numerical simulations of the couples wave equation under the assumption of perfect phase-matching and no initial signal wave. It can be seen that the OPA phase of the signal wave automatically self-adjust to $\varphi_s = -\pi/4$ and $\varphi_{OPA} = +\pi/2$, allowing the energy flow from the pump to signal and idler. At z = 1 mm, where the pump intensity converges toward zero, the pump phase changes to $\varphi_p = -3\pi/4$, resulting in a OPA phase of $\varphi_{OPA} = -\pi/2$, which reverses the energy flow. As a result, in the range from z = 1 mm to 2 mm SFG between the signal and idler wave of the OPA takes place and the energy is transferred to the pump wave.

The phase relationships during an OPA process (equation 2.14 to 2.16) have various important implications:

- The phase of the amplified idler wave is independent from the initial phase of the pump wave. As a result, the optical quality of the amplified idler can be maintained, even if the applied pump beam obtains spatial aberrations or if the pump pulses have a spatial or temporal varying phase.
- In the case of perfect phase-matching ($\Delta k = 0$), the idler phase doesn't evolve during amplification. Considering a phase-mismatch

($\Delta k \neq 0$), the seeded idler phase is shifted by a constant value, in case of monochromatic waves and constant input intensities ($I_p(0)$ = const., $I_i(0)$ = const.).

- The phase of the generated signal wave just depends on the initial pump and idler phases as well as on the phase-mismatch Δkz. As a result it can be shown, that the signal phase is a constant, in case the idler and pump wave originate from the same laser oscillator [75]. This behaviour is also valid for DFG processes and enables the generation of broadband, mid-IR pulses with a passively stabilized carrier-envelop phase (CEP), which are used for example as seed pulse for the high power OPCPA system presented in section 2.2. A detailed discussion about CEP-stable, mid-IR pulse generation is given in section 2.1.4.
- From equation 2.15 one can also derive the chromatic phase dispersion of the generated signal as a function of the seeded idler dispersion, in the case of spectrally broadband pulses. In the discussions above we considered the three coupled waves as monochromatic, continuous waves (cw). In contrast in the case of spectral broadband pulses, the phases become frequency dependent $\varphi_n(z) = \varphi_n(z, \omega_n)$ and their frequency dependent behaviour can be described by a Taylor expansion. In OPA stages used in OPCPA systems, the seeded idler pulse is normally linearly chirped wherefore the idler phase varies very strongly with the frequency. On the other side the pump pulses are typically transform-limited, spectrally narrow-band pulses with a relative constant phase. As a result, by using the signal phase relationship (equation 2.15) and the energy conservation (equation 2.2) it can be shown, that the high-order phase dispersions with odd orders are directly transferred from the idler to the signal wave and the even high-order phase dispersions are inverted. This means for the specific case of second-order (GDD) and third-order dispersion (TOD):

$$GDD_s = -GDD_i, \tag{2.17}$$

$$TOD_s = +TOD_i. \tag{2.18}$$

Similar to the phase relation in OPA processes, a phase relation for second-harmonic generation (SHG) processes ($\omega_{SHG} = 2\omega_0$) can be derived for the case of perfect phase-matching [74]:

$$\varphi_{SHG} = 2 \cdot \varphi_0 - \frac{\pi}{2}. \tag{2.19}$$

In the case of broadband, chirped seed pulses, the second-order and third-order dispersion of the generated SHG beam is then given by:

$$GDD_{SHG} = \frac{2}{2^2} GDD_0 = \frac{1}{2} GDD_0, \tag{2.20}$$

$$TOD_{SHG} = \frac{2}{2^3} TOD_0 = \frac{1}{4} TOD_0. \tag{2.21}$$

The relations given in equations 2.17 to 2.21 are important for the temporal compressor design of the near-IR outputs of the multi-color OPCPA system presented in section 2.3.

Manley-Rowe relations

Another interesting set of relationships, which can be derived from the coupled wave equations (equation 2.4 to 2.6), are the Manley-Rowe relations (first discribed in [79]; detailed derivation in section 2.5 of [73]):

$$\frac{\mathrm{d}}{\mathrm{d}z}\left(\frac{I_i(z)}{\omega_i}\right) = \frac{\mathrm{d}}{\mathrm{d}z}\left(\frac{I_s(z)}{\omega_s}\right) = -\frac{\mathrm{d}}{\mathrm{d}z}\left(\frac{I_p(z)}{\omega_p}\right). \tag{2.22}$$

This equation describes the coupling between the evolutions of the intensities I_n of the three interacting waves. By expressing the beam intensities as a function of the flux of photons N crossing a surface S per unit time Δt:

$$I_n(z) = \frac{N_n(z) \cdot \hbar\omega_n}{S\Delta t} c_0 \tag{2.23}$$

the Manley-Rowe relations can be written as [75]:

$$\frac{\mathrm{d}N_i(z)}{\mathrm{d}z} = \frac{\mathrm{d}N_s(z)}{\mathrm{d}z} = -\frac{\mathrm{d}N_p(z)}{\mathrm{d}z}. \tag{2.24}$$

The main implications of the equation 2.24 are:

- For each pump photon N_p, which is generated or annihilated, always a signal photon N_s as well as an idler photon N_i has to be annihilated or generated, respectively. A simple picture of this relation based on photon absorption and emission from virtual energy levels is illustrated in figure 2.1. In the case of the OPA process, equation 2.24 implies, that for each annihilated pump photon, not only one idler photon is generated to amplify the total idler beam, but also the same amount of signal photons are generated.

- Since the photon energy for each wave $E_{ph} = \hbar\omega_n$ depends on the respective radial frequency ω_n, the energies transferred from the pump to the idler and signal waves are given by the respective ratios of ω_i/ω_p and ω_s/ω_p.

The validity of the Manley-Rowe relation can also be seen in figure 2.2 (top). In this case the initial pump intensity is normalized to one and the numerical calculation of an OPA process with monochromatic beams and perfect phase-matching reveals, that at the point of total pump depletion (z = 1 mm), the ratio of ω_s/ω_p of the initial pump intensity is transferred to the signal beam and a ratio of ω_i/ω_p is transferred to the idler beam (black dotted lines). In consequence, the maximal pump-to-idler energy conversion efficiency, which could be obtained in our OPCPA (λ_p = 1064 nm, λ_i = 3100 nm; see section 2.2) would be $\omega_i/\omega_p = 34\%$. In reality further parameters, such as for instance broadband phase-matching, spatio-temporal overlap or spatio-temporal walk-off would have to be considered, to properly describe the real amplification process. A detailed description, how to optimize the overall conversion efficiency of an OPA stage can be found in section 3.1.

2.1.3 Phase-matching and amplification bandwidth

In the above theoretical discussions, we considered mostly monochromatic waves under perfect phase-matching. In the case of three spectrally broadband, coupled waves and temporal pulse durations in the femtosecond to picosecond range, it gets more challenging to sustain perfect phase-matching for all interacting wavelengths. When perfect phase-matching cannot be achieved ($\Delta k(\omega) \neq 0$), the phase-mismatch accumulates over the crystal length z and leads to a reduction of the efficiency of the nonlinear process as can be seen from equation 2.4 to 2.6. For example, the influence of phase-mismatch on the conversion efficiency η in a SHG process, can be described in the case of no pump depletion and for neglected group velocity mismatch by [72]:

$$\eta = \eta_{max} \frac{\sin^2\left(\frac{\Delta kz}{2}\right)}{\frac{\Delta kz}{2}}. \tag{2.25}$$

The behaviour of equation 2.25 is shown in figure 2.3, illustrating the importance for a small accumulated phase-mismatch over the spectral range of the interacting waves to achieve efficient broadband nonlinear frequency mixing. It can be seen, that the SHG conversion efficiency drops at Δkz = π to 40% and at Δkz = 2π to zero.

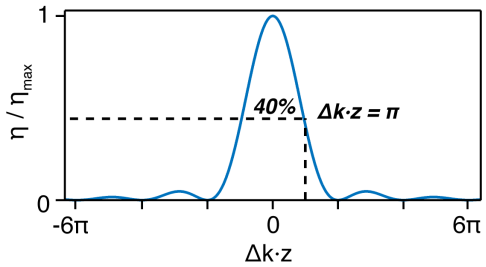

Figure 2.3: Factor by which the conversion efficiency η_{max} of a nonlinear three-wave mixing process is multiplied as function of accumulated phase-mismatch Δkz over the crystal length z (see equation 2.25). At Δkz = π the conversion efficiency is reduced to 0.4 of its original value and at Δkz = 2π the phase-mismatch leads to a vanishing of the conversion efficiency.

In isotropic, homogeneous, normally dispersive media the refractive index n_0 increases with higher frequencies, leading to $n_0(\omega_p) > n_0(\omega_s) > n_0(\omega_i)$ for second-order nonlinear interaction. As result, no phase-matching $\Delta k = k_p - k_s - k_i = 0$ with $k = \frac{\omega n_0}{c_0}$ is possible in isotropic materials. Two possible ways to achieve phase-matching are angular phase-matching in birefringent crystals and quasi phase-matching.

Angular phase-matching in birefringent crystals

In a birefringent crystal the refractive index depends on the polarisation and the propagation direction of the light wave. In the case of uniaxial birefringent materials one direction, the so-called optical axis governs the anisotropy of the refractive index and all directions perpendicular to the optical axis are optically equivalent. Light polarized perpendicular to the optical axis experiences the ordinary refractive index n^o and light which is polarized along the optical axis is governed by the extraordinary refractive index n^e. If the light is not exactly polarized along or perpendicular to the optical axis, the resultant refractive index can be calculated dependent on the phase-matching angle θ by [76]:

$$\frac{1}{n^e(\theta)} = \frac{\cos^2\theta}{(n^o)^2} + \frac{\sin^2\theta}{(n^e)^2}, \tag{2.26}$$

where θ is measured between the wavevector k of the respective wave and the optical axis (see figure 2.4 (a)). Uniaxial crystals can be divided in positive uniaxial crystals with $n^e > n^o$ and negative uniaxial crystals

with $n^e < n^o$. Phase matching in birefringent crystals can be achieved by the proper choice of phase-matching angle as well as polarization and propagation direction for each of the three coupled waves. This kind of phase-matching is called critical or angular phase-matching. In the case, the signal and idler waves have the same polarization and they are perpendicular polarized to the pump wave, the so-called type I phase-matching takes place. On the other side, in type II phase-matching the pump obtains the same polarization direction as the signal or the idler wave.

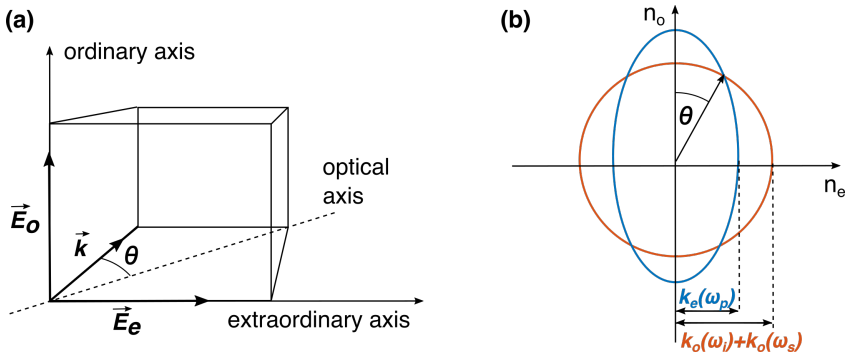

Figure 2.4: (a): Scheme of ordinary and extraordinary direction in birefringent crystals. (b): K-vector scheme of type I, angular phase-matching in a negative, uniaxial crystal. In this case, signal and idler are ordinary beams and the pump is an extraordinary beam, which refractive index is dependent on the phase-matching angle θ. The phase-matching angle θ is chosen to achieve phase-matching ($k_e(\omega_p) = k_o(\omega_s) + k_o(\omega_s)$).

A negative uniaxial crystal which is very important in the course of the thesis, is beta barium borate (BBO). We use BBO in type I phase-matching for the high conversion efficiency generation of femtosecond pulses in the ultraviolet to near-IR spectral range, presented in section 2.3. A k-vector illustration of the type I, angular phase-matching for negative uniaxial crystals such as BBO is shown in figure 2.4 (b).

Quasi phase-matching

Another approach to achieve phase-matching is quasi phase-matching (QPM), where the nonlinear material properties are spatially periodically modulated. In the most common form, the sign of the χ^2 coefficient is reversed periodically each time the accumulated phase-mismatch Δkz reaches π, also known as the coherence length $l_c = \pi/\Delta k$ where the conversion efficiency drops to 0.4 (see figure 2.3). The periodical reversal of the sign of

the nonlinear susceptibility compensates for the non-zero wavevector mismatch and allows the monotonic energy flow from the pump to signal and idler waves [80]. In figure 2.5 are compared for example the intensity evolutions of an OPA process in case of perfect phase-matching (green line), quasi phase-matching (blue line) and non-phase-matching (orange line). It can be seen, that the conversion efficiency for perfect phase-matching is higher than for QPM and it can be shown, that first-order QPM leads to a reduction of the effective nonlinear coefficient of $\pi/2$ compared to perfect phase-matching [80].

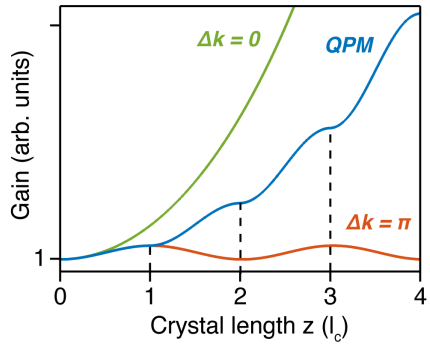

Figure 2.5: Simulated gain evolution of seeded idler beam in an OPA process as function of propagation length z. In the case of perfect phase-matching (green) the gain increases exponential with the crystal length, while in the non-phase-matched case (orange) the gain oscillates with a period of $\Delta kz = 2\pi$. Quasi phase-matching is obtained (blue) by inverting the sign of the d_{eff} after each coherent length $l_c = \pi/\Delta k$ (black dotted line), resulting in an continuous gain increase. The phase-matched as well as the non-phase-matched cases are calculated by the analytical description of equation 2.12. In order to obtain the gain under QPM, the coupled wave equation is solved numerically by a split-step, Runge-Kutta simulation.

In the case of QPM, the phase-matching equation is extended by a grating wave-vector $K_g = 2\pi/\Lambda$ with the modulation period or poling period $\Lambda = 2\pi/\Delta k$ to [80]:

$$\Delta k_{QPM} = k_p - k_s - k_i - K_g. \tag{2.27}$$

Despite the reduced d_{eff}, QPM shows various important advantages compared to angular phase-matching in birefringent crystals:

- In QPM processes phase-matching can be achieved for a huge variety of polarization directions of the three coupled waves, even in the case when all waves are polarized parallel to each other, which is

not possible in angular phase-matching. In this way, the wave polarizations and crystal orientation can be chosen such that the maximal effective nonlinear coefficient d_{eff} is obtained.

- Phase-matching can even be achieved in isotropic materials, such as GaAs. In this case QPM is obtained due to the periodic inversion of the crystallographic orientation, which is called orientation patterned and is achieved during the epitaxial growth of the crystal. More information about orientation-patterned GaAs can be found in [81].
- In QPM interactions it is normally possible to propagate the interacting waves collinear along a crystal axis, aligning the direction of the energy flow (Pointing-vector) along the propagation direction [80]. As result, no spatial walk-off takes place.

Widely used QPM crystals for mid-IR parametric amplification are periodically poled lithium niobate (PPLN) and periodically poled lithium tantalate (PPLT). Both are ferroelectric materials, where the QPM is fulfilled by the periodic inversion of the material polarization. The material polarization is periodically oriented via the application of static electric fields in the kilovolt regime. The most important QPM crystal in the course of this thesis is PPLN, as it is used as main OPA crystal in the high power, mid-IR OPCPA system presented in section 2.2 and 3. PPLN is a very attractive OPA crystal, since it obtains one of the highest d_{eff} compared to other available nonlinear crystals for mid-IR amplification pumped at 1064 nm wavelength. An overview of the most common, mid-IR OPA crystals is given in section 3.2.1. There it can be seen, that PPLN obtains for example a four times higher d_{eff} of 14.8 pm/V compared to the angular phase-matched lithium niobate with -4.0 pm/V. This increase using the same nonlinear crystal, is achieved due to the freedom of polarization directions and crystal orientation in QPM interactions, which allows exploiting the highest χ^2 tensor direction.

Phase-matching bandwidth of broadband nonlinear interactions

In the case of second-order nonlinear interactions of spectrally broadband, ultrashort pulses, the phase-matching condition has to be satisfied over a wide spectral range. The required spectral broadband description of the phase-mismatch $\Delta k = k_p - k_s - k_s$ can be obtained by a Taylor series around the phase-matched central angular frequency ω_0. For simplification we assume a monochromatic pump wave (ω_p = const.), which is the case for example in OPA stages of OPCPA systems. As a result a small change

$\Delta\omega$ of the signal frequency introduces the opposite change of the idler frequency $\Delta\omega = \Delta\omega_s = -\Delta\omega_i$ due to the energy conservation $\omega_p = \omega_s + \omega_s$. The Taylor series of the phase-mismatch around the phase matched central frequency ω_0 can than be written as:

$$\begin{aligned}\Delta k(\omega_0 + \Delta\omega) =& \Delta k_0 - \left(\left.\frac{\partial k_s}{\partial \omega}\right|_{\omega_{s,0}} - \left.\frac{\partial k_i}{\partial \omega}\right|_{\omega_{i,0}} \right) \Delta\omega \\ & - \frac{1}{2} \left(\left.\frac{\partial^2 k_s}{\partial \omega^2}\right|_{\omega_{s,0}} - \left.\frac{\partial^2 k_i}{\partial \omega^2}\right|_{\omega_{i,0}} \right) \Delta\omega^2 + ...\end{aligned} \tag{2.28}$$

with $\Delta k_0 = k_{p,0} - k_{s,0} - k_{i,0}$. Note that the first derivation of the k-vectors describes the respective inverse group velocities $v_n = (\partial k_n/\partial\omega|_{\omega_{n,o}})^{-1}$ and the second derivation represents the group velocity dispersions $g_n = \partial^2 k_n/\partial\omega^2|_{\omega_{n,o}}$ of each wave.

In order to achieve broadband phase-matching, Δk_0 and all derivatives of Δk have to be zero. The first derivative is equal to zero in the case of group velocity matching between the signal and idler wave ($v_i = v_s$). This is the case in for example narrowband, degenerative ($\omega_i = \omega_s$), type I interactions. In non-degenerative processes $\omega_i \neq \omega_s$, group velocity matching can be achieved by the use of non-collinear beam geometries. In figure 2.6 is given the k-vector scheme in a non-collinear geometry, where α is the angle between the pump and signal k-vector and β the angle between the pump and idler k-vector. The phase-matching condition parallel and perpendicular to the pump wave-vector can than be written as [82]:

$$\Delta k_{\parallel} = k_p - k_s \cos\alpha - k_i \cos\beta, \tag{2.29}$$

$$\Delta k_{\perp} = k_s \sin\alpha - k_i \sin\beta. \tag{2.30}$$

The group velocity matching in the non-collinear geometry can be achieved at $v_s = v_i \cos(\alpha+\beta)$ [82]. Operation at degeneracy or in non-collinear beam geometries can typically yield very large phase-matched spectral bandwidth due to the vanishing first-order variation of Δk with ω. In broadband interactions where the pump wave can not be simplified as monochromatic wave, the group velocities of all three waves have to be similar ($v_p \approx v_s \approx v_i$) in order to achieve broadband phase-matching.

Group velocity matching is also important for the temporal walk-off between frequency-mixed, pulsed waves. Especially in nonlinear processes between ultrafast pulses with sub-100 fs duration, a group velocity mismatch can easily cause a temporal pulse walk-off longer than the pulse durations. In this case the nonlinear interaction is substantially weakened

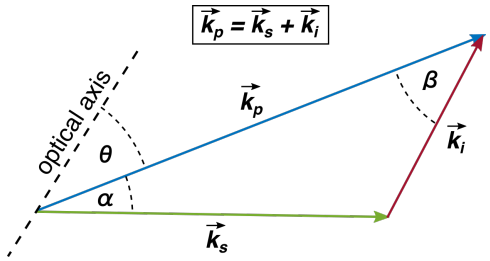

Figure 2.6: K-vector scheme of pump, signal and idler waves in a non-collinear, three-wave interaction geometry. Normally the non-collinear angle α between the pump and signal k-vector and the phase-matching angle θ are used to distinctly describe the geometry.

or interrupted, limiting the overall conversion efficiency. For example, using collinear, type I SHG in a BBO crystal of a Ti:sapphire laser output at 800 nm wavelength, would cause a temporal walk-off of around 190 fs per 1 mm crystal lengths. As result, the SHG driving pulse would require a pulse duration of at least 200 fs, or a shorter nonlinear crystal would have to be used, in order to ensure efficient frequency conversion over the full crystal length. A detailed discussion about temporal walk-off effects in femtosecond, nonlinear interactions can be found in [75]. In OPCPA systems the effect of temporal walk-off can be normally neglected, since pulse durations in the picosecond regime are used, which is far above typical walk-off times in the case of millimeter thick OPA crystals.

An important parameter for the description of the amplification bandwidth of a broadband three-wave mixing process, is the so-called parametric bandwidth. The parametric bandwidth is defined as the condition under which the accumulated phase-mismatch of a nonlinear process $|\Delta k \cdot l_c|$ is not greater than π. By combining this condition, with the Taylor series expression of the phase-mismatch Δk given in equation 2.28, an analytical express for the parametric bandwidth can be obtained. A generalized form of the parametric bandwidth $\Delta\lambda$ in wavelength, which is derived from the solution for $\Delta\omega$, is given by [82]:

$$\Delta\lambda = \begin{cases} \dfrac{\lambda^2}{c} \cdot \dfrac{|u_{si}|}{l_c} & \text{if } \dfrac{1}{u_{si}} \neq 0 \\ \dfrac{0.8\lambda^2}{c}\sqrt{\dfrac{1}{l_c|g_{si}|}} & \text{if } \dfrac{1}{u_{si}} = 0 \end{cases} \tag{2.31}$$

using the parameters u_{si}, g_{si} and β:

$$\frac{1}{u_{si}} = \frac{1}{v_i \cos(\alpha+\beta)} - \frac{1}{v_s}, \tag{2.32}$$

$$g_{si} = \left[\frac{1}{2\pi v_s^2}\tan(\alpha+\beta)\tan\beta\left(\frac{\lambda_s}{n_s} + \frac{\lambda_i\cos(\alpha+\beta)}{n_i}\right) - (g_s+g_i)\right], \tag{2.33}$$

$$\beta = \arcsin\left(\frac{n_s}{n_i}\frac{\lambda_i}{\lambda_s}\sin\alpha\right). \tag{2.34}$$

In the case of a collimated beam geometry, α and β are set to zero. Interestingly in case of no group velocity matching ($1/u_{si} \neq 0$), the parametric bandwidth scales inverse to the crystal length $\Delta\lambda \propto 1/l_c$, while under group velocity matching ($1/u_{si} = 0$), $\Delta\lambda$ scales inverse with the square root of the crystal length $\Delta\lambda \propto \sqrt{1/l_c}$. The equations 2.31 to 2.34 are used in the course of this thesis to estimate the suitable crystal length for the performed nonlinear, broadband interactions. This is especially important for the design of the multiple broadband OPA and SHG stages used in the OPCPA systems which are presented in chapter 2 and 3.

2.1.4 CEP-stable, mid-IR seed generation schemes

One important parameter for pulsed laser systems achieving output pulse durations in the range of few optical cycles is the carrier-to-envelop phase (CEP), which describes the phase of the carrier wave with respect to the pulse envelope (see figure 2.7 (a)). At these short pulse durations, a different CEP influences strongly the maximal electric field strength, therefore having a huge influence on optical processes which dependent nonlinearly on the instantaneous electric field. The stabilization and control of the pulse-to-pulse (or shot-to-shot) CEP value is crucial for example in the field of attoscience allowing among others the generation of isolated attosecond pulses via high harmonic generation [33, 34]. Another application is the controlled synthesis of few-cycle, optical waveforms via the superposition of multiple, CEP-stable electric field [40].

The CEP of the output pulses of mode-locked oscillators, which are used for the seed generation in every ultrafast laser source, typically changes shot-to-shot by a phase slippage dependent on the offset between group velocity and phase velocity in the cavity [83]. One possibility of CEP stabilization is active stabilization, where the pulse propagation inside the cavity is influenced by for example the insertion of a prism [84] or via a change of the Kerr effect due to a pump power change of the oscillator [85]. The CEP

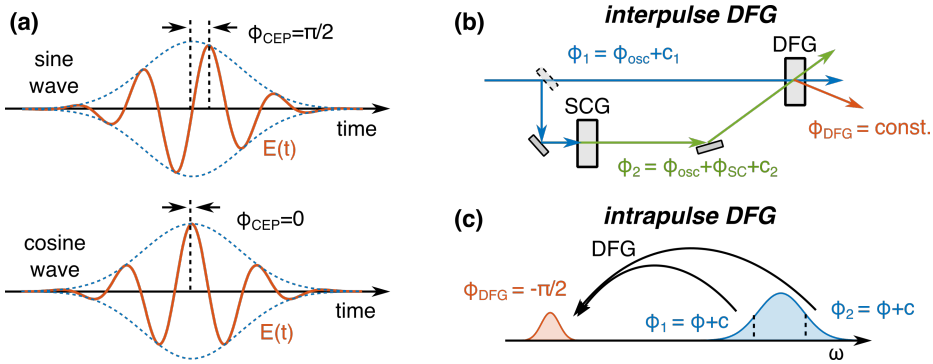

Figure 2.7: Concept of the carrier-envelop phase (CEP) of a laser pulse (a), which is the phase between the carrier wave (orange) and the electric field envelope (blue, dotted). Shown are examples of a sine wave ($\varphi_{CEP} = \pi/2$) and a cosine wave ($\varphi_{CEP} = 0$). The CEP can be passively stabilized via interpulse DFG between two, frequency-shifted pulses originating from the same oscillator (b) or by intrapulse DFG between the different frequency components of one driving electric field (c). Figure is inspired by [74].

can also be passively stabilized, with the advantage that in this all-optical technique no additional, electronic feedback-loop is required, contrary to the case of active CEP stabilization.

Passive CEP stabilization schemes are based on DFG processes between pulses originating from the same oscillator. The phase relations between the three interacting waves in a DFG process are the same, as in the case of OPA (see equations 2.14 to 2.16). These relations are valid in case of monochromatic, three-wave interactions, but they can also be applied for the CEP relations in case of pulsed, interacting laser pulses. Assuming a DFG stage, where pump and signal pulses are seeded, the CEP φ_i of the generated idler wave is [74]:

$$\varphi_i = \varphi_p - \varphi_s - \frac{\pi}{2}. \tag{2.35}$$

One experimental realization of passive CEP stabilization is intrapulse DFG, where just one seed pulse acts as pump as well as signal wave (see figure 2.7 (c)). The CEP of the generated idler pulse $\varphi_i = -\pi/2$ is then constant and independent of the seeded CEP value. Intrapulse DFG is a commonly used technique in for example ultrafast, THz spectroscopy, for the generation of near single-cycle, CEP-stable pulses in the THz spectral range [86]. The drawback of intrapulse DFG is the typically very low conversion efficiencies of below 1%.

Passive CEP stabilization can also be achieved in interpulse DFG between two frequency-shifted pulses, which originate from the same oscillator and which are temporal synchronized by a delay line (see figure 2.7 (b)). In the case of a common mode-locked oscillator, the output pulses obtain a different CEP φ_{osc} value for each laser shot. To achieve passive CEP stabilization, the output pulse is split and one part is spectrally broadened and frequency shifted via supercontinuum generation (SCG) in for example optical fibers or by filamentation in solid media. A detailed description of the mechanisms and applications of SCG are discussed in chapter 4. During the spectral broadening the original CEP of the driving pulse is shifted by a constant nonlinear phase $\varphi_{SC} = \varphi_{osc} + c_{sc}$. Additionally the non-shifted as well as the frequency shifted pulses perceive constant phase shifts (c_1, c_2) due to the different optical path lengths and by propagation through optical elements. As consequence the CEP of the non-shifted (φ_{nonSC}) and of the frequency shifted pulse φ_{SC} can be written as:

$$\varphi_{nonSC} = \varphi_{osc} + c_1, \tag{2.36}$$

$$\varphi_{SC} = \varphi_{osc} + c_{sc} + c_2. \tag{2.37}$$

In the case of a DFG process between these two pulses, the phase of the generated, third wave is than:

$$\varphi_{DFG} = \varphi_{nonSC} - \varphi_{SC} - \frac{\pi}{2} = c_1 - c_{sc} - c_2 - \frac{\pi}{2} = \text{constant}. \tag{2.38}$$

The resulting CEP φ_{DFG} is constant and independent from the CEP of the original cavity oscillator φ_{osc}. Note that the preservation of CEP stability during SCG is crucial for the passive CEP stabilization scheme based on interpulse DFG. In fact, the nonlinear phase offset φ_{SC} acquired during the spectral broadening is strongly coupled to the driving energy, since the broadening mechanism is based on nonlinear processes. The introduced CEP jitter related to the intensity-to-phase coupling during SCG in a third order nonlinear medium was measured for example by Baltuška *et al.* for spectral broadening in bulk materials [87]. As a consequence, a high output energy stability of the seeding mode-locked oscillator is required, in order to obtain high passive CEP-stability from the interpulse DFG scheme.

The mid-IR OPCPA system presented in the course of this thesis (see section 2.2 and section 3.3) uses the passive interpulse CEP stabilization scheme in order to obtain broadband, CEP-stable seed pulses in the mid-IR regime. Additionally we can obtain a mid-IR spectral bandwidth, supporting sub-3 optical cycle pulse durations, due to the fact, that both interpulse DFG inputs are ultrabroadband, ultrafast pulses. In our case, the

mode-locked oscillator as well as the required supercontinuum generation is based on optical fiber technology, therefore providing perfect short- and long-term energy and spectral stability. A detailed description of the CEP-stable, mid-IR seed generating front-end is given in section 2.2.2. Further information for the interested reader about passive CEP stabilization schemes and their application in ultrafast optics can be found in [74,83,88].

Once the CEP-stable, mid-IR seed pulse is generated, the CEP-stability is maintained during amplification via the OPA process, which can also be seen in the OPA phase relation (equation 2.14): $\varphi_i(z) = \varphi_i(0) - \frac{\Delta k z}{2} + \frac{\Delta k \gamma_i^2}{2} \int \frac{\mathrm{d}z}{f+\gamma_i^2}$. The CEP of the seeded idler is preserved, but shifted by a constant phase offset. Note that in case of operation close to pump depletion and assuming a high pump shot-to-shot intensity fluctuation, the added phase offset fluctuates, introducing a CEP phase jitter. In our OPCPA system this CEP jitter is minimized, by using a high-stability pump laser (see section 2.2.3).

The CEP stability can be measured by interferometric methods, such as for example f-to-2f or f-to-3f interferometers [83]. These techniques can typically only measure the CEP shot-to-shot stability, which is linked to the relative CEP change. In order to obtain information about the absolute CEP value, techniques like for example electro-optical sampling [89] or strong-field ionization in a Stereo-ATI [35] have to be used.

2.1.5 Design of stretcher and compressor arrangement

A combination of a temporal pulse stretcher and compressor device is used in OPCPA architectures to stretch the seed pulses in time, avoiding material damage during amplification, and to re-compress the high energy pulses at the output of the laser. To be able to design an appropiate stretcher/compressor combination, the dispersion introduced by each optical element in the system has to be taken into account. One possibility to analyse the introduced dispersion of a sequence of optical elements is to calculate the optical beam path b through the system as function of the angular frequency ω. The optical path length is than related to the frequency dependent phase delay ϕ through [72]:

$$\phi(\omega) = \frac{\omega \cdot n(\omega)}{c} \cdot b(\omega), \tag{2.39}$$

where c is the speed of light in vacuum and $n(\omega)$ the material refractive index. In the analytic approach to obtain the introduced dispersion, the phase

delay $\phi(\omega)$ is achieved for a specific compound of optical elements using geometric considerations and then the analytic expression of the second order dispersion GDD = $\frac{\partial^2\phi}{\partial\omega^2}$ and third order dispersion TOD = $\frac{\partial^3\phi}{\partial\omega^3}$ is calculated. A comprehensive overview of analytic expressions for the most common compression schemes can be found in [72]. In contrast, in the numerical approach the specific optical path length is obtained for each frequency by for example the use of a so-called ray-tracing program, and the GDD and TOD is afterward obtained by numerically calculating the second and third order derivatives of the phase delay.

The applicable stretcher/compressor scheme for a specific OPCPA design has to take also the used amplification scheme into account. For example, all of the few other reported mid-IR OPCPA sources [47, 49–52] (see section 1.3) use a stretched near-IR signal beam as seed, but finally compress and extract the idler beam at the end of the system, which is generated during the parametric amplification process. In this case, one would have to consider the phase transfer relation between the signal and idler waves in the OPA process (see equations 2.14 and 2.15) in order to design a suited compressor scheme. In contrast, in our system we already seed with CEP-stable, mid-IR pulses; these idler pulses are then amplified in a sequence of OPAs and finally compressed at the output of the OPCPA system. In this case, the stretcher/compressor scheme can be uniquely focused on the dispersion of the idler wave.

Up-to-date a variety of dispersive optical elements are reported, which can be used for temporal pulse stretching and compression. Aside from bulk compressors, which exploit the dispersion introduced by propagation through bulk material, a number of dispersion delay line schemes exploit additionally angular dispersion. Examples are grating compressors [90], prism pairs [91], grating compressors in combination with an imaging system (also called Martinez compressor) [92] or grism pairs (combination of grating and prism) [93]. Alternative approaches such as chirped mirrors [94] or chirped volume Bragg gratings [95] are based on the Bragg reflection condition and are designed in a manner that different frequencies of an incident pulse are reflected in varying depth of the optical element. Other elements, so-called pulse shapers allow the modulation of spectral amplitude and phase of the transmitted electric field, which also permits the compensation of high dispersion orders. Common pulse shapers use optical Fourier transformation grating-setups in combination with a pulse shaping mask placed in the Fourier plane [96], which is typically a liquid crystal spatial light modulator or an acousto-optic modulator. A different approach is the acousto-optic programmable dispersive filter (AOPDF) [97], which

permits the programmable high-order dispersion control using a relatively simple transmission configuration.

In the OPCPA design, which is presented in this section, as well as in the fundamentally rebuild power-upgrade presented in chapter 3, we apply a combination of bulk material and Martinez-type grating arrangement as stretcher/compressor combination. Below, we first state the analytic expressions for the dispersion of grating and bulk compressors and afterwards determine the appropriate combination of bulk material and specific grating for our OPCPA system. The analytical expressions of the added dispersion after propagation though bulk material is given by [98] to:

$$GDD_{material} = \frac{\lambda^3}{2\pi c^2} L \left(\frac{\mathrm{d}^2 n}{\mathrm{d}\lambda^2} \right), \tag{2.40}$$

$$TOD_{material} = -\frac{\lambda^4}{4\pi^2 c^3} L \left[3\frac{\mathrm{d}^2 n}{\mathrm{d}\lambda^2} + \lambda \frac{\mathrm{d}^3 n}{\mathrm{d}\lambda^3} \right], \tag{2.41}$$

where L is the material length and n the linear refractive index. It is known, that due to the particular wavelength dependent behavior of the linear refractive index, solid dielectric media exhibit negative GVD in the mid-IR spectral range, while semiconductor exhibit positive GVD (see also figure 4.1). In contrast, the TOD of dielectrics as well as of semiconductors is positive over the full spectral range. The analytic expressions for the dispersion introduced by a grating pair in a Treacy configuration (first order diffraction, single pass; see figure 2.8 (a)) is given by [99]:

$$GDD_{grating} = -\frac{\lambda^3 G}{2\pi c^2 d^2 \cos^3 \theta_{dif}}, \tag{2.42}$$

$$TOD_{grating} = \frac{3\lambda^4 G}{4\pi^2 c^3 d^2 \cos^3 \theta_{dif}} \left[1 + \frac{\lambda \sin \theta_{dif}}{d \cos^2 \theta_{dif}} \right], \tag{2.43}$$

$$\begin{aligned} FOD_{grating} = -\frac{3\lambda^5 G}{8\pi^3 c^4 d^2 \cos^3 \theta_{dif}} \Big[4 + \frac{8\lambda \sin \theta_{dif}}{d \cos^2 \theta_{dif}} \\ + \frac{\lambda^2}{d^2} (1 + 6\tan^2 \theta_{dif} + 5\tan^4 \theta_{dif}) \Big], \end{aligned} \tag{2.44}$$

where d is the grating line separation, G the spacing between the gratings parallel to their normal and θ_{dif} is the frequency dependent diffraction angle, which is related to the input angle θ_{in} by the grating equation (assuming first diffraction order): $d \cdot (\sin(\theta_{dif}) + \sin(\theta_{in})) = \lambda$. When analyzing the analytic expressions, it can be seen that the GVD of a Treacy grating compressor is always negative while the TOD is positive.

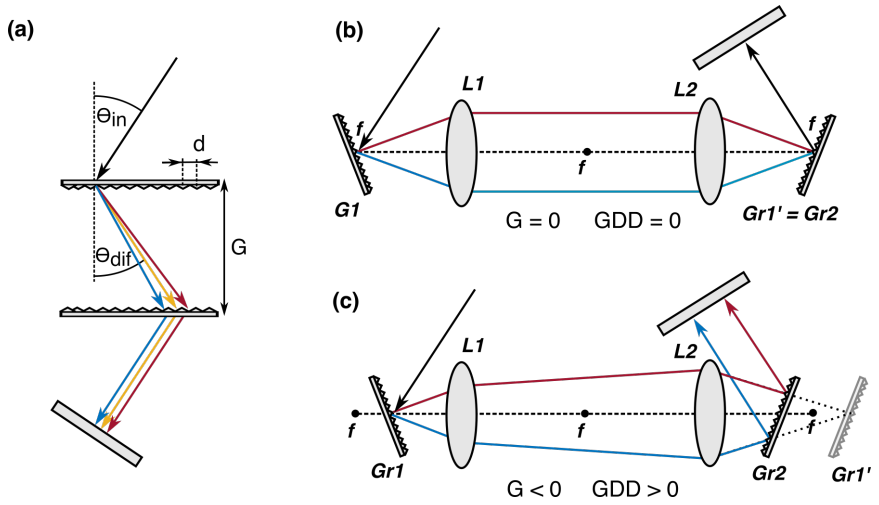

Figure 2.8: Layout and working principle of Treacy (a) and Martinez (b,c) grating compressor. The illustrated Treacy compressor applies transmission gratings for a better visibility of the grating pair parameters. The Martinez grating is shown in the zero dispersion configuration (b) and the configuration for inverted dispersion (c). In latter case, the first grating is imaged (Gr1') behind the second grating Gr2, resulting in a negative effective grating separation G, yielding positive GDD and negative TOD.

When the grating pair is used in a so-called Martinez-configuration, where an imaging telescope is placed between both gratings [92], the sign of dispersion can be inverted and the introduced dispersion can even be magnified, in case the imaging system consist of two focusing elements with different focal lengths. In figure 2.8 (b, c) is shown the working scheme of a Martinez grating compressor. We assume that both lenses have the same focal length and that both gratings are equally spaced to the closest lens. The first grating Gr1 is imaged by the two-lens imaging system on Gr1'. The location of Gr1' relative to the second grating Gr2 determines the effective grating separation G and therefore the introduced dispersion. In the case, when Gr1' is exactly imaged onto Gr2 (figure 2.8 (b)) no additional dispersion apart from the lens material dispersion is introduced. In the case, when Gr1 is placed closer to the lens L1 (figure 2.8 (c)), Gr1' is projected behind Gr2 and the effective grating distance G is negative. This results in a sign inversion of the introduced GDD and TOD, since the grating distance G scales linear in equation 2.42 and 2.43.

In table 2.1 is given an overview of the dispersion signs introduced by propagation through bulk media or grating compressors. It can be seen, that a

	GDD	TOD
Dielectric bulk material, mid-IR range	-	+
Semiconductor, mid-IR range	+	+
Treacy grating pair	-	+
Martinez compressor	+	-

Table 2.1: Introduced sign of the second and third order dispersion for various dispersive optical elements. It can be seen, that a combination of dielectric bulk material and a Martinez grating compressor could be used as stretcher/compressor scheme in the mid-IR spectral range.

combination of Martinez compressor and dielectric bulk media can be chosen to compensate second and third order dispersion. We preferred the use of bulk dielectrics in comparison to Treacy grating pairs, due to their easier alignment and typically lower transmission losses.

In order to determine an optimal stretcher/compressor combination, the ratio TOD/GDD is compared for various optical elements. Since the GDD and TOD of bulk and grating compressors scales linear respective to the material length or grating separation, the TOD/GDD coefficient of stretcher and compressor should match in order to allow proper dispersion compensation. In figure 2.9 are shown the TOD/GVD coefficients for various dielectric materials and grating compressors featuring different line spacings d and diffraction angles θ_{dif}. The diffraction angles are given relative to the Littrow angle θ_{Litt}, which is defined as configuration where $\theta_{in} = \theta_{dif} = \theta_{Litt}$. Typically it is desirable to use gratings under Littrow angle, since common commercial gratings are designed to maximize their reflection efficiency for this configuration. Additionally the line spacing should lie in the range of the diffracted wavelength to permit optimal diffraction efficiencies. In figure 2.9 can be seen, that a combination of material dispersion in sapphire and a Martinez-type grating compressor with a line separation of 5 µm (equivalent to line density of 200 lines/mm) is perfectly suited as stretcher/compressor scheme. The tunability of the TOD/GDD ratio by the grating incidence angle allows also the compression fine adjustment for compensating the additional dispersion introduced by the nonlinear OPA phase (last term in equation 2.14) and the delay phase due to linear propagation through other optical elements of the system, such as lenses or nonlinear crystals.

In general one has also to take into account, that the analytic dispersion equations just give a rough estimate, since they assume infinitely small beam sizes and an aberration free imaging system. When applying beams

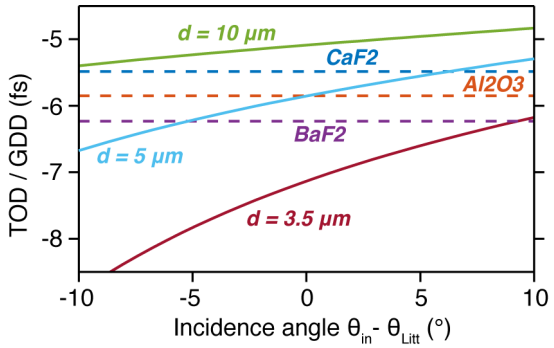

Figure 2.9: Calculated TOD/GDD ratio of various bulk materials at a center wavelength of 3.05 µm using the respectrive Sellmeier equations [100–102] (dotted lines). Also shown is the behaviour of the TOD/GDD ratio for Martinez-type grating compressors with different line spacings d as function of the beam incidence angle θ_{in} minus the Littrow angle θ_{Litt}.

with broadband spectra and large beam sizes on the imaging system, chromatic and spherical aberrations will occur. One way to estimate the effect of aberrations is by using ray-tracing programs, which allow to numerically calculate the accumulated dispersion due to propagation thought a specific set of optical elements. For the accurate modelling of the Martinez compressor, we used the ray-tracing software Optica3 (from Wolfram Research Inc.). In order to reduce the simulated aberrations, the lenses in the original scheme (see figure 2.8 (b)) are substituted by spherical reflective optics (f = 200 mm) to reduce chromatic aberrations. Further a mirror is placed in the Fourier plane in order to fold the Martinez setup and to reduce the footprint. Figure 2.10 shows the ray-tracing simulation of the final Martinez-type grating configuration used in the presented mid-IR OPCPA system. This ray-tracing simulations using our mid-IR pulse properties showed minimal aberrations and yield GVD and TOD values close to the result from the analytic equations.

In conclusion, in the OPCPA design, which is presented in the following section 2.2, as well as in the fundamentally rebuilt power-upgrade presented in chapter 3, we use a combination of sapphire bulk material and a folded Martinez-type grating arrangement with a grating line density of 200 lines/mm as stretcher/compressor combination. On one side the arrangement is relatively simple and easy to align compared to more elaborated schemes including for example grism pairs or multi-prism pair combinations and allows on the other side the full compensation of second and

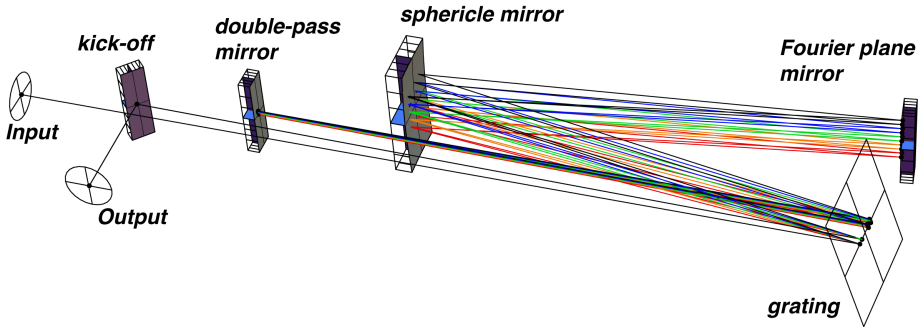

Figure 2.10: Ray-tracing simulation performed with Optica3 software of folded, all-reflective Martinez-type grating compressor. The final compressor version used in our mid-IR OPCPA system applies spherical mirrors (f=200 mm) instead of lenses to avoid chromatic aberrations. Further the setup is folded by placing a mirror in the Fourier plane in order to facilitate the alignment and to reduce the compressor size.

third order dispersion.

2.2 Mid-IR OPCPA

This section describes the general design and building blocks of the high power, mid-IR OPCPA source. First, in section 2.2.1 a short overview about the OPCPA layout and the main design considerations are given and in the following sections the individual OPCPA parts are discussed in detail. The final output parameters of the system are then described in section 2.2.6.

2.2.1 General layout

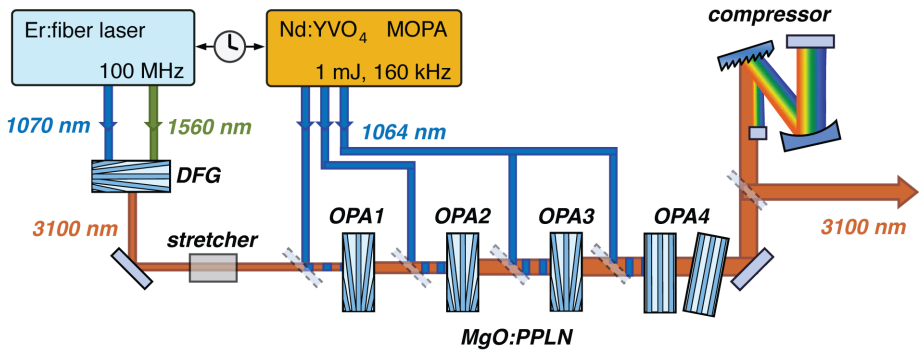

Figure 2.11: Layout of high power, mid-IR OPCPA system. The mid-IR seed is generated via difference frequency generation (DFG) between the two outputs of a fiber laser and afterwards amplified in a chain of four OPA stages.

Figure 2.11 shows the OPCPA scheme, highlighting the individual building blocks. The main advantages of the chosen system design is summarized below:

- **Fiber laser based, mid-IR front end.** The mid-IR seed pulses of the OPCPA system are generated via difference frequency mixing between both output arms of a two-color, Er:fiber laser system. The use of a fiber laser in the OPCPA front-end ensures excellent long-term stability of the spectrum, pulse energy as well as beam pointing of the generated mid-IR seed pulses. The DFG process between the two femtosecond output arms of the fiber laser, permits spectral bandwidth of the mid-IR seed pulse supporting transform-limited pulse durations of sub-3 optical cycles. Since both DFG input beams originate from the same fiber oscillator, the carrier-envelope phase (CEP) of the mid-IR seed pulse is passively stabilized (see section

2.1.4) and the absolute CEP value can be tuned, by a change of the relative time delay between the two DFG input pulses.

- **Industrial-grade, high power pump laser.** As pump laser a state-of-the-art, high power, picosecond pump laser is used, providing a total pulse energy of 1 mJ at 160 kHz and excellent beam qualities of M^2 of 1.15. The industrial-grade of the pump laser ensures long-term reliability of the beam pointing and output energy, which is crucial for long-term operation of the OPCPA system, since the OPA process is highly dependent on the pump peak intensity and on the temporal-spatial overlap of pump and idler pulses (see equation 2.13).
- **Amplification in OPA chain.** The mid-IR seed pulses are amplified via optical parametric amplification (OPA). The advantages compared to common laser amplification, which is based on stimulated emission, are many-fold, such as for instance an absence of energy storage in the gain media and a tuneable amplification bandwidth depending on the phase-matching conditions (see section 2.1.3). In our case, a chain of four consecutive OPA stages ensures a high total energy gain of 66 dB ($\sim$4 million), while maintaining a mid-IR spectral bandwidth, supporting few-cycle pulse durations of 5 optical cycles.
- **Stretcher/compressor combination.** The mid-IR seed pulses are stretched by propagation through solid bulk material and after amplification temporally recompressed by a Martinez-type grating device. This carefully chosen stretcher/compressor combination (see section 2.1.5) is simple to align and ensures the temporal compression of the mid-IR pulses close to the transform-limited few-cycle pulse duration of around 5 optical cycles.

2.2.2 Front-end for mid-IR seed generation

The mid-IR front-end which generates the seed pulses of the OPCPA system consists of a commercial fiber-based laser providing femtosecond pulses with center wavelengths at 1075 and 1560 nm and a difference frequency generation (DFG) stage between those pulses. The schematic setup is pictured in figure 2.12. As fiber laser we use the Femtofiber Scientific (FFS) laser system from Toptica Photonics AG which consists of an Erbium (Er) doped fiber oscillator and subsequent fiber amplifiers operating at 100-MHz repetition rate. After the oscillator, the beam at a center wavelength of 1560 nm is split into two arms. One is further amplified and provides after compression in a prism assembly an output energy of

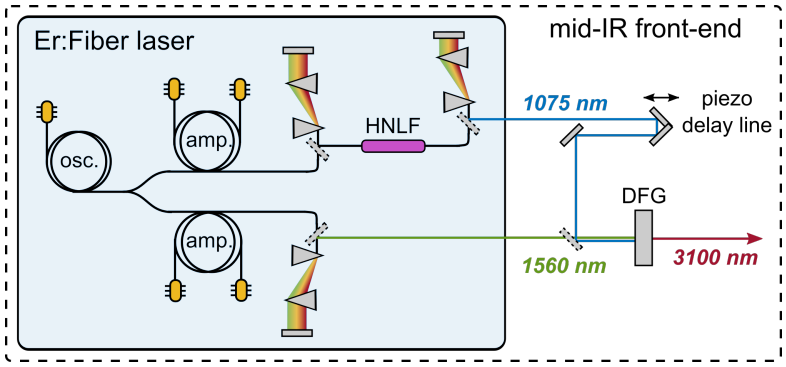

Figure 2.12: Setup of OPCPA front-end for mid-IR seed generation, consisting of a two-color output fiber laser and a difference frequency generation (DFG) stage based on a MgO:PPLN crystal. The mid-IR output is passively CEP-stabilized, since both inputs origin from the same oscillator (see section 2.1.4). HNLF: highly nonlinear fiber; osc.: oscillator; amp.: amplifier.

2.5 nJ at 1560 nm wavelength and a pulse duration of 79 fs. The second arm is also amplified, temporally compressed and then fed into a nonlinear fiber to undergo supercontinuum generation. The obtained spectrally broadened pulses are compressed in another prism assembly and after spectral filtering exhibit a center wavelength of 1075 nm and an energy of 100 pJ at a pulse duration of 35 fs. The amplitude and phase of the electric fields of both fiber laser outputs are characterized by a SHG-FROG device (see appendix B) and the results are shown in figure 2.13. Since all beams and optical components inside the fiber system are, except for the prism compressors, completely fiber coupled, the system provides a stable and hands-off operation and was continuously operating over the course of the presented thesis without a significant drop of output energy or change of beam pointing.

The mid-IR pulses, which are used as seed for the OPCPA system, are generated via difference frequency generation (DFG) of both fiber laser outputs in a 5% magnesium oxide doped periodically poled lithium niobate (MgO:PPLN) crystal. The MgO:PPLN is poled in a fan-out geometry, permitting a wide tunability of the DFG center wavelengths. Figure 2.14 illustrates the spectral output performance of the DFG stage. In the ideal case of perfect phase-matching and transform-limited input pulses, the DFG spectrum would span a $1/e^2$ bandwidth of 1300 nm wavelength (grey area) from 2900 to 4200 nm. The real DFG setup provides less spectral bandwidth mainly due to residual chirp of the fiber output pulses and due to

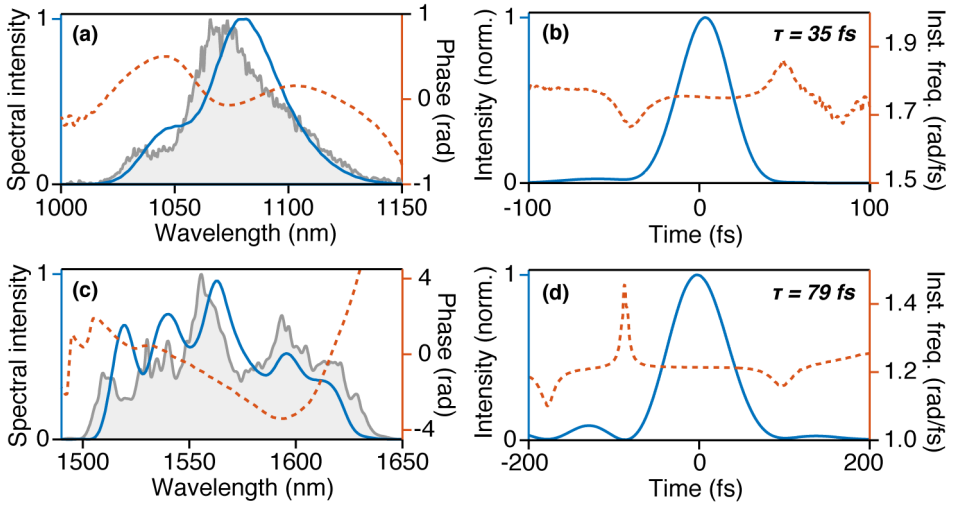

Figure 2.13: Spectro-temporal characterization of the two output beams of the FFS Toptica fiber laser. (Left side): Retrieved spectral intensity (blue line) and amplitude (orange dotted line) from the output beams at 1075 nm (a) and at 1560 nm (c) center wavelength obtained by a SHG-FROG device (see appendix B). Grey shaded areas show the measured spectrum obtained by a FTIR spectrometer. (Right side): Retrieved temporal intensity (blue line) and phase (orange dotted line) revealing a pulse duration of 35 fs for the output at 1075 nm (b) and a pulse duration of 79 fs at a pulse duration for the output at 1560 nm wavelengths (d).

phase-matching considerations of the 1 mm long DFG crystal. The orange and blue lines in figure 2.14 show two tuning possibilities of the DFG output spectrum, obtained by fine adjustment of the temporal overlap and the applied quasi-phase matching period of the fan-out MgO:PPLN crystal. By optimization for maximal DFG pulse energy of 11 pJ (blue line) a spectral bandwidth of 600 nm supporting a transform-limited pulse duration of $\sim$41 fs is obtained. The DFG output $1/e^2$ bandwidth can be further increased to 850 nm (orange line) at the expense of a reduced pulse energy of 3.5 pJ. This broader output DFG spectrum supports a transform-limited pulse duration of 30 fs, which corresponds to sub-3 optical cycles at the center wavelengths of 3150 nm. For seeding the following OPA chain (see section 2.2.5) the DFG settings with high output energies is used (blue line).

Note, that the generated mid-IR pulses feature passive CEP stability, due to the fact that both DFG input pulses originate from the same fiber oscillator (for theoretical background see section 2.1.4). The absolute CEP value

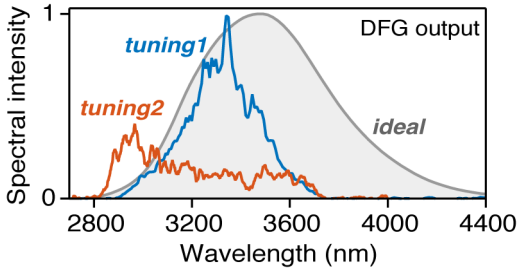

Figure 2.14: DFG output characteristics. Grey shaded area shows the calculated DFG spectrum, assuming perfect phase-matching and transform-limited input pulses. The real DFG output is spectrally narrower, due to phase-matching considerations, achieving output pulse energies of up to 11 pJ (blue line) and a $1/e^2$ spectral bandwidth of up to 850 nm (orange line), which yields a transform-limited pulse duration of 30 fs (2.8 optical cycles). The DFG spectrum can be tuned by changing the used phase matching period of the fan-out MgO:PPLN crystal and by changing the temporal delay between both input pulses.

can be changed by adjusting the temporal delay between the two DFG input beams over the range of the length of an optical cycle. Since both DFG input pulses exhibit multi-cycle pulse durations, this delay change hardly influences the overall DFG output energy. In our setup the temporal delay between the DFG input pulses is controlled by a change of the beam propagation path of one input beam via a piezoelectric actuator delay line.

2.2.3 Pump laser system

The pump energy for the optical parametric amplifiers is provided by a commercial Hyper-Rapid laser in combination with a Hyper-Rapid Booster Amplifier produced by Coherent Inc. The laser is a diode-pumped solid-state laser (DPSSL) based on laser amplification in neodymium-doped yttrium orthovanadate (Nd:YVO_4) and uses a semiconductor saturable absorber modelocked, master oscillator power amplifier (MOPA) architecture. The system provides an overall pulse energy of around 1 mJ divided in three individual lines of 105 µJ, 260 µJ and 690 µJ energy at a pulse repetition rate of 160 kHz. The output pulses at the center wavelength of 1064 nm feature a transform-limited duration of around 9.5 ps.

Since the OPA process is strongly dependent on the peak intensity of the pump beam (see equation 2.13), an excellent short- and long-term energy stability of the pump laser is crucial for stable operation of the OPCPA sys-

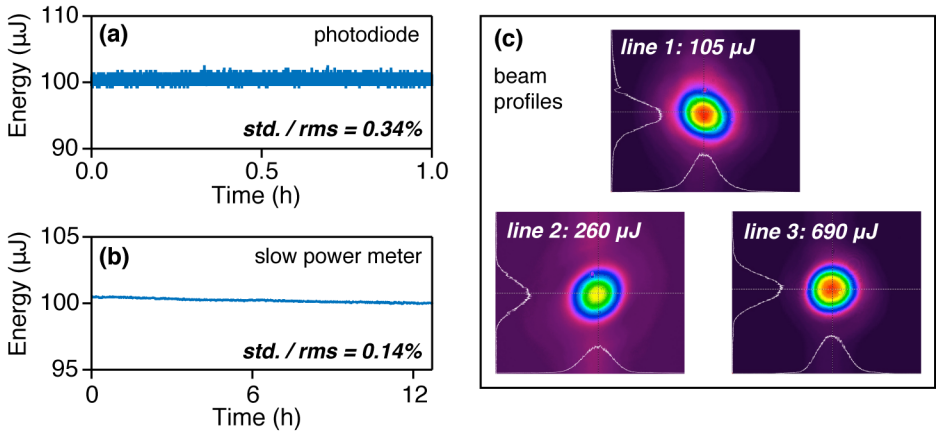

Figure 2.15: Output energy stability and spatial profile of Hyper-Rapid laser system used as pump source for the OPA chain. (a): With a photodiode measured shot-to-shot energy stability of output line1 obtaining 0.34% energy fluctuations over the course of 1 h. (b): With a pyro-electric power meter (time average of 1 s) measured long-term energy stability of output line1 obtaining 0.14% energy fluctuations over the course of 12.5 h. (c): Spatial profile of the three collimated output beams indicating the respective pulse energies.

tem. The shot-to-shot energy stability of the first pump output is measured with a photodiode revealing a stability of 0.34% fluctuations over the course of 1 hour (see figure 2.15 (a)). In figure 2.15 (b) is illustrated the long-term stability measurement featuring a slow reacting pyro-electric powermeter (1 s averaging) over the span of 12.5 hours obtaining 0.14% energy fluctuations. Note that the energy stabilities of the second and third outputs are similar as from the first pump output. In figure 2.15 (c) is shown the measured spatial profiles in the far-field of all output beams. The beam quality factor of all beams is given by the manufacturer to a M^2 value of around 1.15.

2.2.4 Temporal synchronization of pump and seed laser

The optical parametric amplification process is instantaneous and strongly dependent on the spatio-temporal overlap of the seed and pump pulses. Therefore, in order to achieve good shot-to-shot reproducibility of the amplified output pulses, the temporal overlap of the seed and pump pulses has to show a small temporal jitter compared to the pulse lengths. In contrary, a varying temporal overlap would strongly influence the shot-to-shot

amplification gain. Moreover the output spectrum would change from pulse to pulse due to the fact that the seed wavelengths are linearly dispersed in time and therefore at different delays, different parts of the seed spectrum would experience the maximum gain.

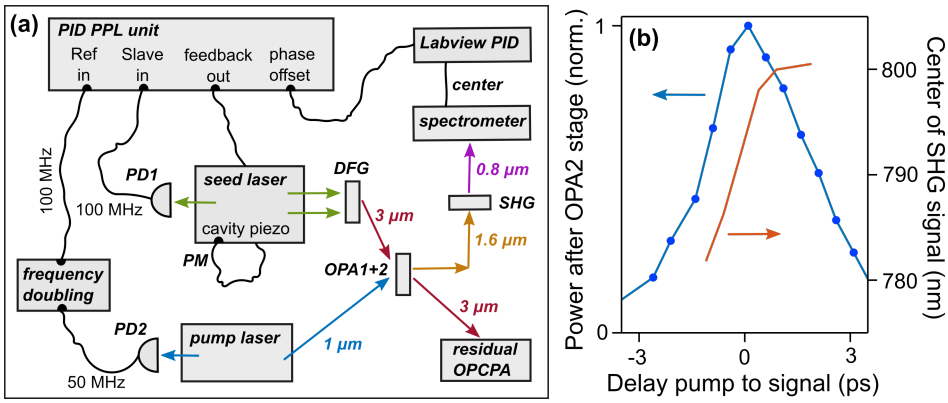

Figure 2.16: Setup of temporal synchronization of pump and seed laser oscillators (a). The oscillator repetition rates (PD1, PD2) are electronically phase-locked by adjusting the cavity length of the seed fiber laser (PM). Long-term stabilization is performed by a secondary, optical feedback-loop which adjusts the phase-offset of the electronic phase-lock loop to a fixed center wavelength of the SHG of the signal obtained after the second OPA stage. The calibration curve (b) of this secondary feedback-loop shows a linear behavior between the SHG center wavelengths and the pump-to-seed time delay around the position of the maximal output power with a linear slope of 9 nm/ps over a delay range of 2 ps.

In our case, where the seed laser and pump laser are derived from separated oscillators, a harmonic of their repetition rates f_1, f_2 have to be synchronized. Otherwise, the repetition rate offset $f_0 = f_1 - f_2 \neq 0$ would cause both laser pulses to continuously separate in time. The synchronization of two mode-locked oscillators is typically achieved, by locking the cavity round trip length L and therefore the repetition rate f = c_0/L of the slave oscillator to the repetition rate of the master oscillator. This synchronization can be implemented for example by a electronic phase-lock loop (PLL) [103].

In figure 2.16 (a) is shown the synchronization concept implemented in our OPCPA system. The repetition rates of the oscillators of the pump and seed laser are detected with two photodiodes (PD1, PD2). Afterwards the electric signal of the pump repetition rate of 50 MHz is frequency doubled

by a combination of a commercial electronic band-pass amplifier and band-pass filters in order to match the seed laser repetition rate of 100 MHz. A commercial, electronic PLL unit (FFS-SYNC-PPL from Toptica Photonics AG) is used to lock both repetition rate signals to a constant phase offset adjusting the cavity length of the fiber laser by translating a cavity mirror, mounted on a piezoelectric crystal (PM). In phase-locked operation, the PLL unit shows a synchronization jitter of around 350 fs rms, which is just a few percent of the durations of the stretched seed pulses or the pump pulses in the OPA stages.

Additionally to this primary synchronisation loop, a home-built, secondary optical feedback-loop is used to ensure a long-term stabilized phase-offset between the two locked cavity repetition rates. A common scheme of such optical feedback loop applies a parametric cross-correlation setup, generating for example a SFG signal between the two pulse trains and monitoring the signal strength of the SFG signal over time. A change of the SFG signal strength indicates a change of the repetition rate phase offset between the seeded pulse trains and can be used as feedback signal to the primary PLL unit. More elaborated schemes use even two balanced parametric cross-correlators [83]. In contrast, our approach uses an already existing OPA stage of the OPCPA system (see figure 2.16 (a)) to obtain the feedback signal and therefore avoids complex, additional cross-correlation setups.

After the second OPA stage, the generated signal wave at a center wavelengths around 1.6 µm is separated by a dichroic optic, frequency doubled in a BBO crystal and the resulting spectrum is monitored with a standard Silicon-based spectrometer. The center frequency is calculated and can be used as feedback signal for the temporal overlap of mid-IR seed and pump pulses. A change of the temporal overlap between the seed and pump pulses would result in a changing center frequency of the generated SHG of the signal, due to the fact that the mid-IR seed frequency is linearly dispersed in time. In figure 2.16 (b) is pictured the calibration curve of the feedback-signal. Around the temporal delay with the best pump-to-seed overlap yielding maximal amplification (blue line), the center wavelength of the SHG of the signal wave (orange line) exhibits a linear behaviour, allowing the use as feedback signal. Figure 2.17 shows the performance of the secondary feedback-loop in open-loop (left side) and closed-loop (right side) operation. Pictured are the temporal evolution over the course of 30 minutes of the pump-to-seed delay which is calculated using the calibration curve from figure 2.16 (blue line) as well as the amplified output energy after the second OPA stage. In the open-loop case strong power drops occur within the time frame of minutes introduced by an oscillating synchroniza-

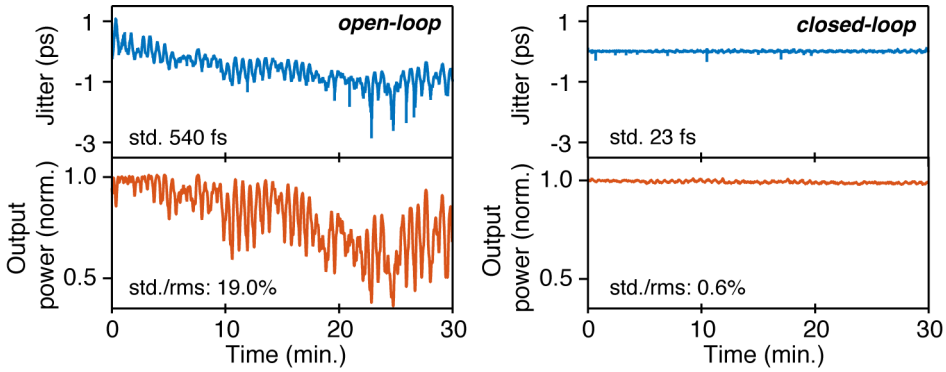

Figure 2.17: Performance of secondary, optical feedback-loop with a 20 Hz feedback rate for the temporal synchronization between pump and seed laser. The blue line indicates the temporal jitter and the orange line shows the resulting behavior of the output power measured after the second OPA stage (orange line). In the open-loop case (left graph) strong power drops occur within the time frame of minutes introduced by an oscillating synchronization jitter with a peak-to-peak height of 0.5 ps within minutes and slow jitter drift within 30 minutes. By closing the feedback-loop (right graph) the synchronization jitter is reduced to a standard deviation of 23 fs resulting in a power-stability better than 0.6% rms.

tion jitter with a peak-to-peak height of 0.5 ps within minutes and slow jitter drift within 30 minutes. The jitter standard deviation is around 540 fs yielding a fluctuation of the second OPA stage output power of 19% rms. By closing the secondary feedback-loop the synchronization jitter is reduced to a standard deviation of 23 fs resulting in a power-stability better than 0.6% rms.

2.2.5 Pulse stretcher and OPA chain

For an effective parametric amplification of the initially sub-100 fs, mid-IR seed pulses by the ps long pump pulses, their temporal durations have to converge to similar pulse lengths. According to the theoretical considerations discussed in section 3.1.1, the temporal idler-to-pump ratio should be around 0.4 to permit a good energy conversion efficiency while allowing broadband spectral amplification. The mid-IR seed pulse is stretched by propagation through a 50 mm long sapphire rod, which adds -29,200 fs^2 GDD at a center wavelength of 3.05 µm and stretches the DFG seed pulse from initial sub-100 fs to around 3.5 ps pulse duration, resulting in a idler-to-

pump duration ratio of 0.37. The amplification of the stretched, mid-IR seed pulses is performed in an OPA chain consisting of four consecutive amplification stages using collinear beam geometry. All OPA stages are based on amplification in MgO:PPLN crystals, due to their high damage threshold, good mid-IR transparency, broad phase-matching bandwidth and very high nonlinear coupling coefficient d_{eff} (see table 3.1). A detailed discussion about available parametric amplification crystals for mid-IR radiation can be found in section 3.2. In each stage, the pump and seed diameters are adjusted to provide optimum energy transfer from the pump to the mid-IR idler wave and after each stage the residual pump and generated signal beams are filtered out using specially designed dichroic filters.

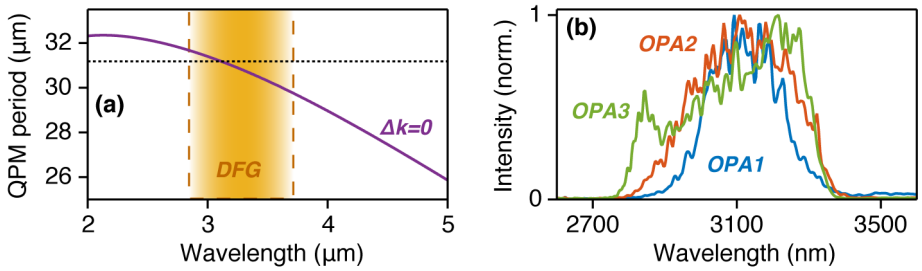

Figure 2.18: (a): Wavelength dispersion (purple line) of the quasi phase-matched (QPM) period for a MgO:PPLN crystal assuming a pump wavelength at 1064 nm. The calculation is performed using equation 2.27 in combination with the Sellmeier equation of MgO:PPLN [104]. The orange area indicates the wavelength range supported by the DFG stage and the black dotted line shows the QPM period, where the OPA1 to OPA3 are driven. (b): Normalized, amplified output spectra after the OPA1, OPA2 and OPA3 stages.

The first three OPA stages use commercial available, fan-out MgO:PPLN crystals (HCP photonics corp.) featuring a crystal aperture of 2 mm and a quasi-phase-matching periods (QPM) of 21 to 35 µm. The corresponding phase-matching curve is illustrated in figure 2.18 (a) and shows the tunability of the phase-matching idler wavelength (purple line) from 2 µm to over 5 µm assuming a pump wavelength of 1.064 µm. For the use of the presented OPA chain, the amplified center bandwidth is set to ∼3.1 µm wavelength obtained at a QPM period of 31.2 µm (black dotted line). In the first stage 22 µJ of pump energy are focused to a peak intensity of ∼25 GW/cm^2, amplifying the mid-IR pulse energy from 10 pJ to 60 nJ, featuring a gain of ∼6000. Additional stretching is performed between the first and second OPA stages by propagation of the mid-IR pulses through a 20 mm long sapphire rod to optimize the energy extraction efficiency in the second

OPA. The second and third OPA stage, which are operated close to the saturation regime, use pump peak intensities around 20 GW/cm^2 and achieve mid-IR output energies of 2.5 µJ and 12.5 µJ, obtaining gains of $\sim$40 and 5 respectively. In figure 2.18 (b) is shown the spectra of the amplified output pulses after the respective OPA stages. It can be seen, that the spectral bandwidth is slightly broadened in each consecutive OPA stage due to the saturated amplification regime in which the OPA2 and OPA3 stages are driven.

For pumping the fourth OPA stage, 620 µJ of pump pulse energy is available. In order to keep the intensity below the material damage threshold and below the onset of a beam distortion process particular for MgO:PPLN crystals, which is in detail discussed in section 3.2.3, the pump beam waist would have to be considerably bigger than in the previous OPA stages. In order to avoid diffraction from the edges of the amplification crystal, the commercially available, 2 mm aperture MgO:PPLN crystals used in the former OPAs, cannot be used. Instead, large aperture (5$\times$5 mm^2) MgO:PPLN crystals with a fixed quasi-phase matching period of 31.2 µm obtained from a collaboration with professor Hideki Ishizuki and professor Takunori Taira from the Laser Research Center for Molecular Science in Okazaki (Japan) are used [105, 106].

In order to improve the overall amplified spectral width and shape in the fourth OPA two identical, 2 mm long, large aperture crystals are used in series under different incidence angles. By tilting the crystals, the original quasi phase-matching period $pp_{orig.}$ can be increased to an effective quasi phase-matching period pp_{eff} due to Snell's law to:

$$pp_{eff} = pp_{orig.} \cdot \cos\left(\arcsin(\sin\left(\frac{\alpha}{n_{LN}}\right))\right)^{-1}, \tag{2.45}$$

where α is the beam incidence angle and n_{LN} the material refractive index. The tuning behaviour of the phase-matched spectrum as a function of the incidence angle of the co-propagating pump and mid-IR beam on the MgO:PPLN crystal surface is picture in figure 2.19 (a). The amplified center wavelength can be tuned from 3.25 µm at an incidence angle of 2°to 2.9 µm at an incidence angle of 25°. By using two crystals with different effective periods at incidence angles of 0° and 20° in series, the amplification of super-Gaussian spectral shape with a 1/e^2 spectral width of 500 nm can be achieved (see figure 2.19 (b)). The mid-IR output pulses obtain energies of 40 µJ and the spectrum supports a transform-limited pulse duration of 51 fs, which are 5 optical cycles at the center wavelength of 3.05 µm.

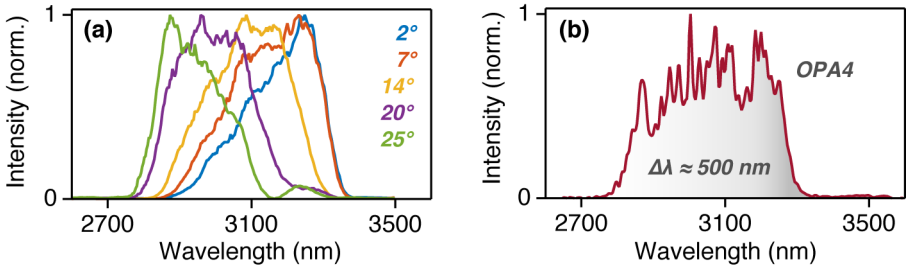

Figure 2.19: (a): Background subtracted, amplified spectra out of the fourth OPA stage using different incidence angles of the collinear propagated pump and idler beams onto the 5×5 mm^2 aperture MgO:PPLN crystals. The respective incidence angles are given for each spectrum in the respective color code. (b): The fourth OPA takes advantage of the spectrally tuneable gain bandwidth by using two identical MgO:PPLN crystals in series under beam incidence angles of 2° and 20°. This combination yields a 500 nm spanning (1/e^2 width) super-Gaussian shaped spectrum with pulse energies of 40 µJ.

2.2.6 Pulse compression and mid-IR output performance

After the parametric amplification in the OPA chain, the high energy mid-IR pulses are compressed by propagation through a folded, all-reflective Martinez-type grating compressor. The choice of the compressor device is guided by former considerations about suited stretcher/compressor combinations for mid-IR pulses presented in section 2.1.5. In table 2.2 is given the overview of the total dispersion, which is acquired during propagation through the mid-IR OPCPA system. It can be seen, that the Martinez compressor is able to compensate the former introduced dispersion, when applying an effective grating separation G of -10.7 mm, a grating line density of 200 lines/mm and an input angle θ_{in} of 16.04°. For this calculation we neglect the nonlinear OPA phase (see last term in equation 2.14), which can be compensated in the real OPCPA, by fine adjusting the grating separation and grating incidence angle.

The overall transmission efficiency of the compressor is ∼50%, yielding a total mid-IR output pulse energy of 20 µJ at the pulse repetition rate of 160 kHz which corresponds to a mid-IR average power of 3.2 W. The compressed pulse duration of the mid-IR output is measured with a SHG FROG-device (see appendix B) to 55 fs which are 5.4 optical cycles at the center wavelength of 3.05 µm, which is close to the transform-limit of 51 fs. Figure 2.20 shows the retrieved spectral intensity and amplitude (a) and temporal intensity and amplitude of the mid-IR output pulses. The output

Element	Element length or grating separation	GDD in fs^2	TOD in fs^3	FOD in fs^4
negative GDD				
Bulk stretcher	50+20 mm, Al_2O_3	-40,850	+239,050	-1,828,450
OPA crystals	12 mm, MgO:PPLN	-6,330	+42,010	-309,030
Lenses	24 mm, CaF_2	-2,270	+15,010	-100,610
Dichroic filters	17 mm, CaF_2	-1,920	+10,630	-71,270
positive GDD				
Martinez compressor	-10.7 mm, θ_{in}=16.04°	+51,370	-306,700	+2,631,690
Total dispersion		0	0	+322,330

Table 2.2: Overview of acquired dispersion of the cascaded amplified idler beam throughout the mid-IR OPCPA system at a center wavelength of 3.05 µm. The dispersion introduced by propagation though material is calculated using equations 2.40, 2.41 and applying the Sellmeier equations of Al_2O_3 [102], MgO:LN [107] and CaF_2 [101]. The introduced dispersion by the Martinez-type grating-compressor is estimated by applying equations 2.42, 2.43, 2.44 and under the use of d = 200 lines/mm, the grating distance G and the incident angles θ_{in} given in the table.

power stability is measured with a fast photodiode to be below 1% fluctuations over the course of 12.5 h (see figure 2.20 (c)). The spatial beam profile of the collimated output beam is shown in the inset of figure 2.20 and is measured with a microbolometer camera (WinCamD from DataRay Inc.).

For completeness it should be mentioned, that the expected, passive CEP-stability of the mid-IR OPCPA output pulses (details see section 2.1.4) was experimentally proven by my colleagues Alexandre Thai and Michaël Hemmer. Using a f-to-2f interferometer, they could measure a CEP stability of less than 250 mrad fluctuations over the course of 11 minutes. A detailed description of the CEP measurement can be found in [68].

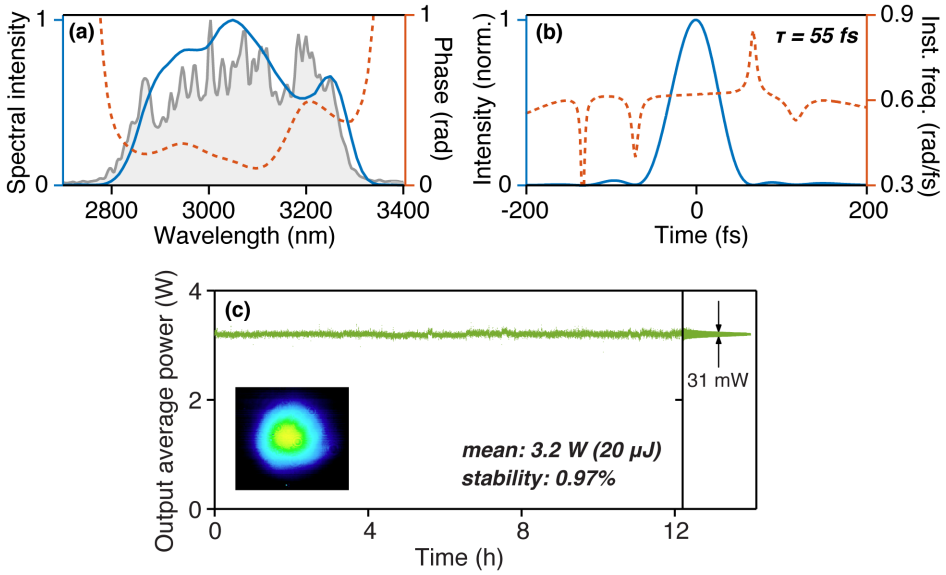

Figure 2.20: Output parameters of mid-IR OPCPA system. (a): From FROG algorithm retrieved spectral intensity (blue line) and spectral phase (orange dotted line) in comparison with the measured spectral intensity (grey area). (b): Retrieved temporal intensity and instantaneous frequency, obtaining a pulse duration of 55 fs. (c): The output power stability is measured with a photo diode over the course of 12.5 h to a stability of less than 1% rms fluctuations. The inset shows the spatial output beam profile, which is measured with a microbolometer camera.

2.3 UV to near-IR multi-color upgrade

This section describes the general design and building blocks of the ultraviolet (UV) to mid-IR upgrade of the high power, mid-IR OPCPA source. First, in section 2.3.1 a short overview about the layout of the multi-color upgrade is given and in the following sections the individual building blocks are discussed in detail. The final output parameters of the multi-color OPCPA upgrade are then described in section 2.3.5.

2.3.1 General layout

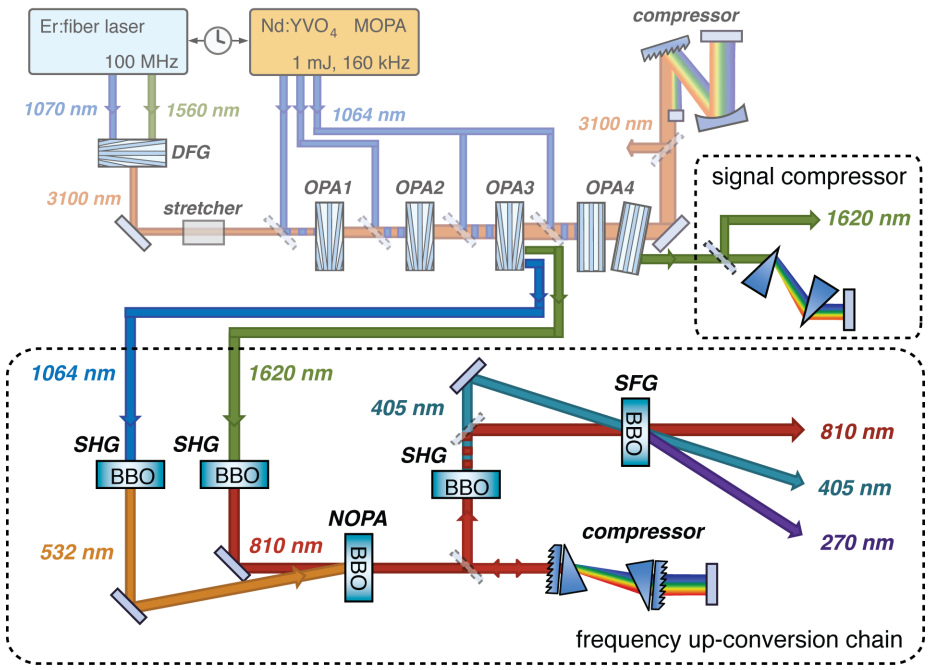

Figure 2.21: Layout of the multi-color OPCPA upgrade. A combination of the in section 2.2 described mid-IR OPCPA (top, transparent) with a signal wave compressor setup (top, right) and a high conversion-efficiency, frequency up-conversion chain (bottom) enables the generation of high peak power pulses from the ultraviolet to the mid-IR spectral range at 160 kHz repetition rate.

Figure 2.21 shows the general layout of the multi-color upgrade of the mid-IR OPCPA system presented in section 2.2. A high peak power, near-IR output at 1600 nm center wavelength is derived by extracting and temporally compressing the signal wave from the mid-IR OPCPA system. The

further outputs in the ultraviolet and visible spectral range are achieved via cascaded parametric harmonic generation in nonlinear optical crystals; an approach, which is commonly used in combination with Ti:sapphire based laser systems. In our case, this cascaded frequency up-conversion chain is driven by the recycled pump and signal beam after the third OPA stage of the mid-IR OPCPA system and provides high energy, femtosecond pulses at 270 nm, 400 nm and 800 nm wavelengths at a 160 kHz repetition rate. The combination of the mid-IR OPCPA with the multi-color upgrade enables the generation of all-optically synchronized, high peak-power, femtosecond pulses ranging from the ultraviolet to the mid-IR spectral range.

In our case, the design of the frequency up-conversion chain is governed by the specific output parameters which are required to enable multi-color, pump-probe experiments in the strong-field regime (see more details in section 1.2). Below are explained the main design considerations which influenced the setup of the multi-color OPCPA upgrade:

- **Optical synchronization.** In order to allow reliable pump-probe experiments, the temporal jitter between the involved pulses has to be considerably smaller than the pulse durations, which is especially demanding in case of femtosecond pulses. When the pump and probe pulses are derived from independent oscillators, an active synchronization of the cavity repetition rates is required (see also section 2.2.4), which limits the minimal temporal jitter typically to a few tens of femtoseconds of even to below one femtosecond in dependence of the applied active synchronization scheme [108, 109]. However active synchronization scheme are always linked to an increase complexity of the radiation source. A more elegant approach, allowing a much smaller temporal pulse jitter, is optical synchronization, where all involved pulses are derived from the same laser system and the pulse repetition rates are therefore passively synchronized. In this case temporal pulse delay jitters are mostly defined by small changes of the beam path lengths by for example pointing instabilities or airflow induced refractive index changes of free space beam paths. In our multi-color upgrade all wavelengths are derived from the mid-IR OPCPA system and are therefore passively synchronized to each other, which allows minimal temporal pulse jitter. Another advantage of this layout scheme is the use of the excellent laser output parameters from the pump laser and mid-IR OPCPA system for driving the generation of the multi-color outputs, especially considering the power-stability, beam profiles and high repetition rate of the driving system.

- **Conversion efficiency versus spectral bandwidth.** In order to enable multi-color experiments in the strong-field ionization regime, the different outputs of the frequency up-conversion chain have to reach peak intensities in the 10^{13} to 10^{14} W/cm^2 regime. This requires good beam focusing ability and a sufficiently high output peak power - defined as the quotient of pulse energy divided by pulse duration - in the tens to hundreds of MW regime. One possibility to increase the output pulse energy, which is linked to the energy conversion efficiency during the cascaded parametric harmonic generation, is the increase of the applied nonlinear crystal lengths (see equation 2.13). However, simultaneously the amplification bandwidth of the nonlinear process will decrease for longer nonlinear crystals (see equation 2.31), possibly leading to a increase of the transform-limited pulse duration, which scales inversely proportional with the output peak power. In the design of the frequency up-conversion chain presented here, the crystal lengths are chosen to obtain maximal conversion efficiencies, while supporting pulse durations between 50 and 100 fs. This temporal range is set to be close to the mid-IR output pulse duration of 55 fs, enabling a temporal resolution of pump-probe experiments in the sub-150 fs range. Additionally, the chosen crystal lengths in the multi-color OPCPA upgrade allow the operation of the SHG and SFG stages at high conversion efficiencies and the use of the non-collinear OPA stage close to pump depletion, yielding high energy-stabilities of the multi-color output pulses inherited from the industrial grade pump laser.

2.3.2 Near-IR output at 1.6 µm wavelength

The near-IR output of the OPCPA system is obtained at the end of the mid-IR OPA chain as a by-product of the three-wave-mixing parametric process. After the fourth OPA stage, the signal, idler and pump waves of the OPA process are separated via dichroic optics. The extracted signal beam contains 22 µJ pulse energy at a center wavelength of 1620 nm and a 1/e^2 bandwidth of 100 nm. The spectrum is shown as grey shaded area in figure 2.22 (b). Since the amplified idler and signal pulse energy in the OPA4 stage are linked due to the Manley-Rowe relation (see equation 2.22), one would expect a higher signal pulse energy E_{sig} of:

$$E_{sig} = \frac{\omega_{sig}}{\omega_{idl}}\left(E_{idl,out} - E_{idl,in}\right) = 2.0 \cdot (40\mu J - 12.5\mu J) = 55\mu J, \quad (2.46)$$

where $E_{idl,in}$ and $E_{idl,out}$ are the input and output pulse energies of the idler pulse in the fourth OPA stage, given in section 2.2.5. The discrepancy between obtained and expected signal pulse energies is caused by the used custom-made dichroic optics, which are designed to maximize the transmission efficiency at the main OPCPA output in the mid-IR range and which are not perfectly optimized for the signal wavelength range.

The signal beam is temporally compressed in a folded, silicon-based prism compressor. The compressor design was chosen under considerations of the expected dispersion of the signal wave. After the fourth OPA stage of the OPCPA setup, the mid-IR beam is expected to exhibit a GDD of around -51,000 fs^2 and a TOD of around +300,000 fs^3 (see table 2.2). Due to the phase relation of the OPA process and assuming transform-limited pump pulses with no dispersion, the signal wave should therefore obtain similar GDD and TOD values as the mid-IR beam, but with an inverted sign of the GDD (see equations 2.17 and 2.18). The required compressor device has therefore to be able to add a negative GDD and a negative TOD to temporally compress the near-IR signal output. Compressors purely relying on bulk propagation or gratings do not fulfill this requirement (see table 2.1). Instead we used a prism compressor based on silicon prisms. The introduced dispersion of such devices can also be estimated analytically (see section 2.5.5 in [72]), but we used the ray-tracing program Optica3 (Wolfram Research, Inc.) to simulate the full compression device. Figure 2.22 (a) shows the obtained ray-tracing simulation of the prism compressor. Using two silicon-prisms (apex angle 32°) under a beam incidence angle close to Brewster angle and with a prism separation of 25 cm from tip to tip, an introduced double-pass dispersion of around -50,000 fs^2 GDD and -470,000 fs^3 TOD is calculated, indicating an overcompensation of the third order dispersion.

The experimental realization of the prism device compresses the near-IR pulses to a temporal duration of 96 fs. The spectral and temporal behaviour of the compressed near-IR pulses are measured with a SHG-FROG (see appendix B) and the retrieved spectro-temporal properties are shown in figure 2.22 (b,c). The retrieved spectral phase (orange dotted line in figure 2.22 b) clearly shows the expected, residual third order dispersion, which explains the difference between the measured pulse duration of 96 fs and the transform-limited duration of 72 fs. The compressor has a transmission efficiency of around 70%, resulting in output pulse energies of 15 µJ, which yields a peak power of 156 MW.

The obtained pulse duration of the near-IR output is sufficiently short for

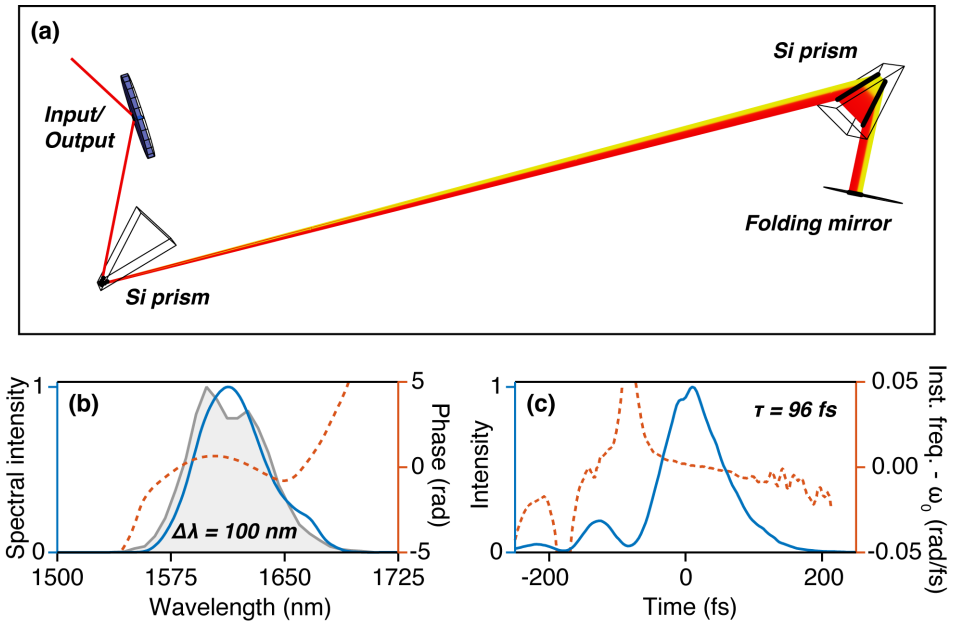

Figure 2.22: (a): Layout of silicon-prism compressor used for temporal compression of the near-IR OPCPA output. (b): Retrieved spectral intensity (blue) and spectral phase (orange, dotted) of the near-IR output obtained by a SHG-FROG device in comparison with the measured spectrum (grey area). The $1/e^2$ bandwidth is around 100 nm and the spectrum supports a transform-limited pulse duration of 72 fs. (c): Retrieved temporal intensity (blue) and instantaneous frequency (orange, dotted) of the near-IR output, yielding a pulse duration of 96 fs.

its purpose in pump-probe experiments with sub-150 fs resolution or as molecular alignment beam in strong-field experiments on gas targets (see section 1.2). In case, a better pulse compression would be required, the third order dispersion could possibly be compensated by the use of grism compressors or by a combination between prism and grating compressor, possibly yielding higher total transmission losses as the compression scheme presented here.

2.3.3 High energy, few-cycle pulses at 800 nm

Figure 2.23 illustrates the detailed setup for generation of the high energy, femtosecond pulses at a center wavelength of around 800 nm. After the third OPA stage of the high power OPCPA (see section 2.2), the temporally stretched signal wave at 1620 nm wavelengths as well as the residual pump

wave at 1064 nm wavelength are extracted via dichroic optics. Both beams are frequency doubled in high efficiency SHG stages and afterwards the frequency-doubled signal wave is amplified in a non-collinear OPA stage pumped by the frequency doubled pump wave.

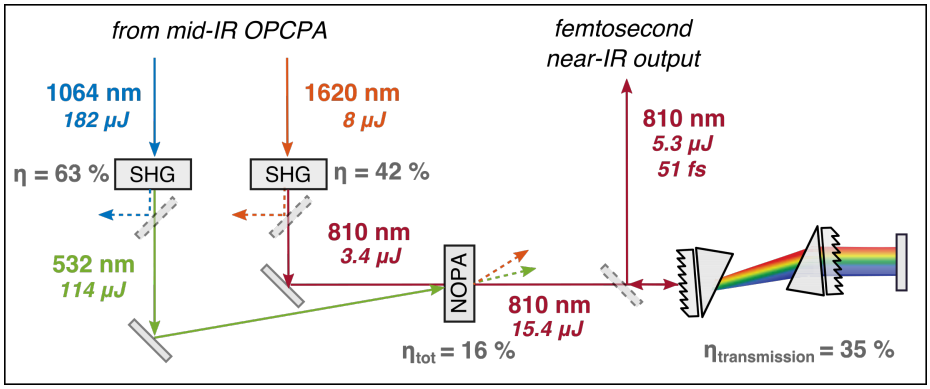

Figure 2.23: Generation scheme of femtosecond, high energy pulses at 810 nm wavelength, which is part of the multi-color OPCPA upgrade. Shown are the obtained pulse energies and energy conversion efficiencies of each second harmonic generation (SHG) or non-collinear optical parametric amplification (NOPA) stage.

The used nonlinear crystals as well as their phase-matching conditions and crystal length are chosen in order to allow maximal energy conversion efficiencies, while permitting a phase-matching bandwidth of the 800 nm beam supporting sub-50 fs pulse durations.

In table 2.3 is given an overview of the amplification crystals used in our setup, including information about the phase-matching (PM) parameters such as phase-matching angle and non-collinear angle as well as specific crystal properties such as the crystal length and the resulting phase-matching bandwidth. In figure 2.24 (a, b, c) are illustrated the phase-matching behaviours for each crystal configuration as a function of the phase-matching angle. In both SHG stages we use beta barium borate (BBO) crystals in collinear beam geometry and type 1 phase-matching configuration, using crystal lengths of 2 mm and 5 mm for frequency doubling of the beams at 1620 nm and 1064 nm wavelengths respectively. In the consecutive amplification stage, a 5 mm long BBO crystal is used in a non-collinear beam geometry with an angle of 2.45° in order to achieve a broad phase-matching bandwidth via group-velocity matching for the amplification of the 800 nm pulses. Figure 2.24 (c) shows, how the phase-matching behaviour evolves in case of a distinct non-collinear angle.

crystal	Interaction (wavelength in nm)	d_{eff} (pm/V)	crystal length	non-coll. angle	PM angle	PM bandwidth
BBO	1620 (o) + 1620 (o) = 810 (e)	1.94	2 mm	0°	19.8°	176 nm at 810 nm
BBO	1064 (o) + 1064 (o) = 532 (e)	2.01	5 mm	0°	22.9°	8.8 nm at 1064 nm
BBO	1550 (o) + 810 (o) = 532 (e)	2.08	5 mm	2.45°	23.9°	250 nm at 810 nm

Table 2.3: List of nonlinear crystals applied in frequency up-conversion chain to generate high energy, femtosecond pulses at 800 nm. Given are the phase-matching (PM) parameters like d_{eff}, non-collinear (non-coll.) angle and phase-matching angle. The resultant phase-matching bandwidth is calculated for the given crystal length, using equation 2.31 and Sellmeier equation [110].

In the two SHG stages as well as in the NOPA stage we use BBO crystals due to their higher nonlinear interaction constant d_{eff} compared to other bulk crystals, which are commonly used for near-IR frequency mixing processes such as lithium triborate (LBO) or potassium dihydrogen phosphate (KDP). The nonlinear crystal with the closest amplification behaviour to BBO in the near-IR spectral range is bismuth triborate (BiBO), which features a slightly higher d_{eff} as BBO, but which is not used in our setup due to the smaller acceptance bandwidth in the case of a pump wave at 532 nm wavelength. Also in the literature, BBO is the typically used amplification crystal in OPCPA systems delivering high power, femtosecond outputs at near-IR wavelengths around 800 nm [6, 111, 112].

The specific choice of the nonlinear crystal parameters enables high energy conversion efficiencies in each parametric frequency-mixing stage. In the presented frequency up-conversion setup, 8 µJ pulse energy at 1620 nm wavelengths are obtained after the third OPA stage of the mid-IR OPCPA (see figure 2.23). These pulses are frequency doubled to 3.4 µJ energy pulses at 810 nm wavelength, yielding a high conversion efficiency of 42% while maintaining a wide bandwidth. In parallel, after the third OPA stage also 182 µJ pulse energy of the residual pump at 1064 nm wavelength are recycled. These transform-limited, picosecond pulses are frequency doubled with a high conversion efficiency of 63% to 114 µJ pulses at 532 nm center wavelength. The energy scaling behaviour of this SHG stage is shown in figure 2.25 (a), indicating an operation close to depletion of the fundamental driving wave, which yields high output power stabilities. The power stability at 532 nm is measured with a pyro-electric

detector to fluctuations of 0.2% of the rms over the course of 30 minutes, making this output beam ideally suited as pump wave for an OPA stage.

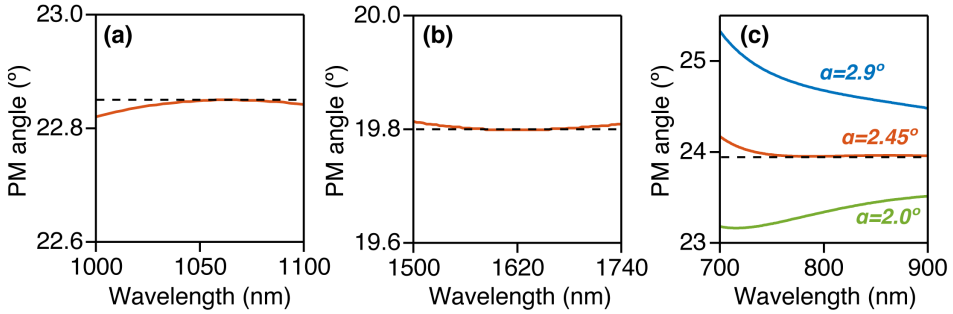

Figure 2.24: Phase-matching behavior for perfect phase-matching Δk=0 for each optical parametric stage as a function of wavelength. Shown are the phase-matching curves for the SHG of 532 nm wavelength (a), the SHG of 1620 nm wavelength (b) and the non-collinear amplification stage for the 810 nm pulses (c). In the latter case, the phase-matching curves for three different non-collinear angles α are given. The black dotted lines indicate the used phase-matching angle.

In the consecutive non-collinear OPA stage the near-IR pulses at 810 nm wavelengths are amplified from the initial 3.4 µJ energy to 15.4 µJ energy applying the 114 µJ pump energy at 532 nm wavelengths. A pump-to-signal energy conversion efficiency η_{sig} of 10.5% and a corresponding total energy conversion efficiency of $\eta_{tot} = \eta_{sig} \cdot (1 + \omega_{idl}/\omega_{sig}) = 16.0\%$ is obtained, which is relatively high in the case of broadband parametric amplification and Gaussian-like spatio-temporal beam profiles (see section 3.1.2). Figure 2.25 (b) illustrates the signal wave amplification behaviour of the NOPA stage as function of the seeded pulse energy (blue line). The calculated evolution of the pump-to-signal conversion efficiency (orange line) indicates an operation close to the pump depletion regime.

After amplification, the stretched, picosecond pulses at 810 nm are compressed by a custom-made grism compressor designed to compensate the theoretical expected dispersion of the near-IR beam at 810 nm wavelength. Similar to the argumentation in section 2.3.2, the mid-IR idler pulses in the third OPA stage of the OPCPA system are expected to exhibit a GDD of -51,000 fs^2 and a TOD of +300,000 fs^3 (see table 2.2). Due to the phase relationship in the OPA process, the generated signal beam at 1620 nm wavelength is expected to obtain the same TOD value, but an inverted GVD value of +51,000 fs^2 in comparison to the mid-IR idler (see equations 2.17, 2.18). After frequency doubling of the signal wave at 1620 nm

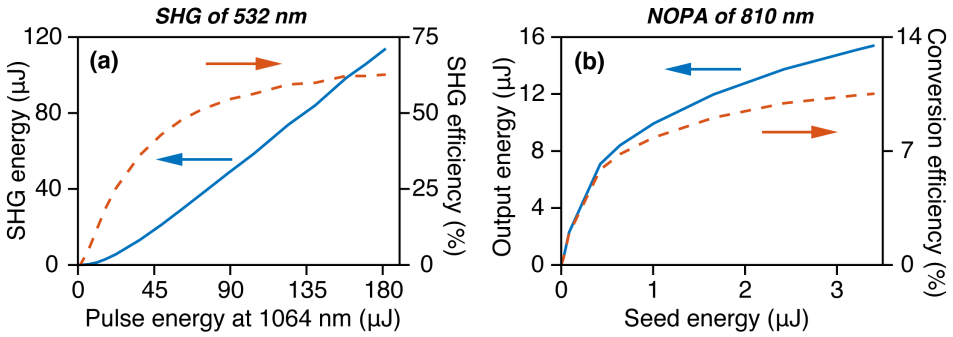

Figure 2.25: (a): Power-scaling behaviour of the SHG stage for the generation of 532 nm wavelength pulses as a function of the driving pulse energy at 1064 nm wavelength. (b): Amplification behaviour of NOPA stage for amplification of the 810 nm wavelength pulses as a function of the pump pulse energy at 532 nm wavelength. Shown are also the corresponding energy conversion efficiencies, indicating a efficiency saturation at high driving energies in the case of the SHG stage as well as in the NOPA stage.

wavelength, the generated pulses at 810 nm wavelengths are supposed to obtain half the GDD and a quarter of the TOD as the driving pulses (see equations 2.19, 2.20). Therefore, the required compressor has to be able to introduce -25,500 fs^2 of GDD and -75,000 fs^3 of TOD in order to compress the amplified, near-IR pulses at 810 nm wavelengths close to the transform-limit. In our case, the specific geometric design of the used grism compressor is computed with the ray-tracing program Optica3 (Wolfram Research, Inc.). Figure 2.26 (a) shows the final grism compressor configuration, which consists of two transmission gratings (line density of 1200 lines/mm) and anti-reflection coated BK7-glass prisms with an apex angle of 56 degrees. Using a grism separation of 0.9 mm and a beam incidence angle of 31° to the normal, the compressor should introduce a dispersion of around -25,500 fs^2 GDD and -70,000 fs^3 of TOD. In the figure is illustrated the ray-tracing for beam at 810 nm center wavelength assuming a beam diameter of 2 mm and a spectral span of 40 nm.

The compressed pulse duration is measured with an SHG-FROG device (see appendix B) to be 51 fs at a center wavelength of 810 nm, which is very close to the supported transform-limited pulse duration of 45 fs. In figure 2.26 (b) is shown the retrieved spectral intensity and phase while in figure 2.26 (c) is illustrated the measured temporal intensity and instantaneous frequency of the compressed near-IR pulses. The output pulses show energies of 5.3 µJ, yielding an overall compressor transmission ef-

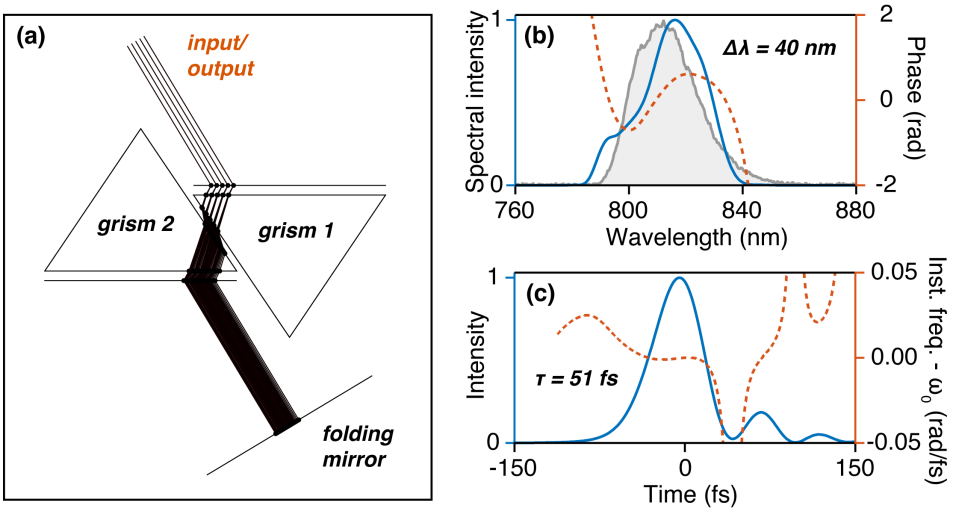

Figure 2.26: (a): Grism device for temporal pulse compression of output pulses at 810 nm wavelength consisting of two transmission gratings (1200 lines/mm) and two BK7-glass prisms (apex angle 56°). The ray-tracing performed by the Optica3 software reveals a required grism separation of 0.9 mm.(b): Retrieved spectral intensity (blue) and spectral phase (orange, dotted) of the UV output obtained by a SHG-FROG device in comparison with the measured spectrum (grey area). The $1/e^2$ bandwidth is around 40 nm and the spectrum supports a transform-limited pulse duration of 45 fs. (c): Retrieved temporal intensity (blue) and instantaneous frequency (orange, dotted) of the UV output, yielding a pulse duration of 51 fs.

ficiency of around 35%. The output power stability is measured with a pyro-electric detector to 0.5% rms fluctuations over 30 minutes.

2.3.4 Frequency up-conversion to the ultraviolet

The output pulses of the multi-color upgrade in the ultraviolet (UV) spectral range are generated by second harmonic generation and cascaded third harmonic generation driven by the femtosecond, near-IR pulses at 810 nm wavelengths, which originate from the first part of the frequency up-conversion chain (see section 2.3.3). Figure 2.27 shows the layout of the cascaded harmonic generation setup, including the measured pulse energies and energy conversion efficiencies for each frequency-mixing stage.

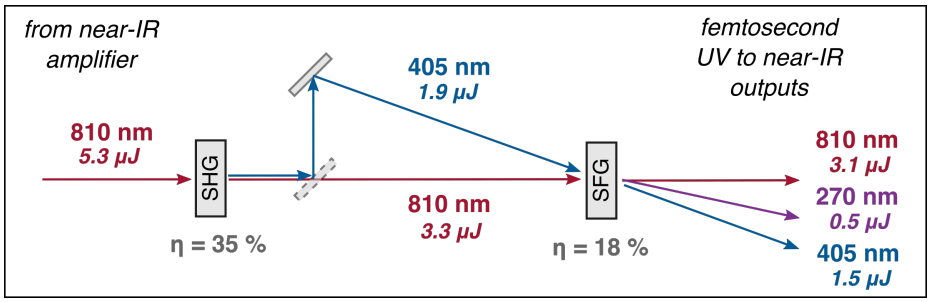

Figure 2.27: Generation scheme of the femtosecond, UV pulses at 405 nm and 270 nm wavelength, which is driven by near-IR pulses at 810 nm wavelength. Indicated are also the obtained pulse energies for each wavelength and the energy conversion efficiencies of each parametric frequency-mixing stage.

In both harmonic generation stages beta barium borate (BBO) crystals are used as nonlinear frequency-mixing material. Table 2.4 shows the phase-matching parameters of the applied crystal configurations. In the case of the SFG of the deep-UV pulses at 270 nm, the phase-matching parameters for collinear as well as for non-collinear beam geometry are given and the non-collinear scheme is used in our setup, due to its higher amplification bandwidth. In general, BBO is chosen for the parametric harmonic generation, due to its high nonlinear interaction constant d_{eff} and a broad amplification bandwidth, compared to other common nonlinear crystals. As example, the boride crystals CBO and LBO feature a roughly three times smaller d_{eff} as BBO in the case of SHG of the 820 nm pulse. Nevertheless, one drawback of BBO is material degeneration induced by high peak-power density, deep-UV radiation [113]. In fact in our setup, we observed a slow decrease of the generated pulse energy at 270 nm wavelength, when operating over hours. The original output pulse energy could be recovered, by slight displacement of the BBO crystal.

In the last decade, huge effort has been undertaken to improve the crystal

crystal	Interaction (wavelength in nm)	d_{eff} (pm/V)	crystal length	non-coll. angle	PM angle	PM bandwidth
BBO	810 (o) + 810 (o) = 405 (e)	2.00	0.2 mm	0°	28.9°	14.3 nm at 405 nm
BBO	810 (o) + 405 (o) = 270 (e)	1.88	0.2 mm	0°	43.5°	1.7 nm at 270 nm
BBO	810 (o) + 405 (o) = 270 (e)	1.98	0.2 mm	6.2°	51.7°	4.4 nm at 270 nm

Table 2.4: Phase-matching configurations of BBO crystals used for the generation of UV pulses at 410 nm and 270 nm wavelength. In case of the SFG stage two configurations in collinear and non-collinear beam geometry are shown, from which the non-collinear design is used in the presented system. Illustrated are the phase-matching (PM) parameters such as d_{eff}, phase-matching angle and the non-collinear (non-coll.) angle between signal and pump wave. The resultant phase-matching bandwidth is calculated for the shown crystal length, using equation 2.31 and Sellmeier equation [110].

quality and to discover new crystals for effective ultraviolet pulse generation down to sub-200 nm wavelength. A detailed overview about advances of boride crystals can be found in [114]. One other promising material is potassium fluoroboratoberyllate (KBBF), which has been used for high efficiency femtosecond, SHG down to 200 nm [115]. Unfortunately, this crystal is still not commonly available, very difficult to grow and requires a special, optical contact prism-coupling device for proper phase-matching (for review about KBBF see [116]). Another promising crystal for UV generation is the recently reported, periodically poled lanthanum boron germinate (PP-LBGO) [117], which could allow efficient, broadband generation of UV pulses, due to the absence of temporal walk-off between the interacting waves caused by quasi phase-matching in the periodically poled crystal structure.

In the cascaded harmonic generation setup employed here (see figure 2.27), the 5.3 µJ energy, near-IR pulses at a center wavelength of 810 nm are frequency-doubled in a collinear second harmonic generation (SHG) stage based on a 0.2 mm thick BBO crystal cut at 29.2°. Pulse energies of 1.9 µJ at 405 nm center wavelength are generated, yielding a high energy conversion efficiency of around 35%. For the temporal characterization of the UV pulses no SHG-FROG can be used, in contrast to the case of the mid-IR and near-IR outputs of the presented OPCPA system, due to the absence of a suitable nonlinear SHG crystal in the ultraviolet spectral. In-

stead, the UV pulses are characterized with a home-built self-diffraction (SD) FROG device (see details in appendix B), and the retrieved spectral and temporal pulse information are shown in figure 2.28. The spectral $1/e^2$ bandwidth spans around 9 nm at a center wavelength of 405 nm, while a temporal pulse duration of 47 fs is measured, which is slightly below the 51 fs pulse duration of the near-IR driving pulses.

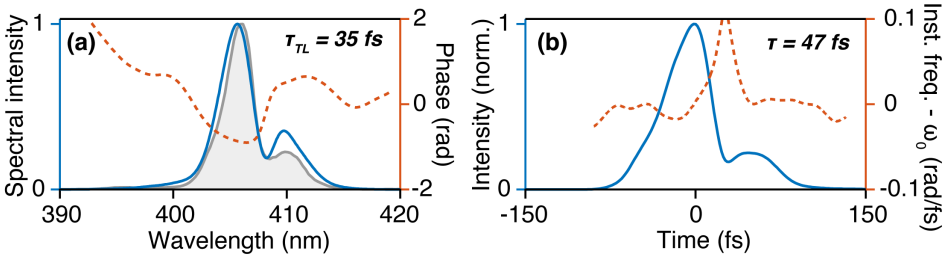

Figure 2.28: (a): Retrieved spectral intensity (blue) and spectral phase (orange, dotted) of the UV output obtained by a SD-FROG device in comparison with the measured spectrum (grey area). The $1/e^2$ bandwidth is around 9 nm and the spectrum supports a transform-limited pulse duration of 35 fs. (b): Retrieved temporal intensity (blue) and instantaneous frequency (orange, dotted) of the UV output, yielding a pulse duration of 47 fs.

Reaching further into the UV is achieved by non-collinear sum-frequency generation (SFG) under an internal, non-collinear angle of 6.2° between the pump and signal waves in a 0.2 mm thick BBO crystal. The non-collinear beam geometry is chosen in order to extend the acceptance bandwidth $\Delta\lambda$ of the SFG process (see $\Delta\lambda$ values for collinear and non-collinear geometry in table 2.4). The generated deep-UV light at 270 nm wavelength reaches a pulse energy of 0.5 µJ and a $1/e^2$ bandwidth of 2.6 nm, yielding a photon conversion efficiency with respect to the 405 nm beam of (0.5 µJ·ω_s)/(1.9 µJ·ω_p) = 18 %, according to the Manley-Rowe relations (equation 2.22). The spectral shape is measured with a monochromator (CS260 1/4 m from Oriel Instruments) in combination with a silicon-based detector and the normalized spectrum is illustrated in figure 2.29 (a). The temporal pulse duration is measured via a two-photon absorption autocorrelation device, which analyses the transmitted beam through the absorbing material (details in appendix B) [118]. In contrast to the measurement with the SD-FROG device, which was not possible due to insufficient peak intensities of the 270 nm pulses, the used autocorrelator does not give any phase information of the electric field and provides just limited information about the temporal pulse shape. In figure 2.29 (b) is shown the obtained two-photon

absorption trace of the 270 nm pulse (orange) together with a Gaussian fit (black, dotted). The fit function has a FWHM of 154 fs, yielding a temporal duration of 109 fs assuming a Gaussian-like temporal pulse profile. This pulse duration of 109 fs obtained by the two-photon autocorrelation measurement sets an upper limit for the real ultraviolet pulse duration, since in case of a strong depletion in the autocorrelation trace, a broadening of the autocorrelation trace is predicted leading to pulse duration overestimates of up to 20% [118].

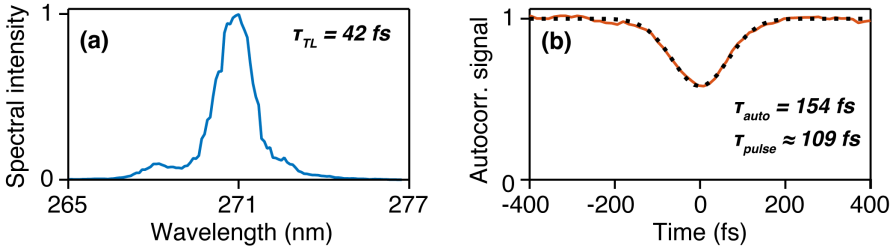

Figure 2.29: (a): Measured spectral power density of the 0.5 µJ energy pulses at 270 nm center wavelength with a $1/e^2$ spectral bandwidth of 2.6 nm. The spectrum supports a transform-limited pulse duration of around 42 fs. (b): Measured two-photon absorption autocorrelation trace of the deep-UV pulses (orange) overlapped with a Gaussian fit (black, dotted), revealing a pulse duration of 109 fs under the assumption of a Gaussian-like temporal pulse shape.

Note, that the generated 270 nm beam is slightly angularly dispersed, due to the non-collinear generation scheme. The general concept of this commonly known effect in broadband, non-collinear frequency mixing is illustrated in figure 2.30 (a). For the spectral and temporal characterization, the generation spot in the nonlinear crystal was re-imaged onto the measurement devices. In order to use the generated deep-UV pulses for experiments, the angular dispersion has to be compensated by another angular dispersive element such as the prism shown in figure 2.30 (c,d). Alternatively, the input pulses of a non-collinear SFG can be angular dispersed by prism or grating arrangements, allowing sum-frequency pulse generation with almost no angular dispersion (see figure 2.30 (b)) [119, 120]. By a careful design of the angular dispersion involved in broadband UV pulse generation and an elaborated dispersion management, the amplification bandwidth can be considerably increased, allowing the generation of down to sub-20 fs pulse durations. For example, Nabekawa *et al.* demonstrated the generation of pulses at 255 nm wavelength, supporting sub-20 fs durations by using SFG with non-collinear angularly dispersed geometry [119],

Baum *et al.* could generate 7 fs pulse at 325 nm by achromatic frequency doubling [121] and Varillas *et al.* generated 9 fs pulses at 340 nm by broadband sum-frequency generation [122]. In contrast, in our setup we chose a rather simple SFG design without angular dispersed input beams, due to less restrictive pulse duration requirements of the UV pulses at 270 nm wavelength.

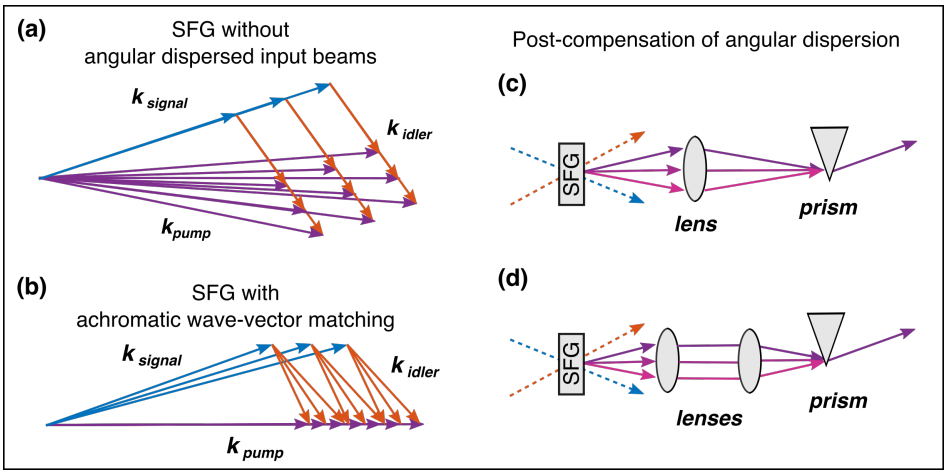

Figure 2.30: Wave-vector k phase-matching behaviour of broadband SFG (a,b) and schemes for post-compensation of angular dispersion (c,d). In the case when the driving signal and idler waves of a broadband SFG stage are not angularly dispersed, like in our setup, the generated pump wave exhibits angular dispersion (a). In achromatic sum-frequency generation, where tailored angularly chirped input beams are used, the angular dispersion of the generated sum-frequency can be substantially reduced (b) [119,120]. Angular dispersion of the generated pump wave can also be post-compensated by for example, prism-based schemes in combination with re-imaging systems (c,d).

The measured pulse duration of 109 fs is considerably longer than the driving pulses with around 50 fs as well as the transform-limited pulse duration of 42 fs. Aside from acceptance bandwidth limitations (see table 2.4), the achievable pulse duration is most likely limited by the residual group-velocity mismatch (GVM) between the interacting beams. Due to the non-collinear beam geometry, the GVM between the 810 nm and 405 nm pulses is reduced to zero, but both pulses obtain a GVM of 55 fs over the crystal length of 0.2 mm in respect to the 270 nm wavelength pulses. Another cause of the longer pulse duration of the deep-UV output, could be the relative strong dispersion of the UV radiation in transmission optics as well as in gases. For example, the propagation of the 270 nm pulses

through 1 m of air adds a second-order dispersion of 95 fs^2 to the pulse and the propagation through a 3 mm thick CaF_2 lens would add 370 fs^2 to the pulse (using Sellmeier equations [101, 123]). Nevertheless, the obtained deep-UV pulse duration are sufficiently short for first pump-probe measurements and yield with the pulse energies of 0.5 µJ a peak power of up to around 5 MW. In the future the deep-UV pulse duration could be considerably shortened by for example the above-discussed approach of SFG with achromatic wave-vector matching or by the use of a shorter nonlinear crystal, which would cause in the latter case a drop of the generated UV pulse energy).

2.3.5 Combined performance of multi-color upgrade

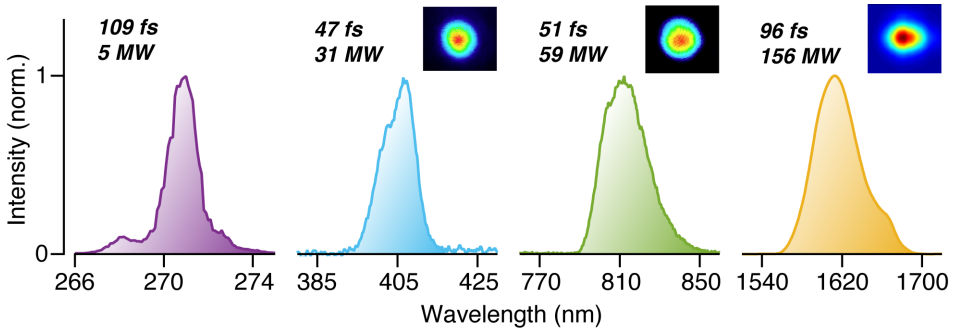

Figure 2.31: Combined output spectra of the multi-color OPCPA upgrade providing high peak-power pulses from the ultraviolet up to the near-IR range. For each output are also given the pulse durations and peak power values. In the insets are shown the respective measured beam profiles, obtained by a Si-CCD camera (for 400 nm and 800 nm) and by a scanning slit beam profiler (for 1600 nm). The beam profile of the output at 270 nm wavelength could not be measured due to the absence of a suitable camera. Figure is similarly published in [71].

In summary, the overall multi-color upgrade of the mid-IR OPCPA source provides high peak power outputs ranging from the ultraviolet up to the near-IR regime. Output pulses at 1620 nm, 810 nm, 405 nm and 270 nm center wavelength with pulse energies of 15 µJ, 3.1 µJ, 1.5 µJ and 0.5 µJ can be generated simultaneously. The respective pulse durations are measured to be 96 fs, 51 fs, 47 fs and 109 fs, yielding peak powers of 156 MW, 59 MW, 31 MW and 5 MW, respectively. All outputs are passively synchronized due to the derivation from the same mid-IR OPCPA system and the sub-110 fs pulse duration of all outputs allow pump-probe temporal resolu-

tions of sub-150 fs, which is sufficient to resolve a large range of ultrafast dynamics. Figure 2.31 shows an overview of the multiple output spectra together with the respective pulse durations and peak powers. In the insets are also shown the beam profiles of the collimated outputs, indicating Gaussian-like spatial distributions.

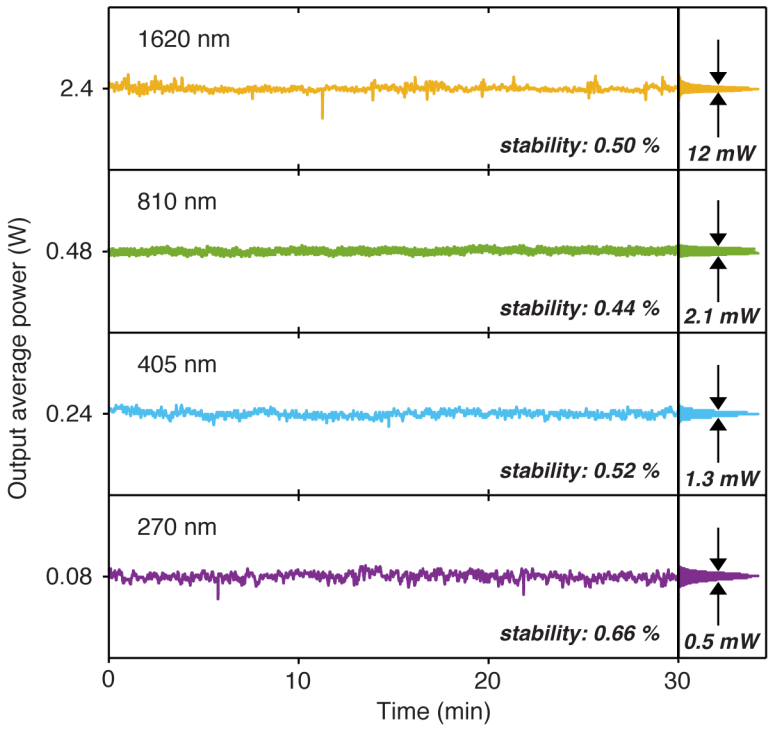

Figure 2.32: Combined power stabilities of the multiple outputs of the multi-color OPCPA upgrade measured over the course of 30 minutes. The outputs at 1620 nm, 810 nm, 405 nm and 270 nm center wavelength obtain power fluctuations below 0.7%. Figure is similarly published in [71].

The power stability of the multiple output beams is analyzed, using a pyroelectric detector. Figure 2.32 illustrates the measured power stabilities over the course of 30 minutes, showing rms power fluctuations of all multi-color outputs to be below 0.7% at 160 kHz pulse repetition rate. Note that a measurement time of 30 min with our system obtaining 160 kHz repetition rate, would be equivalent to 3.3 days measurement time with a typical amplified Ti:sapphire system operating at 1 kHz repetition rates.

2.4 Conclusion and outlook

2.4.1 Conclusion

In this chapter the concepts and design considerations of OPCPA systems were discussed. Afterward we presented the realization of a state-of-the-art, high power, mid-IR OPCPA system, providing passive CEP-stable, few-cycle pulses at 3100 nm center wavelengths at a pulse repetition rate of 160 kHz. In contrast to common, high power, BBO-based OPCPA systems, which emit pulses in the near-IR spectral range [6, 111, 124], our system generates true mid-IR radiation above 3 µm center wavelength. Furthermore, in comparison to typical high energy, mid-IR sources relying on cascaded down-conversion schemes driven by amplified Ti:Sapphire systems [64, 125], the presented mid-IR OPCPA runs at a much higher pulse repetition rates while providing similar pulse energies.

The OPCPA system is able to generate in combination with a frequency up-conversion chain simultaneously multiple high power, femtosecond outputs from the deep-UV up to the mid-IR spectral range. Five outputs at 270 nm, 405 nm, 810 nm, 1620 nm and 3100 nm wavelength provide respective pulse energies of 0.5 µJ, 1.5 µJ, 3.1 µJ, 15 µJ and 20 µJ at 160 kHz repetition rate. The source features high peak powers in the tens to hundreds of MW regime with pulse durations below 110 fs, due to a careful design balancing energy conversion efficiency and amplification bandwidth of the optical parametric stages. All outputs can be focused to peak intensities of 10^{12} to 10^{14} W/cm^2 enabling the investigation and driving of strong-field processes. The optical seeding of the frequency up-conversion chain enables the passive temporal synchronization between all output pulses.

The optical synchronisation of the output pulses combined with sub-110 fs durations and high peak powers make the presented system perfectly suited for time-resolved pump-probe experiments of highly nonlinear processes and strong-field physics in the UV, visible, near-IR and mid-IR spectral region. Compared to other femtosecond, multi-color sources supporting similar pulse energies and wavelengths [40, 126, 127], our OPCPA system shows a two order of magnitude higher repetition rate while permitting output peak intensities sufficient for driving strong-field physical processes. The high repetition rate in combination with the excellent power stability of 0.7% fluctuations over the course of 30 minutes, enables even the investigation of physical effect with very low-cross sections such as for instance the strong-field processes of laser induced electron diffraction (LIED) or double ionization.

The suitability of the presented OPCPA source for novel strong-field experiments was demonstrated multiple times, in particular by the investigation of the low-electron-energy features of strong-field ionisation in the tunnelling regime [19, 20, 128] or by imaging of the molecular structure of small molecules via the LIED [26] or FT-LIED [38] technique. An overview about strong-field experiments performed by the presented OPCPA system is given in attachment A.

2.4.2 Outlook

The development prospects of the multi-color OPCPA system are manyfold and can be divided in the further scaling of the mid-IR OPCPA system and in improvements of the frequency up-conversion chain.

Possibilities for the power-scaling of the mid-IR output are discussed in detail and experimentally realized in chapter 3, where a high power upgrade of the mid-IR OPCPA system is demonstrated, yielding five times higher output energies and mid-IR peak powers up to the GW-level while maintaining the repetition rate. On the other side, chapter 4 focuses on temporal post-compression of the mid-IR output pulses via filamentation propagation in the anomalous dispersion regime of bulk material, resulting in a two-fold temporal pulse shortening down to 3-optical-cycles.

The output pulse durations of the near-IR pulses at 1620 nm wavelength could be reduced close to the transform-limited pulse duration of 72 fs by using an optimized compression device such as a grism compressor, which can compensate the second and third order dispersion (see section 2.3.2). Much stronger pulse shortening of the near-IR outputs at 810 nm and 1620 nm wavelength could be obtained by post-compression via nonlinear propagation in gas-filled hollow-core photonic crystal fibers (HC-PCF). For example, Mak *et al.* demonstrated the compression of 10 µJ energy pulses at 800 nm wavelengths down to 3 optical cycles [129] and Balciunas *et al.* showed the compression of 35 µJ pulses at 1800 nm wavelength down to sub-2 optical cycles [130].

Another development prospect of the frequency up-conversion addresses the generation of wavelengths further in the UV spectral range. Applications like for example pump-probe experiments of photo-isomerization and photo-dissociation [37] processes would strongly benefit from high energy, femtosecond outputs down to sub-200 nm wavelength. The generation of this radiation via cascaded harmonic generation in nonlinear crystals is rather complicated and requires specially designed compensation

schemes for angular dispersion and propagation dispersion in the case of ultrashort, high energy, deep-UV pulses are required (see detailed discussion in section 2.3.4). An alternative, more elegant approach exploits a special case of nonlinear propagation in gas-filled HC-PCF, where the near-IR driving field generates a phase-matched dispersive wave in the deep-UV spectral range [131, 132]. Using this technique, Mak *et al.* [132] demonstrated the generation of up to 40 nJ energy at 200 nm center wavelength with a bandwidth of 6 nm, supporting transform-limited pulse durations of sub-10 fs. The process was driven by 1.7 µJ energy pulses at 805 nm center wavelength. Advantages of this method are the spectral tunability of the generated dispersive wave in the range from 176 to 550 nm by fine adjustment the gas pressure inside the HC-PCF fiber and achieved energy conversion efficiency of around 2% to 6% from the near-IR driving pulses to the UV dispersive waves [132].

Further improvements of the multi-color OPCPA system include modifications to obtain fully CEP controlled outputs, which would enable a variety of novel experimental possibilities, such as electric field waveform synthesis [40, 127] or optimal control over strong-field electron recollision dynamics [133]. In the current layout, the UV to near-IR output pulses are not CEP stabilized, since they are all derived from the OPA signal wave at 1620 nm wavelengths, which CEP value is linearly influenced by the CEP fluctuations of the pump beam according to the OPA phase relations (equation 2.15). In our system, the CEP of the signal wave could be passively stabilized, in case the mid-IR fiber front-end and the pump laser would be seeded by the same oscillator. This could be realized by seeding the oscillator of the pump laser with a fraction of the near-IR output of the fiber laser centered at 1075 nm wavelength. A similar concept to obtain fully CEP controlled outputs to all-optical seeding of an OPCPA system is already demonstrated in the literature [56, 57]. In an alternative, less invasive approach the frequency up-conversion chain could be seeded by the second harmonic of the already CEP-stable idler wave at 3100 nm wavelength instead of the signal wave. Since the frequency doubled mid-IR pulses would obtain a similar spectrum as the recently used signal wave, the same frequency up-conversion chain could be used by applying very similar phase-matching conditions.

Chapter 3

High conversion efficiency OPCPA upgrade

In chapter 2 we demonstrated a state-of-the-art, high power OPCPA system emitting multiple femtosecond outputs from the ultraviolet to the mid-IR spectral range. A further up-scaling of the few-cycle, mid-IR pulses towards GW peak-power levels would enable a multitude of novel experiments especially for strong-field physics such as high flux, soft X-ray generation or tunnel-ionization of molecules with very high ionization potentials. Nevertheless this improvement is hindered by the previous source design and restrictions related to the overall high average powers of the applied optical beams.

In this chapter, we present a mid-IR, GW-level peak-power OPCPA source, overcoming former limitations by a fundamental revision and complete reconstruction of the previous system, reported in chapter 2. The redesigned OPCPA system supports 118 µJ energy, 9-optical-cycle pulses at 160 kHz and holds up-to-date the record for the highest output average power of around 19 W compared to any existing few-cycle, mid-IR source. The five-fold increase of the mid-IR output pulse energy, compared to the former OPCPA configuration, is achieved by a combination of various improvements of the source design. For example on one hand, the precise tailoring of the seed-to-pump stretching factor and the additional reuse of the same pump beams for multiple amplification stages allow the increase of the overall optical conversion efficiency. On the other hand, an in-depth study of various nonlinear crystals for parametric, mid-IR amplification enables the choice of an amplification crystal with negligible average power limitations for the final booster amplifiers. The power-upgrade reported in this chapter was performed together with my colleague Hugo Pires and with the assistance of Ugaitz Elu. The presented comparison of nonlinear crystals for mid-IR parametric amplification is published in [54] and the demonstration of the GW-level, mid-IR OPCPA system is currently being

prepared for publication.

In section 3.1 the theoretical constrains for obtaining high conversion efficiencies during optical parametric amplification are elaborated. Afterwards, the average power induced limitations of mid-IR parametric amplification, which could hinder the upscaling of the system, are investigated in section 3.2 for various common nonlinear crystals. The experimental implementation and performance of the high power OPCPA system is demonstrated in section 3.3. Finally, the future possibilities for the further scaling of the system parameters are presented in section 3.4.

3.1 Theoretical considerations to improve the overall conversion efficiency

In this section we study the influence of the pulse characteristics of the interacting waves in an OPA process on the overall energy conversion efficiency. Specifically the significance of the spatio-temporal overlap and shapes of the seeded idler pulses and the pump pulses are investigated (see subsections 3.1.1, 3.1.2). Additionally the benefits and drawbacks of the multiple use of the same pump pulse in consecutive OPA stages is studied (subsection 3.1.3). All this considerations are afterwards taken into account for the redesign of the former mid-IR OPCPA setup to upscale the mid-IR output peak-powers towards GW-levels.

3.1.1 Influence of the stretching factor in OPCPA systems

In case of a phase-matched OPA process between spatially uniform, monochromatic waves, the maximal energy conversion efficiency is capped by the Manley Rowe relations (see equation 2.22). For example, in the case of a seeded idler wavelength at λ_i = 3100 nm and a pump wavelength of λ_p = 1064 nm, the resultant maximal pump-to-idler energy conversion efficiency is $\omega_i/\omega_p = \lambda_p/\lambda_i$ = 34%.

In contrast, in the case of spectrally broadband, interacting pulses, the non-uniform instantaneous electric field strengths of the interacting waves at each point in space and time influences the strength of which locally the parametric gain is driven and therefore the propagation length at which the complete pump depletion is achieved. As a consequence, the total energy conversion efficiency for a fixed crystal length is reduced and strongly dependent on the spatio-temporal profiles and overlap of the interacting

pulses. Additionally, in case of a phase-mismatch ($\Delta k \neq 0$) between spectral parts of the interacting waves the maximal conversion efficiency will be further decreased.

Let us first focus on the influence of the temporal pulse shape onto the amplified spectrum and energy conversion efficiency. In the special case of an OPA process in an OPCPA system, the pump is commonly a spectrally narrowband, transform-limited pulse with a Gaussian-like or sech^2 temporal profile. On the other side, the seeded, spectrally broadband idler pulse is typically linearly chirped in order to match roughly the pump duration. As a result the frequencies of the idler pulse are dispersed in time and a reduced gain at the front and tail of the idler pulse due to the lower instantaneous pump pulse intensity causes a temporal gain narrowing of the idler pulse duration, which will cause a spectral gain narrowing of the amplified idler spectrum. Figure 3.1 illustrates the effect of spectral gain narrowing in the case of perfect phase-matching and no pump depletion for a Gaussian-shaped idler and pump pulse. It can be seen, that the temporal duration and the related spectral bandwidth of the amplified idler pulse decreases significantly for already relative small gains of around 100. The spectral gain narrowing can be reduced by using a significantly longer pump pulse compared to the idler pulse, where the idler pulse just feels the slowly varying center part of the pump pulse shape. The drawback in this case is that a large fraction of the pump pulse is not contributing to the OPA process, therefore reducing the overall conversion efficiency.

In order to investigate this trade-off between spectral gain narrowing and conversion efficiency in detail, numerical split-step simulations of the coupled wave equation for the OPA process (equations 2.14 to 2.16) are performed using the Runge-Kutta method. The simulation assumes perfect phase-matching and is performed for collinear beam geometry along one dimension (propagation direction z), neglecting the influence of the spatial beam profiles and spatial effects such as spatial walk-off. In order to mimic the experimental conditions of the mid-IR OPCPA presented in section 2.2, the pump pulse shape is chosen to be Gaussian with a FWHM pulse duration of 10 ps and a center wavelength of 1064 nm. In the simulationn, the seeded idler features a Gaussian-shaped spectrum with a spectral FWHM bandwidth of 300 nm and a center wavelength of 3100 nm. The idler is temporally stretched by second order dispersion in order to obtain various FWHM pulse durations from 1 to 10 ps. For the simulation a nonlinear effective index d_{eff} of 14.8 pm/V matching that of MgO:PPLN is chosen. For each idler pulse duration the pulses are propagated until total pump depletion occures in the center of the pump beam. Energy back conversion

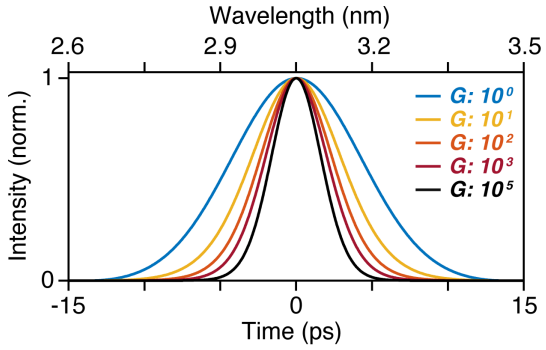

Figure 3.1: Calculated spectral and temporal gain narrowing effect of the idler pulse during an OPA process with no pump depletion. We assume an initial Gaussian-shaped idler and pump pulse with a FWHM pulse duration of 10 ps (blue line). The pulse shape evolution of the amplified idler is calculated for parametric gains $G \propto \exp(\sqrt{I_p})$ at the pulse peak of 10, 10^2, 10^3 and 10^5. Temporal gain narrowing of the idler pulse shape can be observed (bottom axis), which is directly related to spectral gain narrowing in case of a linearly chirped idler (top axis).

from the idler and signal to the pump pulses is avoided, since it leads to distortions of the beam profiles and reduces the beam quality [134].

In figure 3.2 is displayed the simulated evolution of the amplified spectral bandwidth (left) and the pump-to-idler conversion efficiency (right) for various idler-to-pump pulse duration ratios. In contrast to the simple model without pump depletion (figure 3.1), the amplified spectral bandwidth can be enhanced in respect to the initial seed spectrum, assuming a strong pump depletion at the pulse peak which causes a gain saturation and therefore a more equalized gain across the spectro-temporal idler pulse shape. As a result it can be seen, that the amplified bandwidth at short idler pulse durations is considerably larger than the seeded bandwidth of 300 nm (grey dotted line), while at longer pulse durations the amplified bandwidth strongly decreases due to spectral gain narrowing. Calculated are two cases of a high gain OPA stage (I_p/I_i=10^6) and a low gain OPA stage (I_p/I_i=10^2). As expected, it can be seen, that the amplified bandwidth drops faster at higher gain due to the spectral gain narrowing for an increasing idler pulse duration. On the other side, it can also be seen that the pump-to-idler conversion efficiency of a high gain OPA is reduced with respect to a low gain OPA. This dependency is natural, since the stronger temporal gain narrowing in a high gain stage yields a shorter idler pulse duration towards the end of the crystal. As a result the temporal overlap of

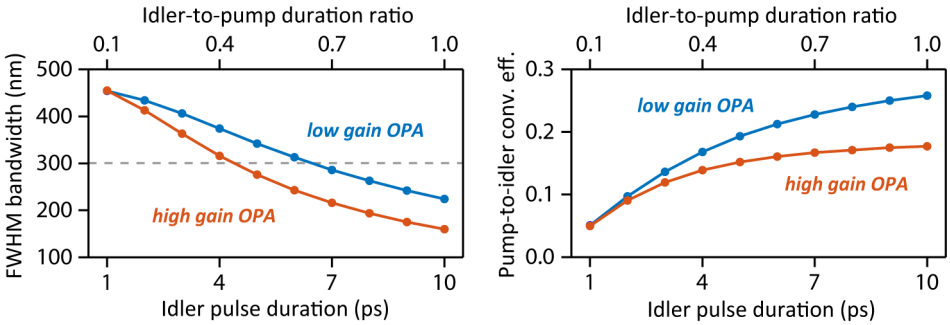

Figure 3.2: Dependency of amplified spectral bandwidth (left) and pump-to-idler energy conversion efficiency (right) as function of the temporal idler-to-pump pulse duration ratio (top axis). Shown are the cases of a high gain OPA stage (I_p/I_i=10^6) and a low gain, high energy OPA stage (I_p/I_i=10^2). At short idler pulse durations the amplified bandwidth is even bigger, than the initial 300 nm (grey dotted line) due to the gain saturation, while at longer pulse durations the spectral gain narrowing causes a strong reduction of amplified bandwidth. The pump-to-idler conversion efficiency grows for bigger idler-to-pump ratios.

idler and pump is worse, causing a reduced conversion efficiency.

From figure 3.2 it can be seen that in order to maintain the seeded spectral bandwidth, in the cases of a high gain OPA and a low gain OPA stage, a respective temporal idler-to-pump ratio of around 0.4 and 0.6 have to be chosen. Note, that for the used center wavelengths ($\lambda_p \approx \frac{1}{3}\lambda_i$) and according to the Manley-Rowe relations, the total pump-to-signal-plus-idler energy conversion efficiency is roughly 3 times higher, than the pump-to-idler conversion efficiency stated in figure 3.2. The achievable conversion efficiencies can also be reduced in a real OPA process due to additional effects such as temporal walk-off and phase-mismatch. In OPCPA systems, the temporal pulse walk-off, which originates from the different group velocities of the interacting pulses, can typically be neglected, since the group velocity mismatches in broadband phase-matched OPAs are typically orders of magnitude below the pulse durations in the ps regime.

One way to overcome the trade-off between spectral gain narrowing and conversion efficiency is the use of pump pulses with a temporal flat-top or super-Gaussian shape. In this case a temporally uniform gain for all spectral components of the idler pulse is ensured and hereby the pump-to-idler conversion efficiency improved. Theoretical studies about the effect of different pump pulse shapes in OPA processes can be found for example in [135, 136].

In the high power OPCPA system presented in this chapter we use two different idler pulse stretch factors in order to find a gain-dependent, optimum compromise between amplified spectral bandwidth and achievable pump-to-idler wave conversion efficiency. In the high gain pre-amplifiers the idler pulse duration is chosen relatively small compared to the pump pulse duration to reduce the effect of spectral gain narrowing. In contrast, in the final low-gain booster-amplifiers the idler pulse duration is elongated to enable high energy conversion efficiencies (see details in section 3.3.4).

3.1.2 Influence of different spatial beam profiles

A similar gain-narrowing effect in OPA processes as it is described in the previous subsection for non-uniform temporal pulse shapes, also occurs in the case of non-uniform spatial intensity distributions of the interacting beams. For example, in the common case of an OPA interaction between spatially Gaussian-shaped beams, the pump intensity and the related parametric gain is smaller on the outer edge of the pump beam compared to the beam center. As a result, the waist of the amplified idler beam profile will shrink for higher parametric gain values, due to the highly nonlinear coupling between the parametric gain and the pump intensity (see equation 2.13). This effect reduces the spatial overlap and the overall conversion efficiency.

Figure 3.4 illustrates the effect of spatial gain-narrowing of the amplified idler beam waist and the influence of the overall energy conversion efficiency in the case of a low-gain ($I_{pump}/I_{seed} = 10^2$) and a high gain ($I_{pump}/I_{seed} = 10^6$) OPA process. The simulation results are obtained by a split-step, Runge-Kutta simulation of the coupled wave equation, which are driven until full pump depletion in the center of the pump beam occurs. As initial parameter we use Gaussian-shaped pump and idler seed beam profiles with equal beam waists. The simulation assumes the interaction of temporally flat-top shaped pulses and neglects any effect of temporal walk-off, dispersion and phase-mismatch.

It can be seen, that in the simulated case of small gain amplification, the amplified idler beam profile is relatively similar to the seeded idler beam shape. In this case a total pump-to-signal-plus-idler conversion efficiency of around 45% can be achieved. In contrast, the simulated case of high gain amplification, the amplified idler beam waist is significantly reduced, leading to a smaller achievable energy conversion of only 22%. In conclusion, the combined effect of temporal and spatial gain-narrowing typically does not permit the combination of high gain and high conversion efficiency

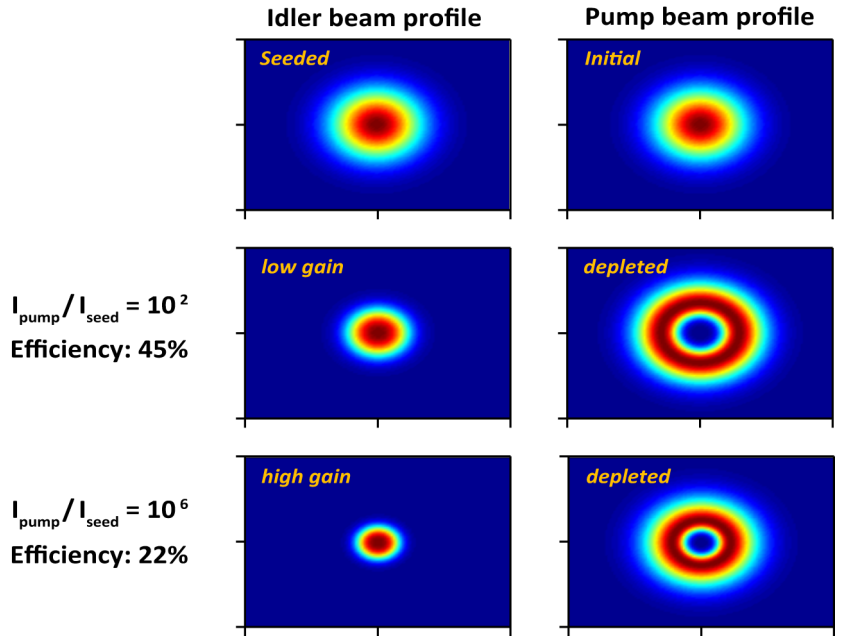

Figure 3.3: Influence of spatial gain narrowing on the beam profile of the amplified idler wave and the depleted pump wave. Also shown is the overall energy conversion efficiency, in case the OPA process is driven until full pump depletion in the center of the beam. The simulation is performed via a slit-step, Runge-Kutte simulation of the coupled wave equation. As initial parameter we use Gaussian-shaped pump and idler seed beam profiles with equal beam waists. The simulation assumes the interaction of temporally flat-top shaped pulses, neglecting any effects of temporal walk-off, dispersion and phase-mismatch.

in the same OPA stage. As a consequence, common OPCPA systems consist of multiple OPA stages with decreasing gains, but increasing pump energy extraction in each consecutive OPA stage. In the literature high energy, high efficiency OPCPA systems are reported, reaching total pump conversion efficiencies of 25% and up to 40% [4, 137–139].

One solution to overcome the trade-off between amplification gain and conversion efficiency is the use of pump pulses with a spatial flat-top or super-Gaussian shape, providing a spatially uniform gain over the full beam profile and hereby increasing the pump-to-idler conversion efficiency. Theoretical investigations about the effect of different spatial pump profiles on the OPA process can be found for example in [134, 135, 140, 141]. In the high power OPCPA system presented in this section, a pump laser with

Gaussian-shape spatial beam profile and sech^2-shaped temporal pulses is used. Beam reshaping devices such as for example diffractive optical elements [142], which would provide flat-top beam profiles are not used, in order to ovoid the additionally introduced setup complexity and transmission losses.

3.1.3 Reusing the pump beam

Another possibility to improve the overall energy extraction of a pump beam is a multi-pass OPA scheme. Hereby the residual pump energy is recycled after the OPA interaction and reused in a consecutive OPA pass. This concept can be repeated for multiple OPA passes. The absolute pulse energy which can be transferred in the respective OPA passes into the signal and idler wave reduces for each consecutive pass, due to the accumulated depletion of the pump pulse energy.

An obstacle, which limits the useful amount of pump-recycling passes is the increasing setup complexity. For each additional pass, the residual pump wave and at least one other wave have to be redirected and again temporally and spatially overlapped in the OPA crystal. Typically it is also beneficial to separate the beams after each pass and then recombine them in the next OPA pass, in order to allow the individual compensation of temporal and spatial walk-off effects and the fine adjustment of the beam sizes which are coupled to the amplification gain.

An example of the scaling behaviour of the amplified idler pulse energy in a multi-pass OPA stage is illustrated in figure 3.4 as a function of the number of amplification passes and the intermediate energy losses between two passes. The shown calculation is based on the assumption of a constant pump-to-idler energy conversion efficiency of 10% in each pass, a signal to idler photon energy ratio of $\frac{\hbar\omega_{sig}}{\hbar\omega_{idl}} = 2$ and an initial pump pulse energy of 100 µJ. Following the simulated case of neglectable inter-pass energy losses (purple line), it can be seen that the idler beam would be amplified in the first pass to 10 µJ, in the second pass to 17 µJ (70% increase), in the third pass to 22 µJ (29% increase) and in the fourth pass to 25 µJ (14% increase). It can be seen, that apart from the reducing absolute idler energy gain in each pass, the relative amplification gain drops significantly with each additional pump-recycling pass. This effect is even enhanced in case reflection losses on the applied optical elements in the OPA setup are considered. As a consequence, the optimum number of pump-recycling passes lies between two and three passes in the case of relative small

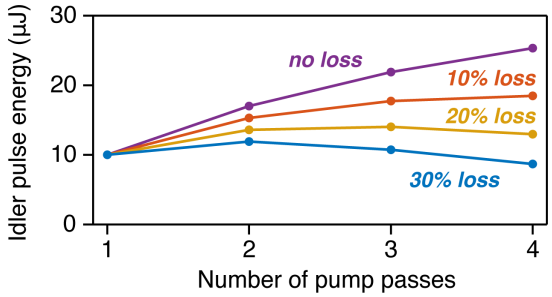

Figure 3.4: Idler pulse energy evolution in a multi-pass OPA stage as function of the number of amplification passes and the intermediate energy losses between two passes. The calculation assumes a total pump pulse energy of 100 µJ and a constant pump-to-idler energy conversion efficiency of 10% in each pass. The benefit of a multi-pass OPA compared to a single-pass OPA is highly dependent on the intermediate energy losses. The optimum number of passes lies between two and three passes assuming relatively small intermediate losses of 10% to 20%.

intermediate losses of 10% to 20%. Nevertheless, a drawback compared to the single pass OPA is the increased optical setup complexity.

For the design of the high power OPCPA setup presented in this chapter, a double-pass OPA scheme is chosen for the last two, high energy, low-gain booster amplifiers in order to achieve a compromise between setup complexity and higher total energy conversion efficiency.

3.2 Nonlinear crystals suited for high power, mid-IR amplification

In this section we will investigate the suitability of multiple nonlinear crystals for high average power, broadband parametric amplification in the mid-IR spectral range. Contrary to traditional laser amplifiers relying on pump power storage, parametric amplifiers are often claimed to be free of thermal loading due to the quasi-instantaneous nature of the nonlinear interaction. It has nonetheless recently been shown in a near-IR BBO-based OPA [53] that residual absorption of the interacting waves can lead to a considerable thermal load in the nonlinear amplification crystal when operated at high average power. In a further study the thermal properties and average power induced amplification limitations of the nonlinear crystals BBO, LBO and BiBO was investigated [143]. It was found, that such thermal

loading sets an upper-bound to the power scalability of OPAs and OPCPA systems as it can lead to undesired effects, such as a reduced efficiency of the parametric amplification due to spatial dependent modifications of the phase-matching conditions and a distortion of the amplified spatial beam profile.

In case of the high power, mid-IR OPCPA system presented in chapter 2, we encountered average power related parametric amplification limitations in the final MgO:PPLN-based amplifiers. In order to design a GW-level, mid-IR OPCPA system, the former mid-IR output energies would have to be multiplied considerably. Therefore an in-depth understanding of the thermal induced parametric amplification limitations for the most promising mid-IR amplification crystals is required. Previously to the performed study shown in this section and published in 2014 [54], no other detailed investigation on average power induced, mid-IR amplification limitations of nonlinear crystals was reported. Only very recently in 2016 and 2017, two other studies about high repetition rate, laser induced damage thresholds of MgO:LN during parametric amplification were published [52, 144], proving the growing interest in using these crystals for high power, mid-IR amplification.

3.2.1 Common nonlinear crystals for mid-IR OPA processes

The choice of the nonlinear crystals satisfying the aim for ultra-broadband parametric amplification is limited to the few oxide crystals exhibiting good transparency in the mid-IR spectral region. The most common nonlinear crystals used for mid-IR amplification are given in table 3.1. For every crystal the material properties of transparency range, and damage threshold is shown. Additionally the optimum phase-matching conditions resulting in the highest effective nonlinear coefficient (d_{eff}) and broadest phase-matching bandwidth is calculated. The choice of the material is dictated by the aim of obtaining the highest output energy simultaneously with the widest amplified spectral bandwidth.

On one hand, potassium niobate ($KNbO_3$) is chosen as it exhibits the highest d_{eff} for bulk materials, a high damage threshold and a wide phase-matchable bandwidth exceeding the spectral extent of the seed pulse. As a drawback it requires resorting to non-collinear interaction, potentially resulting in spatial profile distortions. Further potassium titanyl arsenate (KTA) is chosen as it enables simple collinear amplification. While potassium titanyl phosphate (KTP) offers a higher d_{eff} and wider phase-matchable bandwidth than KTA, the absorption coefficient of KTA in the 3.0-3.5 µm spectral range is at least an order of magnitude smaller than that of KTP [147].

	Transparency range (µm)	PM Angle/QPM period, PM Type	Noncollinear Angle	d_{eff} (pm/V)	PM Bandwidth (nm) at 3.15 µm	Damage Threshold I_{Th} at 1064 nm (GW/cm^2)
Bulk materials						
MgO-doped Lithium Niobate (MgO:LN)	0.33 - 5.5	48.0°, type I	5.7°	-4.0	456 nm	10 (6 ps) / 8 (9 ps)
Lithium Iodate (LIO)	0.3 - 6.0	20.3°, type I	3.2°	1.3	790 nm	19 (45 ps) / 42 (9 ps)
Potassium Niobate ($KNbO_3$)	0.4 - 4.5	40.3°, type I	5.0°	6.0	486 nm	100 (100 ps) / 333 (9 ps)
Potassium Titanyl Arsenate (KTA)	0.35 - 4.0	42.1°, type II	0°	-2.1	222 nm	1.2 (8 ns) / 35 (9 ps)
Potassium Titanyl Phosphate (KTP)	0.35 - 4.5	46.1°, type II	0°	-2.3	266 nm	15 (1 ns) / (158 (9 ps))
Periodically poled materials						
Lithium Tantalate (PPLT)	0.28 - 5.5	31.0 µm	0°	10.4	195 nm	80 (30 ps) / 146 (9 ps)
MgO-doped Lithium Niobate (MgO:PPLN)	0.33 - 5.5	31.0 µm	0°	14.8	233 nm	10 (6 ps) / 8 (9 ps)

Table 3.1: Comparison of nonlinear crystals suitable for parametric amplification of mid-IR radiation. Transparency ranges, optimum phase-matching angles, noncollinear angles and the effective second-order nonlinear coefficients d_{eff} are obtained from SNLO [14]. The parametric phase-matching (PM) bandwidths were computed for a crystal length L = 2 mm at a center wavelength λ = 3.15 µm (calculated according to equation 11 in [82]). The damage threshold I_{Th} for PPLT is taken from [145] and for all other crystals from [146]. Additional to the referenced damage thresholds for varying pulse durations τ_P, it is also given the respective damage thresholds assuming a pump pulse duration of 9 ps by applying the damage threshold scaling law $I_{Th} \propto (\tau_P)^{-0.5}$ (section 12.3 in [73]). Table is published in [54].

Periodically poled materials offer the highest d_{eff} and therefore the best prospects for amplification to high energy. Nonetheless, the very nature of the periodic poling reduces the amplifiable bandwidth and might result in parasitic phase-matching. For this study we chose MgO:PPLN over lithium tantalate (PPLT) since it exhibits both a wider phase-matchable bandwidth and a larger d_{eff}.

Based on these considerations, three crystals with comparable length are selected for an in-depth experimental study:

- 1.8 mm long $KNbO_3$ crystal cut at 40.5° (produced by FEE GmbH)
- large aperture (5x5 mm^2) 2.18 mm long MgO:PPLN crystal with a quasi-phase-matching QPM period of 31.0 µm (fabricated by Ishizuki *et al.* [105])
- 2.0 mm long KTA crystal cut at 41.7° (produced by Altechna Co. Ltd.)

3.2.2 Comparison of amplification performances

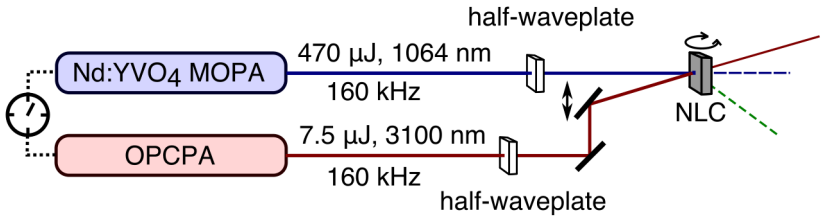

Figure 3.5: Schematic of the experimental test-bed used for investigating the potential of $KNbO_3$, MgO:PPLN and KTA as optical parametric amplification gain media at high average power. The setup allows the fine adjustment of the non-collinear angle as well as the rotation of the linear polarization direction of the pump wave and the seeded idler wave. NLC: nonlinear crystal. Figure is published in [54].

The mid-IR parametric amplification performances of the three chosen nonlinear crystals $KNbO_3$, MgO:PPLN and KTA is investigated using the test bed setup illustrated in figure 3.5. The mid-IR seed pulse is provided by the output of the third OPA stage of the OPCPA system described in section 2.2, supporting 7.5 µJ energy at a center wavelength of 3150 nm and a temporal duration of 3.5 ps at 160 kHz repetition rate. The pump beam featuring 475 µJ pulse energy at 160 kHz with a temporal duration of 9.5 ps is derived from the same Nd:YVO_4-based MOPA system, which pumps the OPCPA system (see details in section 2.2.3). The mid-IR seed pulses and

the pump pulses are temporally synchronized via locking of the repetition rates with a commercial synchronization unit (Toptica Photonics AG) and there relative temporal delay can be changed arbitrarily via an optical delay line. The test bed setup permits changing the spatio-temporal overlap of the pump and seed for collinear, non-collinear, type I or type II interactions. All crystals are mounted without active cooling. In the case of collinear interaction custom dielectric filters are placed in the output beam to separate pump, idler and signal beams, ensuring unambiguous measurement of the amplified energy. The amplified mid-IR idler spectra are measured using a FTIR spectrometer equipped with a calibrated liquid nitrogen cooled HgCdTe (MCT) detector.

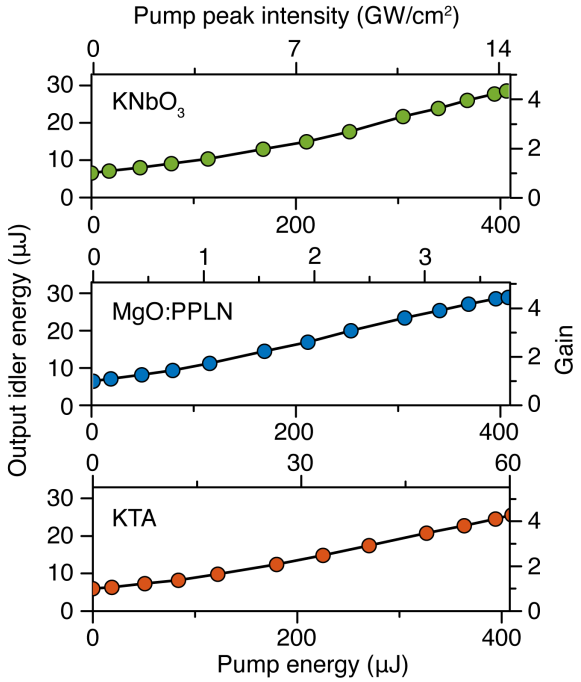

Figure 3.6: Comparison of mid-IR parametric amplification behaviour for various nonlinear crystals. Shown is the mid-IR output pulse energy versus the pump pulse energy (bottom abscissa axis) and the pump peak intensity (top abscissa axis). The pump and idler waist sizes are matched and set to ω = 436 µm for $KNbO_3$, ω = 852 µm for MgO:PPLN, and ω = 214 µm for KTA. The data are corrected to account for Fresnel reflections. Figure is published in [54].

First the potential of each crystal as a high power amplifier medium is investigated. Figure 3.6 shows the idler output power and amplification gain

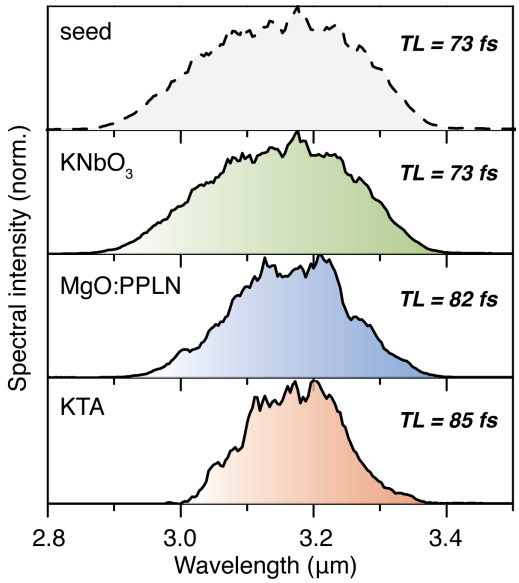

Figure 3.7: Comparison of mid-IR parametric amplification bandwidth for various nonlinear crystals. From top to bottom: measured input seed spectrum and amplified spectrum for $KNbO_3$, MgO:PPLN and KTA at the maximum pump intensity (see intensity values in figure 3.6). Figure is published in [54].

evolution dependent on the applied pump pulse energy. For each crystal the phase-matching condition which support the broadest amplification bandwidth is chosen (see third column in table 3.1). For the power scaling, the pump and seed beam waists ($1/e^2$ radius) are set to 436 µm, 852 µm, and 214 µm for $KNbO_3$, MgO:PPLN and KTA respectively, resulting in maximum pump peak intensities of 14.4 GW/cm^2, 3.8 GW/cm^2 and 64 GW/cm^2. For $KNbO_3$ and MgO:PPLN no smaller beam waists could be chosen while applying the full pump energy, due to the onset of parametric amplification limiting effects, which are described in detail in section 3.2.3. In the case of amplification in KTA no smaller focus size is used, since the resulting pump peak intensity of 62 GW/cm^2 is close to the reported damage threshold (see table 3.1). At the maximum available pump energy of 410 µm onto the sample crystals, an amplification up to 28.6 µJ is achieved in $KNbO_3$, 28.9 µJ in MgO:PPLN and 26.8 µJ in KTA. All crystals provide a similar gain of $\sim$4.4 and a total conversion efficiency of the pump wave to the signal plus idler waves of 16.3% for $KNbO_3$, 16.5% for PPLN and 14.4% for KTA. The linear shape of the power scaling curve (see figure 3.6) indicates that the amplifier was not operated in the pump depletion regime and that higher

energy extraction could be achieved. Considering the pump peak intensity limitations, a high amplification gain would require longer nonlinear crystals at the expense of bandwidth, which was not wanted in the context of this experimental study.

Afterwards, the spectral behaviour of each crystal is investigated. The amplified spectrum for each crystal is recorded at the highest possible output energy level and is reported in figure 3.7. As expected from preliminary calculations (see table 3.1), $KNbO_3$ features an output spectrum similar to the input spectrum. The $1/e^2$ bandwidth of 370 nm supports a transform-limited duration of 73 fs, potentially yielding amplified 7-cycle duration optical pulses. The $1/e^2$ spectral width amplified in MgO:PPLN is 350 nm and yields a transform-limited duration of 82.3 fs, representing a 13.8% increase in duration compared to the seed pulse. The amplified spectrum in KTA is relatively narrow compared to the input spectrum. It exhibits a $1/e^2$ bandwidth of 320 nm corresponding to a transform-limited pulse duration of 85 fs, representing a 16.5% increase compared to the seed spectrum.

3.2.3 Average power dependent amplification limitations

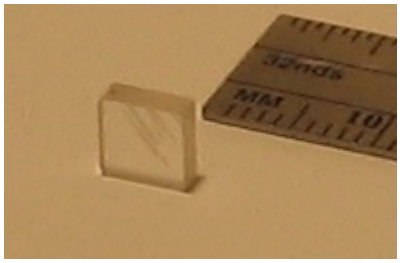

Figure 3.8: Photograph of crystal domain inversions which are visible as diagonal straight lines in a $KNbO_3$ crystal. The permanent domain inversions appear after exposure to excessive thermal stress due to transmission of a tight focused, high average power pump beam at 1064 nm wavelengths.

$KNbO_3$. In the case of $KNbO_3$, intensities of 14.4 GW/cm^2 can not be exceeded, a value well below the reported damage threshold of 100 GW/cm^2 for 100 ps pump pulse durations (see table 3.1). Even the empirical square root scaling rule predicts a factor of two higher damage threshold than observed. For intensities beyond 14.4 GW/cm^2 we observe the formation of lines within the crystal visible to the naked-eye that can partially be removed by sintering the crystal after usage (see figure 3.8). Formation of such lines has previously been reported [148, 149] as differently

oriented domains in the ferroelectric material $KNbO_3$. At room temperature the crystal is in an orthorhombic structure and a formation of a domain pattern, especially at defects in the crystal structure, can occur close to the phase transition temperature ($\sim$220°C) [148] or at lower temperatures via steep temperature gradients or pressure gradients [149]. In our experiment such a temperature gradient was possibly generated by localized heating induced by the residual absorption of the 70 W pump and of the amplified seed, ultimately limiting the achievable peak intensity and amplification. During the experiment care was taken to change the applied pump power very slowly, at a variation rate below 1 Watt per second, in order to avoid a thermal shock or steep temperature gradients.

KTA. In KTA, no limitations are observed and pump beam can be focused to intensities as high as 63.5 GW/cm^2 without inducing any damages. The peak intensity is not further increased since the reported damage threshold is already exceeded and normal anti-reflection coatings would probably not withstand such high peak intensities.

MgO:PPLN. In the case of MgO:PPLN dramatic beam distortions are observed for intensities exceeding 3.8 GW/cm^2 (see figure 3.9), a value less than half the damage threshold (see table 3.1). The beam profile of the pump is measured with a CCD camera placed 75 cm after the crystal. While increasing the pump pulse energy, first a slight decrease of the transmitted beam radius is observed, then concentric ring structures appear, finally an increasing amount of pulse energy is transferred to the ring patterns. These distortions are generated by the pump beam but also affect the spatial profile of the amplified mid-IR idler beam and the second harmonic of the pump beam which is parasitically generated due to high order QPM. No damage is observed in the crystal and after reducing the pump peak intensity below 3.8 GW/cm^2, the original beam profile is restored.

We further investigate the origin of this beam reshaping using only the pump laser. We study average power, peak power and periodic poling as possible causes. First, the applied average power is reduced by a factor of 4 while the beam is focused to a five times smaller size. This allows the peak intensity to be successfully increased to 26.7 GW/cm^2 without any visible beam distortion suggesting an average power related process. We then set the beam parameters back to obtain the concentric ring pattern and investigated spectrally for any nonlinear process. The spectral content of the rings is measured over the 0.2-2.5 µm spectral range and we observe no evidence of spectral broadening, Stokes or anti-Stokes lines, Raman or Brillouin shifted signals. The influence of poling is investigated

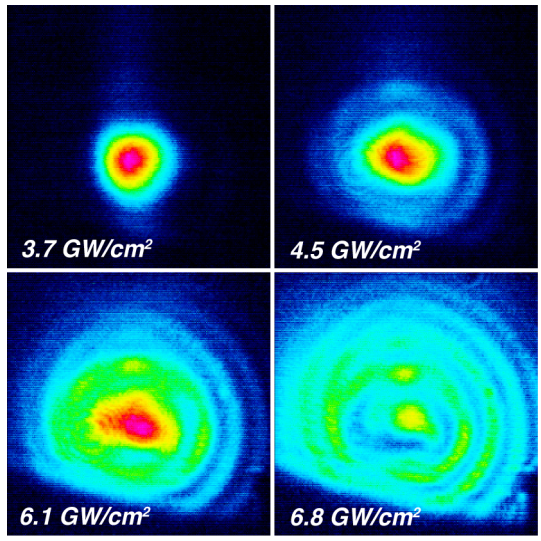

Figure 3.9: Spatial reshaping behaviour of a high average power pump beam transmitted through a MgO:PPLN crystal. Shown are the measured spatial profiles for pump peak intensities of 3.7 GW/cm^2 (top left), 4.5 GW/cm^2 (top right), 6.1 GW/cm^2 (bottom left) and 6.8 GW/cm^2 (bottom right) measured 75 cm after the crystal. The clipping observed for the highest intensities is due to size limitations on the optics directing the beam to the CCD camera. Figure is published in [54].

by replacing the MgO:PPLN by a 2 mm thick equally doped (5%) MgO:LN crystal with a cut angle θ = 47°. For the beam parameters yielding rings in MgO:PPLN, no distortions were observed in MgO:LN indicating that the beam reshaping process is related to the periodic poling or to the stronger second harmonic generated in the poled crystal.

Since average power and poling appeared to cause the observed beam deformations, we tracked reported physical phenomena that could lead to our observations. Thermal lensing induced by linear residual absorption and enhanced by GReen Induced InfraRed Absorption (GRIIRA) [150] driven by the parasitic SHG of the pump is a candidate. Since SHG is much stronger in our test crystal of MgO:PPLN than in MgO:LN probably due to parasitic higher order quasi-phase-matching, we verify whether strong GRIIRA takes place by performing a temperature measurement on both crystals. In case of a strong GRIIRA effect in the MgO:PPLN crystal an additional temperature increase should be measurable, due to an additional absorption of the near-IR pump beam. Applying the full pump power for various focusing conditions for both MgO:PPLN and MgO:LN crystals re-

vealed a constant temperature increase of 5.5 $\pm$ 0.3 K indicating no major contribution of GRIIRA in the periodically poled crystal. Nevertheless the GRIIRA effect could be still present and could cause an increased radially temperature gradient inside the crystal, without a significant overall temperature rise. The focusing length f of the thermal lens purely caused by linear absorption can be estimated by (equation 11 in [151]):

$$\frac{1}{f} = \frac{1}{2 \cdot \kappa} \cdot \frac{\mathrm{d}n}{\mathrm{d}T} \cdot \frac{P_{heat}}{A} = \frac{1}{2 \cdot \kappa} \cdot \frac{\mathrm{d}n}{\mathrm{d}T} \cdot \frac{P_{pump} \cdot (1 - e^{-\alpha \cdot L})}{A}, \tag{3.1}$$

where dn/dT is the temperature induced refractive index change, κ is the thermal conductivity, A is the focus area, P_{heat} is the dissipated average power inside the crystal considering the absorption coefficient α and the crystal lengths L. Setting κ = 3.5 W/(m·K), dn/dT = 3.85·10^{-5} 1/K, and α = 0.003 cm^{-1} (all from [146]), the focal length can be estimated at full pump power of 69 W and a beam waist of ω=852 µm to around 100 m, which is too long to cause a significant contribution to the beam distortion.
Another possible cause for the observed beam distortions is the photorefractive effect, which has been widely studied in lithium niobate (LN) [152]. A coupling between this effect and the observed pyroelectric properties of LN can induce a radial thermally induced refractive index change [153]. But the photorefractive effect and pyroelectric effects typically mitigate, when the lithium niobate crystal is doped by magnesium oxide (MgO) [154, 155], like in our case, where a 5% doping concentration of MgO in PPLN is used.

In resume, we could not clearly identify the cause of the observed beam profile degradation in MgO:PPLN crystals, when high average power, near-IR beams are applied. Possible candidates are the photorefractive and/or pyroelectric effect, maybe in combination with the GRIIRA effect. Future work is needed to fully disentangle the origin of the transmitted beam distortions in MgO:PPLN.

3.2.4 Conclusion of nonlinear crystal comparison

From the three investigated nonlinear crystals for mid-IR parametric amplification, MgO:PPLN exhibits the highest nonlinearity of d_{eff} = 14.8 pm/V and therefore offers the highest amplification gain for similar focusing conditions and crystal lengths. Nevertheless, the use of this crystal for OPA processes is challenging when very high average power beams are used. In this case a non-permanent beam reshaping effect occurs, limiting the further power scaling of OPA and OPCPA system, which are purely based on MgO:PPLN crystals.

$KNbO_3$ is a good candidate to substitute MgO:PPLN in high power OPA stages, since it has the highest nonlinearity of all non-poled, oxide, mid-IR nonlinear crystals (d_{eff} = 6.0 pm/V). Additionally, $KNbO_3$ provides a larger acceptance bandwidth than MgO:PPLN when used in non-collinear beam geometry. But the $KNbO_3$ crystal is very sensitive to internal, absorption-induced temperature gradients which can lead to permanent crystal structure distortions. In our study these distortions appear, when a 70 W average power pump beam is focused to peak intensities above 14.4 GW/cm^2. This peak intensity threshold could probably be increased, in case the crystal would be mounted in a thermally well contacted, temperature stabilizing crystal mount.

The third investigated crystal, KTA is a promising alternative to MgO:PPLN, since if seems to have no average power related amplification limitation allowing focused peak intensities of up to 64 GW/cm^2 of pump beams with around 70 W average power. The drawback of KTA is its small nonlinearity of d_{eff} = -2.1 pm/V, which is 7 times smaller than in MgO:PPLN and 2 times smaller than in $KNbO_3$. Therefore an OPA stage based on KTA, would have to use a rather long crystal lengths, further decreasing the acceptance bandwidth or very small focused beam sizes, potentially diminishing the spatial overlap of pump and seed beams especially in the case of a non-collinear beam geometry.

In conclusion, the nonlinear crystal MgO:PPLN seems a good candidate for the low energy, high gain amplification stages of a high power, mid-IR OPCPA system, since the average power levels of the involved beams are rather low. In contrast, in the final power-booster amplifiers, where the highest pump average power is applied and the maximum output idler and signal power are achieved, the use of the nonlinear crystal $KNbO_3$ is preferred.

3.3 Experimental implementation

3.3.1 General system design

The design and construction of the GW-level peak power, mid-IR OPCPA system presented in this chapter is governed by the theoretical considerations discussed in section 3.1 on how to increase the overall energy pump-to-idler conversion efficiency of an OPA process. At the same time, the fundamental building blocks which seed and pump the OPCPA system are preserved from the former multi-color OPCPA design (see chapter 2) due to their excellent performances and reliability.

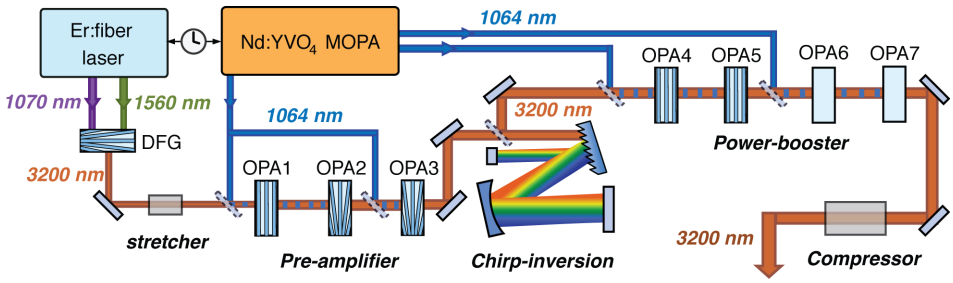

Figure 3.10: Design layout of mid-IR, GW-level peak power OPCPA system.

A schematic overview of the resultant, new OPCPA layout is shown in figure 3.10. The main design considerations leading to this novel scheme are specified and explained below:

- **Chirp-reversal for high power OPAs.** In the new OPCPA design, the chirp sign of the stretched idler pulses is inverted in the booster-amplifiers compared to the pre-amplifier. At the input of the pre-amplifier, the seeded idler pulses are temporally stretched by propagation through a bulk stretcher, adding negative GDD. After the pre-amplifier a Martinez-type grating compressor adds a substantial amount of positive GDD, which over compensates the negative GDD from the input beam. As a result the stretched idler pulses seeded into the booster-amplifiers exhibit positive GDD. After the booster-amplifiers, the idler pulses are compressed down to few-optical cycles by propagation through another bulk compressor which adds negative GDD. A detailed calculation of the overall dispersion management of the entire OPCPA system can be found in table 3.2.
  The new stretcher-compressor arrangement has multiple advantages

compared to the previous multi-color OPCPA design (compare to chapter 2), where just one bulk stretcher and one grating compressor were used. On one side the use of an AR-coated bulk compressor at the end of the system allows a nearly lossless final compression. In contrast, the transmission efficiencies of grating-based compressors are typically in the range of 50% to 70%. For example, the Martinez-type grating-compressor for mid-IR radiation, which is used as chirp-inverter in the OPCPA system (see figure 3.10) just reaches a transmission efficiency of around 50%. On the other side it is also convenient to use a bulk stretcher at the beginning of the OPCPA since the beam alignment is much simpler as it would be in a Martinez-type grating stretcher, especially in the case of very low seed pulse energies as in our case with around 6 pJ seed energy. As result, to be able to use a dielectric bulk stretcher at the beginning as well as a dielectric bulk compressor at the end of the OPCPA system, a chirp-inversion device has to be placed inside the OPA chain. A Martinez-type grating-compressor is perfectly suited as chirp-inverter in our case, since it allows the compensation of second and third order dispersion if combined with sapphire-based bulk stretchers and compressors (see section 2.1.5).

- **Individual idler pulse durations in pre- and booster-amplifier.** Sub-structuring the OPCPA into two parts with different temporal stretch-factors of the idler wave, allows the fine adjustment of the idler pulse durations according to specific requirements of the individual amplifier stages. In the pre-amplifier a relative small idler-to-pump duration ratio is chosen to reduce the effect of spectral narrowing due to high gain amplification. Less spectral narrowing can be obtained since the short, amplified idler pulses feel an effective temporal flat-top profile of the pump beam, instead of the original sech^2-shape. In contrast, in the booster-amplifiers longer idler pulse durations are required in order to achieve high energy conversion efficiencies during the OPA process. How the temporal idler-to-pump duration influenced the pump-to-idler conversion efficiency is studied theoretically in section 3.1.1. Further, section 3.3.4 describes, how the optimum idler-to-pump ratio for the booster-amplifiers is obtained experimentally.

- **Reuse pump beams.** The maximum achievable pump-to-idler energy conversion efficiency of an OPA stage is limited to a certain value dependent on multiple beam conditions (see section 3.1). To overcome this fundamental limitation, the same pump beam can be

recycled after an OPA process and reused in further consecutive OPA stages. This cascaded, multiple use of the same pump beam is theoretically studied in section 3.1.3 and can permit very high net pump-to-idler energy conversion efficiencies. In our redesigned OPCPA scheme, the pump beams in both booster-amplifiers are reused in two consecutive OPA stages. The OPA5 stage is pumped by the recycled pump beam of the OPA4 stage and the OPA7 stage is driven by the recycled pump beam of the OPA6 stage. Additionally, a recycling of a pump beam is also performed in the pre-amplifier, where the stages OPA1 and OPA2 are consecutively driven by the same pump beam. In this case, due to the multiple use of the same pump beam already the OPA2 stage can reach the saturated amplification regime (more details in section 3.3.2), which allows a better overall energy stability of the system.

- **Specific use of MgO:PPLN and $KNbO_3$ crystals.** Optical parametric amplification is typically considered independent of the average power of the involved beams due to the quasi-instantaneous nature of the process. Nevertheless small, residual absorption can lead to thermal load in the nonlinear amplification crystals resulting in amplification limiting or material damaging effects. A detailed study of thermal induced effects limiting the amplification in the most common mid-IR nonlinear oxide crystals is performed in section 3.2. As a consequence, in the last two amplifier stages (OPA6 and OPA7), where the highest average power levels of the pump, idler and signal beams are reached, the nonlinear crystal $KNbO_3$ is used. Its advantage is a better acceptance towards high average power beams compared to the previously used MgO:PPLN crystal. In the pre-amplifier and in the first booster-amplifier (OPA4 and OPA5 stages) MgO:PPLN crystals are still used due to their high nonlinear effective coefficient d_{eff} and a relatively broad acceptance bandwidth.

- **Reduce Fresnel losses.** The reduction of losses due to Fresnel reflections by the use of anti-reflection (AR) coatings is generally desirable in optical amplification systems to increase the overall output energy. In our case the application of a high quality AR-coating is especially required onto the final bulk compressor. If instead an uncoated sapphire rod would be used as compressor, the output idler energy would drop by a total of 14% caused by Fresnel reflections on both surfaces.
  Another critical point, where reflection losses have to be minimized, is in the last booster-amplifiers. In section 3.1.3 (figure 3.4) is shown

for example the influence of high propagation losses onto the total output energy of multi-pass, high energy amplifier stages. In the former multi-color OPCPA design (see chapter 2) multiple dichroic optics were used to overlap and separate the different interacting beams in the collinear OPA stages. Unfortunately, every of these optics showed around 5% of transmission losses of the idler. In the new OPCPA design, these transmission losses are removed in the booster-amplifiers by using the OPA4 to OPA7 stages in non-collinear beam geometry where no dichroic beam combiners are required.

3.3.2 Detailed OPCPA setup description

Fiber based, DFG-front end. The mid-IR seed generation is performed in the same way as in the multi-color OPCPA approach, discussed in chapter 2. The two output beams of an Erbium-based fiber laser are combined in a DFG stage, yielding femtosecond, mid-IR pulses with a Fourier transform limit of sub-3-optical cycles. After the DFG stage the mid-IR pulse energy is 5 pJ at a 100 MHz repetition rate with a center wavelengths of 3.2 µm (see spectrum in figure 3.11 (b)). The use of a fiber laser ensures stable, long-term operation while the DFG process driven by two beams derived from the same oscillator, provides CEP-stable, mid-IR seed pulses. Further details about the mid-IR front-end can be found in section 2.2.2.

Pump laser and temporal synchronization unit. The same pump laser and seed-to-pump temporal synchronization unit as in the former multi-color OPCPA system is used. The Nd:YVO_4 based MOPA pump system delivers an overall pulse energy of around 1 mJ at a center wavelength of 1064 nm and a repetition rate of 160 kHz. The temporal synchronization between the pump laser and the fiber laser which seeds the mid-IR front-end is done by an electrical synchronization unit from Toptica Photonics AG. For further details see sections 2.2.3 and 2.2.4.

Bulk stretcher. The mid-IR seed pulse is stretched via propagation through a 50 mm long sapphire rod, adding a group delay dispersion value of -34,750 fs^2 at a center wavelength of 3.2 µm. The resulting FWHM pulse duration is 1.9 ps, which is about 20% of the pump pulse duration of 9.5 ps. This relatively small temporal idler-to-pump ratio ensures the reduction of the spectral gain narrowing effect during amplification, since the idler feels an effective flat-top temporal profile of the pump beam during amplification (see section 3.1.1). The pulse energy of the mid-IR pulses is reduced to 4 pJ after propagation through the uncoated bulk stretcher.

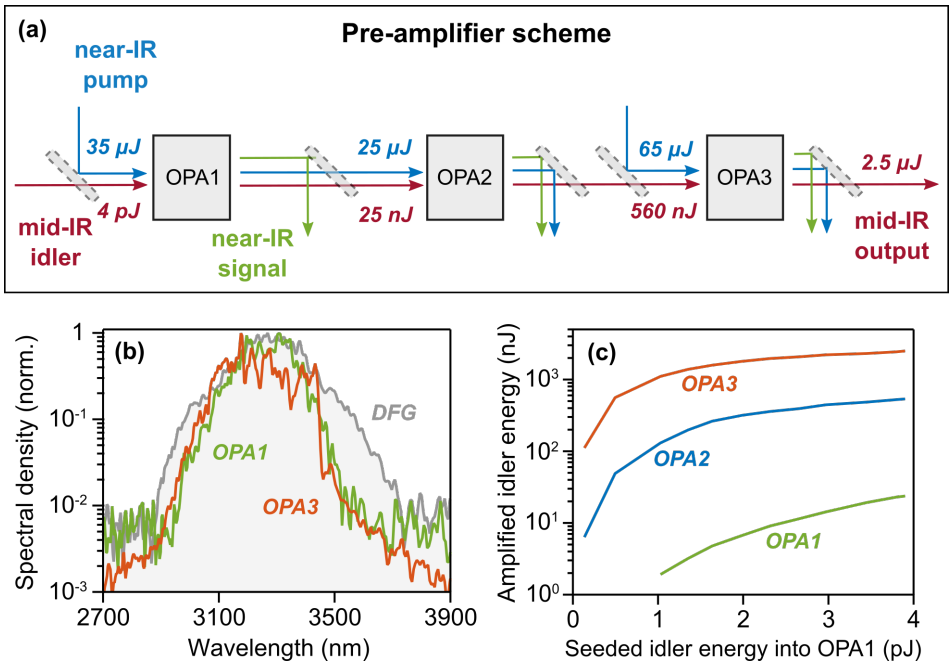

Figure 3.11: Design and amplification characteristics of the pre-amplifier. (a): Scheme of pre-amplifier layout including the pulse energies of idler, signal and pump beams. (b): Measured spectrum of the DFG stage which seeds the pre-amplifier, as well as the amplified spectrum after the OPA1 and OPA3 stages. The OPA stages cannot amplify the full seeded spectrum, resulting in a drop of the transform-limited pulse duration from original 50 fs to 63 fs after amplification. (c): Amplification behaviour of the OPA1, OPA2 and OPA3 stages as function of the seeded idler into OPA1. While the OPA1 amplifies in a rather unsaturated regime, the amplification scaling in OPA2 and OPA3 stagnates due to the approaching pump depletion regime.

Pre-amplifier. The pre-amplifier consists of three consecutive OPA stages (OPA1 to OPA3). The OPA stages are used in collinear beam geometry requiring the use of dichroic optics to combine and separate the idler, signal and pump beams before and after each OPA stage (pre-amplifier setup shown in figure 3.11 (a)). The nonlinear amplification crystals used in the three OPA stages are a 1.4 mm long fan-out MgO:PPLN crystal, a 5 mm long MgO:APPLN crystal and another 5 mm long MgO:APPLN crystal, respectively. In the first OPA stage 35 µJ of pump pulse energy are focused to a peak intensity of 25 GW/cm^2, amplifying the 4 pJ of seeded idler energy with a high gain of 6,250 to around 25 nJ pulse energy. After the OPA1

stage the pump beam is separated from the idler beam by use of a dichroic optic and reused to pump the OPA2 stage. The residual 25 µJ of pump pulse energy is focused to a peak intensity of 15 GW/cm^2, amplifying the idler up to a pulse energy of 560 nJ. For pumping the OPA3 stage a new pump beam with 65 µJ of pulse energy is focused to a peak intensity of 15 GW/cm^2 giving rise to an overall idler output energy of the pre-amplifier of around 2.5 µJ.
Figure 3.11 (b) shows the measured spectra in logarithmic scale after the DFG stage, the OPA1 stage and the OPA3 stage. It can be seen, that the OPA1 stage narrows the bandwidth of the DFG considerably, which elongates the transform-limited pulse duration from 51 fs to 63 fs. After amplification in the OPA2 and OPA3 stages the bandwidth is mostly maintained. We also analyzed the amplification behaviour of the individual OPA stages. By varying the seeded idler pulse energies into the OPA1 stage, the cumulative amplified output energy after the respective OPA stages is measured and the results are shown in figure 3.11 (c). It can be observed, that the first OPA stage does not reach the saturation regime, but that already the OPA2 stage as well as the OPA3 stage are driven in the strong pump depletion regime where the amplification level stagnates. Operation in this regime should result in a high pulse energy stability of the overall pre-amplifier idler output granted that the pump is stable.

Chirp-inverter. As chirp-inverter device we use a folded, all-reflective Martinez-type grating compressor similar to the Martinez-type grating compressor used in the former multi-color OPCPA system (see section 2.2.6 or figure 2.10). The grating device consists of an aluminium coated grating (200 lines/mm, 17.5° of blaze angle), a gold coated spherical mirror (f = 200 mm) which forms the imaging system and a plane, gold-coated mirror placed in the Fourier plane of the imaging system. Further information about the working principle of the Martinez grating compressor can be found in section 2.1.5. The Martinez-type assembly acts as chirp-inverter, since it adds sufficient positive GDD onto the mid-IR beam to overcompensate the original negative GDD introduced by the sapphire bulk stretcher. The second order dispersion of the mid-IR beam is changed from initially around -35,000 fs^2 to around +190,000 fs^2 at a center wavelengths of 3.2 µm (see dispersion overview in table 3.2), resulting in a temporal stretch of the idler pulse to a duration of 7.5 ps, which is around 80% of the pump pulse duration of 9.5 ps. This temporal idler-to-pump ratio is chosen experimentally to optimize the output idler peak power after amplification in the booster amplifiers (more details in sections 3.1.1 and 3.3.4). The overall transmission efficiency of the chirp-inverter is around 50% yielding an

output idler pulse energy of 1.3 µJ, which is seeded into the OPA4 stage.

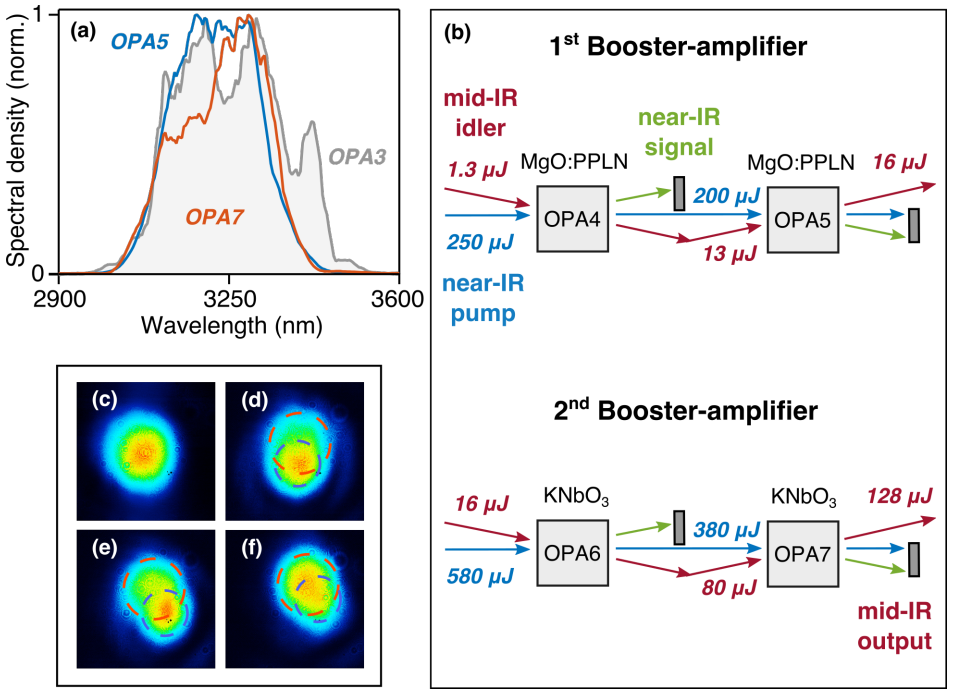

Figure 3.12: Design and amplification characteristics of the first and second booster-amplifiers. (a): Measured output spectrum of the OPA3 stage which seeds the first booster-amplifier, as well as the amplified spectrum after the OPA5 and OPA7 stages. (b): Scheme of booster-amplifier layouts including the pulse energies of idler, signal and pump beams. (c-f): Observed beam distortions of transmitted pump beam after the alternative, finally discarded approach of double-passing one, single MgO:PPLN crystal. (c): The undisturbed pump beam profile after the double-pass at low average powers. (d-f): When the full pump power is applied, the spatial profile of the double-passed, transmitted pump beam reshapes, obtaining two high intensity centers (purple and blue dotted circles), which are strongly dependent on the relative position of the first and second pass through the crystal.

Power booster amplifiers. Two power-booster amplifiers are used in series to push the idler pulse energies beyond the 100 µJ level. Each booster-amplifier consists of two consecutive OPA stages, where the recycled pump of the first OPA stage drives also the second OPA stage. The setup of the booster-amplifiers is shown in figure 3.12 (b). The first booster-amplifier, consisting of the OPA4 and OPA5 stages which both rely on 2 mm long, fan-out MgO:PPLN crystals with a vertical aperture of 2 mm. The second

booster-amplifier, sub-structured in the OPA6 and OPA7 stage uses a 1.8 mm and a 2.3 mm long, antireflection-coated $KNbO_3$ crystals with a cut angle of θ = 40.5° and an aperture of 5 by 5 mm^2. All OPA stages are driven in a non-collinear beam geometry, which increases the acceptance bandwidth of the amplification process for the used crystals. Additionally, the propagation losses of the idler beam through the OPA stages are reduced due to the absence of dichroic optics which would be required as beam combiner or separator in a collinear beam geometry.

In the OPA4 stage the 1.3 µJ pulse energy of the seeded idler beam is amplified to 11 µJ by applying pump pulse energies of 250 µJ with pump peak intensities of 20 GW/cm^2. The non-collinear external angle of 1° in the OPA4 stage enables the easy recycling of the spatially separated pump beam for a consecutive use in the OPA5 stage. In the OPA5 stage the pump beam shows an energy of 200 µJ and a peak intensity of 20 GW/cm^2, amplifying the idler pulse energy up to 16 µJ. In the OPA6 and OPA7 stages an internal non-collinear angle of 5.0 ° is used to achieve the best acceptance bandwidth of the type-I phase-matching of $KNbO_3$ (see also table 3.1). The 16 µJ pulse energy of the idler beam is amplified to 80 µJ after OPA6 and to 128 µJ after OPA7 by applying 580 µJ and 390 µJ of pump energy, respectively. The pump peak intensities in the OPA stages are set to respectively 10 GW/cm^2 and 5 GW/cm^2, well below the damage threshold of 330 GW/cm^2 (see table 3.1) to avoid thermally induced distortions of the $KNbO_3$ crystal structure. A detailed study about the energy conversion efficiencies of the separate amplifiers and the complete OPCPA system can be found in section 3.3.5. The idler spectra amplified in the booster-amplifiers are illustrated in figure 3.12 (a). It can be seen, that the spectral width of the idler wave shrinks considerably after amplification in the first booster-amplifier, but that the further amplification in the second booster amplifier maintains the spectral content. This drop of amplified bandwidth between the output of the pre-amplifier and the booster-amplifiers can be addresses mainly to the 4-fold increase of the idler pulse duration after the chirp-inverter and the resulting smaller pump intensities at the spectral wings.

As alternative to reuse the pump beam in a second OPA stage, we also experimented with a double pass configuration of the pump and idler beams through the same crystal. It turned out, that this double pass is not feasible in the first as well as in the second booster-amplifier due to average-power limitations. It is observed, that when double passing the MgO:PPLN crystal with a high power pump beam, the thermal gradient introduced by the first pass, influences also the pump transmission in the second pass. Fig-

ure 3.12 (c-f) shows the behaviour of the collimated pump beam profile measured after a double-pass beam geometry. The beam profile at small pump energies is pictures in figure 3.12 (c) and shows no spatial perturbations. When the full pump power is applied (figure 3.12 (d-f)), the spatial profile of the transmitted pump beam reshapes, displaying two intensity centers (purple and blue dotted circles), which are strongly dependent on the relative position of the first and second pass through the crystal. As a result, the amplified idler beam profile would strongly depend on the relative pump beam positions on the double-passed crystal, making a reliable and stable long-term operation of the overall OPCPA scheme challenging. When trying a double pass amplification in the $KNbO_3$ crystal the permanent crystal domain inversions (discussed in section 3.2.3) appear at much smaller pump energy fluencies, therefore setting a further, unwanted limit on the pump peak intensity. This behaviour is likely caused by the complex spatial thermal gradient distribution of a double-passed, partially absorbed pump beam.

Bulk compressor. The amplified idler pulses out of the booster-amplifiers are temporally compressed by transmission through a material bulk compressor consisting of an anti-reflection coated, 10 cm long sapphire rod, which is used in a double pass configuration. The reflection losses on each coated sapphire surface are around 1.3% per surface and the reflection efficiency of the folding mirror is measured to 97%. The overall transmission efficiency of the double-pass bulk compressor is therefore 92%, resulting in an idler output energy of 118 µJ at 160 kHz pulse repetition rate, which corresponds to an average power of 18.9 W.

The total transmission length of 20 cm adds a GDD of around -140,000 fs^2 to the idler pulses at a center wavelengths of 3.2 µm wavelength. Since the bulk compressor length cannot be fine adjusted, the optimum temporal compression of the mid-IR OPCPA output pulses has to be achieved by the precise setting of the second and third order dispersion, which is introduced by the Martinez-type chirp-inverter device. The beam incidence angle on the gratings in the chirp-inverter fixes the relative ratio between the third and second dispersion order and the effective grating distance influences the overall introduced dispersion. In table 3.2 is shown the analytical calculated second (GDD), third (TOD) and fourth (FOD) dispersion order, which is introduced by the different optical elements in the OPCPA system onto the mid-IR idler pulses. By using the Martinez-type chirp inverter at Littrow-angle $\theta_{Littrow}$ = 18.7° the full GDD can be compensated, but a residual TOD of -10,000 fs^3 remains. By changing the grating incidence angle slightly to θ = 19.4° the entire GDD and TOD of the stretched pulses

Element	Element length or grating separation	GDD in fs^2	TOD in fs^3	FOD in fs^4
negative GDD				
Bulk stretcher	50 mm, Al_2O_3	-34,730	+214,630	-1,754,700
MgO:PPLN crystals	16 mm, n_e	-10,450	+71,590	-564,520
$KNbO_3$ crystals	4.1 mm, n_x	-2,070	+13,380	-92,140
Lenses	33 mm, CaF_2	-4,400	+25,200	-178,790
Dichroic filters	10 mm, CaF_2	-1,330	+7,640	-54,180
Bulk compressor	200 mm, Al_2O_3	-138,910	+858,510	-7,018,900
positive GDD				
Chirp-inverter	35.2 mm, θ=18.7°	+191,890	-1,200,590	+10,859,330
	35.6 mm, θ=19.4°	+191,890	-1,190,806	+10,683,470
Total dispersion	for θ=19.4°	0	+150 $\approx$ 0	+1,020,240

Table 3.2: Overview of acquired dispersion of the cascaded amplified idler beam throughout the OPCPA system at a center wavelength of 3.2 µm. The dispersion due to transmission though material is calculated using equations 2.40, 2.41 and applying the Sellmeier equations of Al_2O_3 [102], MgO:LN [107], $KNbO_3$ [156] and CaF_2 [101]. The introduced dispersion by the Martinez-type grating-compressor (chirp-inverter) is estimated by applying equations 2.42, 2.43, 2.44 and under the use of d = 200 lines/mm and the respective effective grating distances and incident angles given in the table.

can be compensated. The residual fourth order dispersion of 1,020,240 fs^4 is negligible and will not stretch significantly the mid-IR pulse, which can be numerically verified by applying the dispersion onto the equation of a electromagnetic pulse $\tilde{E}(t) = \int\{\tilde{E}(\omega)\cdot\exp(i\cdot\frac{1}{4!}10^6 \text{fs}^4)\}\mathrm{d}t$ [72].

When considering bulk materials as temporal compressors for high energy pulses, one has to make sure to not add a considerable nonlinear phase to the transmitted beam in order to avoid unwanted, nonlinear effects such as self-phase modulation or self-focusing. The during propagation accumulated nonlinear phase ϕ_{NL}^{max}, also called B-integral can be calculated by equation 4.3 and depends, among others, on the peak intensity and therefore on the beam size and pulse duration. Hence, in order to calculate the integrated nonlinear phase, one has to take into account the change of the mid-IR pulse duration during propagation through the sapphire rod. In figure 3.13 (a) is illustrated the pulse duration evolution obtained by applying the respective GDD at each propagation length onto the mathematical description of a transform-limited, electromagnetic wave packet. By using the pulse duration evolution together with equation 4.3, the accumulated

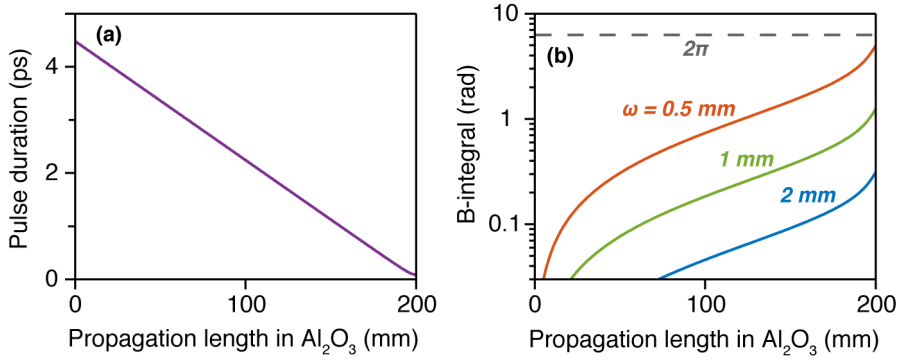

Figure 3.13: Analysis of B-integral or accumulated nonlinear phase shift, which is obtained by propagation of the high energy, mid-IR pulse through the 20 cm long sapphire bulk compressor. (a): Evolution of mid-IR pulse duration during temporal compression in bulk compressor. (b): Accumulated nonlinear phase shift behaviour of a mid-IR pulse calculated for $1/e^2$ beam radii of 0.5 mm, 1 mm and 2 mm and a pulse energy of 128 µJ by using equation 4.3.

B-integral during propagation is calculated and the result is shown in figure 3.13 (b). It can be seen, that for idler beam sizes (radius at $1/e^2$) of 0.5 mm, 1 mm and 2 mm, an integrated, nonlinear phase of 5.0, 1.2 and 0.3 is obtained, respectively. In order to avoid the appearance of nonlinear effects the accumulated nonlinear phase should be considerably smaller than 2π. Therefore, the minimum $1/e^2$ beam radius during the mid-IR pulse compression in the sapphire bulk compressor should be around 1 mm or even 2 mm to ensure the absence of any nonlinear propagation effects acting on the mid-IR pulse.

3.3.3 OPCPA output performance

An overview of all output parameters of the OPCPA system is given in figure 3.14, including: (a) spectral content, (b) pulse duration, (c) pulse energy stability and beam profile in inset, (d) pointing stability and (e, f) M^2 parameter. All measured pulse and beam characteristics are explained in detail below.

Mid-IR pulse characteristics. The mid-IR output spectrum is centered at 3220 nm wavelength and covers a bandwidth of 330 nm at $1/e^2$. The pulse lengths is measured with a SHG-FROG device and shows a pulse duration of 95 fs at FWHM, which is close to the transform-limit of 86 fs and

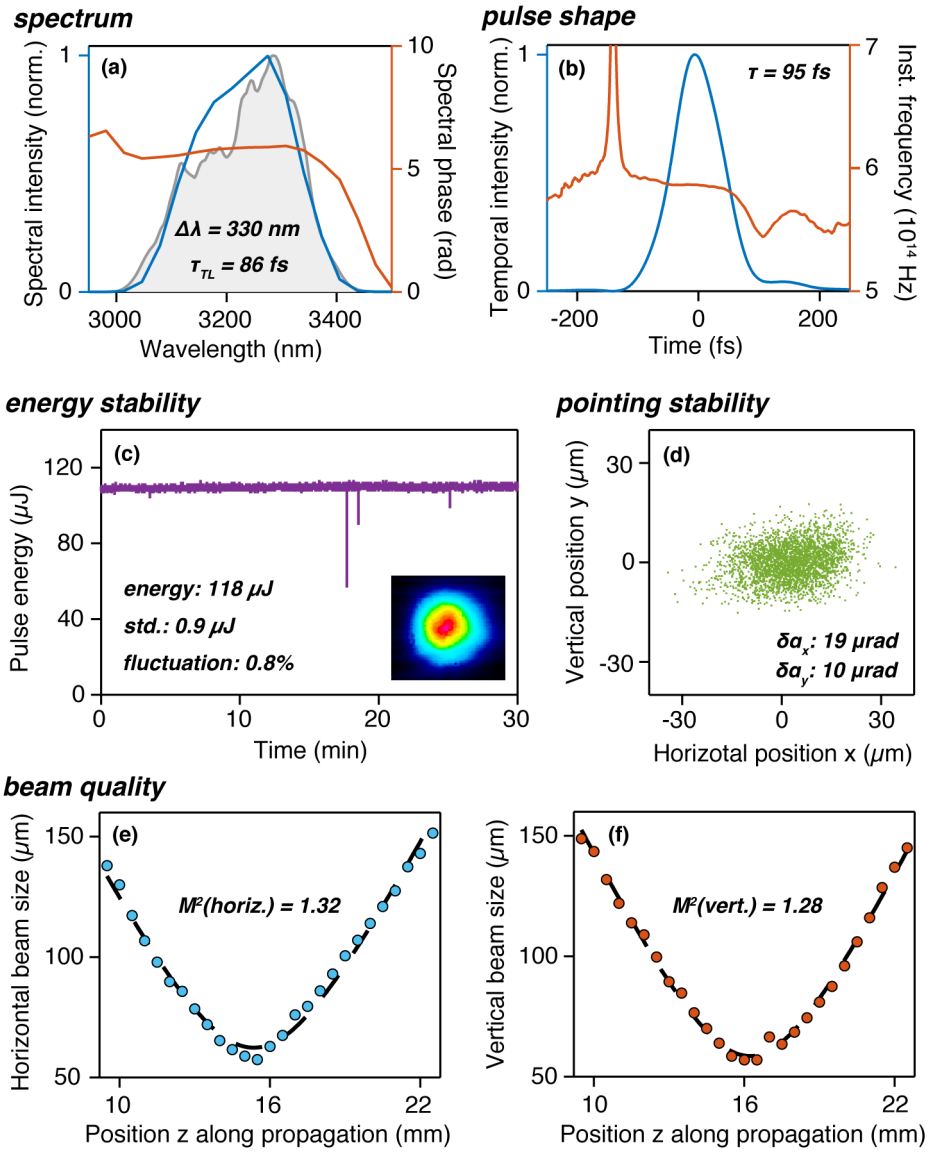

Figure 3.14: Overview of all output characteristics of the GW-level, mid-IR OPCPA source. (a) Retrieved (blue line) and measured (shaded area) mid-IR spectrum obtaining a center wavelength of 3.2 µm and a transform limit of 86 fs. (b) Retrieved temporal pulse shape revealing a pulse duration at FWHM of 95 fs. (c) Pulse energy stability measured over 30 min. showing a fluctuation of 0.8% of the output energy of 118 µJ. (d) Pointing stability measurement over 5 min. featuring a angular stability of 19 µrad in horizontal and 10 µrad in vertical direction. Inset is shown the spatial profile of the collimated output beam. (e,f) Measurement of the beam quality factor M^2 obtaining an average value of 1.3.

corresponds to 8.9 optical cycles. The retrieved spectral phase shown in figure 3.14 (a) reveals primarily a residual third order dispersion elucidating the discrepancy between the transform limit and actual pulse duration.

Pulse energy. The mid-IR pulse energy at the output of the OPCPA system is measured to be 118 µJ at 160 kHz, which corresponds to an average power of 18.9 W. Combined with the 95 fs pulse duration a GW-level peak power of 1.24 GW is reached. When blocking the mid-IR seed pulse of the OPCPA system, no measurable amplified superfluorescence could be detected at the output. The shot-to-shot pulse energy stability is measured with a mid-IR sensitive photodiode to 0.8% fluctuations over the course of 30 minutes (see figure 3.14 (c)). The two sharp drops in pulse energy around the measurement time of 18 minutes last less than 20 ms and are caused by delayed adjustments of the temporal pump-to-seed synchronization due to the electronic synchronization unit (see section 2.2.4) and do not influence the overall energy stability considerably.

Beam quality. In figure 3.14 (c, inset) is shown the spatial profile of the collimated output beam exhibiting a Gaussian-like shape without a sign of spatial energy hot spots. The spatial beam profile was measured with a microbolometer camera. In order to obtain the beam quality factor M^2, the evolution of the beam radius at $1/e^2$ along the propagation direction of the mid-IR beam is measured after focusing with a reflective, off-axis parabolic mirror in order to avoid spherical and chromatic aberrations. Afterwards, the beam caustic is fitted to the evolving beam width equation of Gaussian-like beams to achieve the M^2 beam quality factor (see figure 3.14 (e,f)):

$$\omega(z, \omega_0, z_0, M^2) = \omega_0 \cdot \sqrt{1 + \frac{\lambda^2}{\pi^2} \cdot \left(\frac{M^2 \cdot (z - z_0)}{\omega_0^2} \right)^2}, \tag{3.2}$$

where ω is the $1/e^2$ beam radius at the position z in propagation direction, ω_0 is the focus beam waist at the position z_0 and λ the center wavelength. After fitting, a M^2 value of 1.32 and 1.28 is obtained in horizontal and vertical direction, respectively. This evolving beam waist equation is only suited for Gaussian-like beams. For the M^2 measurement of more complex spatial beam profiles the linear second momentum diameter $D_{4\sigma x}$ has to be taken into account instead of the $1/e^2$ beam radius ω (for more information see [157]).

Pointing stability. The beam pointing stability can be described by the

beam angular stability $\delta\alpha$ defined by the following equation [157]:

$$\delta\alpha = \frac{2 \cdot s}{f} = \frac{2}{f} \cdot \sqrt{\frac{1}{N-1} \sum_{i=1}^{N} (x_i - \overline{x})^2}, \tag{3.3}$$

where f is the focus length of the used focusing element and s is the standard deviation of the beam center position x_i. To measure the angular pointing stability, the full power, mid-IR output beam is focused by a lens with a focal length of 250 mm. The spatial center position is measured in the focus by an automatized scanning slit beam profiling device (NanoScan from Ophir Optronics Solutions Ltd.) with a 10 Hz sampling rate. In figure 3.14 (d) is shown the measured variation of the focus beam position over the course of 5 minutes. The standard deviation s of the beam center position is 2.4 µm in horizontal and 1.3 µm in vertical direction which is below 2% of the focus beam waist of around 120 µm. Applying equation 3.3 a beam angular stability of 19 µrad in horizontal and 10 µrad in horizontal direction is obtained.

3.3.4 Source evaluation: Choice of idler stretching factor in power-booster amplifier

In order to obtain the GW-level output peak powers of the mid-IR OPCPA system reported in section 3.3.3, various source design parameters had to be optimized. One critical parameter is the optimization of the stretched idler pulse duration in the final booster-amplifiers. The influence of this parameter is theoretically studied in detail in section 3.1.1. In general, idler-to-pump pulse duration ratios closer to one improve the temporal overlap of idler and pump pulses and therefore can increase the overall pump-to-idler energy conversion efficiency. But a very large temporal idler-to-pump ratio can also lead to a decreasing amplified spectral bandwidth due to spectro-temporal gain narrowing, which limits the possible compressed output pulse duration. To achieve the maximum possible output peak power of the OPCPA system, a stretched idler duration has to be chosen, supporting an optimum between high output pulse energy and transform-limited output pulse duration.

In this section we study the influence of the stretched idler pulse duration in the booster-amplifiers on the overall parametric amplification performance of the OPCPA system. The pulse duration of the idler wave which is seeded into the OPA4 stage is a result of the group delay dispersion (GDD) gained after propagation through the chirp-inverter device (see OPCPA scheme in

figure 3.10). This GDD can be influenced by changing the effective grating distance of the Martinez-type chirp-inverter (more details see section 2.1.5). The energy of the seeded idler pulse is 1.3 µJ with a $1/e^2$ spectral bandwidth of 380 nm, supporting a transform-limited pulse duration of 69 fs. The idler and pump beam sizes in the OPA4 to OPA7 are matched close to a 1:1 ratio. The beam waists are chosen such that the pump peak intensities are close to the material damage thresholds. All pump beam parameters are similar to the detailed description of the individual OPAs in section 3.3.2, except that in this study two different nonlinear crystals are used in the OPA6 and OPA7 stages. In the OPA6 stage an uncoated, 1.8 mm long $KNbO_3$ crystal is used, while in the OPA7 stage an AR-coated, 1.7 mm long MgO:PPLN crystal is used.

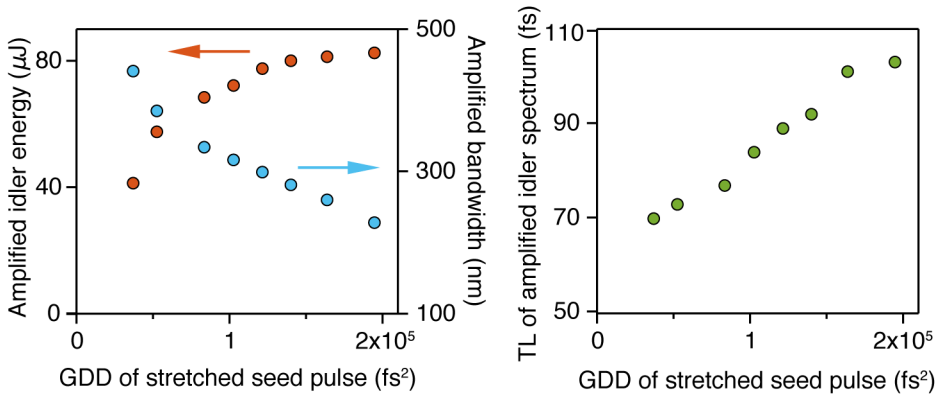

Figure 3.15: Amplification behaviour of booster amplifiers (OPA4 to OPA7) as a function of the seed stretch factor. The stretched pulse duration of the idler wave is adjusted by applying different group delay dispersions (GDD) in the grating-based chirp-inverter. (left): Measured idler pulse energy and spectral bandwidth at $1/e^2$ height after amplification. (right): Calculated transform-limited pulse duration (TL) of the amplified idler output spectrum.

In figure 3.15 (left) is illustrated the influence of the GDD of the seed idler pulse on the output idler pulse energy after all booster amplifiers. This energy is measured before transmission through the final bulk compressor. Additionally, for each seed pulse duration the amplified idler spectrum is measured and the bandwidth at $1/e^2$ height is given. The GDD values of the seeded idler pulses introduced by the chirp-inverter are calculated for a center wavelength of 3.2 µm using equation 2.42.

Figure 3.15 (left) shows that the amplified idler pulse energy increases rapidly to 70 µJ for GDD values up to 80,000 fs^2 and then saturates at pulse

energies around 80 µJ for higher GDD values. At the same time the amplified spectral density drops fast from initially 450 nm to 330 nm at a GDD of 80,000 fs^2 and then decreases for higher GDD values very slowly down to 230 nm. For each seed pulse duration the Fourier transform-limited (TL) pulse duration is calculated from the amplified spectrum and the obtained values are shown in figure 3.15 (right). It can be seen, that the TL pulse duration increase rather linearly from 70 fs at a GDD of 40,000 fs^2 up to 105 fs at a GDD of 200,000 fs^2.

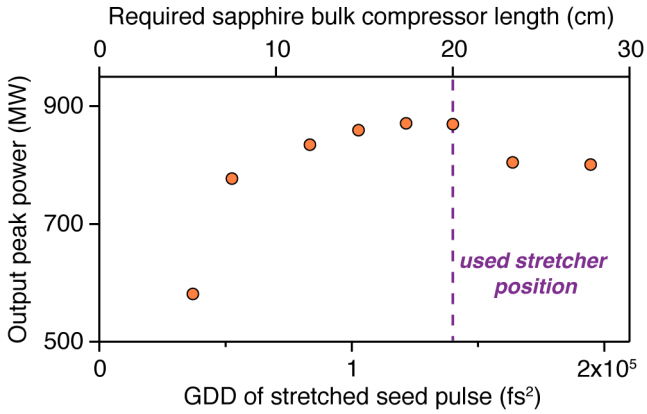

Figure 3.16: Output idler peak power of the mid-IR OPCPA system in function of the seed stretch factor applied in the booster-amplifiers (OPA4 to OPA7). The stretched pulse duration of the idler wave is adjusted by applying different group delay dispersions (GDD) in the grating-based chirp-inverter. The top axis shows the estimated length of a sapphire bulk compressor that would be required to recompress the stretched idler pulses after amplification. In purple is marked the final GDD in the booster-amplifiers, which allows a high output peak power and convenient pulse compression with a 20 cm long sapphire bulk compressor.

To identify the optimal seed pulse duration to operate the booster-amplifiers, the achievable output idler peak powers are calculated by dividing the amplified output energy by the TL pulse duration. The obtained peak powers are illustrated in figure 3.16. Additionally, on the top abscissa axis is shown the respective sapphire bulk compressor length, which is required to compress the respective stretched seed pulses and to compensate the total GDD. In figure 3.16 can be seen, that the available idler peak power grows fast until a GDD of 50,000 fs^2 and stagnates at around 850 MW peak power for higher GDD values. The final OPCPA system is operated at a GDD of the stretched mid-IR pulse of around 140,000 fs^2, which allows the tempo-

ral compression of the amplified output pulses due to propagation through a 20 cm long sapphire bulk compressor (purple sign in figure 3.16). This chosen stretch factor ensures simultaneously a high output peak power of 880 MW and a high pulse energy of 80 µJ, while the transform-limited pulse duration lies around 90 fs.

Posterior to the seed pulse duration scan, the amplification crystals in the OPA6 and OPA7 stages were exchanged by AR-coated $KNbO_3$ crystals, allowing the upscaling of the OPCPA output characteristics to the values presented in section 3.3.3 obtaining a final idler pulse energy of 118 µJ, a compressed pulse duration of 95 fs and a peak power of 1.24 GW.

3.3.5 Source evaluation: Total conversion efficiency and saturation behaviour of last amplifiers

In this section we will analyze the obtained conversion efficiencies in the different parts of the GW-level OPCPA system in order to evaluate the impact of the applied source design improvements (see section 3.3.1).

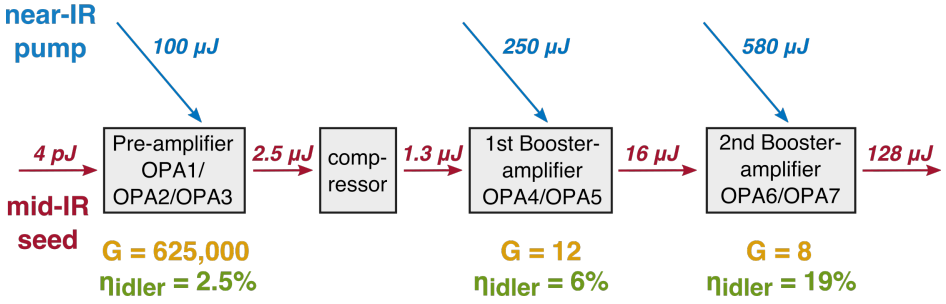

Figure 3.17: Overview of the pump-to-idler energy transfer by optical parametric amplification in the mid-IR OPCPA system. Shown are the pulse energies of the cascaded amplified idler wave (red) and the pulse energies of the applied pump waves (blue) used for each amplifier block. The achieved amplification gain is displayed in yellow and the respective pump-to-idler energy conversion efficiencies are given in green and calculated with equation 3.4.

First, we focus on the overall energy flow and the conversion efficiency of each building block of the high power OPCPA system. Figure 3.17 shows the pulse energy distribution inside the OPCPA source, indicating the cascaded amplified mid-IR idler wave in red and the applied pump pulse energies in each amplifier block in blue. The pump-to-idler energy conversion

efficiency η_{idler} can be calculated for each amplifier by:

$$\eta_{idler} = \frac{E_{idler,out} - E_{idler,in}}{E_{pump}} \tag{3.4}$$

Where $E_{idler,in}$ is the input and $E_{idler,out}$ the amplified output pulse energy of the idler and E_{pump} is the applied pump pulse energy. The experimentally obtained pump-to-idler conversion efficiencies are shown in green. According to the energy conservation in the OPA process the total pump-to-(signal+idler) conversion efficiency η_{total} is given by the Manley-Rowe relation to $\eta_{total} = \frac{\omega_{pump}}{\omega_{idler}} \cdot \eta_{idler} = 3.0 \cdot \eta_{idler}$ (see equation 2.24). In figure 3.17 it can be seen, that the pump-to-idler conversion efficiencies in the high gain pre-amplifier is relatively low with 2.5% and afterwards increases considerably to 6% and 19% in the first and second booster-amplifier, respectively. The overall pump-to-idler conversion efficiency η_{idler} of the whole system is 128 µJ/ 930 µJ=13.8% resulting in a total conversion efficiency of η_{total}=3·13.8%=41.4%. The consecutive increase of the conversion efficiency for each stage is partially attributed due to the larger idler stretching factor in the booster-amplifiers compared to the pre-amplifier (see section 3.1.1), but is mainly the result of the strong pump depletion regime in which the parametric amplification in the high energy, booster-amplifier stages are driven. Especially in the second booster-amplifier due to the high seed energy and by use of the nonlinear crystal $KNbO_3$ which does not exhibit the average power limitations of MgO:PPLN (see section 3.2.3), very tight beam focusing conditions can be chosen, resulting in an OPA process operating in the strong pump depletion regime.

For a further investigation of the saturation behaviour of the second booster-amplifier, the amplified idler output is measured after OPA6 and after OPA7 as a function of the seeded idler energy into OPA6, illustrated in figure 3.18 (left). The reader is reminded, that the second booster amplifier is a compound of the chained OPA6 and OPA7, where the pump beam of OPA6 is recycled to pump OPA7 (see scheme in figure 3.12). A half-wave plate followed by a polarizer is placed in front of the booster-amplifier, allowing the fine adjustment of the seed energy into OPA6 while maintaining the polarization and pulse duration of the seed pulses. The resulting pump-to-idler energy conversion efficiency is shown in figure 3.18 (right) and is calculated using equation 3.4. It can be seen, that the seed pulse energy of 16 µJ is amplified in the OPA6 to 80 µJ energy and afterwards in OPA7 further boosted to 128 µJ. The resulting pump-to-idler conversion efficiency of OPA6 reaches up to 10% (blue line), while the internal conversion efficiency of OPA7 increases up to 13% (orange line). The internal conversion efficiency of OPA7 is calculated by dividing the idler energy gained in OPA7

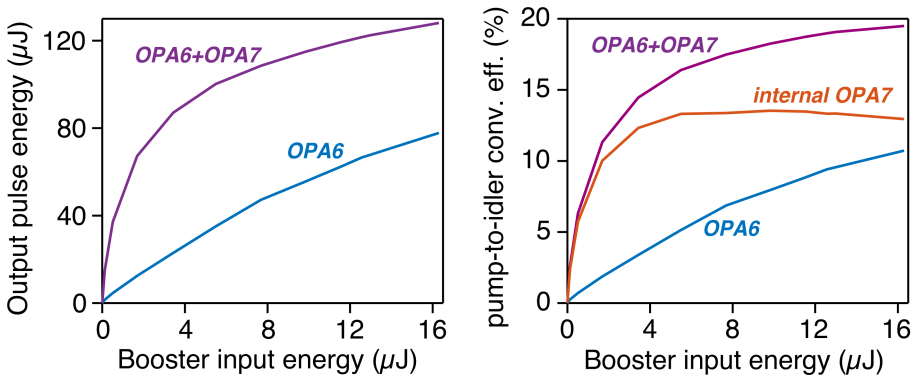

Figure 3.18: Scaling behaviour of the parametric amplification process in the final booster-amplifier constisting of OPA6 and OPA7, where latter is pumped by the recycled pump beam out of OPA6. (left): Scaling of the output pulse energy amplified in OPA6 (blue line) as well as in OPA6 and OPA7 (purple line) in dependence of the input mid-IR seed energy into OPA6. (right): Calculated pump-to-idler energy conversion efficiency for OPA6, for OPA7 and for the overall booster amplifier (OPA6+OPA7). The calculated conversion efficiency of OPA7 uses the pulse energy of the recycled pump, which is reduced by the former amplification in OPA6.

by the reduced pulse energy of the pump wave, which is recycled after OPA6. The scaling behaviour of the OPA6 conversion efficiency shows first a rather linear increase and starts to slow down slightly at high seed energies. In contrast, the OPA7 pump-to-idler conversion efficiency exhibits a strongly roll over behaviour, showing first a quick rise to over 10% for low seed energies and afterwards a rather constant evolution around 12% for seed energies above 4 µJ. This roll over behaviour of OPA7 is the result of a complex interplay between seed and pump energy coupled into OPA7 since both beams are strongly influenced by the previous amplification in OPA6. For higher seed energies into OPA6, the seed energy into OPA7 increased considerably, while the pump energy reduces due to the previous energy extraction in OPA6. The strong saturation behaviour of OPA7 transfers to the overall conversion efficiency scaling of the OPA6 and OPA7 booster-amplifier compound, leading to a pump-to-idler conversion efficiency of up to 19% (figure 3.18, purple line). The resulting total conversion efficiency from pump to idler plus signal wave reaches therefore up to 3·19%=57%.

One can summarize, that the high output pulse energies of 128 µJ of the GW-level OPCPA system is a result of the strong total conversion efficiencies in the last booster amplifiers. The last OPA stages obtain total conver-

sion efficiencies from pump to signal plus idler waves of up to 3·13%=39%. Combined with the doubled use of the high energy pump beams in two consecutive OPA stages, a total OPCPA system conversion efficiency of 41% can be reached. This efficiency is comparable to values obtained by previously reported, high conversion efficiency OPCPA systems which emit in the more common visible and near-IR wavelength regime [4, 137–139]. Furthermore, driving the OPA stages in the strong pump depletion regime allows a very stable source operation, including an excellent shot-to-shot as well as long-term stability.

3.3.6 Source evaluation: Parasitic processes

An interesting phenomenon in optical parametric amplification is the generation of parasitic waves at additional frequencies, which are the product of other parametric processes such as second harmonic generation, difference frequency generation or sum frequency generation between two of the three main optical waves. In contrast to the desired main 3-wave-interaction, the parasitic wave generation is typically poorly phase-matched, resulting in very low conversion efficiency. Nevertheless in strongly saturated parametric amplifiers, the pulse energy of the parasitic waves can increase considerably, due to their still exponential growth in the unsaturated amplification regime, while the main idler and signal wave generation is saturated. Therefore the investigation of the origin and conversion efficiency of each parasitic wave generation can give insight, how much pulse energy is stolen from the main parametric amplification process and if the parasitic processes affect the pump-to-idler conversion efficiencies of the OPA stage significantly.

For the study of the parasitic wave generation all emitted beams after the 7th OPA stage of the high power OPCPA discussed in section 3.3.1 are measured and analyzed. This particular amplification stage is chosen due to the strong saturation regime in which the phase-matched, main 3-wave-interaction is driven (see section 3.3.5). Additionally, the non-collinear beam geometry of the $KNbO_3$ based OPA stage allows the disentanglement of each independent parametric frequency generation process for all parasitic waves. This disentanglement can be done by means of the momentum and energy conservation laws ($\vec{k}_p = \vec{k}_s + \vec{k}_i$ and $\hbar\omega_p = \hbar\omega_s + \hbar\omega_i$), which are linked to the emission angle and frequency content of each parasitic wave. The average power of each output beam is measured by means of a pyro-electric power meter and the angular dependent spectral content by fiber coupled spectrometers. To cover the full spectral range from

the visible up the mid-IR range, a combination of a silicon based CCD spectrometer (HR4000 from Ocean Optics Inc.), an InGaAs based CCD spectrometer (NIR256 from Ocean Optics Inc.) and a FTIR spectrometer applying a liquid nitrogen cooled MCT detector (MIR8025 from Newport Corporation) is used.

In figure 3.19 are illustrated the measured, normalized frequency distribution of all emitted beams after OPA7 as a function of the respective emission angles α, in relation to the pump beam direction at $\alpha = 0°$. At an emission angle of $\alpha = 0°$ the pump beam can be seen at f = 280 THz and the related second harmonic at f = 560 THz. At f = 90 THz is shown the mid-IR idler wave and around the emission angle of $\alpha = 5°$ the angular dispersed signal wave and its related second and third harmonic wave can be seen at f = 190 THz, 380 THz and 570 THz respectively. Apart from the three fundamental waves (I, S, P) and their harmonics (SH-S, TH-S, SH-P) also four other parasitic waves (SFG-1, SFG-2, DFG-1, DFG-2) can be observed, which result from sum or difference frequency generation processes. The beam SFG-1 at f = 470 THz is generated by sum frequency mixing between the pump (P) and the signal wave (S) and the beam SFG-2 at f=660 THz is created by the sum frequency generation between the second harmonic of the signal wave (SHG-S) and the idler wave (I). In contrast, the beam DFG-1 at f = 290 THz is generated by difference frequency generation between the second harmonic of the signal (SHG-S) and the idler (I), while the wave DFG-2 at f = 480 THz is created by difference frequency generation between the third harmonic of the signal (THG-S) and the idler (I). The interactions SFG-2, DFG-1 and DFG-2 are quite surprising, since they are not just a direct interaction between the main waves (I, S, and P), but instead a frequency mixing process between a fundamental wave and another parasitic wave, resulting in cascaded parasitic frequency generation.

Figure 3.20 shows the combined spectral content of all emitted beams after OPA7 in a logarithmic scale. For each beam the pulse energy is measured and used for the calibration of the respective spectral energy density. It can be seen, that the waves with the highest energy densities are the idler, signal and pump waves, while the spectral energy densities of all parasitic waves is at least 2 orders of magnitude smaller. The strongest parasitic wave is the second harmonic of the signal (SHG-S), which reaches spectral energy densities of up to 60 nJ/THz.

In conclusion, the energy content of all parasitic wave is negligible compared to the main 3-wave-interaction and does not influence the amplifi-

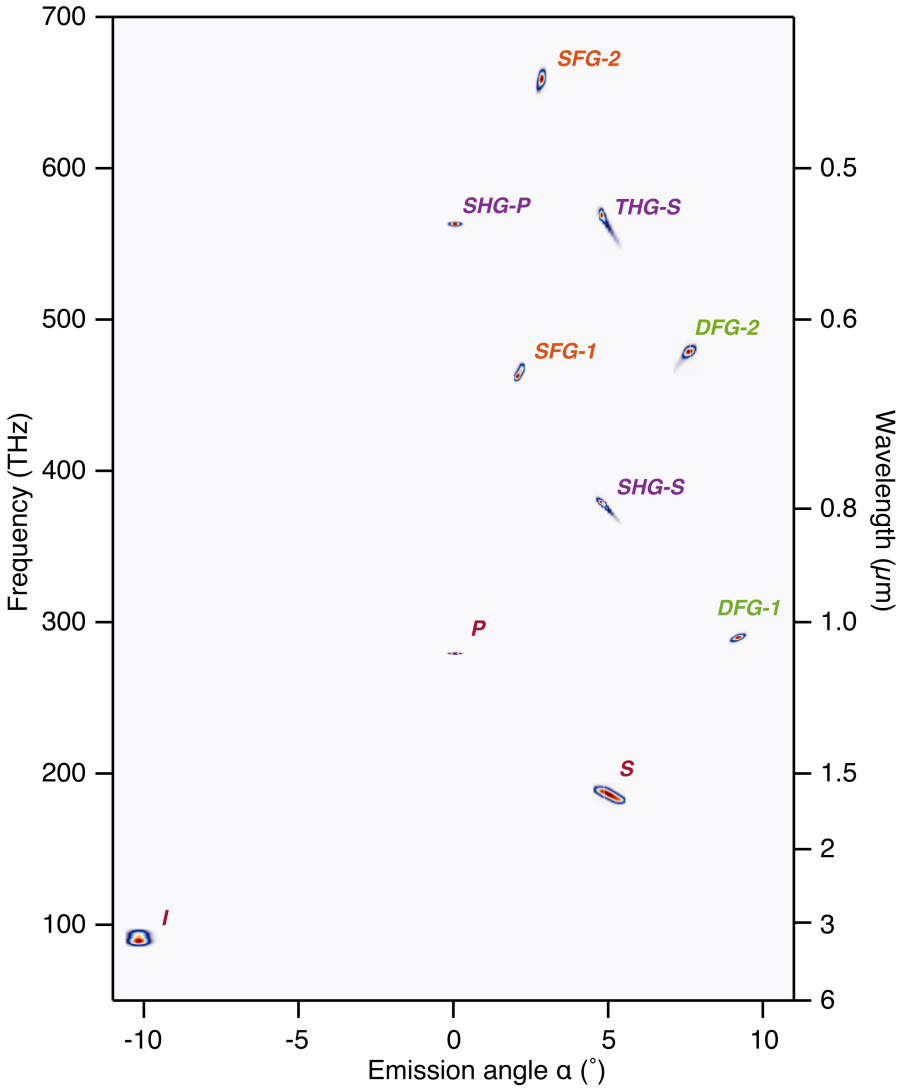

Figure 3.19: Measured, normalized, angular distribution of parasitic frequency generation in the final high energy parametric amplifier stage of the GW-level OPCPA (7th OPA stage). The emission angle α is given relative to the pump propagation direction. The picture shows the main pump (P), the idler (I) and the signal (S) waves, as well as the second harmonics (SHG-P, SHG-S) and a third harmonic (THG-S) of these fundamental waves. Also visible are further parasitic waves which are the product of sum frequency generation (SFG-1, SFG-2) or difference frequency generation processes (DFG-1, DFG-2).

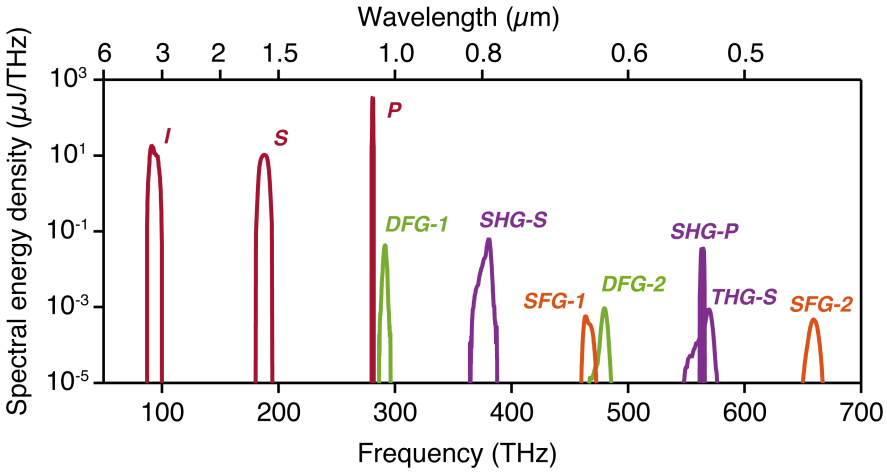

Figure 3.20: Measured energy content of parasitic frequency generation in the final high energy parametric amplifier stage of the GW-level OPCPA (7th OPA stage). Illustrated is the spectral energy density distribution of all emitted beams after the NOPA stage in logarithmic scale. The spectral energy density of any parasitic wave (SHG-P, SHG-S, THG-P, SFG-1, SFG-2, DFG-1, DFG-2) is orders of magnitude below the fundamental waves (P, I, S).

cation efficiency of the mid-IR idler and near-IR signal considerably. For a comprehensive investigation, a similar study could be performed for a PPLN-based OPA stage such as for OPA7, due to the different phase-matching conditions compared to a $KNbO_3$ based NOPA. Nevertheless it is unlikely, that the non-phase-matched, parasitic frequency generation would be orders of magnitude stronger to have a huge impact on the overall amplifier behaviour.

3.4 Summary and outlook

3.4.1 Summary

In this chapter we demonstrated the first implementation of a high power, mid-IR OPCPA system delivering GW-level output peak powers at a repetition rate beyond 100 kHz. The source provides 118 µJ energie pulses with a sub-9 optical cycle duration at a center wavelength of 3220 nm. The presented source supports a 3 times higher mid-IR output energy and a 20% higher peak power in comparison to other up-to-date reported mid-IR, high repetition rate OPCPA systems (see figure 1.1) [50–52, 56, 158]. Combined with an excellent beam quality factor of M^2=1.3, the system allows focused peak intensities of up to 10^{15} W/cm^2, enabling novel mid-IR driven strong-field experiments at high repetition rate, such as the potential generation of high flux X-ray radiation up to keV photon energies via high harmonic generation [24].

The huge increase of the mid-IR output energy compared to the previous OPCPA design shown in chapter 2, is enabled by various layout improvements which were undertaken in order to maximize the overall energy conversion efficiency. By exploiting a combination of the reuse of the pump pulses in two consecutive OPAs (see section 3.1.3), the reduction of Fresnel losses of the final compressor (see section 3.3.2) and by the implementation of a chirp-reversal in the system, which enabled an optimized dispersion adjustment for each OPCPA section (see section 3.3.4), an overall pump energy extraction efficiency of 41% could be reached. This extraction efficiency is very high for Gaussian-like spatio-temporal beam shapes (see section 3.1.2) and is comparable to high conversion efficiency systems emitting in the near-IR spectral range [4, 137–139]. The resultant average powers of the pump, signal and idler waves, used in the system reached the tens to hundred Watt regime, limiting the use of certain nonlinear amplification crystals such as MgO:PPLN due to the appearance of thermally induced beam distortions (see section 3.2.3). As a result, we investigated various nonlinear crystal in respect to their suitability for high power, mid-IR parametric amplification and finally used $KNbO_3$ crystals in the last booster-amplifier stages OPA6 and OPA7.

The presented GW-level peak power OPCPA is still compatible with the multi-color upgrade presented in section 2.3, which enabled additional high energy, femtosecond output pulses in the ultraviolet to near-IR spectral range. In this case, the recycled signal and pump beams obtained after the OPA5 stage could be used as driving pulses for the multi-color module.

In consequence, the only required change to the original layout would be an adjustment of the previous compressor schemes for the 800 nm wavelength beam, due to the inverse dispersion used in the booster-amplifier stages.

3.4.2 Outlook

The output parameters of the presented high power OPCPA system could be further improved by a number of upgrades, which are more or less invasive to the original source design. For example, the already high pump energy extraction efficiency in the OPCPA system could be further increased by applying spatio-temporal flat-top pump profiles (theory in sections 3.1.1, 3.1.2). It was demonstrated, that the Gaussian-like spatial profile of common picosecond pump lasers could be transformed to a flat-top profile via the use of spatial apodizers [159], refractive optical systems [160] or diffractive optical elements (DOE) [142]. These devices were already used in some OPCPA systems to obtain higher conversion efficiencies [137]. On the other hand, the temporal profile of the pump laser could be modified from a sech^2-like shape to a super-Gaussian or flat-top shape by exploiting coherent pulse stacking techniques, using for example fiber Bragg gratings [161] or pulse-stacking interferometers [162]. An additional advantage of the use of pump beams with a flat-top-like temporal profile is the possible increase of the amplified spectral bandwidth, resulting in shorter transform-limited output pulse durations.

Another technique, which could enable the generation of broader output spectra is frequency domain optical parametric amplification (FOPA) [163], where the OPA stage is placed in the Fourier plane of a 4f imaging system, enabling an influence on the spectral gain by changing the applied spatial pump distribution. As alternative, one could exploit the method of temporal allocation of pump intensity remainder (TAPIR) [164], where the OPA seed pulses are stretched to be several time longer than the pump pulses. In this case, a different temporal delay between the pump and signal pulses in each stage result in the amplification of different parts of the seed spectrum, which enables the controlled shaping of the amplified spectrum by adjusting the amplification gain in each stage. An example for a experimental realization of the TAPIR method can be found in section 4.2 of [165].

Further, a substantial output energy upgrade of our mid-IR front-end by three orders of magnitude is enabled by the technological advancement of ytterbium-doped fiber amplifiers over the last decade. Cruz *et al.* [166]

demonstrated, that a similar front-end as used in our OPCPA system (see section 2.2.2) in combination with a chirped pulse (CPA) ytterbium-doped fiber amplifier, can provide 5 nJ energy, broadband mid-IR pulses, instead of the 11 pJ energy previously obtained in our OPCPA. This up-scaling of the mid-IR front-end performance could allow the reduction of the number of OPA stages in the pre-amplifier of our OPCPA system and therefore reduce the complexity of the overall source.

Another possibility for the up-scaling of our OPCPA system is the use of novel high power pump sources, which got accessible over the last years. In this context, the reader is reminded, that the main obstacle in the energy scaling of high repetition rate lasers, is the rising average power and related energy storage inside the laser gain material which can yield thermal lensing and which has to be continuously extracted by external cooling. The pump laser used in our high power OPCPA system is a water-cooled, diode-pumped solid state laser system and provides 1 mJ energy, 10 ps duration pulses at 160 kHz repetition rate, resulting in 160 W of average power (see section 2.2.3). Over the last decade, especially ytterbium-doped YAG (Yb:YAG) has emerged as a novel and excellent gain medium for the generation of picosecond pulses at simultaneously high energy and high repetition rates. Recently, Zapata *et al.* demonstrated the generation of 2.5 mJ energy pulses at 100 kHz repetition rate (250 W) by using a cryogenic cooled Yb:YAG-based multi-pass amplifier [167]. Further Rußbüldt *et al.* reported the generation of 3.5 mJ energy pulses at 100 kHz (350 W) by using a Yb:YAG-based 9-pass amplifier in a Innoslab arrangement [168]. And Negel *et al.* could even provide 4.7 mJ pulse energy at 300 kHz (1400 W) using a Yb:YAG-based thin-disk laser amplifier with 24 passes [169]. Finally, Kienel *et al.* demonstrated the generation of 7.4 mJ energy pulses at 100 kHz (740 W) and of 12 mJ energy pulses at 56 kHz (670 W) by using a Yb:YAG-based CPA fiber amplifiers in a specially designed multidimensional coherent pulse addition arrangement [170]. A detailed overview of the recent pump laser developments for OPCPA systems can be found in [171] and more specific reviews about the progress on high power fiber lasers, high power innoslab laser and high power thin-disk lasers can be found respectively in [172], [173] and [174].

Chapter 4

Few-cycle, mid-IR pulse generation via temporal self-compression in bulk materials

In chapters 2 and 3 we demonstrated the generation of CEP-stable, high power mid-IR pulses with time durations of 5 or 9 optical cycles with pulse energies of 20 µJ or 118 µJ respectively, depending on the OPCPA architectures. Further pulse shortening does require additional spectral broadening and temporal compression due to the absence of sufficient spectral bandwidth of the OPCPA output pulses. In this chapter one of the first realizations of a novel temporal post-compression technique in the mid-IR range is discussed, achieving pulse compression down to sub-3 optical cycles. These results are reached by means of filamentary propagation in the anomalous dispersion regime in a bulk medium. Primarily, due to the interplay of self-phase modulation and anomalous dispersion during the highly nonlinear propagation, the input pulses are self-compressed without the need of an additional post-dispersion compensation stage. The results, reported in this chapter are published in [175]. The experimental work was performed together with my colleagues Michaël Hemmer and Alexandre Thai. The detailed numerical simulations used for comparison with the experimental results in section 4.3 were carried out by our collaborator Prof. Arnaud Couairon from the Centre de Physique Théorique, École Polytechnique in France.

In the following an overview of existing high energy pulse-compression techniques will be given in section 4.1 and the underlying fundamental concepts will be elaborated in section 4.2. Afterwards, in section 4.3 the obtained temporal compression results will be presented and compared with numerical simulations. Finally, concepts for the further scaling of the presented scheme towards higher output energies and shorter temporal compression will be discussed in section 4.4.

4.1 Introduction to high energy, nonlinear, pulse-compression schemes

High energy, CEP-stable laser pulses with near single optical cycle pulse durations open up a variety of experimental possibilities especially for attosecond and strong-field physics. These pulses allow for example the reliable generation of extreme ultraviolet and soft X-ray radiation with time durations in the attosecond regime [34] and give access to material carrier dynamics in the sub-femtosecond time range [176]. Despite their attractiveness, the generation of few optical cycle pulses directly by a laser or parametric source is extremely challenging. For high energy amplified laser systems the main limitation is the emission bandwidth of the laser gain material and the spectral gain narrowing. While Ti:Sapphire based laser oscillators support output pulse durations down to 5 fs (2 optical cycles) [177, 178], amplified Ti:Sapphire lasers are typically limited to above 15 fs output pulse durations (6 optical cycles) [179, 180]. On the other side, for optical parametric amplifier systems, the shortest possible output pulses are mainly constrained by phase-matching considerations and dispersion control. Despite the recent demonstrations of various parametric systems obtaining 2 optical cycle outputs [111, 127, 181], their widespread use is hindered by the high system complexity and their strong requirements on dispersion control. Therefore, nowadays the common approach for near-IR, few-cycle pulse generation is the use of an additional post-compression scheme, based on nonlinear spectro-temporal reshaping of the driving electric field during high intensity propagation through gaseous media. Hereby, the high energy laser output is first spectrally broadened and afterwards the dispersion introduced by the nonlinear interaction has to be compensated by a dispersion delay line in order to achieve a temporally compressed final pulse. The required, strong nonlinear interaction over a long range is commonly achieved either by propagation through guiding structures such as gas filled hollow-core fibers or by nonlinear self-guiding, also called filamentation. Below, the most common compression techniques will be shortly presented and the obstacles for a direct application driven by the mid-IR, high power OPCPA output pulses, demonstrated in chapter 2 and 3, will be discussed.

4.1.1 Gas filled hollow-core fibers

Noble gas filled hollow-core fibers, also called glass capillaries, were first demonstrated by Nisoli *et al.* in 1997 [182]. The first realisations used

hollow-core fibers with static gas pressures, which typically limited the driving energy to sub-millijoule level, due to the onset of ionisation and higher order nonlinearities. In 2005, Suda *et al.* [183] proposed instead the use of a gradually increasing gas pressure along the hollow-core fiber, enabling the spectral broadening of pulse energies of a few millijoule regime. During propagation in the hollow-core fiber the nonlinear spectro-temporal reshaping is mainly driven by self-phase modulation (SPM), leading to a positive group delay dispersion of the spectrally broadened output pulses (see section 4.2.3 for more information). The required temporal post-compression is normally performed by chirped mirrors and allow compression of near-IR pulses down to sub-2 optical cycles. The shortest compressed Ti:sapphire pulses reached durations of 3.8 fs (1.5-optical-cycles), resulting in 15 μJ pulse energy in the case of static pressure hollow-core fibers [184] and around 1 mJ pulse energy applying gas pressure gradients [185, 186]. The main advantages of hollow-core fiber compression compared to e.g. filamentation are the excellent output beam quality and spectral homogeneity across the beam profile [187]. Additionally, hollow-core fibers applying a gas pressure gradient do permit higher driving pulse energies in the near-IR regime compared to compression by gas filamentation.

4.1.2 Filamentation in gaseous media

Filamentation is a self-guiding process, allowing beam propagation through a medium without diffraction. The transversal confinement of the propagating beam in a dielectric material is typically achieved by a dynamic balance between self-focusing due to the optical Kerr effect and plasma induced beam defocusing [188] (for more details see section 4.2.5). While filamentary propagation can be achieved in solids, liquids and gaseous media, for the temporal post-compression of high energy, near-IR pulses typically filamentation in noble gases is used. The first optical filament of a femtosecond pulse was demonstrated in 1995 by Braun *et al.*, reporting a 20 m long filament in air [189]. In 2004, Hauri *et al.* [190] showed the first application of filamentation for few-cycle pulse compression achieving 5.7 fs durations at 380 μJ energy and 800 nm wavelengths, applying a scheme of two, cascaded filamentation stages. By an in-depth study and optimization of the setup parameters, the compressed pulse duration could be further decreased to 5 fs with sub-millijoule energies [191, 192]. All these results used chirped mirrors for the dispersion compensation and temporal compression. The maximum compressible energy obtained via filamentation is limited for Ti:Sapphire driving lasers to around 1 mJ due to the appearance

of multiple filaments. The biggest advantage of filamentary pulse compression compared to hollow-core fiber compression is the absence of the requirement for the precise coupling into the guiding structure, making the beam alignment simpler and more robust. Additionally compression by filamentation has typically higher energy throughput then hollow-core fibers, due to the absence of coupling losses into the guiding structure [193]. The peak intensities during filamentary propagation are typically in the range of 10^{13} to 10^{14} W/cm^2 [194], which is much higher than peak intensities during guided propagation in hollow-core fibers. Hence, the propagation material is partially ionized and an electron-ion (in gases) or electron-hole (in solids) plasma is formed, promoting additional nonlinear effects like plasma induced frequency blue shift or defocusing. The highly nonlinear light-matter interaction during filamentary propagation leads to a strong spatio-temporal reshaping of the electric field. Under certain conditions the competing nonlinear processes can lead to a temporal shortening of the driving pulse during propagation without the requirement of an additional dispersion control stage. This so called temporal self-compression was first demonstrated in 2005 by Stibenz *et al.* [195] achieving compression from 45 fs down to 7.8 fs duration with 3.8 mJ energy at 800 nm wavelengths (3 optical cycles) by filamentation in a Xenon gas cell. Theoretical calculations from Couairon *et al.* predicted even the possibility for self-compression down to the single-cycle limit [196, 197]. In 2007 the compression technique was extended for longer wavelengths by Hauri *et al.* [198], reporting self-compression driven by a 2 µm laser achieving 18 fs (sub-3-optical cycles) pulse durations. More recently, Mitrofanov *et al.* [199] reported self-compression in the mid-IR range at a center wavelength of 3.9 µm, where the 15 mJ energy driving pulses were compressed from 100 fs down to 35 fs (sub-3-cycles) duration due to filamentation in a nitrogen gas cell.

4.1.3 Mid-IR filamentation in bulk materials

The previously discussed temporal compression techniques for high energy, few-cycle pulses cannot be directly applied to our mid-IR OPCPA system discussed in chapter 2 and 3, due to the absence of sufficient driving pulse energies and therefore insufficient or no spectral broadening. While pulse compression by hollow-core fibers or filamentation in gaseous media is typically driven by pulse energies of a few hundreds of microjoule to millijoule level at hertz to kilohertz repetition rates, the presented mid-IR source delivers 10 µJ to 100 µJ at a much higher repetition rate of 160 kHz. This obstacle can be overcome by using solid-state, dielec-

tric media as propagation materials, which typically exhibit a two to three order of magnitude higher nonlinear refractive index compared to gases. In the last decade there has been a strong development of solid core, optical fibers, with the primary focus on the generation of broad supercontinuum generation [200, 201]. Furthermore, various implementations of temporal pulse compression using propagation in solid core fibers have been demonstrated [202–204]. Nevertheless solid core fiber compression cannot be applied for our mid-IR OPCPA source, since the typical energies for guiding in optical fibers are in the nJ regime and the high energies and Watt-level average powers of our system would damage the fiber guiding structures. The alternative is filamentary propagation in solid, bulk materials. In contrast to filamentation in gases, most dielectric media feature a negative group delay dispersion or anomalous dispersion at wavelengths above 1.5 µm. This fact is beneficial for temporal self-compression, since the interplay between SPM and anomalous dispersion favours pulse compression instead of temporal pulse stretching (see section 4.2.5). Additionally it is reported, that the lengths of filaments in solids increase for driving frequencies in the anomalous dispersion regime [205] and that stable spatio-temporal wavepackets, also called light bullets can be formed during filamentary propagation in case of anomalous dispersion [206]. Furthermore elaborate dispersion compensation setups such as chirped mirrors are still not available in the mid-IR range, making temporal post-compression after the spectral broadening more challenging.

In summary, self-compression due to filamentary propagation in the anomalous dispersion regime of a solid medium seems the best suited approach for the temporal compression of the high power, mid-IR OPCPA output reported in chapter 2 and 3. Previous to the results shown in this chapter, there have been just a few publications about filamentation characteristics in the anomalous dispersion regime of bulk media [206–208], non of which investigated temporal self-compression dynamics.

4.2 Physical effects during filamentary propagation

When a high peak-intensity, femtosecond pulse travels through a transparent medium, multiple competing nonlinear effects occur and reshape the temporal, spectral and spatial distribution of the driving electric field. In the following section a short overview of the most important nonlinear effects and their interactions will be given.

4.2.1 Basic linear and nonlinear effects

Group velocity dispersion Solids, liquids and gases are chromatic dispersive media, which means that the optical refractive index is frequency dependent $n_0 = n_0(\omega)$ and as result the phase velocity v_{ph} and group velocity v_{gr} of propagating electromagnetic waves in the material are also dependent on the frequency. The optical dispersion can be mathematically described by the Taylor expansion of the wavenumber k as a function of the angular frequency ω around a center angular frequency w_0:

$$k(\omega) = \frac{n(\omega)\omega}{c} = k_0 + k'(\omega - \omega_0) + \frac{1}{2}k''(\omega - \omega_0)^2 + \frac{1}{6}k'''(\omega - \omega_0)^3, \quad (4.1)$$

where the first order term k' describes the inverse group velocity and the second order term k'' contains the group velocity dispersion (GVD) or second order dispersion. In the normal dispersion regime of a material, the group velocity dispersion k'' is positive (k''>0) and as a result the low frequency constituents of a pulse travel faster than high frequency ones. In contrast, in the anomalous or negative dispersion regime, where k''<0, high frequencies will move to the front and low frequencies to the back of an initially transform-limited pulse. Most solid materials which are transparent in the visible wavelength range, reach anomalous dispersion in the mid-IR wavelength range with the zero dispersion point (k''=0) lying around 1.2 to 1.5 µm. On the other hand, semiconductors feature normal dispersion for the entire visible up to mid-IR spectral range. In figure 4.1 the variation of the group velocity dispersion k'' for multiple dielectrics, semiconductor materials and gases are illustrated. Note the different order of magnitude of the GVD values for the different material classes (GVD$_{semiconductors}$ >> GVD$_{dielectrics}$ >> GVD$_{gases}$).

Optical Kerr effect The optical Kerr effect describes a quasi-instantaneous change of the material refractive index dependent on the instantaneous and local intensity $I(r,t)$ of the pulse. In an optically isotropic material the Kerr effect can be described to first order by [73]:

$$n = n_0 + n_2 \cdot I(r,t), \quad (4.2)$$

where n_0 is the linear refractive index and n_2 is the second-order refractive index or nonlinear refractive index. The second order refractive index is related to the third order susceptibility $\chi^{(3)}$ by $n_2 = 3\chi^{(3)}/\ (4\epsilon_0 c n_0^2)$, with the speed of light c, and the permittivity of vacuum ϵ_0. In order to estimate the influence of the nonlinear refractive index for the spatio-temporal

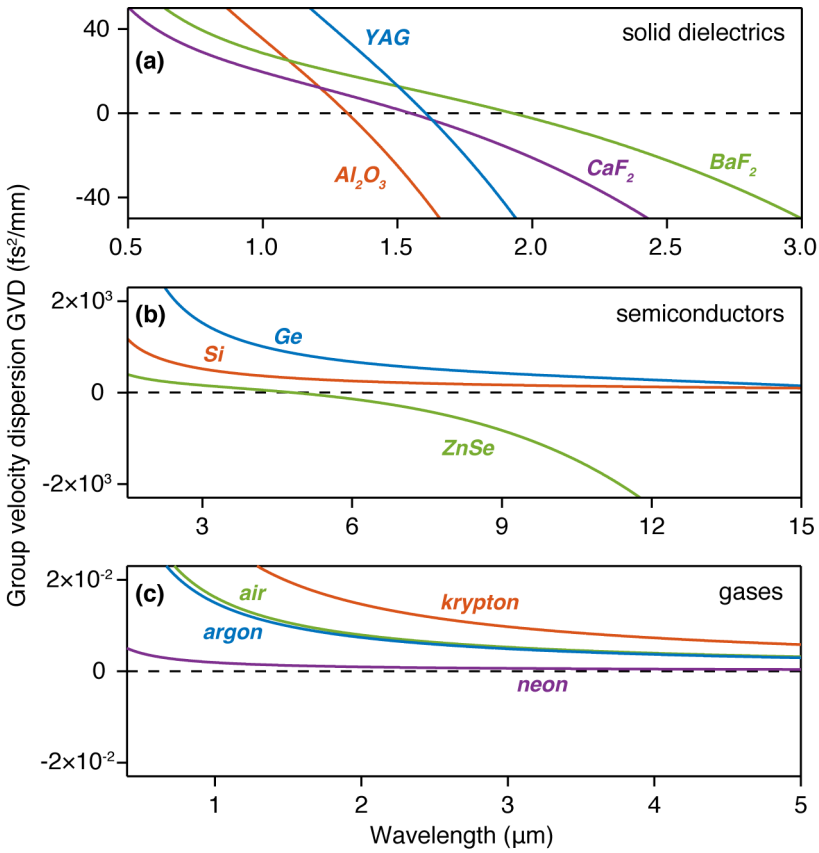

Figure 4.1: Wavelength dependence of group velocity dispersion (GVD=$\frac{\partial^2 k}{\partial \omega^2}$) for: (a) common dielectric solid media, (b) semiconductors and (c) gases. At the mid-IR output wavelength (2.8 to 3.4 μm) of our mid-IR OPCPA system solid dielectrics obtain typically anomalous dispersion (GVD<0), while semiconductors and gases feature normal dispersion (GVD>0). Note the different order of magnitude of the GVD values for dielectrics, semiconductors and gases.

behaviour of the electric field, one can calculate the B-integral, or accumulated maximal nonlinear phase shift $\Delta\varphi_{NL}^{max}$ during propagation through a Kerr medium with the length L:

$$\Delta\varphi_{NL}^{max} = \frac{\omega}{c}\int_0^L n_2 \cdot I(z)\mathrm{d}z. \tag{4.3}$$

Typically, nonlinear effects such as self-phase modulation or self-focusing start to reshape considerably the electric field when the accumulated nonlinear phase overcomes a value of 2π. Higher order nonlinear refractive indices (n_4, n_6, n_8, ..) are typically not considered for nonlinear pulse propagation dynamics.

Multi-photon ionization and plasma generation When the peak intensity of a laser pulse traveling through transparent media reaches intensities of 10^{13} W/cm^2 to 10^{14} W/cm^2, the valence electrons can be excited by optical field ionisation. The ionisation process can take place due to multi-photon or tunnelling ionisation. Which process occurs predominantly can be estimated by the Keldysh parameter [16]. In the case of gases, the atoms or molecules get ionized and the electrons are excited into the vacuum continuum, generating an electron-ion plasma. In contrast, in the case of solids the electrons are promoted from the valence to the conduction band and create an electron-hole plasma. The generation of a free electron plasma leads to a reduction of the refractive index [209]:

$$n \cong n_0 - \frac{\rho(r,t)}{2\rho_c}, \tag{4.4}$$

with the free electron density $\rho(r,t)$ and the material dependent critical plasma density ρ_c above which the plasma becomes opaque. The yield of the electron plasma generation depends linearly on the ionization rate of free electrons $W(I)$, which is strongly peak intensity dependent and scales proportional to $I \cdot K$, where K is the number of driving laser photons necessary to liberate an electron. For example, in the case of a driving laser at 3.1 µm center wavelength (0.4 eV) which propagates through YAG material (E_{gap} = 4.71 eV [210]), the ionization rate would scale highly nonlinear with K=12. Therefore the onset of plasma generation in the case of self-focusing and filamentation generation starts very abruptly once the ionization threshold is overcome. The ionization process is also coupled to absorption losses. On one hand, photons get absorbed during multi-photon or tunnel ionization. On the other hand, absorption of photons occurs during propagating through the plasma due to inverse Bremsstrahlung (for more details see section 1.2.10 in [209]).

4.2.2 Self-steepening

Self-steepening is a temporal reshaping mechanics of an ultrashort laser pulse due to the optical Kerr effect. The intensity dependent change of the refractive index $\Delta n(t) = n_2 \cdot I(t)$ (see equation 4.2) leads to a different propagation velocity of the peak of the laser pulse compared to the leading and trailing edges. For materials with positive n_2 the pulse peak slows down compared to the group velocity of the pulse and a steep edge at the trailing part of the pulse can be formed (see figure 4.2). When the slope of the pulse trailing edge gets infinitely steep, a so called shock wave is formed and can give rise to effects such as wave breaking and temporal envelope oscillations trailing the main pulse [211].

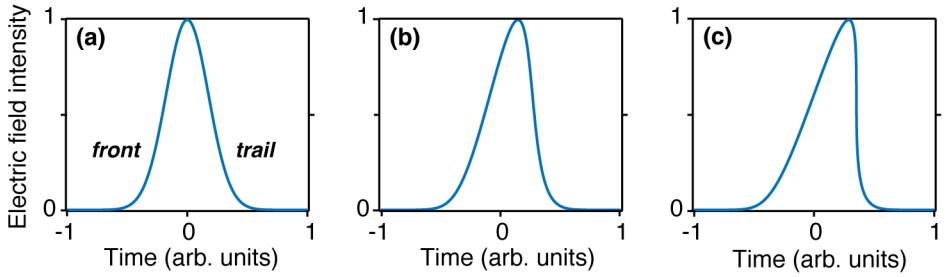

Figure 4.2: Temporal evolution of the laser pulse intensity envelop undergoing self-phase steepening. (a): Initial pulse with a Gaussian-like intensity envelope profile. (b): Steepening of the trailing edge (time>0) due to a smaller propagation velocity of the pulse peak compared to the slopes of the pulse. (c): Formation of a shock wave at the trailing edge of the pulse, where the time dependent intensity gradient converges towards minus infinity.

4.2.3 Self-phase modulation and interplay with dispersion

The temporal phase $\varphi(t)$ of the electric field of a high intensity laser pulse traveling through a medium with a length L is quasi-instantaneously modulated by the optical Kerr effect:

$$\varphi(t) = \varphi_{Lin} + \varphi_{NL}(t) \tag{4.5}$$

With

$$\varphi_{NL}(t) = -\frac{\omega}{c} n_2 I(t) L. \tag{4.6}$$

A more intuitive picture of this so-called self-phase modulation (SPM) is given by the instantaneous angular frequency, which is defined as the time-

derivative of the phase:

$$\omega(t) = \frac{\mathrm{d}\varphi(t)}{\mathrm{d}t} = \omega_0 + \delta\omega(t) = \omega_0 + \frac{\mathrm{d}}{\mathrm{d}t}\varphi_{NL}(t), \tag{4.7}$$

where ω_0 is the angular center frequency and $\delta\omega$ the variation of the instantaneous angular frequency. During self-phase modulation, the time dependent intensity envelope maintains its shape while the instantaneous frequency experiences a modification (assuming neglectable material dispersion). As consequence the spectrum of the transmitted pulse will be reshaped, normally leading to spectral broadening. In figure 4.3 (a) is shown the typical form of the instantaneous angular frequency obtained by high intensity propagation of a Gaussian shaped laser pulse through a Kerr medium with $n_2 > 0$. At the leading edge of the initially transform-limited pulse red frequencies are generated, while on the trailing edge of the pulse blue frequencies are created. The obtained spectral broadening for various values of the maximal nonlinear phase shift φ_{NL} is illustrated in figure 4.3 (b) for a center angular frequency of 0.6 PHz (3.1 µm wavelengths). The spectral modulation pattern occurs due to interferences between the same frequency components (instantaneous frequencies) at different times.

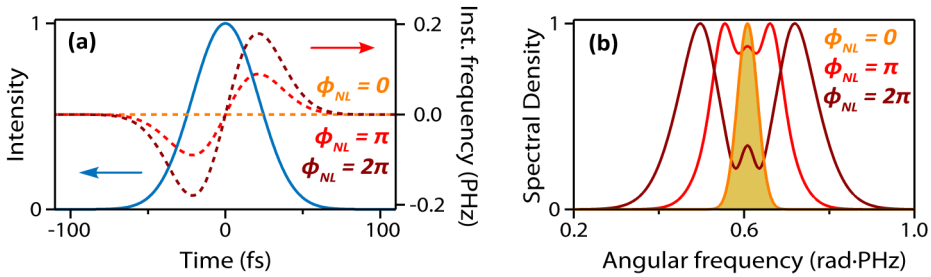

Figure 4.3: Effect of self-phase modulation (SPM) on the temporal and spectral properties of an electro-magnetic pulse. (a): Temporal intensity distribution and by SPM introduced instantaneous angular frequencies for various maximal nonlinear phase shifts φ_{NL}. (b): Frequency spectrum of the initially transform-limited pulse (orange area) and spectral broadening due to SPM (red and dark red lines).

In figure 4.3 (a) it can be seen, that as result of the self-phase modulation effect in materials with n_2>0, the instantaneous angular frequency obtains a steady, linearly growing slope at time positions around the intensity peak (time=0). This behaviour leads to a positive chirp of the laser pulse (front part of the pulse oscillates with lower frequency, than the back part). The positive chirp introduced by the SPM effect will be influenced by the material dispersion, which the pulse experiences while propagating though

matter, resulting in a temporal compression or stretching dependent on the dispersion sign.

The effect of the interplay between SPM and the material group velocity dispersion onto the spectro-temporal evolution of a mid-IR pulse during nonlinear propagation is illustrated in figure 4.4. The displayed results are obtained by a 1-dimensional, slit-step simulation of the Maxwell equation, just considering the effects of SPM and GVD. From the simulated spectrograms (see figure 4.4, a) it can be seen, that SPM alone results in a spectral broadening during propagation with lower frequencies at the front and higher frequencies at the tail of the pulse, while the temporal pulse profile is maintained. In case of normal dispersion in the propagation material (GVD>0), the higher frequencies will be additionally delayed in respect to the lower frequencies, resulting in an increased positive chirp and a temporal stretch of the pulse. In contrast, by propagating in the anomalous dispersion regime (GVD<0), the high frequencies will catch up with the low frequencies, leading to temporal self-compression and a decrease of the spectral chirp. The described relation can be also seen in figure 4.4 (b), where the resulting pulse shapes for each case are illustrated. The difference of the temporal pulse shapes is also coupled to a change of the generated spectral shapes, shown in figure 4.4 (c).

Note that in the rare case of a material with a negative nonlinear refractive index n_2, the introduced chirp via SPM is inverted. Therefore, in this case temporal self-compression caused by the interplay between SPM and GVD, will only occur in the normal dispersion regime (GVD>0) of the material.

4.2.4 Filamentation

When a high intensity laser beam enters a medium, the refractive index will be altered according to the intensity distribution across the spatial beam profile (see equation 4.2). For a Gaussian-like intensity distribution and in materials with a positive nonlinear refractive index n_2, this altering of the refractive index acts like a positive lens, also called optical Kerr lens. If the lensing effect overcomes the intrinsic divergence of the Gaussian beam propagation, the beam will self-focus. The peak power required to reach this condition is described by the critical peak power P_{SF} [212]:

$$P_{SF} = \frac{3.77 \cdot \lambda_0^2}{8\pi \cdot n_0 \cdot n_2}. \tag{4.8}$$

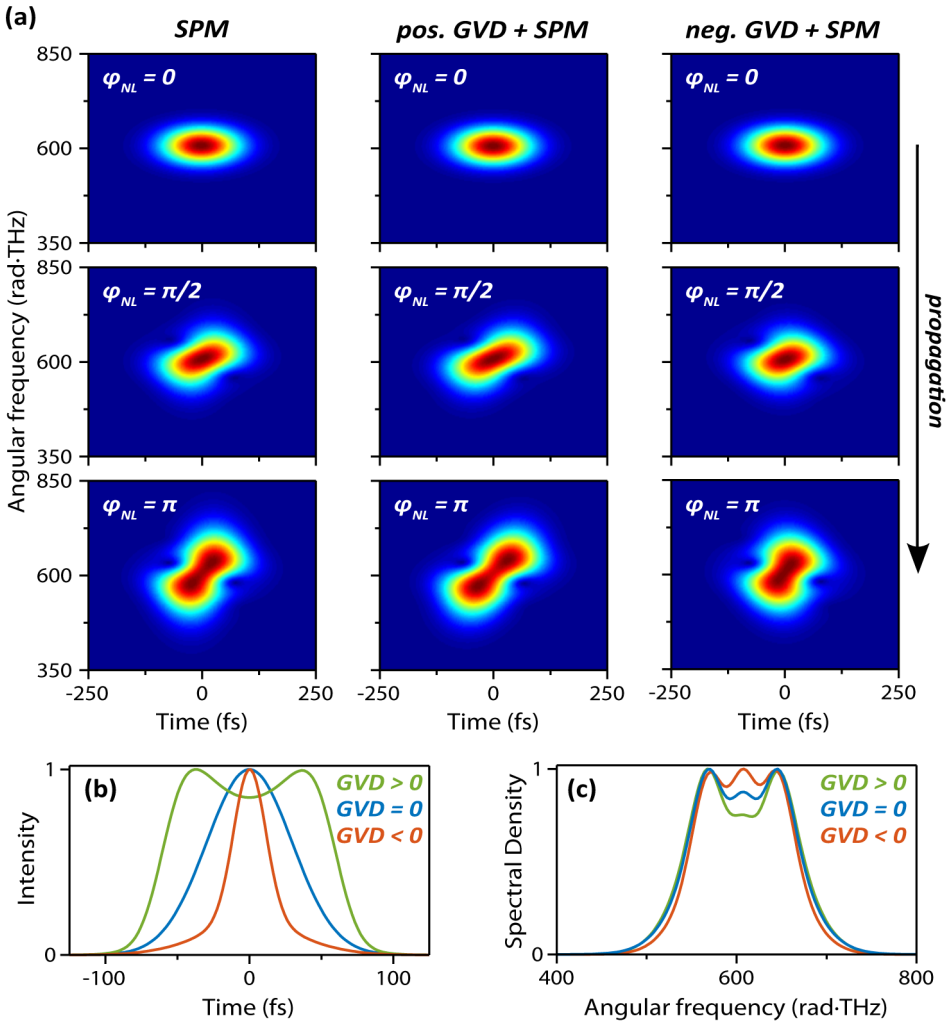

Figure 4.4: Representation of interplay between self-phase modulation (SPM) and group velocity dispersion (GVD) onto the spectro-temporal evolution of a mid-IR pulse during nonlinear propagation. Shown are the simulated spectrograms (a), the resulting temporal pulse envelopes (b) and the spectral shapes (c) for the different signs of GVD and in the case of no GVD. If only SPM acts on the pulse, the temporal pulse shape maintains, while the spectrum is broadened. In contrast, under the additional effect of positive GVD the pulse is stretched in time, while in case of negative GVD the pulse is temporally self-compression. Both cases also influence the spectral shape. The shown results are obtained by a 1-dimensional, slit-step simulation assuming constant peak intensities.

Notice that the critical peak power is not only dependent on the material specific parameters, but also on the center wavelength λ_0 of the driving beam. Self-focusing is a self-enforcing process. This means, the more the beam size shrinks, the higher will be the peak intensity and therefore the stronger will be the Kerr lens effect ($n(r,t) = n_0 + n_2 \cdot I(r,t)$, see equation 4.2). Eventually, the peak intensity of the collapsing beam will reach a point, where the material will be ionized by multi-photon or tunneling ionization. The resulting electron plasma will reduce the refractive index $n(r)$:

$$n(r) \cong n_0 - \frac{\rho(r)}{2\rho_c} \tag{4.9}$$

leading to a plasma induced defocusing effect. The generation of the free-electron plasma $\rho(r)$ scales highly nonlinearly with the square of the instantaneous and spatially dependent field amplitude. By neglecting the time accumulating nature of electron plasma generation and just considering the time averaged peak intensity $I(r)$, the local change of the refractive index can be simplified to:

$$\Delta n_{plasma}(r) \propto -I(r)^{\kappa}, \tag{4.10}$$

where κ is the number of photons necessary to liberate an electron. The self-focusing introduced by the Kerr effect and the plasma induced defocusing can go in a dynamic equilibrium, allowing the beam to propagate with a very small beam waist over a range much longer than the Rayleigh length (see figure 4.5). Hereby the beam waist does not have to be static and is more defined by a dynamically competition between self-focusing and plasma induced defocusing, dependent on the spatio-temporal pulse dynamics. It has been shown, that filamentation in the normal dispersion regime of solids is more likely to undergo repeating focusing-defocusing cycles, while filamentation in the anomalous dispersion regime of solids favours the formation of longer filaments with less focusing-defocusing cycles [205, 206].

This self-guiding process, also called filamentation is characterized by a partially ionized spatial core region and a surrounding region of low ionization. If the pulse peak power is considerably stronger than the critical peak power, the pulse can spatially split during the initial self-focusing process and form simultaneously multiple filaments. In this case, each filament has to contain at least the critical peak power. Multi-filamentation is typically initiated by imperfections in the initial spatial intensity or phase front distribution or by inhomogeneities in the medium. The onset of multi-filamentation is therefore strongly dependent on the spatial quality of the driving beam

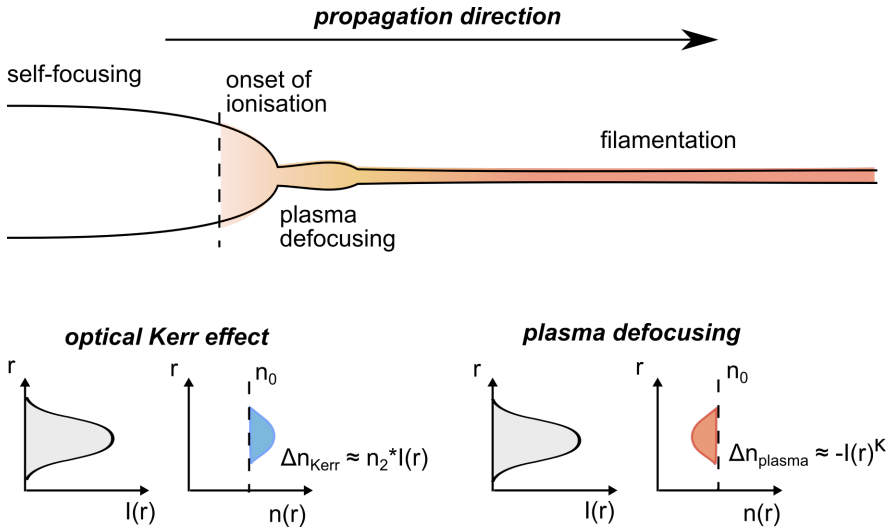

Figure 4.5: Generation and propagation scheme of a filament in a nonlinear medium. The general influences of the optical Kerr effect and the plasma defocusing on the spatial distribution of the refractive index are illustrated in a simplified manner below.

profile and occurs for Gaussian-like beams typically at 10 to 50 times the critical peak power. The regime of multi-filamentation is normally avoided in experiments, since the different spatio-temporal dynamics in each filament lead to unstable spatial and spectral interference pattern at the output of the filamentary propagation.

The length of a filament is normally limited to the point, until the pulse peak power drops below the critical power. This can happen for example due to absorption losses during filamentation, due to spatio-temporal spread and pulse splitting dynamics or due to the transition into another propagation material with a higher critical peak power. Nonlinear propagation of femtosecond laser pulses in air, filaments of several hundreds of meters [213] and up to the km-range [214] have been demonstrated. In contrast, the typical lengths of filaments in dielectric solids are in the few millimeter to centimeter range. The main cause of this discrepancy is the approximately three orders of magnitude higher electron plasma density during filamentation in solids, resulting in much stronger plasma absorption losses. Additionally, the group velocity dispersion in solid is also considerably longer than in gases (see figure 4.1), which can lead to a fast reduction of the peak intensity due to temporal pulse splitting and pulse stretching dynamics during filamentary propagation. Another important difference between gases

and dielectric solids for filamentary propagation is a three order of magnitude higher second-order nonlinearity n_2, resulting in critical powers for self-focusing in the megawatt instead of the gigawatt regime. Interestingly, once the stable filamentation regime is established, the peak intensities in the core of the filament in gases, as well as in solids are very similar, in the range of 10^{13}-10^{14} W/cm^2. Hereby, the diameters of a single filament is typically around 100 µm in gases and around 10 µm in solids [209].

4.2.5 Spatio-temporal reshaping and self-compression during filamentation

Multiple, competing nonlinear effects reshape the electric field during self-focusing and filamentary propagation and give rise to complex spatio-temporal dynamics, which can lead to temporal self-compression even in the regime of normal dispersion. On one side are quasi-instantaneous effects such as self-focusing, self-phase modulation and self-steepening. On the other side are plasma defocusing, and plasma absorption, which are linked to the plasma density and therefore accumulate toward the trailing edge of the driving pulse. Figure 4.6 illustrates the simplified, schematic evolution of the spatial-temporal pulse shape evolution during the formation of a filament.

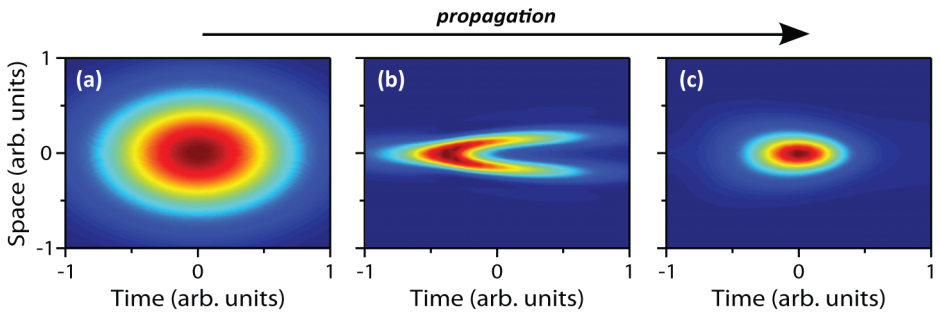

Figure 4.6: Schematic evolution of the spatio-temporal pulse shape during self-focusing and plasma ionization. The interplay between self-focusing and plasma-defocusing can result in temporal self-compression during the highly nonlinear propagation (a, b, c). The shown pulse shape evolution was simulated by Arnaud Couairon and published in [175].

In figure 4.6 (a) is shown the pulse shape at the initial filament formation stage, where the driving pulse has already undergone some self-focusing, but without the occurrence of material ionization. At the point when the ionization threshold is overcome, the generation of free electrons will scale

highly nonlinearly with the local pulse intensity. Since the lifetime of the electron plasma is much longer than the temporal duration of the femtosecond laser pulse, the plasma density will increase strongly toward the trailing edge of the pulse, where plasma defocusing will overcome the self-focusing effect. As a result, the leading edge of the pulse will still undergo further self-focusing, while the trailing edge will defocus on-axis due to plasma defocusing, resulting in a conical V-shape pulse in space-time (see figure 4.6 (b)). During propagation, the two wings at the trailing part of the pulse will further defocus and meanwhile self-steepening will transfer energy from the ascending part of the pulse toward the pulse peak, resulting in an overall temporal compression of the initial driving pulse (figure 4.6 (c)). The dynamics described in this section assume a small or negligible influence of chromatic dispersion and are the main mechanism for pulse self-compression due to filamentation in gases. Simulations predicted the possibility of close to single-cycle compression [196, 197] and experiments at various driving wavelengths confirmed pulse shortening to the few-cycle regime [195, 198, 199, 215]. For more detailed information see [209, 216].

4.2.6 Material choice for mid-IR filamentation experiments

In order to achieve filamentary propagation in a Kerr medium, the peak power of the driving femtosecond laser pulse has to overcome the critical power for self-focusing P_{SF} (see equation 4.8). This critical power is a function of laser pulse parameters (wavelength) as well as material properties (linear and nonlinear refractive index). It is possible to translate the critical peak power in a critical pulse energy E_{SF}, for the system parameters of a specific laser source.

In figure 4.7 is illustrated the scaling of the critical pulse energy (solid red lines) dependent on the material specific refractive indexes n_0 and n_2. The critical pulse energy is calculated by $E_{SF} = P_{SF} \cdot \tau$, assuming the parameters of the mid-IR OPCPA system presented in chapter 2, which are a center wavelengths of 3.1 µm and a pulse duration τ of 55 fs. The vertical dotted lines in figure 4.7 indicate the product of linear and nonlinear refractive index for different materials and the horizontal orange bar indicates the accessible output pulse energies of the mid-IR OPCPA.

From figure 4.7, it can be concluded that various solid dielectric materials (blue dotted lines) could be chosen as target materials in order to drive filamentary propagation with our laser source. In contrast, the nonlinearity in gases (green dotted lines) is too small for filamentation with these laser parameters and semiconductors (purple dotted line) would most likely yield

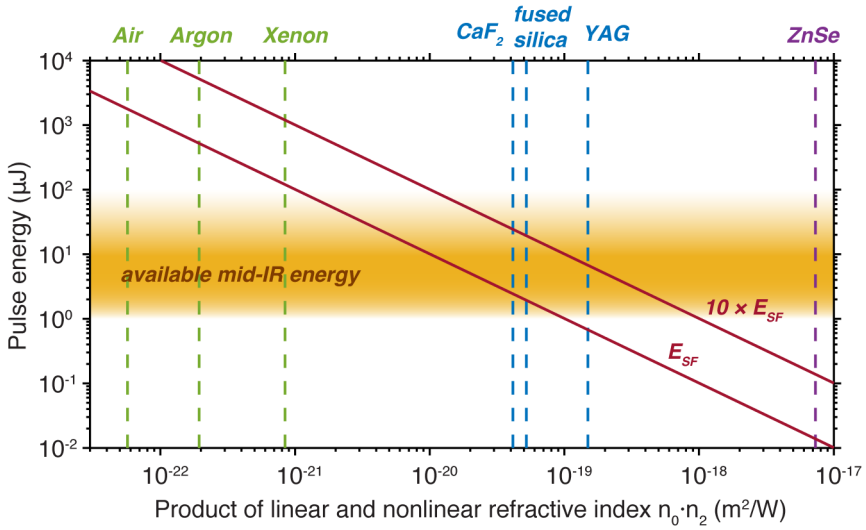

Figure 4.7: Scaling of the critical energy E_{SF} corresponding to the critical power P_{SF} for different materials (red line). Also shown is the behaviour of the critical energy multiplied by 10 ($10\times E_{SF}$). To calculate the critical energy from the critical peak power for self-focusing, a pulse duration of the driving field of 55 fs and a center wavelength of 3.1 µm is assumed. The vertical dotted lines illustrate the product of linear and nonlinear refractive index $n_0 \cdot n_2$ for common gases (green), solid dielectrics (blue) and semiconductors (purple). The horizontal orange bar indicates the accessible output pulse energies of the mid-IR OPCPA. The nonlinear refractive index n_2 for solids is obtained from [73] and for gases at a pressure of 1 bar from [217].

the unstable multi-filamentation regime, since the peak power exceed the critical powers by multiple orders of magnitude. Additional material selection criteria for possible filamentation experiments are a good transparency in the mid-IR range, a high damage threshold which can withstand the peak intensities during filamentation and an anomalous dispersion at the driving wavelength of 3.1 µm. Furthermore the material should possibly be optically isotropic to avoid any rotation effects on the initial polarization during propagation. In table 4.1 are shown the material properties of the most common dielectric solid material, which satisfy all these requirements.

For the experimental study in section 4.3 we choose yttrium aluminium garnet (YAG) as target material due to its high nonlinearity allowing a wide input parameter scanning range. Additionally, it features a broad transmission window spanning from around 250 nm to 6000 nm wavelengths and a

Materials	n_2 in m^2/W	P_{SF} at 3.1 µm	GVD at 3.1 µm
Barium fluoride (BaF_2)	$1.9 \cdot 10^{-20}$	51.4 MW	-57 fs^2/mm
Calcium fluoride (CaF_2)	$3.1 \cdot 10^{-20}$	32.7 MW	-120 fs^2/mm
Yttrium aluminium garnet (YAG)	$7.0 \cdot 10^{-20}$	11.6 MW	-408 fs^2/mm
Sapphire, n_o axis (Al_2O_3)	$3.7 \cdot 10^{-20}$	22.9 MW	-620 fs^2/mm

Table 4.1: Overview of most common dielectric solids usable for mid-IR supercontinuum generation through filamentary propagation. Shown are the material properties of the nonlinear refractive index n_2, the critical peak power for self-focusing P_{SF} and the second order dispersion. Additionally, the properties of the birefringent material Al_2O_3 is given, since it is a common material for bulk supercontinuum generation driven in the visible or near-IR spectral range. The nonlinear refractive indices n_2 for BaF_2 is obtained from [218], for YAG from [219] and for CaF_2 and Al_2O_3 from [73]. The second order dispersion GVD=$\frac{\partial^2 k}{\partial \omega^2}$ is calculated at a center wavelength of 3.1 µm using the Sellmeier equations of BaF_2 [100], CaF_2 [101], YAG [220] and Al_2O_3 [102].

high damage threshold of around 50 GW/cm^2 (reported for 8 ns pulses at a center wavelength of 1064 nm [221]).

In order to estimate the feasibility of YAG for ultrabroadband supercontinuum generation and temporal pulse self-compression, the spectral-temporal dynamics are estimated by means of a simple, one-dimensional split-step simulation of the Maxwell wave equation using the RungeâĂŞKutta method. The results of the simulation are shown in figure 4.8. In this basic simulation any spatial-temporal coupling is neglected and a constant electric field peak intensity during the whole propagation is assumed. The split-step simulation is performed by alternating between the electric field in frequency and in time space. The effect of SPM is applied for every propagation slice in time and the effect of dispersion and linear absorption is calculated in frequency space. As simulation input parameters we choose an estimated maximum peak intensity of $1.3 \cdot 10^{13}$ W/cm^2, an initial pulse duration of 70 fs, a YAG plate thickness of 0.5 mm and a transform-limited spectrum around 3.1 µm wavelength. The chromatic dispersion and group velocity dispersion are obtained by the Sellmeier equation of YAG [220].

In the numerical simulation, illustrated in figure 4.8, it can be seen that after the propagation through a 3 mm thick YAG plate, the initially mid-IR spectrum is considerably broadened and the pulse is self-compressed to a duration of 14 fs. The finding confirms the general suitability of YAG material for mid-IR self-compression experiments. Nevertheless, the simple simu-

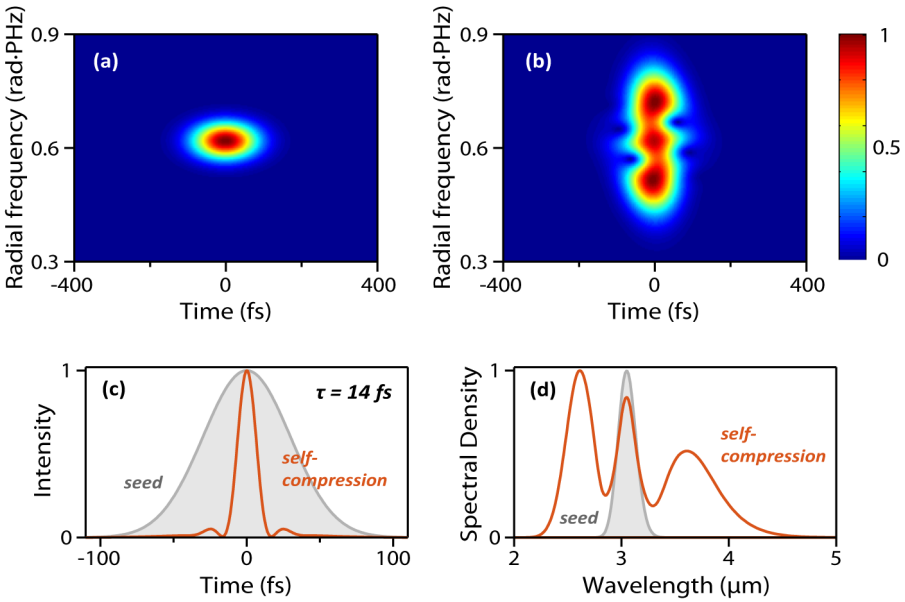

Figure 4.8: Simplified simulation of spectro-temporal evolution of a mid-IR pulse during the nonlinear propagation through YAG material, verifying the general feasibility of temporal self-compression. The 1-dimensional, split-step simulation only considers the propagation effects of SPM and GVD. (a, b): Simulated spectrograms of spectro-temporal pulse shape before (a) and after (b) the nonlinear propagation. Below are shown the temporal profiles (c) and spectral shapes (d) before (grey area) and after (orange line) the nonlinear propagation.

lation model is insufficient, if numerical predictions of the self-compression dynamics are required. A more accurate simulation of the propagation dynamics requires the full 3-dimensional calculation of the propagation dynamics based on the forward Maxwell wave equation. Additionally the effects of self-focusing, multi-photon ionization and plasma effects would have to be taken into account. Such, more comprehensive simulation is described in the following subsection.

4.2.7 Numerical simulation model

The simulation results shown in section 1.3 are obtained by numerical calculations of the filamentary propagation process. These simulations were performed by Arnaud Couairon from the Centre de Physique Théorique, École Polytechnique in France. The simulations are used as a tool for a better interpretation and understanding of the dynamics during pulse prop-

agation. They were also used for a rough estimate of the required optimal YAG crystal lengths and can give insight into processes that are challenging to quantify, such as the origin of absorption losses during filamentary propagation. The simulation is based on a radially symmetric form of the unidirectional propagation equation based on the forward Maxwell wave equation [222]:

$$\begin{aligned}\frac{\partial E(z,\omega,r)}{\partial z} =& i\big[k(\omega)-\omega/v_g\big]E + \frac{i}{2k(\omega)}\nabla_\perp^2 E \\ &+ \frac{1}{2\epsilon_0 c n(\omega)}\big[i\omega P(z,\omega,r) - J(z,\omega,r)\big]\end{aligned}. \tag{4.11}$$

Where $E(z,\omega,r)$ describes the Fourier components of the electric field $E(z,t,r)$ with the radial coordinate r and the propagation direction z. The first term on the right hand side of equation 4.11 denotes the effect of chromatic dispersion via the frequency dependent wavenumber $k(\omega)$ and group velocity v_{gr}. The second term describes the influence of diffraction. The third term expresses the nonlinear response of the medium. The nonlinear polarization accounts for the effects of self-phase modulation, third-harmonic generation, and self-steepening. The current source term $J(z,t,r)$ describes plasma effects including ionization, plasma defocusing, absorption and nonlinear absorption. The spatio-temporal dynamics of the electron-hole plasma density is described by a system of three coupled equations (see equations 3 to 5 in [222]), and includes plasma generation by optical field ionization as well as avalanche ionization. A detailed description of the simulation model is given in [216, 222, 223]. As simulation parameters for the material properties of YAG we used a band gap energy of 6.5 eV, the Sellmeier equation from [224] and a nonlinear, dispersionless nonlinear refractive index n_2=7·10^{16} W/cm^2 [219].

4.3 Experimental results

4.3.1 Spectral characterization

First, a spectral characterization of the generated supercontinuum is performed in order to evaluate the spectral extent and to choose a suitable temporal pulse measurement device, which covers all the spectral range with considerable energy density. For this investigation the mid-IR OPCPA output at 3.1 µm center wavelengths is focused with an uncoated calcium fluoride lens (f=50 mm) onto a 2 mm thick single-crystal yttrium aluminium garnet (YAG) plate. The pump pulse duration was 85 fs and the pulse energy was set to 6.5 µJ, yielding a peak power of 76 MW on target, which is 6.5 times the critical peak power. The formation of a stable filament inside the dielectric is visible and the input spectrum is broadened upto the visible range, observable in the visible conical emission in the far-field after the YAG plate (see inset in figure 4.9). Additionally, the smooth spatial intensity distribution indicates an absence of multi-filamentation, which would be observable by spatial interference structures evolving in time. The supercontinuum was generated continuously over days, without any visible sign of material damage or degradation of the YAG material. For the spectral characterization, the generated supercontinuum was refocused with an uncoated CaF_2 lens onto various, fiber-coupled spectrometers. In order to acquire the entire supercontinuum spectrum, four different spectrometers had to be used. A silicon based CCD spectrometer (HR4000 from Ocean Optics Inc.), an InGaAs CCD spectrometer (NIR256 from Ocean Optics Inc.) and a Fourier Transform Infrared (FTIR) spectrometer (MIR8025 from Newport Corporation) with a thermoelectric cooled InGaAs detector and a liquid nitrogen cooled mercury cadmium telluride (MCT or HgCdZnTe) detector. All four spectrometers were intensity and spectrally calibrated. The spectral energy density distribution of the generated supercontinuum is shown in figure 4.9.

The supercontinuum spectrum spans 3.3 octaves, from 450 nm to 4500 nm wavelength and shows high spectral energy densities from 2 pJ/nm to 10 nJ/nm over the full spectral range. The spectral characterisation of the supercontinuum is reported in [225] and was at the time of publication the broadest, demonstrated supercontinuum generated by filamentation in a bulk medium. The asymmetric spectral broadening between the lower and higher frequencies originates from the interplay between various nonlinear processes. While mainly self-phase modulation causes a symmetric spectral broadening, other effects such as self-steepening and plasma

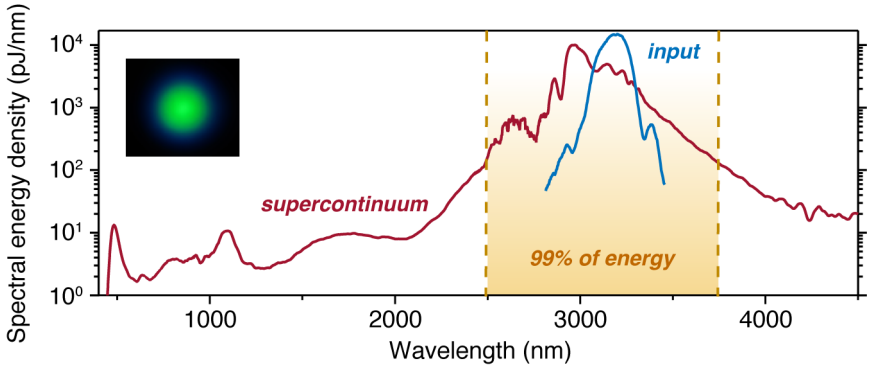

Figure 4.9: Measured seed spectrum (blue line) and supercontinuum spectrum (red line) obtained after filamentary propagation of the mid-IR seed pulse through a 2 mm thick YAG plate. The supercontinuum spans 3.3 frequency octaves and features high spectral energy densities from 2 pJ/nm up to 10 nJ/nm. For the further temporal investigation of the self-compression behaviour we focus on the spectral range from 2500 nm to 3700 nm where 99% of the pulse energy is contained (orange area).

blueshift cause a much stronger extension of the supercontinuum towards higher frequencies until the absorption edge of YAG at around 400 nm wavelengths. In contrast, on the low frequency side the spectral density vanishes with an exponential-like decay behaviour. Note, that the overall spectral shape of the supercontinuum is smooth, without signs of interferences, indicating that no major temporal pulse splitting happens during the filamentary propagation. The spectral peak at 1100 nm can be attributed to third harmonic generation and the peak at 500 nm can be identified as the dispersive wave, which is the wavelength which travels with the same group velocity as the driving field. An in-depth analysis and discussion of the dispersive wave and the implications for the angular momentum spectrum can be found in the PhD thesis of of my colleague Francisco Silva [226] and in the paper from Silva *et al.* [225].

For the following investigation of the temporal self-compression behaviour during supercontinuum generation, we focus only on the mid-IR spectral range between 2500 nm and 3700 nm wavelength, since 99% of the overall pulse energy is concentrated in this area (orange shaded area in figure 4.9).

4.3.2 Temporal pulse measurement

Due to the interplay of various nonlinear effects during filamentation, the output pulse duration will depend on multiple experimental parameters such as, input pulse duration and energy, YAG plate thickness, beam caustic and respective distance between focusing lens and YAG plate. Some of these parameters were fixed, in order to narrow down the parameter space and to allow a systematic study of the self-compression behaviour. According to preliminary simulation results indicating parameters for best compression, the YAG plate thickness was set to 3 mm. The input pulse energy was set to 3 µJ and the pulse duration to 70 fs, which was the shortest available duration at the time of this experiment. The obtained peak power of 55 MW is 5 times larger than the critical peak power of YAG. The focusing lens was changed to a f=100 mm lens in order to reduce the numerical aperture. The obtained $1/e^2$ beam waist was 20 µm. Lenses with a focal lengths of 50 mm and 75 mm were also tried, but result in worse temporal compression. The measurement setup is illustrated in figure 4.10. The generated supercontinuum was collimated behind the YAG plate by a silver-coated, concave, spherical mirror and directed towards a second-harmonic frequency resolved optical gating (FROG) device. This FROG device is specially designed for broadband, ultrashort pulse measurements in mid-IR regime (for a detailed description see appendix B or [227]). On one side, the FROG device features apart from a pellicle beamsplitter only reflective optics to avoid additional dispersion on the investigated pulses. Furthermore a 0.3 mm thick silver gallium sulfide ($AgGaS_2$) crystal is chosen as SHG crystal, supporting a 1600 nm wide phase-matching bandwidth at a center wavelength of 3100 nm, therefore covering the entire region of interest.

The remaining free parameter is the position of the YAG plate in the beam waist, influencing the peak intensity as well as the beam divergence of the pump beam when hitting the front surface of the YAG plate. To investigate the self-compression dynamics, the YAG plate was scanned over a 6 mm long range in 0.5 mm steps trough the focus. At each YAG position a FROG trace was recorded, the pulse duration was retrieved and the supercontinuum spectrum was measured by means of the FTIR spectrometer. Figure 4.11 and 4.12 show the experimental results of the temporal and spectral measurements, overlaid by result of the numerical simulations performed by Arnaud Couairon. For details on the simulation code the reader is referred to section 4.2.7 and for the detailed information on the applied simulation parameters to Hemmer *et al.* [175]. The origin point of the plate positions shown in figure 4.11 and 4.12 is referred to the focal plane, which

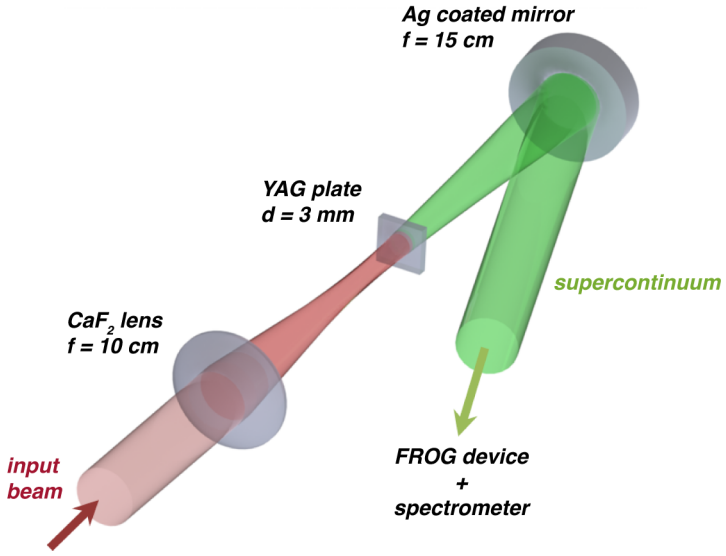

Figure 4.10: Layout of the self-compression setup. The input mid-IR beam at a center wavelength of 3.1 µm is focused by a 10 cm focal length CaF_2 lens into a 3 mm-thick YAG plate. The beam emerging from the plate is collimated with a 15 cm focal length, silver coated mirror and directed toward diagnostic tools. The pulse duration is measured with a SHG-FROG device and the spectrum with a FTIR spectrometer featuring a nitrogen cooled MCT detector. The YAG plate can be moved along the beam propagation axis to investigate the behavior of the self-compression process. Figure is similarly published in [175].

is obtained by a measured beam caustic in air. The value of the plate positions represents the distance of the front facet of the YAG plate with respect to the focal plane; bigger YAG positions are further away from the focusing lens.

4.3.3 Evolution of compression dynamics

Figure 4.11 (a) shows the evolution of the retrieved temporal pulse shape, while the YAG plate is scanned along the beam propagation direction. A strong reshaping and shortening of the pulse can be observed at positions close to the focus. The self-compression seems well behaved, with the absence of strong pulse splitting. Nevertheless small splitting dynamics can be observed at the plate positions around -1 mm. From the retrieved temporal pulse shapes, the FWHM pulse durations are extracted and shown in figure 4.11 (b) together with an overlay of the expected pulse durations

obtained by the numerical simulations. The driving pulse duration of 70 fs shrinks during self-compression down to durations between 35 fs and 45 fs, with the shortest pulses at the onset of temporal pulse splitting around the focal plane at a YAG position of 0 mm. It can be seen, that the temporal self-compression dynamics agree quantitatively very well with the simulation results.

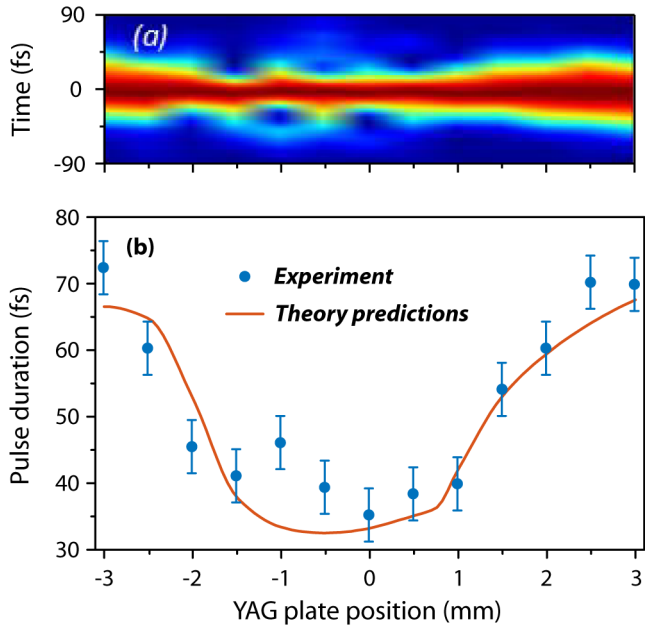

Figure 4.11: Measured and simulated evolution of the pulse duration as the seed pulse undergoes self-compression as the YAG plate is scanned through focus. (a): Retrieved experimental temporal profile of the pulse intensity as a function of the YAG plate position. The temporal pulse profile is measured by a SHG-FROG device. (b): Experimentally measured (black dots) and simulated (blue line) evolution of the pulse duration as a function of YAG plate position through the beam focus. Figure is similarly published in [175].

The evolution of the measured spectrum as a function of the YAG plate position is pictured in figure 4.12 (a). A clear spectral broadening and red shift at plate positions close to the focus plane can be seen. The seed spectrum broadens from around 600 nm width at $1/e^2$ to nearly 1000 nm width at $1/e^2$. At the same time the center wavelength experiences a red shift by up to 300 nm from 3100 nm to 3400 nm. The numerical simulation can reproduce qualitatively the general behaviours of the spectral red shift and broadening, but the amount of red shift is underestimated (see

figure 4.12 (b)). The maximal simulated red shift is 50 nm compared to a shift of 300 nm of the experimental behaviour. This discrepancy can be attributed to the fact, that many of the material properties, which are used as the input parameters for the simulation, are not exactly known in the mid-IR regime. For example, the absence of information about the Raman-response in YAG for the mid-IR regime makes a more accurate simulation complicated. Numerical tests performed by our collaborator Prof. Arnaud Couairon, varying the simulation input parameters for the Raman response revealed that the simulated spectral red shift could be moderately increased, when the frequency shift in the Raman response was modulated considerably. At the same time, the simulated pulse durations of the self-compressed pulses were not significantly affected, indicating that in order to find the optimum self-compression parameters for our experimental conditions, the exact knowledge about the Raman-Kerr response is not necessary.

Since the measured and simulated spectral-temporal evolution of the self-compressed pulse match qualitatively well, the simulation can also be used for a deeper analysis of the propagation process, such as the origin of absorption losses during filamentation, discussed in section 4.3.5.

4.3.4 Shortest self-compressed pulse duration

Via fine adjustment of the YAG plate position around the focal plane, the shortest, self-compressed output pulse yielding a FWHM pulse duration of 32 fs (2.9-cycle) can be obtained. Figure 4.13 (a) and (c) show the retrieved temporal pulse shapes of the input pulse and of the self-compressed pulse together with the instantaneous frequencies. Figure 4.13 (b) and (d) represents the retrieved spectra in black lines and the measured spectra as shaded areas, respectively.

During self-compression, the spectral bandwidth (see figure 4.13 (b) and (d)) gets strongly broadened from 430 nm to 620 nm bandwidth at $1/e^2$. Meanwhile the center wavelength shifts from 3100 nm to around 3250 nm. The qualitatively good agreement between the measured and retrieved spectra proves the reliability of the retrieved spectral-temporal pulse information. The input pulse duration is compressed from 70 fs (6.8 optical cycles) down to 32 fs (2.9 optical cycles). Meanwhile the pulse energy drops from 3 µJ input energy to 2 µJ after filamentation. While the instantaneous frequency of the input pulse is rather flat, the self-compressed pulse obtains a small uncompressed linear instantaneous frequency in the main peak, indicating further compressibility. Assuming one could compensate

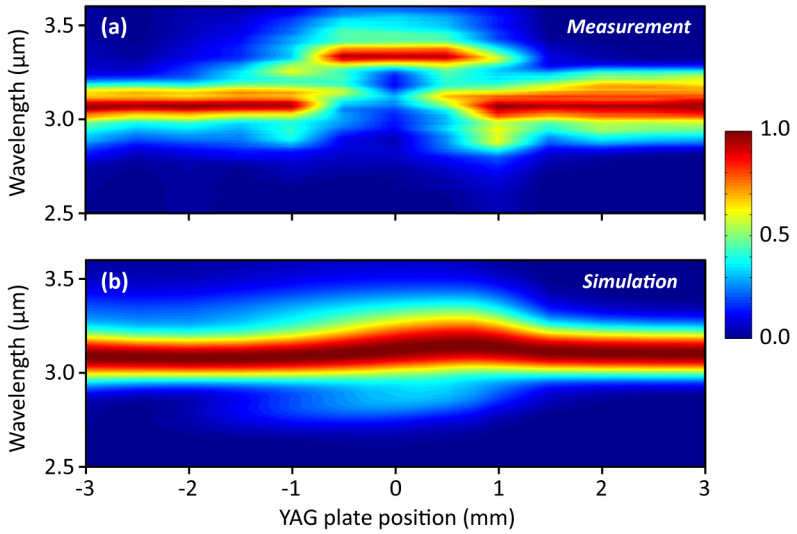

Figure 4.12: Measured and simulated spectral evolution of the pulse undergoing self-compressed while the YAG plate is scanned through the focus. (a): Measured evolution of the spectral intensity profile as a function of the YAG plate position. (b): Simulated evolution of the spectral intensity profile. The plate position (abscissa axis) refers to the position of the front surface of the YAG plate in respect to the focal plane of the beam. Figure is similarly published in [175].

all higher chirp orders, the pulse duration could be even shortened to the transform-limited pulse duration of 29 fs (2.7 optical cycles).

4.3.5 Usability for strong-field experiments

An important parameter affecting the usability of the compression technique, is the transmission efficiency after compression. In figure 4.14 (a) are shown the measured transmission efficiencies dependent of the YAG plate position in the focus. For large beam sizes or using a collimated pump beam a transmission of around 83% is measured, corresponding to the Fresnel losses of the uncoated target. When the YAG plate is scanned through the focus, the transmission efficiency drops to around 65%. The transmission curve can be well reproduced by the numerical simulations (see figure 4.14, a). Moreover the calculations can be used to explain the origin of the additional losses during self-compression. According to the simulation, up to 14% of the pulse energy is lost due to the ionization process and 9% is lost due to absorption in the electron-hole plasma which is

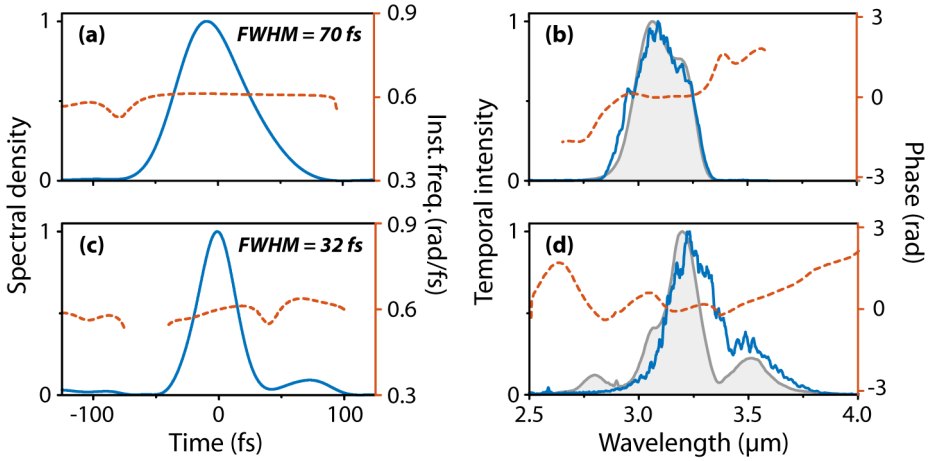

Figure 4.13: Measurement of spectro-temporal profile of the shortest self-compressed pulses. (a): Retrieved temporal intensity profile of the mid-IR seed pulse yielding a FWHM pulse duration of 70 fs (6.8-cycles). (b): Measured (black line) and retrieved (shadow) spectra of the seed pulses. (c): Retrieved temporal intensity profile of the self-compressed pulse yielding a FWHM pulse duration of 32 fs (2.9-cycle). (d): Measured (black line) and retrieved (shadow) spectra of the self-compressed pulses.

created by the material ionization (see figure 4.14, (b)).

Notice that the best compression position is around 0 mm plate position, while the highest plasma related losses are at a plate position of -1.5 mm. This shift can be explained by the different divergence the pump beam has, when entering the Kerr lens has to overcome in order to form a filament. The converging pump beam at negative plate positions favors the Kerr lens focusing and therefor allows a quick filamentary formation and higher overall ionization and plasma losses. In contrast at positive plate positions, the pump beam enters the YAG plate with a divergent wavefront, resulting in a longer path until the Kerr lens focused beam reaches the intensity to form a filament, therefore yielding less overall ionization and plasma losses.

The overall transmission efficiency of 65% to 70% at the best compression position is comparable to the efficiencies of other temporal compression techniques commonly used for Ti:sapphire systems. For example temporal compression using gas-filled capillaries achieve typically transmission efficiencies of around 50%, while compression based on filamentary propagation in a gas cell obtain normally efficiencies around 90% [193]. For a further increase of the transmission efficiency of the presented self-

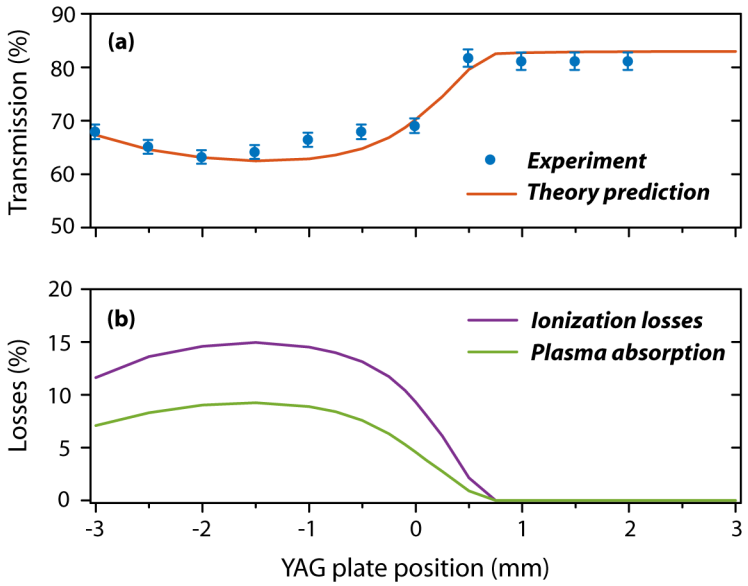

Figure 4.14: Measured and simulated transmission of the mid-IR driving pulse through the self-compression setup as a function of the YAG plate position. (a): Simulated (blue line) and measured (squares) transmission reveal the high efficiency of the process of around 65 to 70% for best pulse compression (compare figure 4.11). By application of an anti-reflection coating onto the YAG plate, the losses could be reduced by around 15%, yielding a possible overall transmission efficiency of 80%. (b): Calculated contribution of ionization (black curve) and plasma absorption (red curve) to the transmission losses as a function of the YAG plate position. Figure is similarly published in [175].

compression method, the YAG plate could be anti-reflection coated, possibly reaching an overall transmission efficiency of around 80%. Another method to reduce the Fresnel losses, could be performed by placing the YAG plate under the Brewster angle, with the disadvantage of a possible angular dispersion of the output beam.

Important beam characteristics for the usability of the self-compressed pulses for experimental applications are energy stability, beam profile and focusability. Therefore, the shot-to-shot energy stability of the self-compressed pulses are investigated with a fast photodiode over the course of 10 minutes, which reveals a standard deviation of 0.8% fluctuation of the 2 µJ output energy. This value is comparable to the stability of the driving field, implying that the single filament propagation does not introduce additional energy instabilities. Furthermore, the spatial beam profile after

self-compression is measured using the knife-edge technique, confirming a spatial profile similar to the driving beam. The good focusability of the beam is confirmed indirectly by the realization of strong-field ionization experiments in a low density Argon gas jet, which required peak intensities in the 10^{14} W/cm^2 range. The results of this high intensity ionization experiment which exploits the self-compressed, mid-IR pulses are reported in [128].

Another important beam characteristic for laser pulses in the sub-2 to sub-3 optical cycle regime, is the question of CEP stability. Especially for such short pulse durations, the effect of the electric field is very different from the field envelop. It was demonstrated that filamentary propagation can maintain the relative CEP stability, but adds a driving intensity dependent CEP offset phase, assuming the filamentation is driven in the stable single-filamentary regime [87]. Since our driving mid-IR OPCPA source provides intrinsically CEP-stable pulses, the self-compressed pulses should therefore also be CEP stable. The CEP-stability of the self-compressed pulses was verified by means of an f-to-2f interferometer. A CEP-stability of 250 mrad rms fluctuations over 11 minutes was measured, indicating the suitability of the self-compressed pulses for CEP-sensitive few-cycle experiments. The details of this CEP-measurement where reported by Thai *et al.* [68] and are not subject of this PhD thesis.

4.3.6 Power scalability

In order to investigate the power scalability of the temporal self-compression process the pulse energy onto the target is increased from 3 µJ to 15 µJ, which was the highest available output energy of the mid-IR OPCPA system at the time of the experiment. Meanwhile, the beam focusing conditions where maintained such as in section 4.3.2. At the YAG plate position of around 0 mm, where in section 4.3.3 the best temporal compression is achieved, multi-filamentation was observed. This is not surprising, considering that 15 µJ pulse energy and 70 fs pulse duration yield a peak power of 214 MW, which is 18 times the critical peak power in YAG (see table 4.1). Nevertheless, by moving the YAG plate further away from the focusing lens (plate position around 2.5 mm) a single, stable filament could be again achieved.

The self-compressed pulses were measured with the SHG-FROG device (see appendix B) and the retrieved temporal shape and spectral information of the shortest pulse are shown in figure 4.15. At the condition of the high input energy, the input pulse duration of 70 fs is compressed down to 38 fs

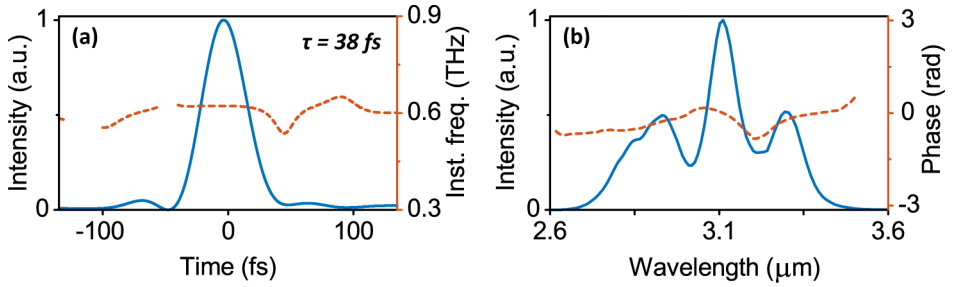

Figure 4.15: Shortest mid-IR, self-compressed pulse applying high driving energies of 15 µJ (seed pulse similar as in figure 4.13). (a): Retrieved temporal intensity profile (blue) and instantaneous frequency (orange) of the self-compressed pulse yielding a FWHM pulse duration of 38 fs (3.7-cycle). (b): Retrieved spectrum (blue) and spectral phase (orange) of the self-compressed pulses.

duration, which is equal to 3.7 optical cycles at 3.1 µm center wavelength. Meanwhile an output pulse energies of 10 µJ could be measured, yielding a similar transmission efficiency as in the low energy case of around 65% (see section 4.3.4). The spectral $1/e^2$ width broadens from the seeded 430 nm to 700 nm.

The further energy scaling of the presented self-compression method by filamentation in YAG toward the 100 µJ energy-levels will be limited by the onset of multi-filamentation and material damage. A detailed discussion about alternative mid-IR pulse-compression approaches, which could overcome this limitation, are given in the following section.

4.4 Summary and outlook

4.4.1 Summary and most recent advances in the field

In conclusion, we have demonstrated one of the first two-fold temporal self-compression experiments of mid-IR femtosecond pulses at 3.1 µm wavelength, exploiting filamentation in the anomalous dispersion regime of YAG. Pulse durations of 2.9 optical cycles with 2 µJ energy and 3.7 optical cycles with 10 µJ of energy could be achieved. A good agreement with numerical simulations performed by a 3-dimensional, nonlinear propagation code permits insight on the involved nonlinear processes and underlying dynamics. The compact and robust compression scheme is a suitable, novel approach for few-cycle compression of high repetition rate, mid-IR pulses in the tens

of µJ energy range, closing the gap between solid core PCF fibers, usually used for nJ energy ranges and on the other side gas filled hollow-core fibers and gas filaments, typically applied for mJ pulse energies.

Our investigation has strongly contributed to the fast growth of the field of filamentary propagation in the anomalous dispersion regime of media. In the last few years, there have been multiple demonstrations of self-compression using filamentation in the anomalous dispersion regime of bulk media, extending the experimental range towards different driving wavelengths and propagation materials. An overview of these studies is given in table 4.2. The interested reader is also refered to a review published in 2016 by Couairon *et al.* [222], which highlights the recent advances in the understanding of filamentation in the anomalous dispersion regime of solids.

Despite the recent advances, self-compression in the anomalous dispersion regime of solids remains a very novel technique and further investigations are required to be able to reach the single optical cycle limit and to scale the usable pulse energies to the 100 µJ range. In the mid-IR range above 3 µm wavelength there has been so far just one other experimental realization by Heese [228] in BaF_2 which only achieved self-compression down to 5 optical cycles at 6 µJ pulse energy.

4.4.2 Outlook for further scalability

One possibility for the further power scaling would be the use of other solid Kerr media with lower second order nonlinearities n_2 as propagation material in order to avoid multi-filamentation at high driving energies (see table 4.1). However, since the exact damage threshold of most materials is unknown for femtosecond pulses in the mid-IR range, it is unclear which solid Kerr material could withstand mid-IR filamentary propagation with pulse energies as high as 100 µJ while simultaneously allowing temporal self-compression. Shumakova *et al.* overcome this problem by interrupting the nonlinear pulse propagation in a solid before the self-focusing beam could collapse and form a filament [230] and therefore limiting the maximal peak intensity. This method allowed the self-compression of 20 mJ driving energy pulses to 2.3 optical cycles at 3.9 µm wavelengths [230]. Nevertheless, this approach is likely unsuited for the temporal self-compression of 100 µJ range pulses, since the lower driving peak intensities at absent filamentary propagation would probably not yield sufficient nonlinear coupling with the host material to support ultra-broadband supercontinuum generation.

Reference	Material	Energy / Wavelength	Pulse duration
Filamentary self-compression in anomalous dispersion of bulk			
Hemmer *et al.*, 2013 [175]	YAG	2 µJ at 3.2 µm	32 fs (2.9 cycles)
		10 µJ at 3.2 µm	38 fs (3.7 cycles)
Heese, 2012 [228]	BaF_2	6 µJ at 3.4 µm	56 fs (4.9 cycles)
Durand *et al.*, 2013 [205]	Fused silica	20 µJ at 1.9 µm	20 fs (3.1 cycles)
Liang *et al.*, 2015 [229]	CaF_2	8.5 µJ at 2.2 µm	14 fs (1.8 cycles)
	BaF_2	6 µJ at 2.2 µm	23 fs (3.1 cycles)
Self-compression without formation of a filament in anomalous dispersion of bulk			
Shumakova *et al.*, 2015 [230]	YAG	20.000 µJ at 3.9 µm	30 fs (2.3 cycles)
Broadening in normal dispersion regime and compression in anomalous dispersion regime of bulk			
Lanin *et al.*, 2014 [231]	GaAs (superc.) BaF_2 (compr.)	1.7 µJ at 5.9 µm	29 fs (1.5 cycles)

Table 4.2: Overview of investigations about the temporal self-compression behaviour of mid-IR pulses driven in the anomalous dispersion regime of solid media (GVD<0). We don't consider studies applying external guiding structures like solid-core fibers or waveguide as well as studies where the driving wavelength lies in the normal dispersion regime. Given are the used solid material as well as the driving energy, center wavelengths and the temporal duration of the self-compressed pulses.

On the other side, to optimize temporal self-compression of mid-IR pulses closer towards the single-cycle limit, one could employ a cascaded self-compression scheme using multiple, independent filamentation stages. Two self-compression stages after each other would give the possibility of an intermediate dispersion adjustment and an individual control of the beam focusing conditions for each compression stage. In the case of mJ level, near-IR driving pulses such cascaded compression schemes are already demonstrated exploiting filamentation in gases [197] or coupling in gas-filled capillaries [184], yielding sub-2 optical cycle pulse durations.

The simultaneous upscaling to higher pulse energies and shorter time durations of the self-compressed mid-IR pulses presented in this thesis, could be performed by the implementation of a post-amplification stage featuring a frequency dependent parametric gain. In this way, the spectral shape could be individually tailored, possibly yielding a shorter pulse duration. The idea could be realized by applying the frequency domain optical parametric amplification (FOPA) scheme [163]. A sketch for a possible FOPA setup is illustrated in figure 4.16 (a). In the FOPA method, the seeded supercontinuum spectrum is spatially spread in the Fourier plane of a grating-based 4f-setup, which inherently stretches the few-cycle input pulse to picosecond durations in each focal spot in the Fourier plane, allowing parametric amplification pumped by picosecond pulses. Moreover, the amplified spectrum can be spectrally reshaped, if a spatially tailored pump pulse for the amplification in the Fourier plain is used. Such modification of the spatial pump profile can be achieved via for example special aspheric telescopes using Powell lenses [232]. Figure 4.16 (b) shows the spectral shape of the supercontinuum obtained in section 4.3 overlaid with an example of a spectrally modulated, parametric gain curve. Note, that the huge variations of the gain curve are experimentally simple to achieve due to the highly nonlinear relationship between parametric gain and pump peak intensity (see equation 2.13 in section 2.1.2). The illustrated spectral gain would result in a considerable spectral broadening of the seeded supercontinuum, which is illustrated in figure 4.16 (c). In consequence, the transform-limited, FWHM pulse duration of the amplified supercontinuum would shrink to a sub-one cycle duration (7.1 fs). For this gedankenexperiment we only considered the supercontinuum spectral region, which lies in the anomalous dispersion region of YAG (at wavelengths above 1.6 µm), allowing a relatively good temporal compressibility of all spectral components (see section 4.2.3).

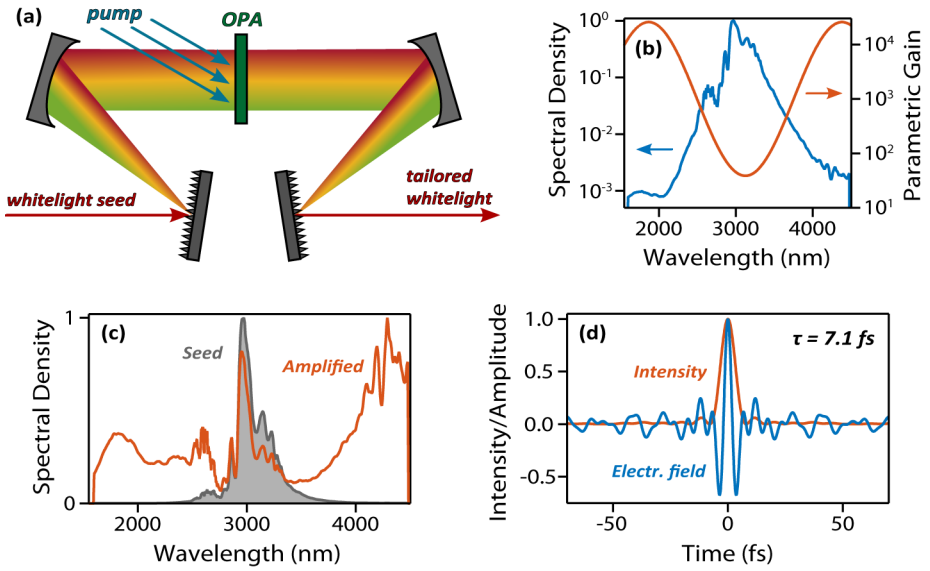

Figure 4.16: Proposal for a scheme, which would allow the controlled spectral tailoring of the self-compressed pulses via the FOPA technique giving access to sub-cycle pulse generation. (a): Scheme of FOPA setup. (b): Measured supercontinuum spectrum and proposed parametric gain of the OPA process. (c): Calculated supercontinuum spectra before and after amplification in FOPA setup in linear scale. (d): Transform-limited temporal pulse shape of the supercontinuum after amplification in the FOPA setup yielding a FWHM pulse duration of 7.1 fs.

4.4.3 Other, novel approaches for few-cycle pulse generation

Aside from filamentation in the anomalous dispersion regime of solids, there have been proposed other compression schemes, which could allow efficient compression of mid-IR, µJ-energy range laser pulses. Bache *et al.* proposed that exploiting non-critical, strongly phase-mismatched cascaded second-harmonic generation (SHG) in mid-IR nonlinear frequency conversion crystals could lead to supercontinuum generation and pulse compression [233]. Numerical simulations assuming initial pulse parameters close to the output of our mid-IR OPCPA, suggest the compressability of pulses at 3 µm wavelengths from 50 fs down to 15 fs (1.5 optical cycles) pulse duration. In recent experimental studies Bache *et al.* could already demonstrate the broadening of 40 µJ, 70 fs pulses at 3.6 wavelengths to an octave spanning spectrum, but the verification of mid-IR temporal compression by means of this method is still pending [234].

Another novel compression technique for µJ-level, mid-IR pulses could be temporal self-compression by guided propagation in gas-filled hollow-core photonic crystal fibers (HC-PCF). Conventional gas-filled hollow-core glass capillaries (see section 4.1.1) require large ($\sim$200 µm) bore diameters to achieve low transmission losses, which implies pulse energies in the mJ-regime to obtain sufficient peak intensities to drive spectral broadening for temporal compression. In contrast, kagomé-structured HC-PCFs allow the downscaling of the bore area by an order of magnitude at high transmission efficiencies, enabling efficient spectral broadening at pulse energies around 10 to 100 µJ. Moreover kagomé-structured HC-PCFs permit pulse propagation in the anomalous dispersion regime and a strong tunability of the dispersion relation in dependence of the applied gas pressure, enabling temporal soliton generation and self-compression due to the interplay of SPM and anomalous dispersion [235]. Few-cycle, temporal self-compression exploiting this technique was demonstrated at multiple visible and near-IR wavelength, but still not in the mid-IR spectral range. For example Mak *et al.* showed the compression of 10 µJ energy pulses at 800 nm wavelength down to 6.8 fs (3 optical cycles) [129], and recently Balciunas *et al.* reported the self-compression of 35 µJ energy pulses at 1.8 µm wavelength down to 4.5 fs duration (sub-2 optical cycles) [130]. A good overview for the interested reader about the state-of-the-art and the concepts of ultrafast nonlinear optics in gas-filled HC-PCF can be found in [236, 237].

Chapter 5

Conclusion and outlook

The presented thesis focuses on the improvement and development of a unique, few-cycle, high power, mid-IR radiation source based on the OPCPA architecture. The three main achievements of the thesis work are: (i) the output peak-power upscaling to the GW-level, (ii) the pulse post-compression to the few-cycle regime and (iii) the construction of a multi-color module providing optically synchronized femtosecond outputs from the ultraviolet up to the mid-IR spectral range.

This chapter gives a comprehensive summary and conclusion of the thesis, followed by a general outlook of the scientific fields it could impact. More specific summaries and discussions about future prospects can be found at the end of the respective thesis chapters (2.4, 3.4, 4.4).

5.1 Summary

High power, ultraviolet to mid-IR OPCPA

In chapter 2 we presented the successful development a state-of-the-art, high power, mid-IR OPCPA system, providing passive CEP-stable, few-cycle pulses at 3100 nm center wavelength at a pulse repetition rate of 160 kHz. Afterwards, we demonstrated an additional frequency up-conversion module, which extended the available OPCPA output wavelength from the mid-IR down to the visible and ultraviolet spectral range.

The combined multi-color OPCPA system generates simultaneously multiple high power, femtosecond outputs from the deep-UV up to the mid-IR spectral range. Five outputs at 270 nm, 405 nm, 810 nm, 1620 nm and 3100 nm wavelength provide respective pulse energies of 0.5 µJ, 1.5 µJ, 3.1 µJ, 15 µJ and 20 µJ at 160 kHz repetition rate. The power stabilities were measured to show fluctuations of less than 1% over the course of 30 minutes. All outputs exhibit measured pulse durations below 110 fs and are

passive temporally synchronized owing to the optical seeding scheme. The source features high peak powers in the tens to hundreds of MW regime, allowing focused peak intensities of all outputs from 10^{12} up to 10^{14} W/cm^2.

High conversion efficiency OPCPA upgrade

In chapter 3 we demonstrated the first realization of a high power, mid-IR OPCPA system delivering 1.25 GW output peak powers at repetition rates in the 100 kHz range. It is also the first femtosecond, mid-IR OPCPA source reaching average powers far beyond 10 W, which is comparable to the performance of the more common, high power OPCPA systems emitting in the visible or near-IR spectral range.

The presented mid-IR OPCPA system provides CEP-stable output pulses with 118 µJ energies and a sub-9 optical cycle duration at a center wavelength of 3220 nm. The long-term power stability was measured to below 0.8% rms fluctuations over the course of 30 minutes. Combined with an excellent beam quality factor of M^2=1.3, the system allows focused peak intensities of up to 10^{15} W/cm^2. The huge increase of the mid-IR output energy compared to the former OPCPA design was enabled by various layout improvements, leading to an overall conversion efficiency of 41%. On one side, a chirp-reversal was implemented in the system, which enabled an optimized dispersion adjustment for each OPCPA section. Furthermore, the losses of the final pulse compressor were substantially reduced by changing from a grating-based to a bulk device. Additionally, a high pump energy extraction was achieved in the last booster-amplifiers, by using a pump double-pass scheme in two consecutive OPAs. All these changes were motivated beforehand by general theoretical considerations of the OPA process. Finally, the amplification to mid-IR average powers of up to 19 W in the last OPA stages were only enabled by an previous, in-depth analysis of multiple common mid-IR OPA crystals. The crystals were analyzed regarding their thermal induced amplification limitations in case of applied high power beams. As a result, the high power booster amplifiers featured $KNbO_3$ crystals instead of the more common MgO:PPLN crystals, due to their better suitability for high power amplification.

Few-cycle, mid-IR pulse generation via temporal self-compression in bulk materials

In chapter 4 we showed one of the first demonstration of temporal self-compression to few-cycle duration via nonlinear propagation in the anoma-

lous dispersion regime in solid, dielectric media. Exploiting this technique, we demonstrated temporal pulse shortening of the high energy, mid-IR output pulses of the presented OPCPA system down to sub-3 cycle duration.

Hereby, the 3 µJ energy, 70 fs (6.8 optical cycles) driving pulses at 3.1 µm center wavelength were compressed via filamentary propagation in a 3 mm thick YAG plate down to a 32 fs (2.9 optical cycles) duration, while the transmitted pulse energy dropped to 2 µJ. The further energy scalability was proven by the self-compression of a higher driving pulse energy of 15 µJ, yielding a compressed pulse duration of 38 fs (3.7 optical cycles) at 10 µJ energy. The pulses emerging from this compact and efficient self-compression setup exhibit an excellent pulse-to-pulse stability with 0.8% rms fluctuations over 10 minutes at 160 kHz repetition rate. Furthermore, focused peak intensities in the 10^{14} W/cm^2 range could be reached, enabling for example strong-field ionization experiments of atomic or molecular gas media. The measured spectro-temporal behaviour of the self-compressed pulses were found to be in good agreement with a 3-dimensional, numerical simulation, which supported the experimental findings and provided insight into the involved nonlinear processes. As a consequence the processes of plasma ionization and plasma absorption could be identified as main contributions for the energy loss during filamentary propagation. In conclusion, the demonstrated compression scheme was found to be a suitable, novel approach for few-cycle compression of high repetition rate, mid-IR pulses in the µJ energy range.

5.2 Conclusion and outlook

The development and investigation of high energy, mid-IR OPCPA systems with high pulse repetition rates is a fast growing scientific field due to their many possible applications. The presented thesis has strongly contributed to the general effort to reach mid-IR OPCPA source parameters that can compete with the established high power OPCPA systems emitting in the common visible and near-IR spectral range. On one side, we demonstrated the average power upscaling up to 19 W and the peak-power upscaling to the GW-level range at high repetition rates of 160 kHz. Furthermore the output, mid-IR pulse duration could be self-compressed to the sub-3 cycle range by a novel compression technique and the spectral range of output frequencies could be extended from the mid-IR down to the ultraviolet regime.

All these OPCPA parameter improvements provide a unique toolbox for

future investigations of strong-field ionization processes at driving wavelengths from the ultraviolet up to the mid-IR regime. The high repetition rate in combination with the excellent power stability, enables even the investigation of physical effects with a very low interaction-cross sections such as for instance the strong-field processes of laser induced electron diffraction (LIED) or double ionization. An overview of all strong-field experiments, which were enabled and driven by the presented OPCPA system is given in the attachment A.

Specifically the high power, multi-color OPCPA system permits a variety of ultraviolet to mid-IR time-resolved pump-probe experiments of highly nonlinear and strong-field processes. The pump-probe experiments are enabled by the low temporal jitter between the different color outputs, introduced by the optical synchronization scheme, in combination with the sub-110 fs pulse durations and the high peak power levels of all output pulses. Such unique system enables also a new kind of UV pump, mid-IR probe experiment in which the UV pulses - with high energy photons - could be used to trigger dynamic structural changes of molecular gases, while the mid-IR pulses probe the molecular structure via the LIED technique. The described concept could open a pathway towards achieving a molecular movie, giving novel insight into the dynamics of photo-chemical reactions. Additionally the near-IR output pulses at 800 nm or 1600 nm wavelength could be used for the controlled preparation of the investigated molecular sample via the molecular alignment method.

The GW-level peak power OPCPA upgrade should enable novel, mid-IR driven strong-field experiments at high repetition rate, which require driving peak-intensities in the 10^{15}-10^{16} GW/cm^2 range, such as for example the generation of X-ray radiation up to keV photon energies via high harmonic generation. In contrast to previous realizations of mid-IR driven high harmonic generation [24], our source exhibits a multiple order of magnitude higher repetition rate, which should potentially result in a much higher photon-flux of the generated X-ray radiation.

Furthermore, the demonstrated few-cycle, mid-IR self-compression scheme is a perfect tool for future strong-field physics or attoscience investigations, whenever few-cycle or CEP dependent effects are studied. Especially the high stability, transmission efficiency and focusability of the output pulses make this method a suitable and widely usable, novel approach for few-cycle compression of high repetition rate, mid-IR pulses in the µJ energy range.

Appendix A

Realized strong-field ionization experiments driven by mid-IR waveforms

The presented mid-IR OPCPA system has enabled a multitude of novel investigations on strong-field ionization processes due to its outstanding output pulse characteristics in the mid-IR spectral region. This chapter provides a brief overview of the experimental studies performed in the course of this theses, where I was involved in [19,20,26,27,32,38,71,128,238]. An in-depth description and analysis of most of the mentioned investigations is given in the thesis of my colleague Benjamin Wolter [239].

For the realization of the strong-field experiments, the high power OPCPA system was combined with a reaction microscope (REMI) detection system, which enables the detection of the complete 3-dimensional momentum vectors of all charged particles after the strong-field ionization process. In the experiments, the OPCPA output pulses were tightly focused onto a supersonic gas jet target inside the REMI device. After strong-field ionization, the ejected electrons and the parent ions are separated by an applied homogeneous electric field onto two separated, 2-dimensional micro-channel plate (MCP) detectors. A simultaneously applied homogeneous magnetic field tailors the particle trajectory in order to allow the full 3-dimensional detection of emitted particles. The impact position on the MCPs in combination with the measured time of flight allows the calculation of the full momentum distribution of all produced particles during the strong-field ionization process. The detected electrons and ions are measures event-based and in coincidence with each other to a) eliminate background signal from unwanted processes and b) to allow the assignment of electrons corresponding to different ion partners. Strong-field ionization can result in different types of ionization processes such as single ionization, double ionization or molecular dissociation. A detailed descrip-

tion of the working principle of REMI devices can be found in [240] and the experimental advantages of our high repetition rate OPCPA system in combination with our REMI device are explained in detail in [32].

Most of the realized studies are performed by a collaboration of many scientists, due to the complexity of the experimental realization, data analysis and theoretical understanding of the investigated strong-field ionization processes. For the different experiments the laser system was operated by my colleagues A. Thai, M. Hemmer, H. Pires and myself. The operation of the REMI setup as well as the data analysis and interpretation was performed in the different studies by my colleagues B. Wolter, M. G. Pullen, M. Sclafani, J. Dura and A. Britz under the supervision of J. Biegert. Additionally, most of the strong-field investigations were performed in collaboration with other scientific research groups. Some of the collaborators are N. Camus, A. Senftleben, C. D. Schröter, J. Ullrich, T. Pfeifer and R. Moshammer from the Max-Planck-Institut für Kernphysik in Heidelberg, Germany; A.-T. Le and C. D. Lin from the Kansas State University, United States; C. Lemell and J. Burgdörfer from the Vienna University of Technology, Austria; X.-M. Tong from the University of Tsukuba, Japan; K. Doblhoff-Dier from the Leiden Institute of Chemistry, Netherlands; S. Gräfe from the Friedrich-Schiller University Jena, Germany; O. Vendrell from the Aarhus University, Denmark; X. Wang from the Kansas State University, United States and J. H. Eberly from the University of Rochester, United States.

Transition from multi-photon to tunnel-ionization

Strong-field ionization can take place in the multi-photon ionization regime, where multiple photons are absorbed by the target system (noble gas atoms and small molecules) causing the electron ejection. Alternatively, tunnel ionization can occur, is sufficiently tilted by the strong electric field of the mid-IR laser pulse to enable tunneling of a valence electron throught the Coulomb barrier. The Keldysh parameter γ gives a rough estimate, which process is predominant for given laser conditions (multi-photon for $\gamma > 1$ and tunneling for $\gamma \ll 1$) [16]. Both regimes are experimentally clearly distinguishable by the resulting shape of the kinetic energy distribution of the ejected electrons. Multi-photon ionization causes the above threshold ionization (ATI) peaks, for more photons absorbed than necessary to overcome the ionization potential. The ATI peaks are energetically separated by the driving photon energy. In contrast, tunnel ionization causes a rather smooth, continuum-like electron kinetic energy distribution.

Our multi-color OPCPA system is a perfect tool to investigate the transition between both ionization regimes due to the inverse scaling of the Keldysh parameter with the driving wavelength ($\gamma \propto \frac{1}{\lambda}$). In the publication by Baudisch *et al.* [71] we performed strong-field ionization experiments of xenon gas driven by the near-IR and mid-IR OPCPA output pulses. By using driving wavelength at 800 nm, 1600 nm and 3100 nm, yielding respective Keldysh parameters of 1.47, 1.14 and 0.55, we could experimentally demonstrate the transition from the multi-photon to the tunneling ionization regime. Despite the fact that this transition had been studied previously [241, 242], we could show the first experimental investigation driven by near-IR to the mid-IR pulses originating from a single light source. Furthermore this experiment verified the capability of our multi-color OPCPA to drive strong-field ionization experiments at various output wavelengths.

Low to zero kinetic energy structures

The REMI device is capable of detecting electrons over a very large kinetic energy range. On one side electron kinetic energies far below eV levels and with meV resolution can be detected, while on the other side measurements of kinetic energies up to hundreds of eV are enabled. The measurement capabilities of very small kinetic energies allowed us to discover a novel structure, the so called zero kinetic energy structure (ZES) in the electron energy and 3D momentum distribution of singly ionized atoms and molecules.

In the article by Dura *et al.* [19] we reported for the first time the observation of this new ZES signature for mid-IR driven tunnel ionization of argon atoms. In the article by Wolter *et al.* [128] we presented a follow-up, joint experimental and theoretical study of the higher-order low-energy structures in strong-field ionization of argon. The ZES structure was identified as high-lying Rydberg states, which are field ionized by the extraction field of the ReMi. Furthermore the so-called very-low-kinetic energy structure (VES) of strong-field ionized argon was investigated under the variation of the driving mid-IR pulse duration from 4 to 14 optical cycles [128]. For this investigation we exploited the pulse compression technique of self-compression in solid media, which is highlighted in chapter 4. Afterwards, in an article by Pullen *et al.* [20] we presented a comparative study of high resolution electron momentum and energy distributions for strong-field ionized argon and nitrogen, specially comparing the behaviours of the low-kinetic-energy structures (LES), the VES and the ZES. In another study

by Wolter *et al.* [32] we performed a similar investigation on singly ionized xenon atoms, showing that the behavior of the kinetic energy structures are universal hence target independent.

Mid-IR driven, strong-field double ionization

Aside from single ionization processes, also double or higher ionized atoms and molecules can be investigated with the REMI device. The distinction between the different ionization orders is given by the REMI detection. By exploiting the combination of OPCPA and REMI, we could demonstrate in [32] the first coincidence measurement of strong-field double ionized xenon atoms driven by mid-IR electromagnetic fields. We also investigated the correlated two-electron momentum distribution featuring a cross-like shape.

In a further investigation of the double-ionized xenon in [238], we gained deeper insight in the underlying double ionization process. Double ionization can take place in the non-sequential regime or for higher driving peak intensities in the sequential regime. In [238] we demonstrated experimentally and theoretically for the first time the transition from non-sequential to sequential double ionization of xenon atoms, which could never fully be shown in strong-field ionization experiments driven by common 800 nm laser fields. To probe this transition we investigated the ionization yield and the correlated two-electron momentum distribution as function of the driving peak intensities.

Resolving static and dynamically changing molecular structure

An electron, which is ejected during a strong-field ionization process can be redirected by the driving laser field and scatter off the parent ion. The rescattered electron exhibits then structural information of the ionized, parent atom or molecule in the far-field diffraction signal. Via this method of laser-induced electron diffraction (LIED) the structural information of bond length of small molecules can be extracted by an in-depth analysis of the detected electron momentum distribution [243].

In [32] we demonstrated the feasibility of our detection setup for LIED measurements by investigating the LIED signitures of gaseous xenon atoms.

Additionally, in [26] we reported the first implementation of the LIED technique on a polyatomic molecule. Hereby we could obtain bond length information with few picometer resolution of the carbon-carbon and carbon-hydrogen bonds of the investigated acetylene molecules (C_2H_2). A similar technique to obtain molecular structural information is a Fourier analysis-based 1D version of LIED, also called FT-LIED or FABLES [244]. In [38] we investigated the structural information of diatomic O_2 and polyatomic C_2H_2 via a simple empirically background-subtracted FT-LIED methodology. Furthermore we could prove the evidence that atomic-scale diffraction imaging via FT-LIED does not require the alignment of the target molecule like it was previously claimed by Xu *et al.* [244].

In a recent publication by Wolter *et al.* [27] we could further investigate a dynamic dissociation process of double ionized acetylene. The LIED technique enabled us to track the cleavage of the C-H bond 9 femtoseconds after double ionization. Furthermore, using molecular alignment by the near-IR OPCPA output at 1600 nm wavelength, we could also demonstrate the control over the ultrafast dissociation process and resolved different bond dynamics in case of molecules aligned parallel versus perpendicular to the mid-IR probe field.

Appendix B

Pulse characterization

In this section we briefly describe the employed pulse characterization techniques and setups which are used in the course of the presented thesis. In detail, we used the methods of second harmonic generation frequency-resolved optical gating (SHG-FROG), self-diffraction frequency-resolved optical gating (SD-FROG) and two-photon absorption (TPA) autocorrelation in order to cover all wavelengths emitted from the OPCPA system, which range from the deep-UV up to the mid-IR regime.

SHG-FROG

In the frequency-resolved optical gating (FROG) method the investigated, unknown electric field $E(t)$ is gated by a gating-field $g(t)$. Both fields $E(t)$ and $g(t)$ are coupled via a nonlinear process (often χ^2 or χ^3) and the resultant, nonlinear optical response is spectrally recorded for a varying time delay τ between $E(t)$ and $g(t)$. The measured frequency-resolved intensity trace, or Spectrogram $S_F(\tau, \omega)$ can be written as [245]:

$$S_F(\omega, \tau) \propto \left| \int_{-\infty}^{\infty} E(t) \cdot g(t-\tau) e^{-i\omega t} \mathrm{d}t \right|^2 \tag{B.1}$$

In the case of SHG-FROG, the gating field is a copy of the unknown electric field ($g(t) = E(t)$) and the nonlinear interaction is performed by second harmonic generation. Therefore a SHG-FROG measurement is nothing else than a spectrally resolved SHG-autocorrelation measurement.

In the course of the presented thesis, the SHG-FROG method is used to characterize the OPCPA output pulses in the near-IR and mid-IR spectral ranges. The employed SHG-FROG setup is specially designed for the characterization of broadband, ultrashort pulses up to the mid-IR wavelength regime (see detailed description by Bates *et al.* in [227]). The FROG device (see figure B.1) features apart from a very thin pellicle beamsplitter

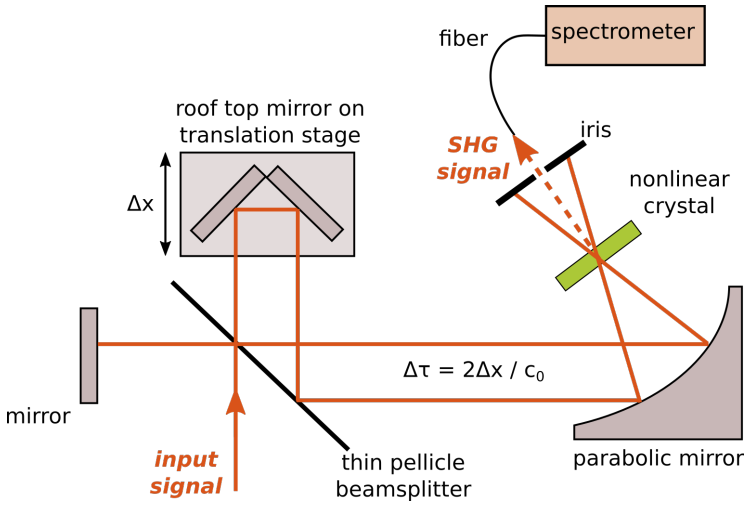

Figure B.1: SHG-FROG setup used for the electric field characterization of the OPCPA output pulses in the visible to mid-IR spectral range.

only reflective optics in order to minimize additional dispersion on the investigated pulse. The incident pulse is replicated via a Michelson interferometer and both pulses are spatio-temporally overlapped in a nonlinear crystal by a off-axis parabolic gold mirror. The non-collinear focusing geometry leads to a spatial separation of the generated SHG signal from the two fundamental beams and the SHG spectrum can be measured by a grating-based spectrometer in dependence of the time delay τ. An overview of the SHG-crystals used for the characterization of the various OPCPA output wavelengths is given in table B.1. Depending on the wavelengths of the generated SHG signal, a Silicon-based spectrometer (HR4000 from Ocean Optics Inc.) or an InGaSe-based spectrometer (NIR256 from Ocean Optics Inc.) are used for the spectral measurement.

fundamental wavelength λ_0	SHG-Crystal	Crystal length (mm)	θ (deg)	$\Delta\lambda$ (nm)	used in section
3.2 µm	$AgGaS_2$	0.3	36.7	1560	2.2.6, 3.3.3, 4.3
1.62 µm	BBO	1.0	19.8	1440	2.3.2
0.81 µm	BBO	0.1	29.2	117	2.3.3

Table B.1: Overview of the SHG crystals used for the various output wavelengths λ_0 of the OPCPA system. Indicated are the crystal length, the phase-matching angle θ and the phase-matching acceptance bandwidth $\Delta\lambda$, according to equation 2.31.

SD-FROG

The above described SHG-FROG technique is normally unsuitable for the characterization of ultraviolet pulses due to the onset of absorption of the generated second harmonic and an unfavorable phase-matching scaling for wavelengths close to the absorption limit. Alternative FROG methods for this case use third-order nonlinearities of the nonlinear crystal such as the self-diffraction (SD) or transient grating (TG) processes.

In the case of SD-FROG, the nonlinear interaction is a χ^3 process, where the interacting pulses induce a nonlinear refractive index grating in the medium, which diffracts one of the pulses into a new direction off to the side, at the wavevector $\vec{k}_{SD} = 2\vec{k}_1 - \vec{k}_2 + \Delta\vec{k}$. The self-diffracting process requires compared to the SHG-process much higher driving peak intensities, but has the advantage of no direction-of time ambiguity unlike the SHG-FROG [246]. For a SD-FROG the spectrogram $S_F(\omega, \tau)$ can be written as [245]:

$$S_F(\omega, \tau) \propto \left| \int_{-\infty}^{\infty} E(t)^2 \cdot E^*(t-\tau) e^{-i\omega t} \mathrm{d}t \right|^2 \tag{B.2}$$

The employed SD-FROG layout is illustrated in figure B.2. The home-build setup is adapted from the SD-FROG scheme reported from Durfee *et al.* [247].

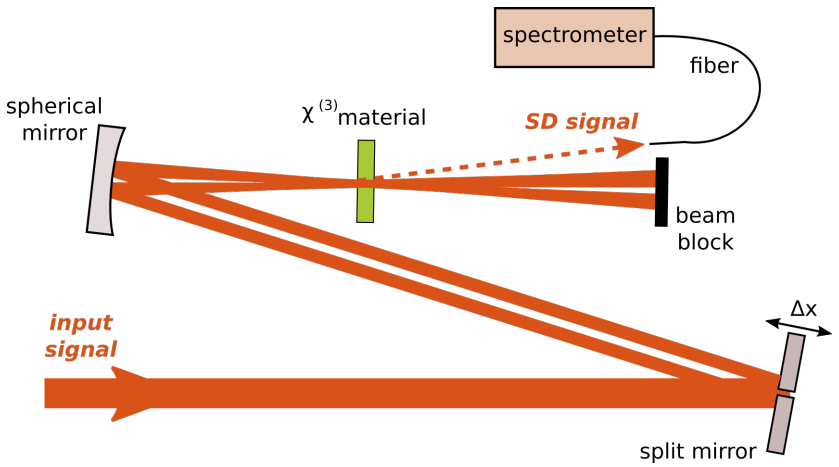

Figure B.2: Setup scheme of the SD-FROG device used for the electric field characterization of the ultraviolet OPCPA output pulses at 410 nm center wavelengths.

The two pulse replica are generated by the reflection of a split-mirror instead from a Michelson interferometer. As a result, the setup is simplified and no transmission optics are requires, which could introduce additional dispersion onto the investigated electric field. After the split-mirror, the two pulse replica are focused by a spherical, aluminium mirror and spatio-temporal recombined in the third-order nonlinear material. For the characterization of the ultraviolet OPCPA output pulses at 410 nm wavelength (see section 2.3.4) a 0.2 mm thick BBO crystal is chosen for the nonlinear interaction. The spectrum of the self-diffracted pulses are measured in dependency of the FROG time delay τ with a silicon-based spectrometer (HR4000 from Ocean Optics Inc.).
The interested reader can find an in-depth analysis and description of the different FROG techniques in the book of one of the FROG inventors Rick Trebino [246].

Two-photon absorption autocorrelation

In the course of this thesis, the two-photon absorption autocorrelator is used to characterize the pulse duration of the ultraviolet output at 270 nm wavelengths emitted from the multi-color OPCPA upgrade (see section 2.3.4). In general, the technique of two-photon autocorrelation uses the attenuation by two-photon absorption (TPA) of the incident beam on a thin material plate. As requirement the photon energy of the investigated pulse ($E_{ph} = \hbar \cdot \omega$) has to be higher than half the energy of the material band gap E_{gap} and smaller as the band gap energy ($\frac{1}{2} E_{gap} < E_{ph} < E_{gap}$). TPA autocorrelators use usually photodiodes as detectors, where the strength of the TPA absorption in the photodiode can be directly measured as current. However, this technique cannot easily be adapted for the characterization of ultraviolet pulses, since TPA photodiodes with band gaps below 200 nm are still quite rare and difficult to produce [248, 249].

Therefore we apply an alternative two-photon absorption autocorrelation method proposed by Homann *et al.* [118], which measures the intensity-dependent transmission through the TPA material, instead of the induced current. The used TPA autocorrelation setup is illustrated in figure B.3. The setup is very similar to the above presented SD-FROG scheme. The beam to be characterized split by spatial cutting of the beam profile in a pump and a probe beam via a split mirror. One half mirror can be moved by a delay stage in order to record the autocorrelation trace. Both parts of the reflected beam are focused by a spherical, aluminium mirror and spatio-temporally overlapped in a 200 µm thick BBO crystal, which is used as TPA material.

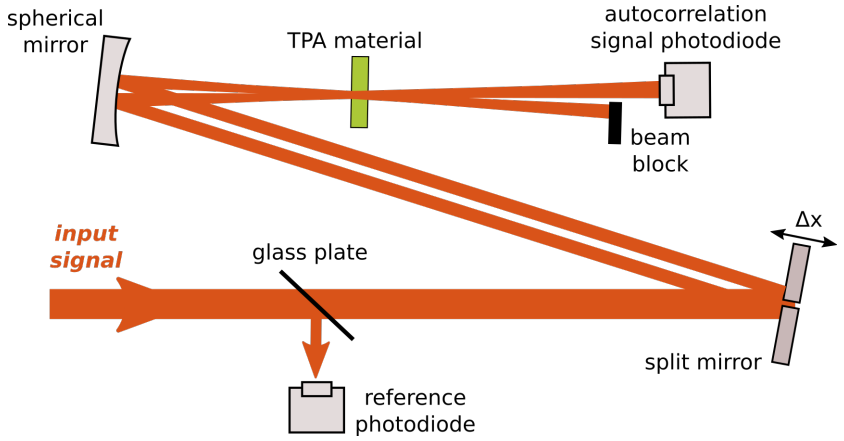

Figure B.3: Layout of two-photon absorption autocorrelator, which is used for the characterization of the ultraviolet OPCPA output pulses at 270 nm center wavelength.

The transmitted probe beam is detected by a photodiode and provides the signal for the autocorrelation trace. The signal-to-noise behaviour of the setup can be further increased by installing a reference photodiode in the unsplit beam and by choosing a high energy ratio between the pump and the probe beam [118].

In contrast to the measurement with the SD-FROG device, which was not possible at 270 nm due to insufficient peak intensities, the TPA autocorrelator does not give any spectral or temporal phase information and provides only limited information about the temporal pulse shape. Under the assumption of a Gaussian-like pulse shape, the FWHM pulse duration τ_{Gauss} can be obtained from the autocorrelation width τ_{AC} by $\tau_{Gauss} = \tau_{AC}/\sqrt{2}$.

Appendix C

List of few-cycle, high energy, mid-IR radiation sources

In table C.1 is given an overview of up-to-date existing, few-cycle, high energy mid-IR radiation sources suitable for strong-field experiments. Considered are only systems, which support sub-10 optical cycle pulse durations, above 10 µJ pulse energies and center wavelengths beyond 3 µm.

The mid-IR sources can be divided in Ti:sapphire laser driven OPA/DFG schemes, novel, mid-IR OPCPA architectures emitting radiation between 3 µm and 5 µm wavelengths and very recent OPA/OPCPA approaches emitting wavelengths above 5 µm wavelengths. A more detailed discussion about the different approaches is given in section 1.3.

Reference	Pulse energy / Center wavelength	Repetition rate	Pulse duration (optical cycles)	Average power
3 µm - 5 µm wavelength, OPCPA systems				
Thesis, chapter 2	20 µJ at 3.1 µm	160 kHz	55 fs (5.4 cycles)	3.2 W
Thesis, chapter 3	118 µJ at 3.2 µm	160 kHz	95 fs (9.0 cycles)	18.9 W
Thesis, chapter 4	2 µJ at 3.25 µm	160 kHz	32 fs (2.9 cycles)	0.3 W
Thesis, chapter 4	10 µJ at 3.1 µm	160 kHz	38 fs (3.7 cycles)	1.6 W
Rigaud *et al.*, 2016 [52]	10 µJ at 3.1 µm	125 kHz	72 fs (7.0 cycles)	1.25 W
Thiré *et al.*, 2017 [51]	40 µJ at 3.1 µm	100 kHz	38 fs (3.8 cycles)	4.0 W
Mayer *et al.*, 2014 [50]	22 µJ at 3.4 µm	50 kHz	44 fs (3.9 cycles)	1.1 W
Mitrofanov *et al.*, 2015 [47, 48]	30 mJ at 3.9 µm	0.02 kHz	80 fs (6.4 cycles)	0.6 W
Zhao *et al.*, 2013 [49]	13.3 mJ at 3.4 µm	0.01 kHz	111 fs (9.8 cycles)	0.133 W
Ti:sapphire laser driven, cascaded frequency down-conversion schemes				
Sugiharto *et al.*, 2008 [42]	100 µJ at 4 µm	1 kHz	130 fs (9.8 cycles)	0.1 W
Chen *et al.*, 2016 [43]	82 µJ at 3.3 µm	1 kHz	70 fs (6.4 cycles)	0.082 W
Fan *et al.*, 2014 [44]	17 µJ at 3.8 µm	1 kHz	70 fs (5.6 cycles)	0.017 W
Schultz *et al.*, 2007 [45]	160 µJ at 3.6 µm	1 kHz	100 fs (8.3 cycles)	0.16 W
5 µm - 8 µm wavelength, OPCPA systems				
Malevich, *et al.*, 2016 [58, 59]	40 µJ at 5.2 µm	1 kHz	100 fs (5.8 cycles)	0.04 W
Grafenstein, *et al.*, 2016 [60]	240 µJ at 5.0 µm	1 kHz	166 fs (9.9 cycles)	0.24 W
Sanchez, *et al.*, 2016 [57]	200 µJ at 7 µm	0.1 kHz	180 fs (7.7 cycles)	0.02 W

Table C.1: Overview of up-to-date existing few-cycle, high energy mid-IR radiation sources suitable for strong-field experiments. Considered are only systems, which support sub-10 optical cycle pulse durations, above 10 µJ pulse energies and center wavelengths beyond 3 µm. Higher pulse repetition rates enable the investigation of physical processes with low interaction cross-sections, while higher pulse energies allow the study of a wider range of highly nonlinear effects.

Acronyms

Al_2O_3	sapphire
AOPDF	acousto-optic programmable dispersive filter
BaF_2	barium fluoride
BBO	beta barium borate
BiBO	bismuth triborate
CaF_2	calcium fluoride
CBO	cesium triborate
CEP	carrier-envelope phase
CPA	chirped pulse amplification
DFG	difference frequency generation
DOE	diffraction optical element
DPSSL	diode-pumped solid-state laser
Er	erbium
FOD	fourth order dispersion
FOPA	frequency domain optical parametric amplification
FROG	frequency-resolved optical gating
FTIR spectrometer	Fourier transform infrared spectrometer
FT-LIED	Fourier-transform laser-induced electron diffraction
Ge	germanium
GDD	group delay dispersion
GVD	group velocity dispersion
HC-PCF	hollow-core photonic crystal fibers
HHG	high harmonic generation
KBBF	potassium fluoroboratoberyllate
KDP	potassium dihydrogen phosphate
$KNbO_3$	potassium niobate
KTA	potassium titanyl arsenate
KTP	potassium titanyl phosphate
LBO	lithium triborate
LIED	laser-induced electron diffraction
LIO	lithium iodate
MCP	micro-channel plate
MgO	magnesium oxide

mid-IR	mid-wave infrared
MOPA	master oscillator power amplifer
Nd:YVO_4	neodymium-doped yttrium orthovanadate
near-IR	near infrared
NOPA	non-collinear optical parametric amplification
OPA	optical parametric amplification
OPCPA	optical parametric chirped pulse amplification
PLL	phase-lock loop
PM	phase-matching
PP-LBGO	periodically poled lanthanum boron germinate
PPLN	periodically poled lithium niobate
PPLT	periodically poled lithium tantalate
QPM	quasi phase-matching
REMI	reaction microscope
SD	self-diffraction
SFG	sum-frequency generation
SHG	second harmonic generation
Si	silicon
SPM	self-phase modulation
TAPIR	temporal allocation of pump intensity remainder
THG	third harmonic generation
Ti:sapphire	titanium-doped sapphire
TOD	third order dispersion
TPA	two-photon absorption
UV	ultraviolet
YAG	yttrium aluminium garnet
Yb:YAG	ytterbium-doped yttrium aluminium garnet
ZnSe	zinc selenide

Bibliography

[1] T. H. Maiman, “Stimulated Optical Radiation in Ruby,” Nature **187**(4736), 493–494 (1960).

[2] A. Dubietis, G. Jonušauskas, and A. Piskarskas, “Powerful femtosecond pulse generation by chirped and stretched pulse parametric amplification in BBO crystal,” Optics Communications **88**(4), 437–440 (1992).

[3] I. N. Ross, P. Matousek, M. Towrie, A. J. Langley, and J. L. Collier, “The prospects for ultrashort pulse duration and ultrahigh intensity using optical parametric chirped pulse amplifiers,” Optics Communications **144**(1), 125–133 (1997).

[4] O. V. Chekhlov, J. L. Collier, I. N. Ross, P. K. Bates, M. Notley, C. Hernandez-Gomez, W. Shaikh, C. N. Danson, D. Neely, P. Matousek, S. Hancock, and L. Cardoso, “35 J broadband femtosecond optical parametric chirped pulse amplification system,” Optics Letters **31**(24), 3665–3667 (2006).

[5] C. Danson, D. Hillier, N. Hopps, and D. Neely, “Petawatt class lasers worldwide,” High Power Laser Science and Engineering **3**(e3), 1–14 (2015).

[6] J. Rothhardt, S. Demmler, S. Hädrich, J. Limpert, and A. Tünnermann, “Octave-spanning OPCPA system delivering CEP-stable few-cycle pulses and 22 W of average power at 1 MHz repetition rate,” Optics Express **20**(10), 10870–10878 (2012).

[7] M. Puppin, Y. Deng, O. Prochnow, J. Ahrens, T. Binhammer, U. Morgner, M. Krenz, M. Wolf, and R. Ernstorfer, “500 kHz OPCPA delivering tunable sub-20 fs pulses with 15 W average power based on an all-ytterbium laser,” Optics Express **23**(2), 1491–1497 (2015).

[8] F. K. Tittel, D. Richter, and A. Fried, “Mid-Infrared Laser Applications in Spectroscopy,” Solid-State Mid-Infrared Laser Sources, Topics Applied Physics **89**, 445–516 (2003).

[9] W. Petrich, “Mid-infrared and raman spectroscopy for medical diagnostics,” Applied Spectroscopy Reviews **36**(2-3), 181–237 (2001).

[10] G. L. Richmond, “Molecular Bonding and Interactions at Aqueous Surfaces as Probed by Vibrational Sum Frequency Spectroscopy,” Chemical Reviews **102**(8), 2693–2724 (2002).

[11] M. T. Zanni and R. M. Hochstrasser, “Two-dimensional infrared spectroscopy: a promising new method for the time resolution of structures,” Current Opinion in Structural Biology **11**(5), 516–522 (2001).

[12] S. Garrett-Roe and P. Hamm, "Purely absorptive three-dimensional infrared spectroscopy," The Journal of Chemical Physics **130**, 164510 (2009).

[13] C. R. Baiz, D. Schach, and A. Tokmakoff, "Ultrafast 2D IR microscopy," Optics Express **22**(15), 18724–18735 (2014).

[14] J. D. Cyran and A. T. Krummel, "Probing structural features of self-assembled violanthrone-79 using two dimensional infrared spectroscopy," The Journal of Chemical Physics **142**, 212435 (2015).

[15] B. M. Luther, K. M. Tracy, M. Gerrity, S. Brown, and A. T. Krummel, "2D IR spectroscopy at 100 kHz utilizing a Mid-IR OPCPA laser source," Optics Express **24**(4), 4117–4127 (2016).

[16] L. V. Keldysh, "Ionization in the field of a strong electromagnetic wave," Zh. Eksperim. Teor. Fiz. **47** (1964). [Sov. Phys. JETP 20, 1307 (1965)].

[17] C. I. Blaga, F. Catoire, P. Colosimo, G. G. Paulus, H. G. Muller, P. Agostini, and L. F. DiMauro, "Strong-field photoionization revisited," Nature Physics **5**(5), 335–338 (2009).

[18] C. Y. Wu, Y. D. Yang, Y. Q. Liu, Q. H. Gong, M. Wu, X. Liu, X. L. Hao, W. D. Li, X. T. He, and J. Chen, "Characteristic Spectrum of Very Low-Energy Photoelectron from Above-Threshold Ionization in the Tunneling Regime," Physical Review Letters **109**(4), 043001 (2012).

[19] J. Dura, N. Camus, A. Thai, A. Britz, M. Hemmer, M. Baudisch, A. Senftleben, C. D. Schröter, J. Ullrich, R. Moshammer, and J. Biegert, "Ionization with low-frequency fields in the tunneling regime," Scientific Reports **3**, 2675 (2013).

[20] M. G. Pullen, J. Dura, B. Wolter, M. Baudisch, M. Hemmer, N. Camus, A. Senftleben, C. D. Schroeter, R. Moshammer, J. Ullrich, and J. Biegert, "Kinematically complete measurements of strong field ionization with mid-IR pulses," Journal of Physics B: Atomic, Molecular and Optical Physics **47**(20), 204010 (2014).

[21] P. B. Corkum, "Plasma perspective on strong field multiphoton ionization," Physical Review Letters **71**(13), 1994 (1993).

[22] M. Lewenstein, P. Balcou, M. Y. Ivanov, A. L'Huillier, and P. B. Corkum, "Theory of high-harmonic generation by low-frequency laser fields," Physical Review A **49**(3), 2117 (1994).

[23] B. Shan and Z. Chang, "Dramatic extension of the high-order harmonic cutoff by using a long-wavelength driving field," Physical Review A **65**(1), 011804 (2001).

[24] T. Popmintchev, M.-C. Chen, D. Popmintchev, P. Arpin, S. Brown, S. Ališauskas, G. Andriukaitis, T. Balčiunas, O. D. Mücke, A. Pugzlys, A. Baltuška, B. Shim, S. E. Schrauth, A. Gaeta, C. Hernández-García, L. Plaja, A. Becker, A. Jaron-Becker, M. M. Murnane, and H. C. Kapteyn, "Bright

Coherent Ultrahigh Harmonics in the keV X-ray Regime from Mid-Infrared Femtosecond Lasers," Science **336**(6086), 1287–1291 (2012).

[25] C. I. Blaga, J. Xu, A. D. DiChiara, E. Sistrunk, K. Zhang, P. Agostini, T. A. Miller, L. F. DiMauro, and C. D. Lin, "Imaging ultrafast molecular dynamics with laser-induced electron diffraction," Nature **483**(7388), 194–197 (2012).

[26] M. G. Pullen, B. Wolter, A.-T. Le, M. Baudisch, M. Hemmer, A. Senftleben, C. D. Schröter, J. Ullrich, R. Moshammer, C. D. Lin, and J. Biegert, "Imaging an aligned polyatomic molecule with laser-induced electron diffraction," Nature Communications **6** (2015).

[27] B. Wolter, M. G. Pullen, A.-T. Le, M. Baudisch, K. Doblhoff-Dier, A. Senftleben, M. Hemmer, C. D. Schröter, J. Ullrich, T. Pfeifer, R. Moshammer, S. Gräfe, O. Vendrell, C. D. Lin, and J. Biegert, "Ultrafast electron diffraction imaging of bond breaking in di-ionized acetylene," Science **354**(6310), 308–312 (2016).

[28] F. Krausz and M. Ivanov, "Attosecond physics," Reviews of Modern Physics **81**(1), 163 (2009).

[29] J. Tate, T. Auguste, H. G. Muller, P. Salières, P. Agostini, and L. F. DiMauro, "Scaling of Wave-Packet Dynamics in an Intense Midinfrared Field," Physical Review Letters **98**(1), 013901 (2007).

[30] M. V. Frolov, N. L. Manakov, and A. F. Starace, "Wavelength Scaling of High-Harmonic Yield: Threshold Phenomena and Bound State Symmetry Dependence," Physical Review Letters **100**(17), 173001 (2008).

[31] D. R. Austin and J. Biegert, "Strong-field approximation for the wavelength scaling of high-harmonic generation," Physical Review A **86**(2), 023813 (2012).

[32] B. Wolter, M. G. Pullen, M. Baudisch, M. Sclafani, M. Hemmer, A. Senftleben, C. D. Schröter, J. Ullrich, R. Moshammer, and J. Biegert, "Strong-Field Physics with Mid-IR Fields," Physical Review X **5**(2), 021034 (2015).

[33] G. Sansone, E. Benedetti, F. Calegari, C. Vozzi, L. Avaldi, R. Flammini, L. Poletto, P. Villoresi, C. Altucci, R. Velotta, S. Stagira, S. D. Silvestri, and M. Nisoli, "Isolated Single-Cycle Attosecond Pulses," Science **314**(5798), 443–446 (2006).

[34] E. Goulielmakis, M. Schultze, M. Hofstetter, V. S. Yakovlev, J. Gagnon, M. Uiberacker, A. L. Aquila, E. M. Gullikson, D. T. Attwood, R. Kienberger, F. Krausz, and U. Kleineberg, "Single-Cycle Nonlinear Optics," Science **320**(5883), 1614–1617 (2008).

[35] G. G. Paulus, F. Lindner, H. Walther, A. Baltuška, E. Goulielmakis, M. Lezius, and F. Krausz, "Measurement of the Phase of Few-Cycle Laser Pulses," Physical Review Letters **91**(25), 253004 (2003).

[36] Y. H. Jiang, A. Rudenko, O. Herrwerth, L. Foucar, M. Kurka, K. U. Kühnel, M. Lezius, M. F. Kling, J. v. Tilborg, A. Belkacem, K. Ueda, S. Düsterer, R. Treusch, C. D. Schröter, R. Moshammer, and J. Ullrich, "Ultrafast Extreme Ultraviolet Induced Isomerization of Acetylene Cations," Physical Review Letters **105**(26), 263002 (2010).

[37] H. Sato, "Photodissociation of Simple Molecules in the Gas Phase," Chemical Reviews **101**(9), 2687–2726 (2001).

[38] M. G. Pullen, B. Wolter, A.-T. Le, M. Baudisch, M. Sclafani, H. Pires, C. D. Schröter, J. Ullrich, R. Moshammer, T. Pfeifer, C. D. Lin, and J. Biegert, "Influence of orbital symmetry on diffraction imaging with rescattering electron wave packets," Nature Communications **7** (2016).

[39] H. Stapelfeldt and T. Seideman, "*Colloquium*: Aligning molecules with strong laser pulses," Reviews of Modern Physics **75**(2), 543 (2003).

[40] A. Wirth, M. T. Hassan, I. Grguraš, J. Gagnon, A. Moulet, T. T. Luu, S. Pabst, R. Santra, Z. A. Alahmed, A. M. Azzeer, V. S. Yakovlev, V. Pervak, F. Krausz, and E. Goulielmakis, "Synthesized Light Transients," Science **334**(6053), 195–200 (2011).

[41] D. Shafir, H. Soifer, B. D. Bruner, M. Dagan, Y. Mairesse, S. Patchkovskii, M. Y. Ivanov, O. Smirnova, and N. Dudovich, "Resolving the time when an electron exits a tunnelling barrier," Nature **485**(7398), 343–346 (2012).

[42] A. B. Sugiharto, C. M. Johnson, H. B. d. Aguiar, L. Alloatti, and S. Roke, "Generation and application of high power femtosecond pulses in the vibrational fingerprint region," Applied Physics B **91**(2), 315–318 (2008).

[43] Y. Chen, Y. Li, W. Li, X. Guo, and Y. Leng, "Generation of high beam quality, high-energy and broadband tunable mid-infrared pulse from a KTA optical parametric amplifier," Optics Communications **365**, 7–13 (2016).

[44] H.-T. Fan, C.-H. Xu, Z.-H. Wang, G. Wang, C.-J. Liu, J.-K. Liang, X.-L. Chen, and Z.-Y. Wei, "Generation of broadband 17-μJ mid-infrared femtosecond pulses at 3.75 μm by silicon carbide crystal," Optics Letters **39**(21), 6249–6252 (2014).

[45] K. D. Schultz, C. I. Blaga, R. Chirla, P. Colosimo, J. Cryan, A. M. March, C. Roedig, E. Sistrunk, J. Tate, J. Wheeler, P. Agostini, and L. F. Dimauro, "Strong field physics with long wavelength lasers," Journal of Modern Optics **54**, 1075–1085 (2007).

[46] M. K. Reed and M. K. S. Shepard, "Tunable infrared generation using a femtosecond 250 kHz Ti:sapphire regenerative amplifier," IEEE Journal of Quantum Electronics **32**(8), 1273–1277 (1996).

[47] G. Andriukaitis, T. Balčiūnas, S. Ališauskas, A. Pugžlys, A. Baltuška, T. Popmintchev, M.-C. Chen, M. M. Murnane, and H. C. Kapteyn, "90 GW peak power few-cycle mid-infrared pulses from an optical parametric amplifier," Optics Letters **36**(15), 2755–2757 (2011).

[48] A. V. Mitrofanov, D. A. Sidorov-Biryukov, A. A. Voronin, A. Pugžlys, G. Andriukaitis, E. A. Stepanov, S. Ališauskas, T. Flöri, A. B. Fedotov, V. Y. Panchenko, A. Baltuška, and A. M. Zheltikov, "Subterawatt femtosecond pulses in the mid-infrared range: new spatiotemporal dynamics of high-power electromagnetic fields," Physics-Uspekhi **58**(1), 89 (2015).

[49] K. Zhao, H. Zhong, P. Yuan, G. Xie, J. Wang, J. Ma, and L. Qian, "Generation of 120 GW mid-infrared pulses from a widely tunable noncollinear optical parametric amplifier," Optics Letters **38**(13), 2159–2161 (2013).

[50] B. W. Mayer, C. R. Phillips, L. Gallmann, and U. Keller, "Mid-infrared pulse generation via achromatic quasi-phase-matched OPCPA," Optics Express **22**(17), 20798–20808 (2014).

[51] N. Thiré, R. Maksimenka, B. Kiss, C. Ferchaud, P. Bizouard, E. Cormier, K. Osvay, and N. Forget, "4-W, 100-kHz, few-cycle mid-infrared source with sub-100-mrad carrier-envelope phase noise," Optics Express **25**(2), 1505–1514 (2017).

[52] P. Rigaud, A. V. d. Walle, M. Hanna, N. Forget, F. Guichard, Y. Zaouter, K. Guesmi, F. Druon, and P. Georges, "Supercontinuum-seeded few-cycle mid-infrared OPCPA system," Optics Express **24**(23), 26494–26502 (2016).

[53] J. Rothhardt, S. Demmler, S. Hädrich, T. Peschel, J. Limpert, and A. Tünnermann, "Thermal effects in high average power optical parametric amplifiers," Optics Letters **38**(5), 763–765 (2013).

[54] M. Baudisch, M. Hemmer, H. Pires, and J. Biegert, "Performance of MgO:PPLN, KTA, and $KNbO_3$ for mid-wave infrared broadband parametric amplification at high average power," Optics Letters **39**(20), 5802–5805 (2014).

[55] S. J. Backus, S. Brown, M. Gerrity, X. Zhang, R. Bartels, J. Squier, H. Kapteyn, and M. Murnane, "High Peak and Average Power Near/Mid-IR Femtosecond Laser Sources," in *Imaging and Applied Optics 2014 (2014), paper AM3A.1*, p. AM3A.1 (Optical Society of America, 2014).

[56] M. Mero, F. Noack, F. Bach, V. Petrov, and M. J. J. Vrakking, "High-average-power, 50-fs parametric amplifier front-end at 1.55 μm," Optics Express **23**(26), 33157–33163 (2015).

[57] D. Sanchez, M. Hemmer, M. Baudisch, S. L. Cousin, K. Zawilski, P. Schunemann, O. Chalus, C. Simon-Boisson, and J. Biegert, "7 μm, ultrafast, sub-millijoule-level mid-infrared optical parametric chirped pulse amplifier pumped at 2 μm," Optica **3**(2), 147–150 (2016).

[58] P. Malevich, T. Kanai, H. Hoogland, R. Holzwarth, A. Baltuška, and A. Pugžlys, "Broadband mid-infrared pulses from potassium titanyl arsenate/zinc germanium phosphate optical parametric amplifier pumped by Tm, Ho-fiber-seeded Ho:YAG chirped-pulse amplifier," Optics Letters **41**(5), 930–933 (2016).

[59] T. Kanai, P. Malevich, S. S. Kangaparambil, H. Hoogland, R. Holzwarth, A. Pugžlys, and A. Baltuška, "Sub 100-fs, 5.2-μm ZGP Parametric Amplifier Driven by a ps Ho:YAG Chirped Pulse Amplifier and its application to high harmonic generation," in Lasers Congress 2016 (ASSL, LSC, LAC), OSA Technical Digest (online) (Optical Society of America), paper AW4A.4. (2016).

[60] L. v. Grafenstein, M. Bock, U. Griebner, and T. Elsaesser, "600 µJ, 5 µm, 1 kHz Femtosecond Optical Parametric Chirped Pulse Amplifier Pumped at 2 µm," in *Lasers Congress 2016 (ASSL, LSC, LAC) (2016), paper AW4A.6*, p. AW4A.6 (Optical Society of America, 2016).

[61] P. Malevich, G. Andriukaitis, T. Flöry, A. J. Verhoef, A. Fernández, S. Ališauskas, A. Pugžlys, A. Baltuška, L. H. Tan, C. F. Chua, and P. B. Phua, "High energy and average power femtosecond laser for driving mid-infrared optical parametric amplifiers," Optics Letters **38**(15), 2746–2749 (2013).

[62] M. Hemmer, D. Sánchez, M. Jelínek, V. Smirnov, H. Jelinkova, V. Kubeček, and J. Biegert, "2-μm wavelength, high-energy Ho:YLF chirped-pulse amplifier for mid-infrared OPCPA," Optics Letters **40**(4), 451–454 (2015).

[63] L. v. Grafenstein, M. Bock, U. Griebner, and T. Elsaesser, "High-energy multi-kilohertz Ho-doped regenerative amplifiers around 2 µm," Optics Express **23**(11), 14744–14752 (2015).

[64] V. Petrov, "Frequency down-conversion of solid-state laser sources to the mid-infrared spectral range using non-oxide nonlinear crystals," Progress in Quantum Electronics **42**, 1–106 (2015).

[65] O. Chalus, P. K. Bates, and J. Biegert, "Design and simulation of few-cycle optical parametric chirped pulse amplification at mid-IR wavelengths," Optics Express **16**(26), 21297–21304 (2008).

[66] O. Chalus, P. K. Bates, M. Smolarski, and J. Biegert, "Mid-IR short-pulse OPCPA with micro-Joule energy at 100kHz," Optics Express **17**(5), 3587–3594 (2009).

[67] O. Chalus, A. Thai, P. K. Bates, and J. Biegert, "Six-cycle mid-infrared source with 3.8 μJ at 100 kHz," Optics Letters **35**(19), 3204–3206 (2010).

[68] A. Thai, M. Hemmer, P. K. Bates, O. Chalus, and J. Biegert, "Sub-250-mrad, passively carrier–envelope-phase-stable mid-infrared OPCPA source at high repetition rate," Optics Letters **36**(19), 3918–3920 (2011).

[69] M. Hemmer, A. Thai, M. Baudisch, H. Ishizuki, T. Taira, and J. Biegert, "18-µJ energy, 160-kHz repetition rate, 250-MW peak power mid-IR OPCPA," Chinese Optics Letters **11**(1), 013202 (2013).

[70] M. Baudisch, H. Pires, H. Ishizuki, T. Taira, M. Hemmer, and J. Biegert, "Sub-4-optical-cycle, 340 MW peak power, high stability mid-IR source at 160 kHz," Journal of Optics **17**(9), 094002 (2015).

[71] M. Baudisch, B. Wolter, M. Pullen, M. Hemmer, and J. Biegert, "High power multi-color OPCPA source with simultaneous femtosecond deep-UV to mid-IR outputs," Optics Letters **41**(15), 3583–3586 (2016).

[72] J.-C. Diels and W. Rudolph, *Ultrashort Laser Pulse Phenomena*, 2nd ed. (Academic Press, 2006).

[73] R. W. Boyd, *Nonlinear Optics*, 3rd ed. (Academic Press, 2008).

[74] G. Cerullo, A. Baltuška, O. D. Mücke, and C. Vozzi, "Few-optical-cycle light pulses with passive carrier-envelope phase stabilization," Laser & Photonics Reviews **5**(3), 323–351 (2011).

[75] C. Manzoni and G. Cerullo, "Design criteria for ultrafast optical parametric amplifiers," Journal of Optics **18**(10), 103501 (2016).

[76] G. Cerullo and S. D. Silvestri, "Ultrafast optical parametric amplifiers," Review of Scientific Instruments **74**(1), 1–18 (2003).

[77] Y. Zhang, J. Schröder, C. Husko, S. Lefrancois, D.-Y. Choi, S. Madden, B. Luther-Davies, and B. J. Eggleton, "Pump-degenerate phase-sensitive amplification in chalcogenide waveguides," Journal of the Optical Society of America B **31**(4), 780–787 (2014).

[78] I. N. Ross, P. Matousek, G. H. C. New, and K. Osvay, "Analysis and optimization of optical parametric chirped pulse amplification," Journal of the Optical Society of America B **19**(12), 2945–2956 (2002).

[79] J. M. Manley and H. E. Rowe, "Some General Properties of Nonlinear Elements-Part I. General Energy Relations," Proceedings of the IRE **44**(7), 904–913 (1956).

[80] D. S. Hum and M. M. Fejer, "Quasi-phasematching," Comptes Rendus Physique **8**(2), 180–198 (2007).

[81] T. Skauli, K. L. Vodopyanov, T. J. Pinguet, A. Schober, O. Levi, L. A. Eyres, M. M. Fejer, J. S. Harris, B. Gerard, L. Becouarn, E. Lallier, and G. Arisholm, "Measurement of the nonlinear coefficient of orientation-patterned GaAs and demonstration of highly efficient second-harmonic generation," Optics Letters **27**(8), 628–630 (2002).

[82] L. Hongjun, Z. Wei, C. Guofu, W. Yishan, C. Zhao, and R. Chi, "Investigation of spectral bandwidth of optical parametric amplification," Applied Physics B **79**(5), 569–576 (2004).

[83] H. R. Telle, G. Steinmeyer, A. E. Dunlop, J. Stenger, D. H. Sutter, and U. Keller, "Carrier-envelope offset phase control: A novel concept for absolute optical frequency measurement and ultrashort pulse generation," Applied Physics B **69**(4), 327–332 (1999).

[84] A. Apolonski, A. Poppe, G. Tempea, C. Spielmann, T. Udem, R. Holzwarth, T. W. Hänsch, and F. Krausz, "Controlling the Phase Evolution of Few-Cycle Light Pulses," Physical Review Letters **85**(4), 740 (2000).

[85] L. Xu, T. W. Hänsch, C. Spielmann, A. Poppe, T. Brabec, and F. Krausz, "Route to phase control of ultrashort light pulses," Optics Letters **21**(24), 2008–2010 (1996).

[86] M. Hangyo, M. Tani, and T. Nagashima, "Terahertz Time-Domain Spectroscopy of Solids: A Review," International Journal of Infrared and Millimeter Waves **26**(12), 1661–1690 (2005).

[87] A. Baltuska, M. Uiberacker, E. Goulielmakis, R. Kienberger, V. S. Yakovlev, T. Udem, T. W. Hansch, and F. Krausz, "Phase-controlled amplification of few-cycle laser pulses," IEEE Journal of Selected Topics in Quantum Electronics **9**(4), 972–989 (2003).

[88] A. Baltuska, T. Fuji, and T. Kobayashi, "Controlling the Carrier-Envelope Phase of Ultrashort Light Pulses with Optical Parametric Amplifiers," Physical Review Letters **88**(13), 133901 (2002).

[89] Q. Wu and X.-C. Zhang, "Free-space electro-optic sampling of terahertz beams," Applied Physics Letters **67**(24), 3523–3525 (1995).

[90] E. Treacy, "Optical pulse compression with diffraction gratings," IEEE Journal of Quantum Electronics **5**(9), 454–458 (1969).

[91] R. L. Fork, O. E. Martinez, and J. P. Gordon, "Negative dispersion using pairs of prisms," Optics Letters **9**(5), 150–152 (1984).

[92] O. Martinez, "3000 times grating compressor with positive group velocity dispersion: Application to fiber compensation in 1.3-1.6 μm region," IEEE Journal of Quantum Electronics **23**(1), 59–64 (1987).

[93] S. Kane and J. Squier, "Grating compensation of third-order material dispersion in the normal dispersion regime: Sub-100-fs chirped-pulse amplification using a fiber stretcher and grating-pair compressor," IEEE Journal of Quantum Electronics **31**(11), 2052–2057 (1995).

[94] R. Szipöcs, C. Spielmann, F. Krausz, and K. Ferencz, "Chirped multilayer coatings for broadband dispersion control in femtosecond lasers," Optics Letters **19**(3), 201–203 (1994).

[95] A. Galvanauskas, A. Heaney, T. Erdogan, and D. Harter, "Use of volume chirped Bragg gratings for compact high-energy chirped pulse amplification circuits," p. 362 (IEEE, 1998).

[96] A. M. Weiner, "Femtosecond pulse shaping using spatial light modulators," Review of Scientific Instruments **71**(5), 1929–1960 (2000).

[97] P. Tournois, "Acousto-optic programmable dispersive filter for adaptive compensation of group delay time dispersion in laser systems," Optics Communications **140**(4-6), 245–249 (1997).

[98] S. Kane, "A tutorial on pulse compression systems: how to calculate GVD and TOD of anything that includes materials, gratings, prisms, and reflection grisms," Diffraction Gratings Division, HORIBA Jobin Yvon Inc. (2010).

[99] I. Walmsley, L. Waxer, and C. Dorrer, "The role of dispersion in ultrafast optics," Review of Scientific Instruments **72**(1), 1–29 (2001).

[100] H. H. Li, "Refractive index of alkaline earth halides and its wavelength and temperature derivatives," Journal of Physical and Chemical Reference Data **9**(1), 161–290 (1980).

[101] I. H. Malitson, "A Redetermination of Some Optical Properties of Calcium Fluoride," Applied Optics **2**(11), 1103–1107 (1963).

[102] I. H. Malitson, "Refraction and Dispersion of Synthetic Sapphire," Journal of the Optical Society of America **52**(12), 1377–1379 (1962).

[103] M. J. W. Rodwell, D. M. Bloom, and K. J. Weingarten, "Subpicosecond laser timing stabilization," IEEE Journal of Quantum Electronics **25**(4), 817–827 (1989).

[104] O. Paul, A. Quosig, T. Bauer, M. Nittmann, J. Bartschke, G. Anstett, and J. A. L'huillier, "Temperature-dependent Sellmeier equation in the MIR for the extraordinary refractive index of 5% MgO doped congruent LiNbO3," Applied Physics B **86**(1), 111–115 (2006).

[105] H. Ishizuki and T. Taira, "High-energy quasi-phase-matched optical parametric oscillation in a periodically poled MgO:$LiNbO_3$ device with a 5 mm×5 mm aperture," Optics Letters **30**(21), 2918–2920 (2005).

[106] H. Ishizuki and T. Taira, "Half-joule output optical-parametric oscillation by using 10-mm-thick periodically poled Mg-doped congruent $LiNbO_3$," Optics Express **20**(18), 20002–20010 (2012).

[107] D. E. Zelmon, D. L. Small, and D. Jundt, "Infrared corrected Sellmeier coefficients for congruently grown lithium niobate and 5 mol. % magnesium oxide–doped lithium niobate," Journal of the Optical Society of America B **14**(12), 3319–3322 (1997).

[108] L.-S. Ma, R. K. Shelton, H. C. Kapteyn, M. M. Murnane, and J. Ye, "Sub-10-femtosecond active synchronization of two passively mode-locked Ti:sapphire oscillators," Physical Review A **64**(2), 021802 (2001).

[109] T. R. Schibli, J. Kim, O. Kuzucu, J. T. Gopinath, S. N. Tandon, G. S. Petrich, L. A. Kolodziejski, J. G. Fujimoto, E. P. Ippen, and F. X. Kaertner, "Attosecond active synchronization of passively mode-locked lasers by balanced cross correlation," Optics Letters **28**(11), 947–949 (2003).

[110] D. Zhang, Y. Kong, and J.-y. Zhang, "Optical parametric properties of 532-nm-pumped beta-barium-borate near the infrared absorption edge," Optics Communications **184**(5–6), 485–491 (2000).

[111] S. Prinz, M. Haefner, C. Y. Teisset, R. Bessing, K. Michel, Y. Lee, X. T. Geng, S. Kim, D. E. Kim, T. Metzger, and M. Schultze, "CEP-stable, sub-6 fs, 300-kHz OPCPA system with more than 15 W of average power," Optics Express **23**(2), 1388–1394 (2015).

[112] R. Budriūnas, T. Stanislauskas, J. Adamonis, A. Aleknavičius, G. Veitas, D. Gadonas, S. Balickas, A. Michailovas, and A. Varanavičius, "53 W average power CEP-stabilized OPCPA system delivering 5.5 TW few cycle pulses at 1 kHz repetition rate," Optics Express **25**(5), 5797–5806 (2017).

[113] K. Takachiho, M. Yoshimura, Y. Takahashi, M. Imade, T. Sasaki, and Y. Mori, "Ultraviolet laser-induced degradation of $CsLiB_6O_{10}$ and β-BaB_2O_4," Optical Materials Express **4**(3), 559–567 (2014).

[114] T. Sasaki, Y. Mori, M. Yoshimura, Y. K. Yap, and T. Kamimura, "Recent development of nonlinear optical borate crystals: key materials for generation of visible and UV light," Materials Science and Engineering: R: Reports **30**(1–2), 1–54 (2000).

[115] C. Chen, J. Lu, T. Togashi, T. Suganuma, T. Sekikawa, S. Watanabe, Z. Xu, and J. Wang, "Second-harmonic generation from a $KBe_2BO_3F_2$ crystal in the deep ultraviolet," Optics Letters **27**(8), 637–639 (2002).

[116] C. T. Chen, G. L. Wang, X. Y. Wang, and Z. Y. Xu, "Deep-UV nonlinear optical crystal KBe2BO3F2—discovery, growth, optical properties and applications," Applied Physics B **97**(1), 9–25 (2009).

[117] J. Hirohashi, T. Taniuchi, K. Imai, and Y. Furukawa, "PP-LBGO device with 2nd-order QPM structure for 266nm generation," in *CLEO: 2015 (2015), paper STh3H.5*, p. STh3H.5 (Optical Society of America, 2015).

[118] C. Homann, N. Krebs, and E. Riedle, "Convenient pulse length measurement of sub-20-fs pulses down to the deep UV via two-photon absorption in bulk material," Applied Physics B **104**(4), 783 (2011).

[119] Y. Nabekawa and K. Midorikawa, "Group-delay-dispersion-matched sum-frequency mixing for the indirect phase control of deep ultraviolet pulses in the sub-20-fs regime," Applied Physics B **78**(5), 569–581 (2004).

[120] H. Liu, W. Zhao, Y. Yang, H. Wang, Y. Wang, and G. Chen, "Matching of both group-velocity and pulse-front for ultrabroadband three-wave-mixing with noncollinear angularly dispersed geometry," Applied Physics B **82**(4), 585–594 (2006).

[121] P. Baum, S. Lochbrunner, and E. Riedle, "Generation of tunable 7-fs ultraviolet pulses: achromatic phase matching and chirp management," Applied Physics B **79**(8), 1027–1032 (2004).

[122] R. B. Varillas, A. Candeo, D. Viola, M. Garavelli, S. D. Silvestri, G. Cerullo, and C. Manzoni, "Microjoule-level, tunable sub-10 fs UV pulses by broadband sum-frequency generation," Optics Letters **39**(13), 3849–3852 (2014).

[123] P. E. Ciddor, "Refractive index of air: new equations for the visible and near infrared," Applied Optics **35**(9), 1566–1573 (1996).

[124] Y. Shamir, J. Rothhardt, S. Hädrich, S. Demmler, M. Tschernajew, J. Limpert, and A. Tünnermann, "High-average-power 2 μm few-cycle optical parametric chirped pulse amplifier at 100 kHz repetition rate," Optics Letters **40**(23), 5546–5549 (2015).

[125] F. Seifert, V. Petrov, and M. Woerner, "Solid-state laser system for the generation of midinfrared femtosecond pulses tunable from 3.3 to 10 μm," Optics Letters **19**(23), 2009–2011 (1994).

[126] C. Manzoni, D. Polli, and G. Cerullo, "Two-color pump-probe system broadly tunable over the visible and the near infrared with sub-30fs temporal resolution," Review of Scientific Instruments **77**(2), 023103 (2006).

[127] S.-W. Huang, G. Cirmi, J. Moses, K.-H. Hong, S. Bhardwaj, J. R. Birge, L.-J. Chen, E. Li, B. J. Eggleton, G. Cerullo, and F. X. Kärtner, "High-energy pulse synthesis with sub-cycle waveform control for strong-field physics," Nature Photonics **5**(8), 475–479 (2011).

[128] B. Wolter, C. Lemell, M. Baudisch, M. G. Pullen, X.-M. Tong, M. Hemmer, A. Senftleben, C. D. Schröter, J. Ullrich, R. Moshammer, J. Biegert, and J. Burgdörfer, "Formation of very-low-energy states crossing the ionization threshold of argon atoms in strong mid-infrared fields," Physical Review A **90**(6), 063424 (2014).

[129] K. F. Mak, J. C. Travers, N. Y. Joly, A. Abdolvand, and P. S. J. Russell, "Two techniques for temporal pulse compression in gas-filled hollow-core kagomé photonic crystal fiber," Optics Letters **38**(18), 3592–3595 (2013).

[130] T. Balciunas, C. Fourcade-Dutin, G. Fan, T. Witting, A. A. Voronin, A. M. Zheltikov, F. Gerome, G. G. Paulus, A. Baltuska, and F. Benabid, "A strong-field driver in the single-cycle regime based on self-compression in a kagome fibre," Nature Communications **6** (2015).

[131] F. Belli, A. Abdolvand, W. Chang, J. C. Travers, and P. S. J. Russell, "Vacuum-ultraviolet to infrared supercontinuum in hydrogen-filled photonic crystal fiber," Optica **2**(4), 292–300 (2015).

[132] K. F. Mak, J. C. Travers, P. Hölzer, N. Y. Joly, and P. S. J. Russell, "Tunable vacuum-UV to visible ultrafast pulse source based on gas-filled Kagome-PCF," Optics Express **21**(9), 10942–10953 (2013).

[133] L. E. Chipperfield, J. S. Robinson, J. W. G. Tisch, and J. P. Marangos, "Ideal Waveform to Generate the Maximum Possible Electron Recollision Energy for Any Given Oscillation Period," Physical Review Letters **102**(6), 063003 (2009).

[134] G. Arisholm, R. Paschotta, and T. Südmeyer, "Limits to the power scalability of high-gain optical parametric amplifiers," Journal of the Optical Society of America B **21**(3), 578–590 (2004).

[135] M. J. Guardalben, J. Keegan, L. J. Waxer, V. Bagnoud, I. A. Begishev, J. Puth, and J. D. Zuegel, "Design of a highly stable, high-conversion-efficiency, optical parametric chirped-pulse amplification system with good beam quality," Optics Express **11**(20), 2511–2524 (2003).

[136] J. Moses and S.-W. Huang, "Conformal profile theory for performance scaling of ultrabroadband optical parametric chirped pulse amplification," Journal of the Optical Society of America B **28**(4), 812–831 (2011).

[137] L. J. Waxer, V. Bagnoud, I. A. Begishev, M. J. Guardalben, J. Puth, and J. D. Zuegel, "High-conversion-efficiency optical parametric chirped-pulse amplification system using spatiotemporally shaped pump pulses," Optics Letters **28**(14), 1245–1247 (2003).

[138] N. Ishii, L. Turi, V. S. Yakovlev, T. Fuji, F. Krausz, A. Baltuška, R. Butkus, G. Veitas, V. Smilgevičius, R. Danielius, and A. Piskarskas, "Multimillijoule chirped parametric amplification of few-cycle pulses," Optics Letters **30**(5), 567–569 (2005).

[139] H. Okada, H. Kiriyama, M. Mori, Y. Nakai, T. Shimomura, M. Tanoue, S. Kondo, S. Kanazawa, H. Daido, T. Kimura, and T. Tajima, "Demonstration of highly efficient broadband amplification in a optical parametric chirped-pulse amplifier system," Optical Review **16**(1), 1–3 (2009).

[140] I. A. Begishev, A. A. Gulamov, E. A. Erofeev, É. A. Ibragimov, S. R. Kamalov, T. Usmanov, and A. D. Khadzhaev, "Highly efficient parametric amplification of optical beams. I. Optimization of the profiles of interacting waves in parametric amplification," Soviet Journal of Quantum Electronics **20**(9), 1100 (1990).

[141] I. A. Begishev, A. A. Gulamov, E. A. Erofeev, É. A. Ibragimov, S. R. Kamalov, T. Usmanov, and A. D. Khadzhaev, "Highly efficient parametric amplification of optical beams. II. Parametric interaction of waves with conformal profiles," Soviet Journal of Quantum Electronics **20**(9), 1104 (1990).

[142] W. B. Veldkamp, "Laser beam profile shaping with interlaced binary diffraction gratings," Applied Optics **21**(17), 3209–3212 (1982).

[143] R. Riedel, J. Rothhardt, K. Beil, B. Gronloh, A. Klenke, H. Höppner, M. Schulz, U. Teubner, C. Kränkel, J. Limpert, A. Tünnermann, M. J. Prandolini, and F. Tavella, "Thermal properties of borate crystals for high power optical parametric chirped-pulse amplification," Optics Express **22**(15), 17607–17619 (2014).

[144] F. Bach, M. Mero, M.-H. Chou, and V. Petrov, "Laser induced damage studies of $LiNbO_3$ using 1030-nm, ultrashort pulses at 10-1000 kHz," Optical Materials Express **7**(1), 240–252 (2017).

[145] T. Fuji, N. Ishii, C. Y. Teisset, X. Gu, T. Metzger, A. Baltuska, N. Forget, D. Kaplan, A. Galvanauskas, and F. Krausz, "Parametric amplification of few-cycle carrier-envelope phase-stable pulses at 2.1 μm," Optics Letters **31**(8), 1103–1105 (2006).

[146] V. G. Dmitriev, G. G. Gurzadyan, and D. N. Nikogosyan, *Handbook of Nonlinear Optical Crystals* (Springer, 1999).

[147] G. Hansson, H. Karlsson, S. Wang, and F. Laurell, "Transmission measurements in KTP and isomorphic compounds," Applied Optics **39**(27), 5058–5069 (2000).

[148] L. Xian-jie, Z. Xing-kui, and X. Xiu-ying, "Domain Patterns and Phase Transitions in Ferroelectric Crystal KNbO3," Chinese Physics Letters **13**(8), 621 (1996).

[149] M. M. Shamim and T. Ishidate, "Anomalous mode coupling and phase transition of KNbO3 under high pressure," Solid State Communications **113**(12), 713–717 (2000).

[150] Y. Furukawa, K. Kitamura, A. Alexandrovski, R. K. Route, M. M. Fejer, and G. Foulon, "Green-induced infrared absorption in MgO doped LiNbO3," Applied Physics Letters **78**(14), 1970–1972 (2001).

[151] P. Blau, S. Pearl, A. Englander, A. Bruner, and D. Eger, "Average power effects in periodically poled crystals," pp. 34–41 (International Society for Optics and Photonics, 2003).

[152] A. Ashkin, G. D. Boyd, J. M. Dziedzic, R. G. Smith, A. A. Ballman, J. J. Levinstein, and K. Nassau, "Optically-induced refractive index inhomogeneities in LiNbO3 and LiTaO3," Applied Physics Letters **9**(1), 72–74 (1966).

[153] J. R. Schwesyg, M. Falk, C. R. Phillips, D. H. Jundt, K. Buse, and M. M. Fejer, "Pyroelectrically induced photorefractive damage in magnesium-doped lithium niobate crystals," Journal of the Optical Society of America B **28**(8), 1973–1987 (2011).

[154] Y. Furukawa, K. Kitamura, S. Takekawa, A. Miyamoto, M. Terao, and N. Suda, "Photorefraction in LiNbO3 as a function of [Li]/[Nb] and MgO concentrations," Applied Physics Letters **77**(16), 2494–2496 (2000).

[155] M. Asobe, O. Tadanaga, T. Yanagawa, H. Itoh, and H. Suzuki, "Reducing photorefractive effect in periodically poled ZnO- and MgO-doped LiNbO3 wavelength converters," Applied Physics Letters **78**(21), 3163–3165 (2001).

[156] N. Umemura, K. Yoshida, and K. Kato, "Phase-matching properties of $KNbO_3$ in the mid-infrared," Applied Optics **38**(6), 991–994 (1999).

[157] ISO_11146:2005, "Lasers and laser-related equipment - Test methods for laser beam widths, divergence angles and beam propagation ratios," (2005).

[158] A. Thai, R. Maksimenka, C. Ferchaud, N. Thiré, and N. Forget, "Few-Cycle Mid-IR OPCPA Front-end At 100 kHz with sub-50 mrad CEP-Stability," in *Conference on Lasers and Electro-Optics (2016), paper SM3I.1*, p. SM3I.1 (Optical Society of America, 2016).

[159] W. W. Simmons, G. W. Leppelmeier, and B. C. Johnson, "Optical Beam Shaping Devices Using Polarization Effects," Applied Optics **13**(7), 1629–1632 (1974).

[160] J. A. Hoffnagle and C. M. Jefferson, "Design and performance of a refractive optical system that converts a Gaussian to a flattop beam," Applied Optics **39**(30), 5488–5499 (2000).

[161] J. Rothhardt, S. Hädrich, T. Gottschall, J. Limpert, A. Tünnermann, M. Rothhardt, M. Becker, S. Brückner, and H. Bartelt, "Generation of flattop pump pulses for OPCPA by coherent pulse stacking with fiber Bragg gratings," Optics Express **17**(18), 16332–16341 (2009).

[162] J. A. Fülöp, Z. Major, B. Horváth, F. Tavella, A. Baltuška, and F. Krausz, "Shaping of picosecond pulses for pumping optical parametric amplification," Applied Physics B **87**(1), 79–84 (2006).

[163] B. E. Schmidt, N. Thiré, M. Boivin, A. Laramée, F. Poitras, G. Lebrun, T. Ozaki, H. Ibrahim, and F. Légaré, "Frequency domain optical parametric amplification," Nature Communications **5** (2014).

[164] Y. Deng and F. Krausz, "Method and device for optical parametric chirped pulse amplification," US patent, US 9057930 B2 (2015).

[165] H. Fattahi, "Third-generation femtosecond technology," dissertation thesis, Ludwig–Maximilians–Universität München, Germany (2015).

[166] F. C. Cruz, D. L. Maser, T. Johnson, G. Ycas, A. Klose, F. R. Giorgetta, I. Coddington, and S. A. Diddams, "Mid-infrared optical frequency combs based on difference frequency generation for molecular spectroscopy," Optics Express **23**(20), 26814–26824 (2015).

[167] L. E. Zapata, F. Reichert, M. Hemmer, and F. X. Kärtner, "250 W average power, 100 kHz repetition rate cryogenic Yb:YAG amplifier for OPCPA pumping," Optics Letters **41**(3), 492–495 (2016).

[168] P. H. Rußbüldt, T. Mans, G. Rotarius, D. Hoffmann, R. Poprawe, T. Eidam, J. Limpert, and A. Tünnermann, "Hybrid 400W Fiber-Innoslab fs-Amplifier," in *Advanced Solid-State Photonics (2009), paper MF4*, p. MF4 (Optical Society of America, 2009).

[169] J.-P. Negel, A. Loescher, A. Voss, D. Bauer, D. Sutter, A. Killi, M. A. Ahmed, and T. Graf, "Ultrafast thin-disk multipass laser amplifier delivering 1.4 kW (4.7 mJ, 1030 nm) average power converted to 820 W at 515 nm and 234 W at 343 nm," Optics Express **23**(16), 21064–21077 (2015).

[170] M. Kienel, M. Müller, A. Klenke, J. Limpert, and A. Tünnermann, "12 mJ kW-class ultrafast fiber laser system using multidimensional coherent pulse addition," Optics Letters **41**(14), 3343–3346 (2016).

[171] A. Vaupel, N. Bodnar, B. Webb, L. Shah, and M. Richardson, "Concepts, performance review, and prospects of table-top, few-cycle optical parametric chirped-pulse amplification," Optical Engineering **53**(5), 051507 (2014).

[172] M. N. Zervas and C. A. Codemard, "High Power Fiber Lasers: A Review," IEEE Journal of Selected Topics in Quantum Electronics **20**(5), 219–241 (2014).

[173] P. Russbueldt, D. Hoffmann, M. Höfer, J. Löhring, J. Luttmann, A. Meissner, J. Weitenberg, M. Traub, T. Sartorius, D. Esser, R. Wester, P. Loosen, and R. Poprawe, "Innoslab Amplifiers," IEEE Journal of Selected Topics in Quantum Electronics **21**(1), 447–463 (2015).

[174] A. Giesen and J. Speiser, "Fifteen Years of Work on Thin-Disk Lasers: Results and Scaling Laws," IEEE Journal of Selected Topics in Quantum Electronics **13**(3), 598–609 (2007).

[175] M. Hemmer, M. Baudisch, A. Thai, A. Couairon, and J. Biegert, "Self-compression to sub-3-cycle duration of mid-infrared optical pulses in dielectrics," Optics Express **21**(23), 28095–28102 (2013).

[176] M. Schultze, M. Fieß, N. Karpowicz, J. Gagnon, M. Korbman, M. Hofstetter, S. Neppl, A. L. Cavalieri, Y. Komninos, T. Mercouris, C. A. Nicolaides, R. Pazourek, S. Nagele, J. Feist, J. Burgdörfer, A. M. Azzeer, R. Ernstorfer, R. Kienberger, U. Kleineberg, E. Goulielmakis, F. Krausz, and V. S. Yakovlev, "Delay in Photoemission," Science **328**(5986), 1658–1662 (2010).

[177] I. D. Jung, F. X. Kärtner, N. Matuschek, D. H. Sutter, F. Morier-Genoud, G. Zhang, U. Keller, V. Scheuer, M. Tilsch, and T. Tschudi, "Self-starting 6.5-fs pulses from a Ti:sapphire laser," Optics Letters **22**(13), 1009–1011 (1997).

[178] D. H. Sutter, L. Gallmann, N. Matuschek, F. Morier-Genoud, V. Scheuer, G. Angelow, T. Tschudi, G. Steinmeyer, and U. Keller, "Sub-6-fs pulses from a SESAM-assisted Kerr-lens modelocked Ti:sapphire laser: at the frontiers of ultrashort pulse generation," Applied Physics B **70**(1), S5–S12 (2000).

[179] K. Yamakawa, M. Aoyama, S. Matsuoka, H. Takuma, C. P. J. Barty, and D. Fittinghoff, "Generation of 16-fs, 10-TW pulses at a 10-Hz repetition rate with efficient Ti:sapphire amplifiers," Optics Letters **23**(7), 525–527 (1998).

[180] Y. Nabekawa, A. A. Eilanlou, Y. Furukawa, K. L. Ishikawa, H. Takahashi, and K. Midorikawa, "Multi-terawatt laser system generating 12-fs pulses at 100 Hz repetition rate," Applied Physics B **101**(3), 523–534 (2010).

[181] A. Harth, M. Schultze, T. Lang, T. Binhammer, S. Rausch, and U. Morgner, "Two-color pumped OPCPA system emitting spectra spanning 1.5 octaves from VIS to NIR," Optics Express **20**(3), 3076–3081 (2012).

[182] M. Nisoli, S. D. Silvestri, O. Svelto, R. Szipöcs, K. Ferencz, C. Spielmann, S. Sartania, and F. Krausz, "Compression of high-energy laser pulses below 5 fs," Optics Letters **22**(8), 522–524 (1997).

[183] A. Suda, M. Hatayama, K. Nagasaka, and K. Midorikawa, "Generation of sub-10-fs, 5-mJ-optical pulses using a hollow fiber with a pressure gradient," Applied Physics Letters **86**(11), 111116 (2005).

[184] B. Schenkel, J. Biegert, U. Keller, C. Vozzi, M. Nisoli, G. Sansone, S. Stagira, S. D. Silvestri, and O. Svelto, "Generation of 3.8-fs pulses from adaptive compression of a cascaded hollow fiber supercontinuum," Optics Letters **28**(20), 1987–1989 (2003).

[185] A. L. Cavalieri, E. Goulielmakis, B. Horvath, W. Helml, M. Schultze, M. Fieß, V. Pervak, L. Veisz, V. S. Yakovlev, M. Uiberacker, A. Apolonski, F. Krausz, and R. Kienberger, "Intense 1.5-cycle near infrared laser waveforms and their use for the generation of ultra-broadband soft-x-ray harmonic continua," New Journal of Physics **9**(7), 242 (2007).

[186] J. Park, J.-h. Lee, and C. H. Nam, "Generation of 1.5 cycle 0.3 TW laser pulses using a hollow-fiber pulse compressor," Optics Letters **34**(15), 2342–2344 (2009).

[187] S. Bohman, A. Suda, M. Kaku, M. Nurhuda, T. Kanai, S. Yamaguchi, and K. Midorikawa, "Generation of 5 fs, 0.5 TW pulses focusable to relativistic intensities at 1 kHz," Optics Express **16**(14), 10684–10689 (2008).

[188] P. Sprangle, E. Esarey, and J. Krall, "Self-guiding and stability of intense optical beams in gases undergoing ionization," Physical Review E **54**(4), 4211 (1996).

[189] A. Braun, G. Korn, X. Liu, D. Du, J. Squier, and G. Mourou, "Self-channeling of high-peak-power femtosecond laser pulses in air," Optics Letters **20**(1), 73–75 (1995).

[190] C. P. Hauri, W. Kornelis, F. W. Helbing, A. Heinrich, A. Couairon, A. Mysyrowicz, J. Biegert, and U. Keller, "Generation of intense, carrier-envelope phase-locked few-cycle laser pulses through filamentation," Applied Physics B **79**(6), 673–677 (2004).

[191] C. P. Hauri, A. Guandalini, P. Eckle, W. Kornelis, J. Biegert, and U. Keller, "Generation of intense few-cycle laser pulses through filamentation – parameter dependence," Optics Express **13**(19), 7541–7547 (2005).

[192] X. Chen, X. Li, J. Liu, P. Wei, X. Ge, R. Li, and Z. Xu, "Generation of 5 fs, 0.7 mJ pulses at 1 kHz through cascade filamentation," Optics Letters **32**(16), 2402–2404 (2007).

[193] L. Gallmann, T. Pfeifer, P. M. Nagel, M. J. Abel, D. M. Neumark, and S. R. Leone, "Comparison of the filamentation and the hollow-core fiber characteristics for pulse compression into the few-cycle regime," Applied Physics B **86**(4), 561–566 (2006).

[194] J. Kasparian, R. Sauerbrey, and S. L. Chin, "The critical laser intensity of self-guided light filaments in air," Applied Physics B **71**(6), 877–879 (2000).

[195] G. Stibenz, N. Zhavoronkov, and G. Steinmeyer, "Self-compression of millijoule pulses to 7.8 fs duration in a white-light filament," Optics Letters **31**(2), 274–276 (2006).

[196] A. Couairon, M. Franco, A. Mysyrowicz, J. Biegert, and U. Keller, "Pulse self-compression to the single-cycle limit by filamentation in a gas with a pressure gradient," Optics Letters **30**(19), 2657–2659 (2005).

[197] A. Couairon, J. Biegert, C. P. Hauri, W. Kornelis, F. W. Helbing, U. Keller, and A. Mysyrowicz, "Self-compression of ultra-short laser pulses down to one optical cycle by filamentation," Journal of Modern Optics **53**, 75–85 (2006).

[198] C. P. Hauri, R. B. Lopez-Martens, C. I. Blaga, K. D. Schultz, J. Cryan, R. Chirla, P. Colosimo, G. Doumy, A. M. March, C. Roedig, E. Sistrunk, J. Tate, J. Wheeler, L. F. DiMauro, and E. P. Power, "Intense self-compressed, self-phase-stabilized few-cycle pulses at 2 μm from an optical filament," Optics Letters **32**(7), 868–870 (2007).

[199] A. V. Mitrofanov, A. A. Voronin, D. A. Sidorov-Biryukov, S. I. Mitryukovsky, A. B. Fedotov, E. E. Serebryannikov, D. V. Meshchankin, V. Shumakova, S. Ališauskas, A. Pugžlys, V. Y. Panchenko, A. Baltuška, and A. M. Zheltikov, "Subterawatt few-cycle mid-infrared pulses from a single filament," Optica **3**(3), 299–302 (2016).

[200] G. Genty, S. Coen, and J. M. Dudley, "Fiber supercontinuum sources (Invited)," Journal of the Optical Society of America B **24**(8), 1771–1785 (2007).

[201] J. Swiderski, "High-power mid-infrared supercontinuum sources: Current status and future perspectives," Progress in Quantum Electronics **38**(5), 189–235 (2014).

[202] S. V. Chernikov, D. J. Richardson, D. N. Payne, and E. M. Dianov, "Soliton pulse compression in dispersion-decreasing fiber," Optics Letters **18**(7), 476–478 (1993).

[203] M. D. Pelusi and H.-F. Liu, "Higher order soliton pulse compression in dispersion-decreasing optical fibers," IEEE Journal of Quantum Electronics **33**(8), 1430–1439 (1997).

[204] A. C. Peacock, "Mid-IR soliton compression in silicon optical fibers and fiber tapers," Optics Letters **37**(5), 818–820 (2012).

[205] M. Durand, A. Jarnac, A. Houard, Y. Liu, S. Grabielle, N. Forget, A. Durécu, A. Couairon, and A. Mysyrowicz, "Self-Guided Propagation of Ultrashort Laser Pulses in the Anomalous Dispersion Region of Transparent Solids: A New Regime of Filamentation," Physical Review Letters **110**(11), 115003 (2013).

[206] M. A. Porras, A. Parola, and P. D. Trapani, "Nonlinear unbalanced O waves: nonsolitary, conical light bullets in nonlinear dissipative media," Journal of the Optical Society of America B **22**(7), 1406–1413 (2005).

[207] K. D. Moll and A. L. Gaeta, "Role of dispersion in multiple-collapse dynamics," Optics Letters **29**(9), 995–997 (2004).

[208] M. Kolesik, E. M. Wright, and J. V. Moloney, "Interpretation of the spectrally resolved far field of femtosecond pulses propagating in bulk nonlinear dispersive media," Optics Express **13**(26), 10729–10741 (2005).

[209] A. Couairon and A. Mysyrowicz, "Femtosecond filamentation in transparent media," Physics Reports **441**(2-4), 47–189 (2007).

[210] Y.-N. Xu and W.-Y. Ching, "Electronic structure of yttrium aluminum garnet ($Y_3Al_5O_{12}$)," Physical Review B **59**(16), 10530 (1999).

[211] J. E. Rothenberg and D. Grischkowsky, "Observation of the Formation of an Optical Intensity Shock and Wave Breaking in the Nonlinear Propagation of Pulses in Optical Fibers," Physical Review Letters **62**(5), 531 (1989).

[212] G. Fibich and A. L. Gaeta, "Critical power for self-focusing in bulk media and in hollow waveguides," Optics Letters **25**(5), 335–337 (2000).

[213] B. L. Fontaine, F. Vidal, Z. Jiang, C. Y. Chien, D. Comtois, A. Desparois, T. W. Johnston, J.-C. Kieffer, H. Pépin, and H. P. Mercure, "Filamentation of ultrashort pulse laser beams resulting from their propagation over long distances in air," Physics of Plasmas (1994-present) **6**(5), 1615–1621 (1999).

[214] M. Rodriguez, R. Bourayou, G. Méjean, J. Kasparian, J. Yu, E. Salmon, A. Scholz, B. Stecklum, J. Eislöffel, U. Laux, A. P. Hatzes, R. Sauerbrey, L. Wöste, and J.-P. Wolf, "Kilometer-range nonlinear propagation of femtosecond laser pulses," Physical Review E **69**(3), 036607 (2004).

[215] O. D. Mücke, S. Ališauskas, A. J. Verhoef, A. Pugžlys, A. Baltuška, V. Smilgevičius, J. Pocius, L. Giniūnas, R. Danielius, and N. Forget, "Self-compression of millijoule 1.5 μm pulses," Optics Letters **34**(16), 2498–2500 (2009).

[216] A. Mysyrowicz, A. Couairon, and U. Keller, "Self-compression of optical laser pulses by filamentation," New Journal of Physics **10**(2), 025023 (2008).

[217] Á. Börzsönyi, Z. Heiner, A. P. Kovács, M. P. Kalashnikov, and K. Osvay, "Measurement of pressure dependent nonlinear refractive index of inert gases," Optics Express **18**(25), 25847–25854 (2010).

[218] R. Adair, L. L. Chase, and S. A. Payne, "Nonlinear refractive index of optical crystals," Physical Review B **39**(5), 3337 (1989).

[219] W. F. Krupke, M. D. Shinn, J. E. Marion, J. A. Caird, and S. E. Stokowski, "Spectroscopic, optical, and thermomechanical properties of neodymium- and chromium-doped gadolinium scandium gallium garnet," Journal of the Optical Society of America B **3**(1), 102–114 (1986).

[220] D. E. Zelmon, D. L. Small, and R. Page, "Refractive-index measurements of undoped yttrium aluminum garnet from 0.4 to 5.0 μm," Applied Optics **37**(21), 4933–4935 (1998).

[221] D. E. Zelmon, K. L. Schepler, S. Guha, D. J. Rush, S. M. Hegde, L. P. Gonzalez, and J. Lee, "Optical properties of Nd-doped ceramic yttrium aluminum garnet," pp. 255–264 (International Society for Optics and Photonics, 2005).

[222] A. Couairon, V. Jukna, J. Darginavičius, D. Majus, N. Garejev, I. Gražulevičiūtė, G. Valiulis, G. Tamošauskas, A. Dubietis, F. Silva, D. R. Austin, M. Hemmer, M. Baudisch, A. Thai, J. Biegert, D. Faccio, A. Jarnac, A. Houard, Y. Liu, A. Mysyrowicz, S. Grabielle, N. Forget, A. Durécu, M. Durand, K. Lim, E. McKee, M. Baudelet, and M. Richardson, "Filamentation and Pulse Self-compression in the Anomalous Dispersion Region of Glasses," chapter in "Laser Filamentation", by A. D. Bandrauk et. al., pp. 147-165, Springer International Publishing Switzerland (2016).

[223] A. Couairon, E. Brambilla, T. Corti, D. Majus, O. d. J. Ramírez-Góngora, and M. Kolesik, "Practitioner's guide to laser pulse propagation models and simulation," The European Physical Journal Special Topics **199**(1), 5–76 (2011).

[224] E. D. Filer, C. A. Morrison, G. A. Turner, and N. P. Barnes, *Advanced Solid-State Lasers* (Optical Society of America, 1990).

[225] F. Silva, D. R. Austin, A. Thai, M. Baudisch, M. Hemmer, D. Faccio, A. Couairon, and J. Biegert, "Multi-octave supercontinuum generation from mid-infrared filamentation in a bulk crystal," Nature Communications **3**, 807 (2012).

[226] F. Silva, "Generation of intense few-cycle phase-stable electric fields: from the mid-IR to soft X-rays," dissertation thesis, Universitat Politècnica de Catalunya, Spain (2016).

[227] P. K. Bates, O. Chalus, and J. Biegert, "Ultrashort pulse characterization in the mid-infrared," Optics Letters **35**(9), 1377–1379 (2010).

[228] C. Heese, "High-Power Mid-Infrared Femtosecond Laser Pulses," dissertation thesis, University of Münster, Germany (2012).

[229] H. Liang, P. Krogen, R. Grynko, O. Novak, C.-L. Chang, G. J. Stein, D. Weerawarne, B. Shim, F. X. Kärtner, and K.-H. Hong, "Three-octave-spanning supercontinuum generation and sub-two-cycle self-compression of mid-infrared filaments in dielectrics," Optics Letters **40**(6), 1069–1072 (2015).

[230] V. Shumakova, P. Malevich, S. Ališauskas, A. Voronin, A. M. Zheltikov, D. Faccio, D. Kartashov, A. Baltuška, and A. Pugžlys, "Multi-millijoule few-cycle mid-infrared pulses through nonlinear self-compression in bulk," Nature Communications **7** (2016).

[231] A. A. Lanin, A. A. Voronin, E. A. Stepanov, A. B. Fedotov, and A. M. Zheltikov, "Frequency-tunable sub-two-cycle 60-MW-peak-power free-space waveforms in the mid-infrared," Optics Letters **39**(22), 6430–6433 (2014).

[232] P. Lassonde, N. Thiré, L. Arissian, G. Ernotte, F. Poitras, T. Ozaki, A. Larameé, M. Boivin, H. Ibrahim, F. Légaré, and B. E. Schmidt, "High Gain Frequency Domain Optical Parametric Amplification," IEEE Journal of Selected Topics in Quantum Electronics **21**(5), 1–10 (2015).

[233] M. Bache, H. Guo, and B. Zhou, "Generating mid-IR octave-spanning supercontinua and few-cycle pulses with solitons in phase-mismatched quadratic nonlinear crystals," Optical Materials Express **3**(10), 1647–1657 (2013).

[234] M. Bache, X. Liu, and B. Zhou, "Observation of an Octave-Spanning Supercontinuum in the Mid-Infrared using Ultrafast Cascaded Nonlinearities," in *Research in Optical Sciences (2014), paper HTu1C.4*, p. HTu1C.4 (Optical Society of America, 2014).

[235] P. Hölzer, W. Chang, J. C. Travers, A. Nazarkin, J. Nold, N. Y. Joly, M. F. Saleh, F. Biancalana, and P. S. J. Russell, "Femtosecond Nonlinear Fiber Optics in the Ionization Regime," Physical Review Letters **107**(20), 203901 (2011).

[236] J. C. Travers, W. Chang, J. Nold, N. Y. Joly, and P. S. J. Russell, "Ultrafast nonlinear optics in gas-filled hollow-core photonic crystal fibers [Invited]," Journal of the Optical Society of America B **28**(12), A11–A26 (2011).

[237] P. S. J. Russell, P. Hölzer, W. Chang, A. Abdolvand, and J. C. Travers, "Hollow-core photonic crystal fibres for gas-based nonlinear optics," Nature Photonics **8**(4), 278–286 (2014).

[238] M. G. Pullen, B. Wolter, X. Wang, X.-M. Tong, M. Sclafani, M. Baudisch, H. Pires, C. D. Schröter, J. Ullrich, T. Pfeifer, R. Moshammer, J. H. Eberly, and J. Biegert, "Transition from non-sequential to sequential double ionisation in many-electron systems," arXiv:1602.07840 (2016).

[239] B. Wolter, "Electron re-collision dynamics in strong mid-IR fields for diffraction imaging of molecular structure and its fragmentation," dissertation thesis, Universitat Politècnica de Catalunya, Spain (2017).

[240] R. Moshammer, M. Unverzagt, W. Schmitt, J. Ullrich, and H. Schmidt-Böcking, "A 4π recoil-ion electron momentum analyzer: a high-resolution "microscope" for the investigation of the dynamics of atomic, molecular and nuclear reactions," Nuclear Instruments and Methods in Physics Research Section B: Beam Interactions with Materials and Atoms **108**(4), 425–445 (1996).

[241] E. Mevel, P. Breger, R. Trainham, G. Petite, P. Agostini, A. Migus, J.-P. Chambaret, and A. Antonetti, "Atoms in strong optical fields: Evolution from multiphoton to tunnel ionization," Physical Review Letters **70**(4), 406 (1993).

[242] L. Fechner, "High resolution experiments on strong-field ionization of atoms and molecules: test of tunneling theory, the role of doubly excited states, and channel-selective electron spectra," dissertation thesis, Combined Faculties of the Natural Sciences and Mathematics, Ruperto-Carola-University of Heidelberg, Germany p. 109 (2014).

[243] T. Zuo, A. D. Bandrauk, and P. B. Corkum, "Laser-induced electron diffraction: a new tool for probing ultrafast molecular dynamics," Chemical Physics Letters **259**(3), 313–320 (1996).

[244] J. Xu, C. I. Blaga, K. Zhang, Y. H. Lai, C. D. Lin, T. A. Miller, P. Agostini, and L. F. DiMauro, "Diffraction using laser-driven broadband electron wave packets," Nature Communications **5**, 4635 (2014).

[245] D. J. Kane and R. Trebino, "Characterization of arbitrary femtosecond pulses using frequency-resolved optical gating," IEEE Journal of Quantum Electronics **29**(2), 571–579 (1993).

[246] R. Trebino, *Frequency-Resolved Optical Gating: The Measurement of Ultrashort Laser Pulses* (Kluwer Academic, 2000).

[247] C. G. Durfee, S. Backus, H. C. Kapteyn, and M. M. Murnane, "Intense 8-fs pulse generation in the deep ultraviolet," Optics Letters **24**(10), 697–699 (1999).

[248] A. M. Streltsov, J. K. Ranka, and A. L. Gaeta, "Femtosecond ultraviolet autocorrelation measurements based on two-photon conductivity in fused silica," Optics Letters **23**(10), 798–800 (1998).

[249] N. F. Kleimeier, T. Haarlammert, H. Witte, U. Schühle, J.-F. Hochedez, A. BenMoussa, and H. Zacharias, "Autocorrelation and phase retrieval in the UV using two-photon absorption in diamond pin photodiodes," Optics Express **18**(7), 6945–6956 (2010).

Publications

- **M. Baudisch**, A. Marini, J. D. Cox, T. Zhu, F. Silva, S. Teichmann, M. Massicotte, F. Koppens, L. S. Levitov, F. J. García de Abajo, and J. Biegert, *Petahertz optical response in graphene*, under reviewing process in Nature.

- **M. Baudisch**, B. Wolter, M. Pullen, M. Hemmer, and J. Biegert, *High power multi-color OPCPA source with simultaneous femtosecond deep-UV to mid-IR outputs*, Opt. Lett. 41, 3583-3586 (2016).
  Highlighted in Spotlight on Optics, Highlighted Articles from OSA Journals: T. Y. Hwang, Spotlight Summary, Aug. (2016).

- **M. Baudisch**, H. Pires, H. Ishizuki, T. Taira, M. Hemmer, and J. Biegert, *Sub-4-optical-cycle, 340 MW peak power, high stability mid-IR source at 160 kHz*, J. Opt. 17, 094002 (2015).

- **M. Baudisch**, M. Hemmer, H. Pires, and J. Biegert, *Performance of MgO:PPLN, KTA, and KNbO3 for mid-wave infrared broadband parametric amplification at high average power*, Opt. Lett. 39 (20) 5802 (2014).

- U. Elu, **M. Baudisch**, H. Pires, F. Tani, M. H. Frosz, F. Köttig, A. Ermolov, P. St. J. Russell, and J. Biegert, *Soliton-effect self-compressed single-cycle 9.6-W mid-IR pulses from a 21-W OPCPA at 3.25 µm and 160 kHz*, submitted to Optica.

- H. Pires, **M. Baudisch**, D. Sánchez, M. Hemmer, J. Biegert, *Ultrashort pulse generation in the mid-IR*, Prog. in Quant. Electr. 43, 1-30 (2015).

- D. D. Hudson, **M. Baudisch**, D. Werdehausen, B. J. Eggleton, and J. Biegert, *1.9 octave supercontinuum generation in a As2S3 step-index fiber driven by mid-IR OPCPA*, Opt. Lett. 39 (19), 5752 (2014).

- M. Hemmer, **M. Baudisch**, A. Thai, A. Couairon, and J. Biegert, *Self-compression to sub-3-cycle duration of mid-infrared optical pulses in dielectrics*, Opt. Exp. 21 (23), 28095-28102 (2013).

- D. Sánchez, M. Hemmer, **M. Baudisch**, S. L. Cousin, K. Zawilski, P. Schunemann, O. Chalus, C. Simon-Boisson, and J. Biegert, *7 µm, ultrafast, sub-millijoule-level mid-infrared optical parametric chirped pulse amplifier pumped at 2 µm*, Optica 3 (2), 147-150 (2016).

- B. Wolter, M. G. Pullen, **M. Baudisch**, M. Sclafani, M. Hemmer, A. Senftleben, C. D. Schröter, J. Ullrich, R. Moshammer, and J. Biegert, *Strong-Field Physics with Mid-IR Fields*, Phys. Rev. X 5, 021034 (2015).

- B. Wolter, C. Lemell, **M. Baudisch**, M. G. Pullen, X.-M. Tong, M. Hemmer, A. Senftleben, C. D. Schröter, J. Ullrich, R. Moshammer, J. Biegert, and J. Burgdörfer, *Formation of very low energy states crossing the ionization threshold of argon atoms in strong mid-infrared fields*, Phys. Rev. A 90, 063424 (2014).

- D. Sánchez, M. Hemmer, **M. Baudisch**, K. Zawilski, P. Schunemann, H. Hoogland, R. Holzwarth, and J. Biegert, *Broadband mid-IR frequency comb with CdSiP2 and AgGaS2 from an Er,Tm:Ho fiber laser*, Opt. Lett. 39 (24), 6883 (2014).

- M. Hemmer, A. Thai, **M. Baudisch**, H. Ishizuki, T. Taira, and J. Biegert, *18-µJ energy, 160-kHz repetition rate, 250-MW peak power mid-IR OPCPA*, Chin. Opt. Lett. 11 (1), 013202 (2013).

- S. Chaitanya Kumar, M. Jelínek, **M. Baudisch**, K. T. Zawilski, P. G. Schunemann, V. Kubeček, J. Biegert, and M. Ebrahim-Zadeh, *Tunable, high-energy, mid-infrared, picosecond optical parametric generator based on CdSiP2*, Opt. Exp. 20 (14), 15703-15709 (2012).

- B. Wolter, M. G. Pullen, A.-T. Le, **M. Baudisch**, K. Doblhoff-Dier, A. Senftleben, M. Hemmer, C. D. Schröter, J. Ullrich, T. Pfeifer, R. Moshammer, S. Gräfe, O. Vendrell, C. D. Lin, and J. Biegert, *Ultrafast electron diffraction imaging of bond breaking in acetylene*, Science 354 (6310), 308-312 (2016).

- M. G. Pullen, B. Wolter, A. -T. Le, **M. Baudisch**, M. Sclafani, H. Pires, C. D. Schröter, J. Ullrich, R. Moshammer, T. Pfeifer, C. D. Lin, and J. Biegert, *Influence of orbital symmetry on diffraction imaging with rescattering electron wave packets*, Nat. Comm. 7, 11922 (2016).

- M. G. Pullen, B. Wolter, A.-T. Le, **M. Baudisch**, M. Hemmer, A. Senftleben, C. D. Schröter, J. Ullrich, R. Moshammer, C. D. Lin, and J. Biegert, *Imaging an aligned polyatomic molecule with laser-induced electron diffraction*, Nat. Comm. 6, 7262 (2015).

- M. G Pullen, J. Durá, B. Wolter, **M. Baudisch**, M. Hemmer, N. Camus, A. Senftleben, C. D. Schröter, R. Moshammer, J. Ullrich and J. Biegert, *Kinematically complete measurements of strong field ionization with mid-IR pulses*, J. Phys. B: At. Mol. Opt. Phys. 47, 204010 (2014).

- F. Silva, D.R. Austin, A. Thai, **M. Baudisch**, M. Hemmer, D. Faccio, A. Couairon, and J. Biegert, *Multi-octave supercontinuum generation from mid-infrared filamentation in a bulk crystal*, Nat. Comm. 3, 807 (2012).
  Highlighted in Nature Photonics: O. Graydon, *Supercontinua: Broader than ever*, Nat. Phot. 6 (7), 413 (2012).

- J. Durá, N. Camus, A. Thai, A. Britz, M. Hemmer, **M. Baudisch**, A. Senftleben, C. D. Schröter, J. Ullrich, R. Moshammer, and J. Biegert, *Ionization with low-frequency fields in the tunneling regime*, Nat. Scientific Rep. 3, 2675 (2013).

- M. G. Pullen, B. Wolter, X. Wang, X.-M. Tong, M. Sclafani, **M. Baudisch**, H. Pires, C. D. Schröter, J. Ullrich, T. Pfiefer, Robert Moshammer, C. D. Lin, J. H. Eberly, and J. Biegert, *Transition from non-sequential to sequential double ionisation in many-electron systems*, submitted to Physical Review Letters.